On the role of nonequilibrium processes in intracellular organization

Emanuel Josef Reithmann

Munich 2019

On the role of nonequilibrium processes in intracellular organization

Emanuel Josef Reithmann

A dissertation submitted
to the Faculty of Physics at the
Ludwig–Maximilians–Universität München
for the degree of
Doctor rerum naturalium

Munich, 7th February 2019

First referee: Prof. Dr. Erwin Frey
Second referee: Prof. Dr. Mauro Mobilia
Day of the oral examination: 21st March 2019

Zusammenfassung (Summary in German)

Jeder lebende Organismus ist auf die Fähigkeit angewiesen, Ordnung zu schaffen und aufrechtzuerhalten. Diese Dissertation beschäftigt sich mit Phänomenen, bei denen Prozesse außerhalb des thermischen Gleichgewichts eine entscheidende Rolle für die Strukturbildung in Zellen spielen. Essenziell für diese Strukturbildung ist das interne Proteingerüst, das Zytoskelett, auf dem sich molekulare Motoren bewegen, die die innere Organisation der Zelle wesentlich prägen. Mittels theoretischer Konzepte wurden Prozesse der intrazellulären Strukturbildung auf zwei Ebenen analysiert: (**I**) der Organisation von Proteinen auf einem einzelnen Zytoskelettfilament und (**II**) der zellweiten Organisation von Proteinen.

I **Organisation von Proteinen auf Zytoskelettfilamenten** *mit Himanshu Pandey, Louis Reese, Patrick Wilke, Leah Gheber und Erwin Frey.*
In einem ersten Projekt befassten wir uns mit Proteinen, die die Architektur des Zytoskeletts regulieren. Dabei entdeckten wir, dass eine eindimensionale Diffusion mit einem darauf folgenden Einfangprozess dazu führt, dass diese Proteine effizient zu ihrem Zielbindeplatz gelangen. Für bestimmte Biomoleküle bestätigte sich, dass der oben beschriebene Vorgang wesentlich zu ihrer intrazellulären Funktion beiträgt. Ein zweites Projekt führte zu dem Ergebnis, dass der molekulare Transport entlang von Zytoskelettfilamenten veränderten Prinzipien unterliegt, sobald zwei Arten von molekularen Motoren mit unterschiedlichen „Gangarten“ vorhanden sind. Aufgrund einer Verstärkung von sterischen Wechselwirkungen durch topologische Effekte entstehen bereits bei geringen Konzentrationen dieser Motoren Staus. Daher könnten Stauprozesse auch im lebenden Organismus einflussreicher sein als bisher angenommen. Im dritten Projekt setzten wir uns mit der Richtungsumkehr von Motorproteinen auseinander. Basierend auf experimentellen Erkenntnissen unserer Kollaborationspartner, der Gruppe von Prof. Leah Gheber, entwickelten wir ein neues Modell für den Richtungswechsel von molekularen Motoren. Das Modell zeigte, dass bisherige – scheinbar widersprüchliche – Hypothesen zur Richtungsumkehr unterschiedliche Aspekte ein und desselben Mechanismus sein könnten.

II **Zellweite Organisation von Proteinen** *mit Jonas Denk, Lorenz Huber, Angela Oberhofer, Peter Spieler, Zeynep Ökten und Erwin Frey.*
Im vierten Projekt zeigten wir, dass gekrümmte Polymere, die sich aktiv auf einer zweidimensionalen Oberfläche bewegen, dynamische Ringmuster bilden können. Dies könnte für den Proteinring, der die Zellteilung in Bakterien antreibt und durch einen bisher unbekannten Mechanismus entsteht, von Bedeutung sein. In einem letzten Projekt untersuchten wir die zellweite Organisation von dunklen Pigmentorganellen. Die Reorganisation dieser Organellen in Hautzellen von Fischen und Amphibien ermöglicht eine Veränderung deren Hautfarbe. Mit Hilfe von Simulationen und theoretischen Analysen brachten wir die von unseren Kollaborationspartnern, der Gruppe von Dr. Zeynep Ökten, gemessenen biochemischen Veränderungen von molekularen Motoren mit der zellweiten Organisation der Pigmentorganellen in Zusammenhang.

Summary

Each living organism relies on the ability to establish and maintain order. This thesis addresses multiple cases where processes out of thermal equilibrium fulfill a critical role in the formation of order in cells. A key player in this respect is the cell's internal protein scaffold—the cytoskeleton—which serves as a track for molecular motors that shape the cell's interior organization. By means of theoretical modeling, processes related to intracellular organization were studied on two different levels: Part I focuses on principles of the organization of proteins on an individual cytoskeletal filament. Part II elucidates mechanisms that determine the cell-wide organization of proteins.

I Organization of proteins on cytoskeletal filaments
with Himanshu Pandey, Louis Reese, Patrick Wilke, Leah Gheber, and Erwin Frey
In the first project, we focused on proteins that regulate the cytoskeletal architecture. We revealed that one dimensional diffusion that is followed by a capturing process facilitates the localization of these proteins on their target sites. For several specific biomolecules, we showed that this "diffusion and capture" mechanism contributes essentially to their cellular function. In a second project, we unraveled that the collective dynamics of molecular motors along cytoskeletal filaments exhibits a different phenomenology when two species of molecular motors with different gaits are present as compared to the collective motion of a single species. Due to an amplification of steric interactions of molecular motors by topological effects, the jamming of molecular motors becomes important at low concentrations of these proteins. These findings affect our view on intracellular transport as jamming phenomena might—because of this amplification—be more significant than previously thought. In a third project, we investigated the switching of directionality of specific molecular motors. Based on experimental findings of our collaborators in this project, the group of Prof. Leah Gheber, we suggested a novel model for the directional switching of the collective motion of motor proteins. The model showed that previous—apparently unrelated—hypotheses for the directional switching may be different aspects of the same biomolecular mechanism.

II Cell-wide organization of proteins
with Jonas Denk, Lorenz Huber, Angela Oberhofer, Peter Spieler, Zeynep Ökten, and Erwin Frey.
In the fourth project, we revealed that curved filaments which move actively on a two-dimensional surface can self-organize into dynamic vortex patterns. This might be relevant for the dynamic protein ring that drives bacterial cell division and which forms by a mechanism that is poorly understood. In a last project we addressed the cell-wide organization of dark pigment organelles. The reorganization of these organelles in skin cells enables fish and amphibians to adapt their skin color to environmental factors. Based on *in vitro* results of our collaborators, the group of Dr. Zeynep Ökten, we related measured biochemical changes of molecular motors to a cell-wide organization of these organelles. In this way, we identified basic mechanisms that determine the dynamic redistribution of pigment organelles in a cell and retraced a potential evolutionary pathway.

Abstracts of the projects and contribution

I Localization and association of proteins by the diffusion and capture mechanism

with *Louis Reese, and Erwin Frey.*
Published in "Quantifying Protein Diffusion and Capture on Filaments" (*Biophys. J.* **108** (4), 787–790 (2015)) to which I contributed as first author, and "Nonequilibrium Diffusion and Capture Mechanism Ensures Tip Localization of Regulating Proteins on Dynamic Filaments" (*Phys. Rev. Lett.* **117** (7), 078102 (2016)) to which I contributed as first author.

Background

Precise regulation of the cytoskeleton is vital for all eukaryotic cells and relies on a largely unsolved interplay of a multitude of microtubule associated proteins. In this context, the microtubule tip plays a distinguished role as it serves as a reaction site for many regulating proteins. Efficient localization of the regulating proteins at the microtubule tip is thus essential for the regulation of microtubules. Moreover, recent experimental studies suggested that many microtubule regulation proteins show the capability of diffusing passively on the microtubule lattice. Typically, diffusive motion ceases or is suppressed once the regulating proteins reach the microtubule tip, a process which breaks detailed balance and to which we will refer to as the *diffusion and capture mechanism*.

Research questions

This project elucidated mechanisms by which diffusive motion along the microtubule can facilitate association with a target reaction site, in our case the microtubule tip. Using simple lattice gas models, we addressed the following questions: Can we quantify the association rate of proteins that employ a diffusion and capture mechanism? How much does diffusion and capture contribute to the overall binding rate of regulating proteins to the microtubule tip? Can we theoretically predict the distribution of proteins along the microtubule and thus quantify the localization of proteins at the tip? Do regulating proteins indeed localize at microtubule tips due to the diffusion and capture process and, if so, does the process contribute to the intracellular functions of regulatory proteins?

Key findings and their relevance

Quantifying the association of proteins by means of an effective Michaelis-Menten theory.
In a first step, we developed a theory for enzymatic reactions driven by microtubule

regulating proteins that are subject to a diffusion and capture mechanism. The central result of the theoretical analysis was a novel, effective Michaelis-Menten theory. The effective Michaelis constant of this theory accounts for the current of proteins along the microtubule arising due to the diffusion and capture mechanism. This effective Michaelis constant depends solely on experimentally accessible parameters: the diffusion constant of proteins on a microtubule, the particle attachment rates, and the dwell time of particles on the microtubule bulk and at the microtubule tip. It therefore provides a simple means to predict the efficiency of protein association due to diffusion and capture for regulating proteins.

Diffusion and capture dominates tip binding for many regulating proteins.
Based on this theory, we determined the contribution of filament diffusion to tip binding quantitatively for 17 different previous experiments with microtubule associated proteins. In that way, we broadly assessed the impact of diffusive motion along cytoskeletal filaments to specific binding at a given reaction site: Our analysis predicted that in all the 17 investigated experiments at least 90% of the tip-binding events are due to diffusion and capture. Direct tip-binding events from the solution or cytoplasm were negligible in all cases, making a limitation of this rate by the time scales imposed by three dimensional diffusion mostly irrelevant.

Diffusion and capture correlates particle occupations.
In a second step, we turned to the distribution of the proteins along a microtubule. Using an extended model, we explicitly accounted for growing and shrinking microtubules to apply our theory to a central microtubule depolymerase (MCAK) and a central polymerase (XMAP215). Strikingly, we found that standard approaches to compute the occupation of the microtubule by particles fail due to correlations that extended over large distances. We overcame this limitation by developing a theoretical method that allowed us to include relevant correlations along the whole filament and thereby to compute the particle distribution. We validated our theory with a direct comparison to experimental data for MCAK and XMAP215.

Diffusion and capture operates most efficiently at cellular conditions for two central regulating proteins.
Using our verified theoretical framework, we studied the efficiency of the diffusion and capture mechanism for MCAK and XMAP215. In both cases, we found that localization of the proteins at the microtubule tip due to the diffusion and capture mechanism is most significant at cellular concentrations of these proteins. This suggests that the diffusion and capture mechanism is optimized for cellular conditions and thus of relevance also *in vivo*.

Related publications and contributions
This project resulted in the publications "Quantifying Protein Diffusion and Capture on Filaments" (*Biophys. J.* **108** (4), 787–790 (2015)), and "Nonequilibrium Diffusion and Capture Mechanism Ensures Tip Localization of Regulating Proteins on Dy-

namic Filaments" (*Phys. Rev. Lett.* **117** (7), 078102 (2016)) to which I contributed as first author in both cases. In both publications, I contributed to research design, development of the numerical and analytic methods, interpretation of the results, and writing the manuscript. The other authors are Louis Reese and Erwin Frey, who contributed to the research design, the interpretation of the results, and writing the manuscript.

system is of importance but also their arrangement. Because the network topology of the underlying stochastic process amplifies the impact of steric hindrance, we termed this type of interaction *topological hindrance*.

Jamming in two-species transport depends on the number of lanes and the species fraction. The consequences of topological hindrance showed a dependency on (a) the system width, i.e., the number of lanes composing the cylindrical system, and (b) the fraction of particles from the second species. This exceeds naïve analyses that are based on mean-field approaches, where only the total density is relevant for jamming. Moreover, the effects created by topological hindrance set in already at very small fractions of a second species (approximately 5%) and rapidly increase in relevance when increasing the number of lanes. In the limit of a large number of lanes, topological hindrance becomes the major determinant of particle dynamics.

Two-species transport leads to self-organization and pattern formation. Another surprising observation we made for our two-species model was the emergence of wavelike patterns in the average particle density. In systems with small aspect ratios, i.e., for small system lengths or large numbers of lanes, particles self-organize into patterns that are reflected by oscillations in the average particle density. This opposes most other transport models, where patterns in the particle occupation are absent.

Molecular crowding may take place at significantly lower densities than previously thought. In the last step, we probed the robustness of our findings for model extensions with respect to several biomolecular aspects of motor proteins. We found that also for models that account for many specific biomolecular features of motor proteins the key phenomenology remains unchanged and that topological hindrance is of major importance also in these cases. Therefore, our analyses showed that mixed-species systems start to jam already at much lower particle densities than expected based on the previous knowledge from models for single-species transport. Active transport inside cells may thus exhibit a much richer phenomenology than previously thought.

Related publications and contributions

This project resulted in the publication "Two-Species Active Transport along Cylindrical Biofilaments is Limited by Emergent Topological Hindrance" (*Phys. Rev. X* **8**(3), 031063 (2018)) to which I contributed as a shared first author together with Patrick Wilke. Together with Patrick Wilke, I contributed to research design, development of the numerical and analytic methods, interpretation of the results, and writing the manuscript. The other author on this project was Erwin Frey who contributed to research design, interpretation of the results, and writing the manuscript.

III Directional reversal of the collective motion of kinesins

with *Himanshu Pandey, Leah Gheber, and Erwin Frey*

Background

Over decades, the motion of molecular motors was thought to occur unidirectionally towards the plus-ends of microtubules. In recent years, however, several molecular motors have been shown to switch their direction of motion as a response to a change of diverse experimental conditions or biomolecular properties. For example, it has been shown that specific molecular motors can switch their direction of motion in experiments when forming clusters of multiple particles or when the salt concentration of the buffer changes. While the phenomenon of directional switching has been observed for a multitude of molecular motors, an understanding of the underlying mechanism remained elusive. In this project, we focused on the directional reversal of Cin8, a motor protein of yeast. Building on results from *in vitro* experiments of our collaborators on this project, the group of Prof. Leah Gheber at the Ben-Gurion University of the Negev, we addressed this problem by means of statistical analysis and theoretical modeling.

Research questions

In this project, we studied the following research questions: What are the implications of the *in vitro* measurements of our collaborators for the interaction and motility of directionally switching motor proteins? Is there a simple mechanistic explanation that quantitatively explains the experimental findings of our research partners? Is it possible to unify the various previous hypotheses for a directional switching of the motion of motor proteins and to formulate a single model that explains all observations?

Key findings and their relevance

The Cin8 motor protein of yeast is subject to weak intermolecular attractive interactions.
We showed that the experimental findings of our collaborators can be understood by the presence of attractive forces between individual molecular motors. These attractive forces aggregate particles into small clusters which, in turn, affects their motility by suppressing the motion of individual particles in a cluster. Our methods allowed us to specifically compute the strength of these forces.

An anisotropic response of the Cin8 motor protein to forces that oppose motion reverts the movement of clusters of particles.
Inspired by the finding that attractive forces between individual molecular motors induce a drag in each other's motion we proposed a novel model for the directional switching of these proteins: We postulated that the Cin8 motor protein moves actively in both directions on a microtubule and that these two modes of active motion respond anisotropically to opposing forces. By theoretical modeling, we succeeded in showing (a) that this hypothesis causes a directional switching triggered by clustering of Cin8

and (b) that the proposed model fully reproduces the experimental observations made by our collaborators on a quantitative level.

Our proposed model consistently explains previous experimental results.
Finally, we related our proposed model to previous findings for motor proteins that can switch their direction of motion. We showed that our hypothesis of an anisotropic response of active motion to drag also consistently explains various previous findings. In fact, our analysis showed that apparently unrelated observations might be different aspects of the same mechanism. In this way, our proposed model for the directional switching of molecular motors unifies different existing hypotheses for this phenomenon.

Project contributions
This project is currently prepared for publication in a peer-reviewed journal [1]. In this research project, I contributed to the research design, development of analytic and numerical methods, and the interpretation of results. All experimental data and related analyses were performed by the group of Prof. Leah Gheber at the Ben-Gurion University of the Negev and, in particular, by Dr. Himanshu Pandey. Himanshu Pandey, Maria Popov, Leah Gheber, and Erwin Frey contributed also to the research design, and the interpretation of the results.

IV The formation of dynamic vortex patterns by active curved polymers of the protein FtsZ

with Jonas Denk, Lorenz Huber, and Erwin Frey.
Published in "Active Curved Polymers Form Vortex Patterns on Membranes" (*Phys. Rev. Lett.* **116** (17), 178301 (2016)) to which I contributed as second author.

Background

One of the major players in bacterial cell division is the so-called Z ring, a patchy assembly of overlapping, curved polymers formed by the protein FtsZ. Clear mechanisms by which the Z ring assembles are, however, largely elusive. A recent *in vitro* study emphasized the importance of nonequilibrium processes for the formation of the FtsZ ring [2]: Reconstituted FtsZ polymers on a supported lipid bilayer showed nucleotide dependent treadmilling motion that propelled the polymers over the membrane. Since FtsZ assembles into curved polymers, the motion of these polymers occurred preferentially along circular paths. Strikingly, in the corresponding experiments, the moving filaments self-organized into dynamic rings which led to speculations if active motion also contributes to the formation of the FtsZ ring *in vivo*. Inspired by these findings, we sought for generic mechanisms for the formation of patterns by curved polymers that move actively on a plane. We employed two complementary approaches to study the system: Brownian dynamics simulations, that explicitly take the microscopic structure of extended polymers into account, and a field-theoretic kinetic Boltzmann approach, that provides a mesoscopic description of the system.

Research questions

Based on these complementary approaches, we addressed the following questions: Do self-propelled, curved particles self-organize into patterns? If so, does this behavior explain self-organization into ring-like structures? Under which conditions are these structures stable? Does the field theoretic approach support the existence of nonequilbirium phase transitions in our system?

Key findings and their relevance

Transitions between differently ordered states are predicted consistently by two distinct approaches.
Both of our different approaches consistently predicted transitions between differently ordered states: For low particle densities on the plane or high levels of noise, the system lacked global order. Opposed to that, collective order emerged above a certain density or below a certain level of noise. Remarkably, despite the different nature of both approaches, we found qualitative agreement of the respective phase diagrams.

Active curved filaments on membranes self organize into vortex patterns.
For intermediate densities and intermediate levels of noise, the system self organized into dynamic ring-like structures. These were composed of several curved filaments

that very much resembled the ones observed in the experiment described above [2]. This is relevant for several reasons: First, it shows that ring-like patterns can actually form without attractive interactions between the polymers. Second, the formation of the vortices in our system can be affected efficiently by varying, for example, the density of polymers on the plane. Such a density-dependent response of pattern formation could also be exploited in cell biology to dynamically switch the formation of vortices on and off.

Onset of pattern formation is governed by a novel type of a complex Ginzburg-Landau equation.
Our mathematical analysis based on the kinetic Boltzmann approach revealed that the onset of pattern formation is governed by a novel form of a generalized Ginzburg-Landau equation. A preliminary analysis suggests that this equation shows qualitatively new properties as compared to an analogous equation that describes an ensemble of straight moving particles. While we did not perform a detailed analysis, our preliminary results indicate that pattern formation for particles that move along circular paths might be fundamentally different from that of active-matter systems analyzed previously that were mostly concerned with straight propulsion.

Related publications and contributions
This project resulted in the publication "Active Curved Polymers Form Vortex Patterns on Membranes" (*Phys. Rev. Lett.* **116** (17), 178301 (2016)) to which I contributed as second author. Together with Lorenz Huber, Jonas Denk, and Erwin Frey, I contributed to research design, interpretation of the results, and writing the manuscript. Jonas Denk and Lorenz Huber developed the analytic and numeric methods. The corresponding publication is also reprinted in the PhD theses of Jonas Denk and Lorenz Huber.

V Cell-wide organization of pigment organelles

with Angela Oberhofer, Peter Spieler, Zeynep Ökten, and Erwin Frey.

Background

Many of a cell's functional constituents such as organelles need to be distributed and organized in a highly orchestrated manner within the cell. To this end, they are actively transported by molecular motors on the two cytoskeletal components: microtubules and actin filaments. Although it is long recognized that motion on both of these cytoskeletal components is vital to ensure the proper organization of proteins within a cell, general mechanisms that govern the cell-wide distribution of organelles are elusive. In this project we addressed this problem for the case of dark pigment organelles in highly specialized skin cells of fish and amphibians. By a redistribution of these pigment organelles within a cell, the corresponding animals are capable of adapting their skin color to environmental factors. In collaboration with the group of Dr. Zeynep Ökten at the TU Munich, we related biomolecular changes of individual motors that move the pigment organelles on the cytoskeleton to a cell-wide distribution of the organelles.

Research questions

The goal of this project was to identify basic mechanisms that govern the cell-wide redistribution of pigment-organelles from the biomolecular level up to the level of collective dynamics. In this respect, we asked: What biomolecluar changes of the motor proteins that move pigment organelles are responsible for a dynamic redistribution of pigment organelles? Can we use computational modeling to connect these biomolecular changes to a cell-wide dynamic reorganization of pigment organelles as observed *in vivo*? Are there regulatory principles that might have constrained an evolutionary pathway of biomolecular changes observed from early to lower vertebrates?

Key findings and their relevance

A transfer of pigment organelles between actin filaments and microtubules as measured in vitro *reconstitutes to a cell-wide redistribution of pigment organelles* in silico.

The experimental results from our collaborators revealed that signaling factors that drive a dynamic redistribution of pigment organelles *in vivo* are related to a change in the probability at which single motor proteins that move the organelles switch from actin to microtubule filaments. We used computational modeling to relate this measurement of the switching probabilities of an individual motor protein to the cell-wide organization of pigment organelles in a virtual cell. Strikingly, the sole change of the probability of an organelle to switch from actin filaments to microtubules sufficed to reconstitute a cell-wide redistribution of the pigment organelles *in silico*.

The global redistribution of pigment organelles is regulated efficiently and robustly by a modulation of the cytoskeletal crosstalk as measured in vitro.
Our theoretical approach further allowed us to assess the efficiency of the regulatory mechanism uncovered in the experiments. In this way we could show that a regulation of the intracellular organization of pigment organelles is not only possible due to change of the switching probabilities described above, but that a cell-wide regulation of the organelle distribution in our model is particularly robust and efficient for the switching probabilities quantified *in vitro*.

In silico *modeling identifies potential evolutionary pathways that might have governed the regulation of the cell-wide distribution of organelles.*
Finally, our methods identified potential evolutionary pathways: Our collaborators unraveled that the motor proteins which move pigment organelles in early vertebrates (fish) are regulated differently than those in lower vertebrates (amphibians). Our theoretical analysis provided a rationale for the observed changes: The experimentally measured evolution of the switching probabilities of molecular motors of fish to that of amphibians strongly correlated with changes of parameters that had a strong impact on the cell-wide distribution of organelles in our simulations.

Project contributions
This project is currently prepared for publication in a peer-reviewed journal [3]. In this research project, I contributed to the research design, development of analytic and numerical methods, and the interpretation of results. All experimental data and related analyses were performed by the group of Dr. Zeynep Ökten at the TU Munich and, in particular, by Dr. Angela Oberhofer and Peter Spieler. Angela Oberhofer, Peter Spieler, Zeynep Ökten and Erwin Frey contributed also to the research design, and the interpretation of the results.

Contents

1 Preface

Every living organism depends on its ability to establish and maintain structure. As early as 1790, the philosopher Immanuel Kant defined life as a "self-organizing" process—a concept that is anchored in many current theoretical approaches to understand living systems [4–6]. The emergence of structures and patterns is manifested on all levels of life: A dynamic collective of a group of moving animals is often organized such that an efficient response to the environment is possible and may—in this way—act like a single, large organism [7]. Highly orchestrated processes related to morphogenesis create the functional shape of each living organism [8]. But even on the smallest scale of life—within each single cell—the formation and perpetuation of structure is vital [5, 9–11], which is the topic of this thesis.

To enable the formation of order, living systems permanently transduce energy. From the perspective of theoretical physics, pattern formation and self-organization in biological systems is thus often inherently linked to nonequilibrium physics. However, while general concepts that bridge the behavior of a single component of a system to the collective properties of the system itself are well-known in thermal equilibrium, general theoretical principles for systems out of thermal equilibrium are largely absent. The problem of finding a suitable theoretical framework has thus attracted the interest of many physicists over decades and can currently be regarded as one of the major challenges in physics [12–14]. As it remains unclear whether a general theoretical framework that characterizes nonequilibrium processes exists, a complementary approach is to study systems that are subject to different microscopic rules of interaction separately. In that way, one may hope to recognize similar principles in different systems, which might ultimately guide the way to a general understanding of the formation of order in nonequilibrium systems. In this light, my thesis covers several examples where nonequilibrium processes play an essential role in the formation of order and structure in processes related to cell biology.

A key player of intracellular organization in eukaryotes is the cell's internal protein scaffold, the cytoskeleton [11, 15, 16]. The cyoskeleton consists of two networks of filamentous biopolymers that span throughout the cyoplasm: The actin network, which consists of short and flexible (on the scale of a cell) polymers, and the microtubule network, which consists of long, stiff tubular polymers [17].[1] One particularly fascinating property of the eukaryotic cytoskeleton is its vast variety of different morphologies. Depending on the cell type, the stage of the cell cycle, or the position

1 For simplicity, we do not cover intermediate filaments in this introductory text.

within the cell, otherwise identical biomolecular building blocks create a broad variety of structures that differ widely in their function [17–19]. For example, actin may assemble—depending on the cell region—either in a strongly branched meshwork composing lamellipodia or in tightly connected parallel bundles within filopodia [17, 20–22]. Likewise, cilia rely on the ability to organize microtubules into the highly symmetric and regular axonemes. There, nine parallel microtubule duplets assemble in a circular shape around two more microtubules [17, 23, 24]. However, the most common configuration of microtubules in cells (during interphase) is a much less regular star-like aster that spans throughout the cytoplasm [17]. The fascinating trait of the cytoskeleton to adopt different shapes and structures is also apparent *in vitro*: When mixing the building blocks of the cytoskeleton with proteins that bind to and move on cytoskeletal filaments, these components have been shown to self-organize into a broad range of different structures. For example, microtubular architectures ranging from asters over vortices to bundles were observed [25–28]. Similarly, also actin assembles in a variety of different shapes *in vitro*, such as differently branched meshworks, rings, or bundles [5, 11, 29]. Interestingly, not only crosslinked cytoskeletal filaments but also an ensemble of driven cytoskeletal filaments shows the capability to self-organize into different dynamic patterns: In several experimental studies, collisions and interactions between cytoskeletal filaments that were translocated, for example, by molecular motors, over a planar surface led to the emergence of robust patterns such as polar waves, nematic lanes, or vortices [2, 30–34].

Regarding the role of the cytoskeleton in intracellular organization, nonequilibrium physics enters in two different aspects: The dynamics of the cytoskeleton itself and the dynamics of motor proteins—biomolecular machines that convert chemical energy into motion—-on the cytoskeletal network. We briefly explain both processes in the following.

Although the name cytoskeleton implies a static protein scaffold, its corresponding protein structures are very dynamic and cells critically depend on the ability to change the cytoskeleton's morphology [17, 19, 35, 36]. In fact, assembly and disassembly of the cytoskeletal components is connected to the turnover of ATP or GTP, which turns the (de)polymerization of cytoskeletal filaments into a nonequilibrium process [36, 37]. Only because of the dynamic properties of the actin network, cells are able to move, divide, and exchange large molecules with their environment [20–22]. Another very prominent example in the context of cytoskeletal dynamics is the mitotic spindle: For cell division, the monopolar microtubule aster of interphase disassembles and the bipolar mitotic spindle, that ultimately segregates chromosomes, appears [38, 39]. The vital role of these dynamic properties becomes dramatically evident when disabling the microtubules' intrinsic dynamics: Adding microtubule stabilizing drugs like paclitaxel to a dividing cell causes a failure of the assembly of the mitotic spindle [40]. In this way, dividing cells can be forced into apoptosis—programmed cell death. Therefore, rapidly dividing tissue can be particularly harmed by such drugs, which explains

the central role of microtubule-stabilizing drugs in the treatment of cancer. In fact, changing microtubule or actin dynamics is regarded as one of the most successful strategies in chemotherapy [40, 41].

But not only the dynamics of the cytoskeleton itself plays an important role in the formation of structure within a cell. The cytoskeleton serves as a network of tracks for molecular motors that bind to the cytoskeletal components and translocate along them by transducing chemical energy in the form of ATP [15, 42]. Molecular motors are typically categorized into three large families that each comprise a multitude of members [43–46]: Myosin motors, that move towards the barbed ends of actin filaments, kinesin motors, that move towards the plus ends of microtubules, and dynein motors, that move towards the minus ends of microtubules.[2] These motors significantly shape the interior organization of cells by actively moving organelles and other constituents of the cell [15, 47–52]. One remarkable phenomenon that demonstrates the regulatory power of molecular motors on intracellular organization can be observed in skin cells of amphibians and fish: A cell-wide redistribution of dark pigment organelles leads to a switch between a bright and a dark appearance [15, 53–59]. This is achieved by either aggregating the pigment organelles in the center of the cell or by dispersing them throughout the cell. In this way, fish and amphibians can adapt the color of their skin to environmental cues. The dynamic redistribution of these organelles has by now become a paradigm to study principles of intracellular organization in general and is also subject of Section 3.2 of this thesis.

Throughout this thesis, several examples are discussed where nonequilibrium processes critically shape cell biology and intracellular organization. Specifically, we address principles of the organization of proteins within a cell on two different levels: In Chapter 2, we present nonequilibrium processes that organize proteins along individual filaments of the cyoskeleton. In Chapter 3, we discuss nonequilibrium processes in the context of a cell-wide organization of proteins. In detail, the different research projects cover the following topics:

Projects on the organization of proteins along cytoskeletal filaments (Chapter 2)

- *Localization and association of proteins by the diffusion and capture mechanism*
  The first project is concerned with the localization of proteins that regulate cyoskeletal filaments at the respective filament ends. This is of importance as many regulatory proteins can only function when they are bound to the end of the filaments they regulate. We showed that regulating proteins localize particularly efficiently at the respective ends when they employ one-dimensional diffusion along the filaments. To ensure localization, however, we further

2 It should be noted that several exceptions to the above stated directionalities are known which are, however, neglected here for simplicity. For a discussion on the directionality of kinesin motors see also Section 2.3.

highlighted that it is critical that one-dimensional diffusion ceases once the end is reached. In this way, detailed balance is broken which establishes a current of particles towards the ends of filaments that is key for the localization of proteins there. Thus, the nonequilibrium nature of a capturing mechanism organizes regulating proteins along a filament and thereby contributes to their efficient functioning. Details of this project and the corresponding publications [60, 61] to which I contributed as first author are provided in Section 2.1.

- *Two-species transport and topological hindrance*
  The second project addresses the collective dynamics of two species of molecular motors that move actively along a microtubule. Motivated by recent experimental findings, the two species are distinguished by different gaits: One species walks straight ahead along the cylindrical geometry of a microtubule while the other one follows a helical path. We found that the different network topology of the corresponding stochastic process amplifies steric interactions between the particles and thereby leads to a substantially different phenomenology of the ensuing collective properties as compared to transport in the presence of only a single species. In particular, jamming of molecular motors occurs already at comparably low densities of particles and particles self-organize into wave-like patterns along the microtubule—two findings that contrast previous findings for molecular transport by a single species. Thus, our findings showed that jamming might be more important also at cellular concentrations of molecular motors than previously thought and that multi-species transport follows different physical principles than transport by a single species of molecular motors. An overview of this project and the corresponding publication [62] to which I contributed as shared first author are provided in Section 2.2 of this thesis.

- *Directional reversal of the collective motion of kinesins*
  In the third project we focus on the phenomenon of directional reversal in the motion of molecular motors. Based on experimental results of our collaborating partners on this project, the group of Prof. Leah Gheber at the Ben-Gurion University of the Negev, we developed a novel model that explains directional reversal of the collective motion of the yeast kinesin Cin8. By means of statistical analysis and computational modeling, we showed that these molecules form clusters on a microtubule due to attractive forces between the molecules. Strikingly, clustering of molecules reversed the direction of motion. Our analysis revealed that an anisotropic response of active motion to drag explains the observations made in the experiments quantitatively. Moreover, our model provided a new perspective on the phenomenon of directional switching in general: It showed that several previous apparently unrelated experimental findings on how to trigger the directional switching of the motion of kinesins might be different aspects of our proposed mechanism. Results related to this project

are presented in Section 2.3. A publication related to this research project is currently in preparation [1].

Projects on the cell-wide organization of proteins (Chapter 3)

- *The contribution of vortex formation of active curved polymers to bacterial cell division*
  The topic of the fourth project is the formation of vortices by a collective of actively moving curved polymers on a two-dimensional surface. In detail, we studied the collective dynamics of the protein FtsZ. In bacterial cells, this protein forms the polymer ring that drives the constriction of cells during cell division. The underlying principles that lead to the formation of the FtsZ ring are, however, largely unknown. Our research related to this project was inspired by recent experimental findings which showed that FtsZ forms curved polymers that move actively over an artificial membrane by a treadmilling mechanism [2]. We showed that active motion of curved polymers on a surface leads to their self-organization into dynamic vortices already in the absence of attractive forces: For surface densities above a certain threshold, local interactions between the active polymers suffice to form dynamic vortex patterns reminiscent of the FtsZ ring *in vivo*. Thus, our findings demonstrate that the formation of the Z ring might be governed by general principles related to the active motion of an ensemble of FtsZ polymers while specific interactions are *per se* not required. Details of this project and the corresponding publication [63] to which I contributed as second author are provided in Section 3.1.

- *Cell-wide organization of pigment organelles*
  The last project of this thesis is concerned with the cell-wide distribution of dark pigment organelles that are transported by molecular motors along the cytoskeletal networks in skin cells of fish and amphibians. By redistributing the organelles, the respective organisms can change the color of their skin in response to environmental factors. This redistribution is achieved by either aggregating the pigment organelles in the center of the cell, which causes a bright color of the respective cell, or by dispersing the organelles throughout the cell, which provides a dark color to the respective cell. The group of Dr. Zeynep Ökten at the TU Munich, our research partners in this project, showed experimentally that this change of the cell-wide organization goes along with a changed rate of the transfer of organelles between the two cytoskeletal components, actin filaments and microtubules. By means of computational modeling we related these measurements to the collective dynamics of organelles in a cell. Implementing the results of the experimental measurements in the computational model indeed provoked a cell-wide redistribution of organelles *in silico* that very much resembled the change between organelle aggregation

and dispersion *in vivo*. Moreover, our theoretical analysis provided a rationale for the evolution of biomolecular characteristics determined experimentally for different species: The regulation of the cell-wide organization of pigment organelles was only responsive to biomolecular changes in a limited fashion, which linked regulatory principles to evolutionary changes. Results related to this project are presented in Section 3.2. A publication related to this research project is currently in preparation [3].

2 Organization of proteins on single filaments

2.1 Localization and association of proteins by the diffusion and capture mechanism

---

The topic of this section is the *diffusion and capture* mechanism of proteins that regulate cytoskeletal filaments. This mechanism occurs among many regulating proteins and consists of a one-dimensional diffusive motion along a filament that ceases once the biomolecule reaches the end of the filament. In many cases, the filament end serves as a target site for the regulating proteins: Once captured at this location, the proteins can execute their regulatory function. Concerning the diffusion and capture mechanism, we were able to identify two central functional characteristics: (1) It localizes proteins at the target site and thereby contributes substantially to the functionality of many regulating proteins. (2) Localization goes along with correlations of the occupation of the end with the occupation along the lattice. Therefore, it is not possible to compute the distribution of proteins along a filament by standard mathematical approximations for many-particle systems. We overcame this limitation by developing a novel approximation method that accounts for relevant correlations along the whole microtubule. In a nutshell, these are the central results of our publications *"Quantifying Protein Diffusion and Capture on Filaments"* [60] and *"Nonequilibrium Diffusion and Capture Mechanism Ensures Tip Localization of Regulating Proteins on Dynamic Filaments"* [61], that were published in *Biophysical Journal* and *Physical Review Letters*, respectively. To both publications, I contributed as first author. The following section provides an introduction and the scientific background related to these publications. The corresponding publications are reprinted in sections 2.1.3 and 2.1.4 of this thesis.

2.1.1 Background

2.1.1.1 Regulation of microtubules by associated proteins

As we have already discussed in the prolog, the eukaryotic cytoskeleton shows a fascinating variety of different structures *in vivo*. This integral capability of the cytoskeleton to restructure and rearrange, however, has to be tightly regulated. To this end, the interplay of a plethora of microtubule regulating proteins is required to ensure a proper reorganization and thereby proper functioning of the cytoskeleton [36, 64–67]. However, our understanding of how these regulating proteins determine cytoskeletal structures is limited; Clear principles explaining their astonishing efficiency to accomplish this complex task are only starting to emerge. Over the past years, essential players of the regulatory protein machinery that regulates microtubules were identified and, in particular with the advent of single-molecule microscopy, biomolecular interactions of many microtubule associated proteins could successfully be unraveled [67]. While undoubtedly many biomolecular interactions from different regulating proteins are required to shape the cytoskeleton, here we focus primarily on one crucial class of microtubule regulating proteins: +TIPS [68, 69]. Members of this protein class are distinguished by their ability to localize and track the plus end of microtubules, both, *in vivo* and *in vitro*. Already now a large number of +TIPs which fulfill central roles in cytoskeletal organization or regulation is known. For example, +TIPs are involved in regulating microtubule dynamics, linking microtubules to cellular structures (such as kinetochores or the actin cytoskeleton) and in the recruitment of downstream signaling factors [67, 68]. The members of the +TIPs class share the property that the microtubule tip serves as a reaction site such that it becomes particularly important for them to efficiently localize there. While we focus on +TIPS in this section, it should be noted that by now an equivalent class of regulating proteins has been identified that localizes at the minus ends of microtubules, the so-called -TIPs, and also that several actin-binding proteins show similar behavior [67, 70, 71].

Regarding this vast class of proteins that depends on the ability to localize at filament ends raises the question which strategies these proteins might have developed to associate with microtubule ends in an efficient way. Very generally, proteins may follow three different schemes of motility to target the microtubule end: Besides direct attachment from the solution, the biomolecules may also locate to the microtubule tip following either directed or diffusive motion along the microtubule, see also Fig. 2.1 for an illustration. Interestingly, all three options are employed by different +TIPs: In addition to direct binding from solution, several experimental studies have shown the capability of some +TIPs to move actively towards the plus end or to use molecular motors to “hitchhike” to the end [68]. But also diffusive motion along the microtubule lattice has been observed for many different proteins [68, 72–74]. Together with the experimental discovery of diffusive motion along microtubules

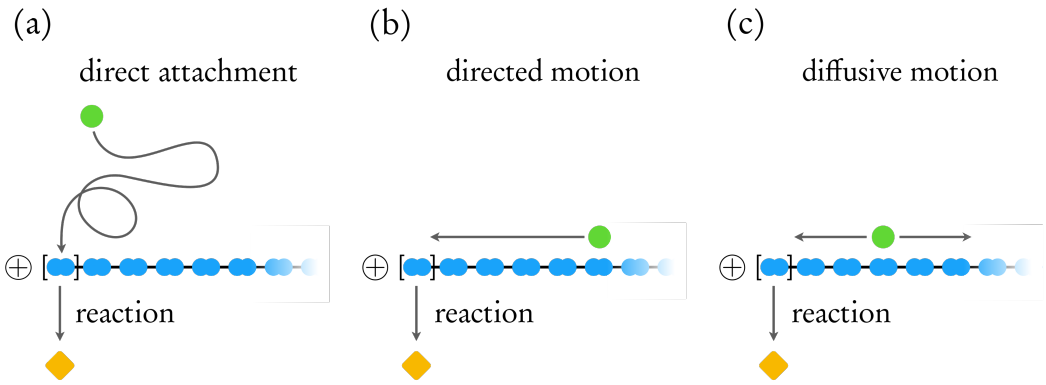

Figure 2.1 Illustration of potential tip-targeting mechanisms. Many regulatory proteins need to associate with the microtubule plus end (left lattice end) to fulfill their regulatory tasks. To bind there, these proteins may follow different mechanisms: **(a)** Direct attachment from the solution to the plus end, **(b)** binding to the microtubule and subsequent directed motion towards the plus end, **(c)** binding to the microtubule and subsequent one-dimensional diffusive motion along the filament. For simplicity, the microtubule is depicted as a one-dimensional array of schematic tubulin heterodimers (blue disks).

the idea has emerged that this mode of motility may enhance their binding to the plus end [72]. In this research project, we followed this line of thought and used computational modeling to address end targeting via one-dimensional diffusion in the specific context of microtubule binding proteins. Specifically, we wanted to ask the questions: Under which conditions is diffusive motion beneficial for end binding? How much does this way of binding to the plus end contribute to the overall rate of protein association there? Is plus-end binding via diffusion on the microtubule of relevance *in vivo*? Concerning the binding of proteins to the microtubule end that occurs subsequent to a directed motion on the microtubule, we refer the interested reader to several recent studies on this topic [75–77].

2.1.1.2 The diffusion and capture mechanism

Before turning to our theoretical considerations, we start with a more detailed look on microtubule regulating proteins that exhibit diffusive motion on the microtubule. Diffusive motion on cytoskeletal filaments is a widespread feature reported for an increasing number of proteins. Purely unbiased motility along the microtubule has been confirmed experimentally, for example, for XMAP215/chTOG [73], kinesin-13 [72, 78], the Ndc80 [79] and Dam1 [80] complexes, tau [81], Aurora-B [82], and Clip-170 [83]. Finally, also myosin-V has been shown to diffuse on microtubules [84] and the actin polymerase VASP is likely to employ diffusion on actin filaments [71].

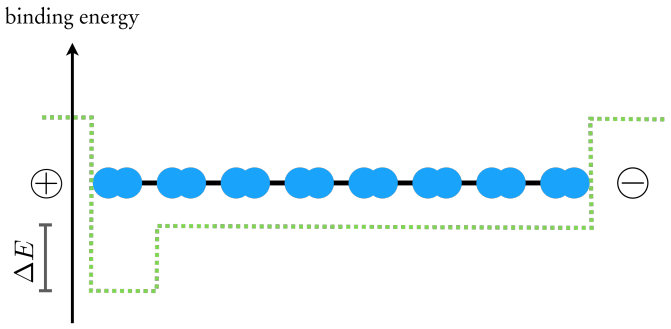

Figure 2.2 Illustration of a hypothetical binding potential of regulating proteins on a microtubule. Due to structural distinctiveness, many regulatory proteins are likely to recognize the plus end (left) of the microtubule [68]. This may lead to a higher affinity of proteins to the plus-end as compared to the microtubule bulk, causing an increase of the binding energy by ΔE. For simplicity, the microtubule is depicted as a one-dimensional array of schematic tubulin heterodimers (blue disks) and the plus end only as one lattice site.

In addition to pure diffusive motion along the microtubule, several kinesins also display diffusive periods in their otherwise directed motion. For a general review on the diffusive interaction of microtubule binding proteins see Ref. [74].

Let us now return to the question: Under which conditions may a diffusive interaction with microtubules be beneficial for targeting microtubule ends? To begin with, we consider the case where particles are subject to passive diffusive motion all along the microtubule. Most +TIPs possess a mechanism to recognize the microtubule end [68].[1] This can, in general, change the affinity of these proteins to the microtubule end as compared to the rest of the microtubule lattice. A sketch of a hypothetical profile of the binding energy is shown in Fig. 2.2. If the regulating proteins follow only passive diffusion on the microtubule, their distribution along the filament converges to a stationary state that equals the corresponding equilibrium distribution. In particular, this distribution is solely determined by the interaction potential. Upon assuming the limit of low concentrations of regulating proteins and neglecting particle interactions, the probability p^{tip} of finding particles at the tip is related to the probability p^{bulk} of finding particles in the bulk of the microtubule [2] via the Boltzmann factor: $p^{\text{tip}}/p^{\text{bulk}} = \exp(-\beta\Delta E)$, where ΔE is the difference of the binding energy at the tip and at the bulk. Moreover, $\beta = \mathrm{k}T$ with k being the Boltzmann constant and T being the temperature. The rate of attachment of particles from the solution is probably limited by the time it takes a protein to reach the binding site by three-dimensional

1 The microtubule end differs structurally from the rest of the microtubule. This is presumably due to a cap of GTP-bound tubulin dimers at the plus end and tapering of protofilaments [68].

2 Here we refer to the bulk as any location on the microtubule other than the plus end.

diffusion in the solution and not by the time related to the binding reaction. Hence it is plausible to assume a constant rate of attachment along the microtubule. A change in the affinity is then completely reflected by a change in the detachment rate. Consequently, $p_{\text{tip}}/p_{\text{bulk}} = \omega_{\text{off}}^{\text{bulk}}/\omega_{\text{off}}^{\text{tip}}$ holds true in equilibrium, where $\omega_{\text{off}}^{\text{bulk}}$ and $\omega_{\text{off}}^{\text{tip}}$ denote the detachment rates at the microtubule tip and bulk, respectively. Does such an equilibrium model already comply with experimental observations? As it is impossible to answer this question in general for all microtubule binding proteins, we will—as an example—consider the special case of XMAP215/chTOG, which is a central microtubule polymerase [85]. XMAP215 is a highly effective +TIP and exhibits particularly strong localization at microtubule plus tips. Its spatial distribution along the microtubule has been measured with very high accuracy and shows a roughly ten-fold increased probability at the tip as compared to the microtubule bulk [86].[3] Our hypothetical equilibrium model is therefore only in agreement with these experiments if the rate for particle detachment (inverse of dwell time) at the tip is approximately ten-fold decreased as compared to that in the bulk. Such a decrease is, however, falsified experimentally: Measurements for XMAP215 [73] revealed that particles remain bound to the bulk of the microtubule for an average of 2.4 seconds whereas they remained, on average, 3.8 seconds at the tip. We therefore conclude that passive diffusion alone can not account for tip localization observed for XMAP215 and that an additional mechanism must enhance the binding to the plus end. Note that also for other regulating proteins it is likely that equilibrium binding is insufficient to explain the observed particle localization at the plus end [72].

One important feature of most +TIPs is, however, to undergo an energy consuming biochemical reaction once bound to the tip [68]. In fact, many +TIPs might therefore represent systems out of thermal equilibrium. For example, for the kinesin-13 MCAK—that has also been shown to diffuse on the microtubule—it is known that its ATPase activity is not required to move along the microtubule. Instead, the plus end triggers an ATP dependent reaction that catalyzes microtubule depolymerization [87]. The fact that passive diffusion is insufficient to explain experimental data together with the consideration that often diffusive motion ceases or is suppressed at the microtubule tip thus leads to a new model for the tip-targeting by proteins that diffuse on cytoskeletal filaments: We proposed a new model where diffusive motion stops once the plus end is reached such that leaving the microtubule end other than by detachment into the solution is not possible. This suppressed motility of particles at the plus end breaks detailed balance and makes our model a nonequilibrium system. In the following, we refer to this mechanism as the *diffusion and capture* mechanism. Intuitively, we expect that the particle dynamics of the model converges towards a stationary flux of particles in the direction of the plus end as a consequence of breaking detailed balance in the way described above, see also illustration in Fig. 2.3. Indeed, it seems very

3 Values refer to measurements at a concentration of 150 nM.

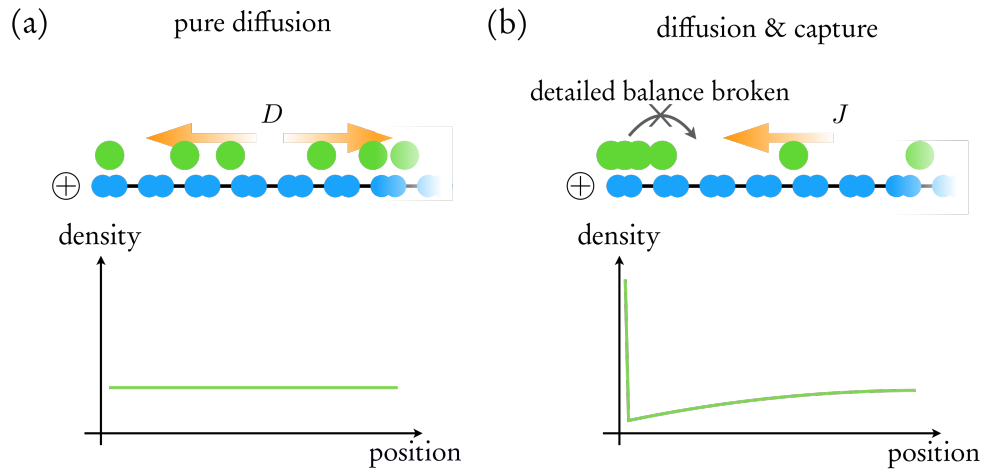

Figure 2.3 Capturing of one-dimensionally diffusing particles at the tip breaks detailed balance and is expected to create a flux of particles towards the plus-end. (a) If particles are only subject to passive diffusion (indicated schematically by the diffusion coefficient D) the corresponding average distribution along the microtubule (density profile) will converge to the homogeneous equilibrium distribution (bottom left). In this illustration, we neglected a potentially different affinity of particles to the plus-ends of microtubules for simplicity. **(b)** In our proposed model for diffusion and capture diffusive motion stops at the plus end (left end) of the microtubule and particles can only leave this binding site by detaching into solution. This breaks detailed balance and—opposed to the case without capturing—leads to flux of particles J in the stationary state. This flux may result in a non-homogeneous average distribution of particles along the microtubule in the stationary state (bottom right). For simplicity, the microtubule is depicted as a one-dimensional array of schematic tubulin heterodimers (blue disks) and the plus end only as a single lattice site. Moreover, while our modeling implements particles that exclude each other, the figure shows multiple particles at a single site for illustrative purposes; This serves to indicate an increased average occupation of the respective site.

plausible that such a flux of particles enhances the probability of finding a protein at the microtubule plus end. The following section provides a first quantitative glimpse on the formation of structure in the particle distribution along a microtubule due to the diffusion and capture mechanism.

2.1.1.3 Mean field and beyond: Approximation methods for driven lattice gases

As a preview on the publications and to support the intuitive arguing of the previous section also briefly on a quantitative level, we will introduce the model for the diffusion and capture mechanism in the following.

The model is defined as follows. Particles populate a discrete one-dimensional lattice with sites $i \in \{1, 2, \cdots, L\}$ where the leftmost site ($i = 1$) represents the plus

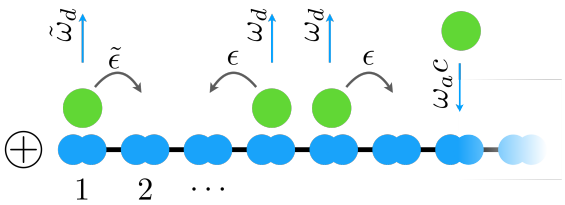

Figure 2.4 Illustration of the model for the diffusion and capture mechanism including a generic release rate. Particles populate a one-dimensional lattice where the left end (site $i = 1$) represents the plus-end of a microtubule. One-dimensional diffusive motion is realized as stochastic hopping events at equal rates ϵ to the neighboring lattice sites on the left and on the right, respectively. A capturing mechanism takes place at the plus-end, as hopping away from this site is suppressed and occurs at a rate $\tilde{\epsilon} < \epsilon$. Particles attach to the lattice stochastically at a rate $\omega_a c$ and leave the lattice stochastically at a rate ω_d. To account for a higher affinity of particles to the plus-end, particles leave the respective site $i = 1$ at a lowered rate $\tilde{\omega}_d$. Particles exclude each other such that the motion of a particle may only occur of if the respective target site is vacant. Note that in this introduction we account for a generic release rate $\tilde{\epsilon}$ for didactic purposes whereas the corresponding publications [60, 61] treat the limiting case of $\tilde{\epsilon} = 0$.

end of the microtubule. Each site can be occupied by at most one particle. Particles are subject to the following Markovian dynamics: On sites $i > 1$, particles perform unbiased diffusive motion, i.e. they move at an equal rate ϵ to neighboring lattice sites on the left and on the right, respectively. Motion from site $i = 1$ to site $i = 2$ occurs at a rate $\tilde{\epsilon} \leq \epsilon$. This "release" rate describes the strength of particle capturing at the microtubule tip. Note that, for didactic purposes, we treat the case of a variable "release" rate of hopping from site $i = 1$ to site $i = 2$. In the corresponding publications, this rate is set to zero. The lattice exchanges particles with a surrounding particle reservoir. In detail, a particle may attach to a lattice site at rate $\omega_a c$ where c is the concentration of particles in the solution. Particles detach at rate ω_d on sites $i > 1$ and at rate $\tilde{\omega}_d$ on site $i = 1$. In this way, the model generically accounts for a distinct affinity of proteins to the plus-end. Particles interact via hard-core repulsion meaning that they exclude each other. Thus, particles can only move to and attach to vacant lattice sites. An illustration of the model is shown in Fig. 2.4.

What are the fundamental changes in the system as particle capturing at the microtubule tip is gradually changed from a value that obeys detailed balance to one that breaks detailed balance? For detailed balance to hold true, the Kolmogorv criterion constrains the release rate to $\tilde{\epsilon}_{\text{equilibrium}} = \epsilon\, \tilde{\omega}_d / \omega_d$. For any value of the

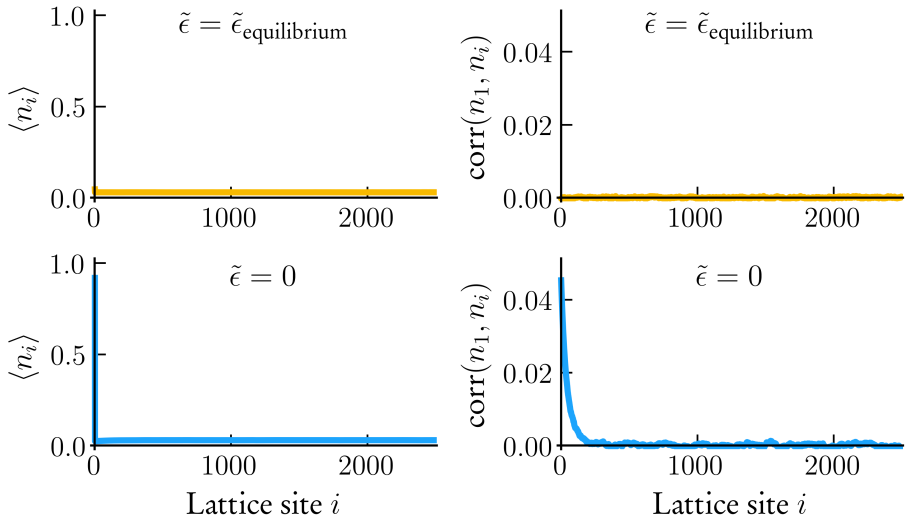

Figure 2.5 Average occupation of the lattice by particles and average correlations between the occupation of the end of the lattice and occupations of the bulk of the lattice in the stationary state. The average occupation of the lattice with particles $\langle n_i \rangle$ (left plots) showed a significantly pronounced localization of particles at the lattice end in the case of a strong capturing mechanism $\tilde{\epsilon} = 0$ (plot on the lower left). Opposed to that, in the case where the model was in equilibrium ($\tilde{\epsilon} = \tilde{\epsilon}_{\text{equilibrium}}$; plot on the upper left), the occupation of the lattice end was only slightly increased due to a higher affinity of particles there. This formation of structure goes along with correlations (right plots): The Pearson correlation coefficient $\text{corr}(n_1, n_i)$ for the occupation of the lattice end $i = 1$ with that of the bulk of the lattice ($i > 1$) showed that correlations in thermal equilibrium (plot on the upper right) are negligible while correlations in the case of a nonequilibrium capture mechanism are significant over approximately hundred lattice sites (plot on the lower right). Parameters were $\epsilon = 4700\,\text{s}^{-1}$, $\omega_a = 6.2 \times 10^{-5}\,\text{s}^{-1}\text{nM}^{-1}$, $\omega_d = 4.1 \times 10^{-1}\,\text{s}^{-1}$, $\tilde{\omega}_d = 2.6 \times 10^{-1}\,\text{s}^{-1}$, $c = 200\,\text{nM}$. Lattice length was $L = 2500$.

release rate $\tilde{\epsilon}$ other than $\tilde{\epsilon}_{\text{equilibrium}}$, the model is out of thermal equilibrium. Moreover, for smaller values than $\tilde{\epsilon}_{\text{equilibrium}}$ a current of particles in the direction of the plus end will emerge in the system. Fig. 2.5 shows the distribution of particles along the lattice (density profiles) for the two limiting cases $\tilde{\epsilon} = \tilde{\epsilon}_{\text{equilibrium}}$ and $\tilde{\epsilon} = 0$ in the stationary state. In the corresponding simulations, parameters were chosen to comply with measurements for XMAP215 (see also the Supplemental Material of our publication "Nonequilibrium Diffusion and Capture Mechanism Ensures Tip Localization of Regulating Proteins on Dynamic Filaments" reprinted in section 2.1.4 for details on the choice of parameters). As already anticipated earlier, the result of the particle current is a strong localization of particles at the microtubule tip: While the model showed only a slightly increased occupation at the tip in equilibrium (reflecting an

increased affinity there), the occupation of the lattice end was significantly enhanced when a nonequilibrium capturing mechanism was implemented. This emergence of structure along the lattice goes along with the formation of correlations. The right plots of Fig. 2.5 display the Pearson correlation coefficient of the occupation of lattice end with the occupation of the lattice

$$\mathrm{corr}(n_1, n_i) = \frac{\mathrm{cov}(n_1, n_i)}{\sigma_{n_1}\sigma_{n_i}}, \tag{2.1}$$

where $n_i \in \{0, 1\}$ denotes whether site i is occupied ($n_i = 1$) or vacant ($n_i = 0$). Furthermore, $\mathrm{cov}(n_1, n_i)$ denotes the covariance, and σ_{n_i} the standard deviation of the occupation number n_i. While correlations are negligible in equilibrium, a nonequilibrium capturing process of particles correlates the occupation of the lattice over a few hundred lattice sites. Fig. 2.6 further supports that the formation of structure in terms of tip-localization of particles is indeed accompanied by the emergence of correlations: Along with an increase of the average occupation of the lattice end $\langle n_1 \rangle$,[4] also the total correlation of this random variable with the occupation of the lattice $\sum_{i=2}^{L} \mathrm{corr}(n_1, n_i)$ increases. Thus, the formation of structure in the occupation of our model is tightly connected to two other factors: (a) breaking of detailed balance, and (b) the emergence of correlations.

How can we cope with the correlations in our system as soon as detailed balance is broken? Indeed, by inspecting Fig. 2.5, it should already be clear that a mean field (MF) approach will fail. This approach relies on neglecting all correlations in a system and, hence, factorizing average occupations of distinct lattice sites, $\langle n_i n_j \rangle \xrightarrow[\mathrm{MF}]{} \langle n_i \rangle \langle n_j \rangle$. Another approach previously applied to driven lattice gases is the so-called finite segment mean field theory (FSMFT) [88, 89]. This method includes correlations locally by specifically solving the master equation within a small segment of a couple of lattice sites. As we show in our publication [61], however, also this method is insufficient to reproduce the density profile and, in particular, the occupation of the lattice end $\langle n_1 \rangle$ with a good quality. The reason is that correlations extend over a few hundred lattice sites, which makes all local approaches unfeasible. To overcome this hurdle, we developed a new approximation method which accounts for those correlations that are relevant for an accurate computation of the occupation of the lattice end on a global scale: The central idea of this correlated mean-field approach (CMF) [61] is to account for correlations of the occupation of the lattice end with that of the bulk over the whole lattice; Correlations of occupations at different positions within the bulk of the lattice ($i > 1$) are, however, neglected. Accounting for tip-bulk correlations over the whole lattice was achieved in an efficient fashion by a

4 Here, angle brackets refer to averaging. As we only focus on steady state properties and as our model is ergodic, ensemble average and time average are equivalent and we do not differentiate between them.

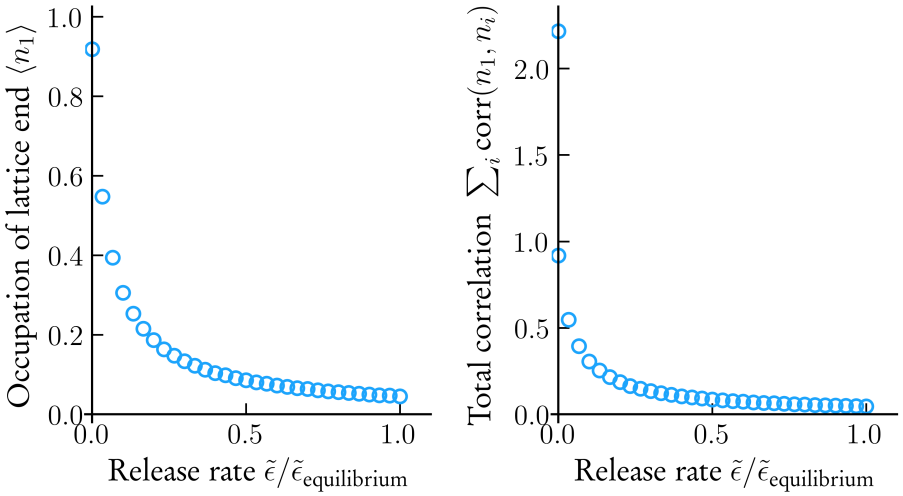

Figure 2.6 Structure formation along the microtubule goes along with the emergence of correlations. When detailed balance is broken by choosing $\tilde{\epsilon} < \tilde{\epsilon}_{\text{equilibrium}}$, the occupation of the lattice end $\langle n_1 \rangle$ (left) increases. Together with this increase, also sum of all correlations ($\sum_{i=2}^{L} \text{corr}(n_1, n_i)$) between the occupation of the lattice end (n_1) with that of the bulk of the lattice (n_i for $i > 1$) increases (right). Thus, a localization of particles at the lattice end due to a nonequilibrium capturing mechanism is inherently connected to the formation of correlations. Parameters were $\epsilon = 4700\,\text{s}^{-1}$, $\omega_a = 6.2 \times 10^{-5}\,\text{s}^{-1}\text{nM}^{-1}$, $\omega_d = 4.1 \times 10^{-1}\,\text{s}^{-1}$, $\tilde{\omega}_d = 2.6 \times 10^{-1}\,\text{s}^{-1}$, $c = 200\,\text{nM}$. Lattice length was $L = 2500$.

hydrodynamic approach: In the standard hydrodynamic mean-field approach for driven lattice gases, one often converts the discrete occupations into a continuous "density field" $\langle n_i \rangle \to \rho(x)$, with $x = (i-1)a$ being the continuous position on the lattice in the continuous limit ($a \to 0$) and a being the spacing of the lattice. We complemented the corresponding equation of motion for $\rho(x)$ by a second equation that describes a "correlation field" $\langle n_1 n_i \rangle \to g(x)$. In this way, our approximation is tailored to adequately include correlations between the occupation of the end of the lattice and that of the bulk of the lattice on a global scale. An overview of the different approximation methods is shown in Fig. 2.7.

At this stage, it should also be noted that—from a conceptional perspective—the hypothesis that a "reduction of dimensionality" in the motion of molecules may enhance binding to specific sites dates back to the seminal work of Adam and Delbrück [90]. The idea has been largely applied to DNA binding proteins, see Refs. [91–94] for recent reviews. The underlying scientific question of these theories is, however, different from our aims as the respective studies typically addressed association times of individual proteins to a target site. Opposed to that, we were interested in

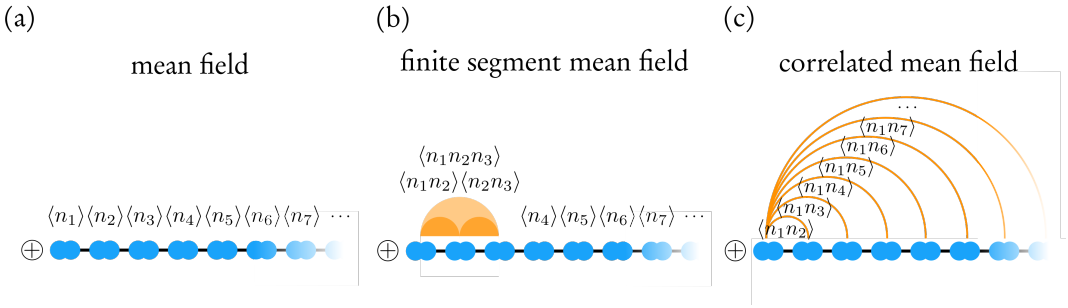

Figure 2.7 Illustration of different approximation methods applied to driven lattice gases. (a) The mean-field approach neglects all correlations by factorizing average occupations at different positions, $\langle n_i n_j\rangle \underset{\text{MF}}{\longrightarrow} \langle n_i\rangle\langle n_j\rangle$. **(b)** In the finite segment mean field theory, correlations are included locally within a small range of a couple of lattice sites. The solution for occupations within this segment is then self-consistently matched to the mean-field solution for the occupation numbers outside of this segment. **(c)** In our correlated-mean field approach, we include correlations $\mathrm{corr}(n_1, n_i)$ along the whole lattice. Other correlations are, however, neglected.

the corresponding many-body problem that allows one to obtain the steady-state distribution of particles along the whole microtubule. It should further be noted that some other studies have also addressed collective systems of one-dimensionally diffusing particles [72, 95, 96]. However, these models are not suitable to address a tip-localization of microtubule regulating proteins. This is the case because the respective models either didn't account for a capturing mechanism [95], introduced it *ad hoc* by absorbing boundary conditions at the microtubule end which, however, neglects the occupation of the end itself [72], or implemented boundary conditions motivated from a different biological process that are, however, not applicable to our model system [96].

2.1.2 Key results

In our work on the tip localization of microtubule binding proteins we developed a comprehensive theory for the diffusion and capture mechanism. The two corresponding publications deal with different aspects of this mechanism: **(1)** An effective Michaelis-Menten theory to quantify protein association due to the diffusion and capture mechanism. This theory is the central component of the publication *"Quantifying Protein Diffusion and Capture on Filaments"* [60]. **(2)** A theoretical approach to compute the occupation of cytoskeletal filaments by proteins that are subject to a diffusion and capture mechanism. Related results are published in the manuscript *"Nonequilibrium Diffusion and Capture Mechanism Ensures Tip Localization of Regulating Proteins on Dynamic Filaments"* [61]. The manuscripts are reprinted in

sections 2.1.3 and 2.1.4, respectively. In both publications I contributed as first author. For a detailed description of author contributions, please refer to the "Abstracts of the projects and contribution" section at the beginning of this thesis. In the following, we briefly summarize the key findings and explicate the scope of these two publications.

The work of publication **(1)** focused on the quantification of the association rate in the diffusion and capture mechanism. The key result is an effective Michaelis-Menten theory for the diffusion and capture mechanism. We found that—for typical biological parameter values—the functional dependency of the occupation of the plus end by proteins closely follows a Michaelis-Menten curve, also when proteins attach by a diffusion and capture mechanism. Based on this observation, we extended the classical (single molecule) Michaelis-Menten equation, that describes attachment via three-dimensional diffusion, by the respective contribution due to diffusion and capture. The result is useful in two ways: First, it provides an analytic expression for the effective association rate due to diffusion and capture. This expression can be directly compared to the association rate of direct binding from solution. Hence, we could quantitatively relate the contribution for protein association to the plus end by direct attachment with the respective contribution due to a diffusion and capture mechanism. Second, our theory is fully quantitative meaning that it only depends on parameters that can be measured in standard experiments and that have been determined for several +TIPs. We applied our theory to quantify tip binding by diffusion and capture for 17 previous experiments with microtubule binding proteins. In all cases diffusion and capture contributed more than 90% to the overall rate of protein binding to the plus end. Hence, diffusion and capture dominates tip binding and outperforms the Smoluchowski diffusion limit [97] for binding via three-dimensional diffusion in all of these experiments.

The work of publication **(2)** focused on the computation of the average stationary occupation of a filament by proteins that are subject to a diffusion and capture mechanism. We did this specifically for two essential regulating proteins: the central polymerase XMAP215/chTOG and the central depolymerase MCAK. Both proteins have been shown to fulfill vital roles in the regulation of microtubules and together reconstitute physiological microtubule dynamics [36, 85, 98, 99]. The extended model explicitly accounted for a dynamic lattice to provide an appropriate theoretical description of catalyzed microtubule growth and shrinkage. The first finding of our theoretical approach was that diffusion and capture correlates particle occupations. In detail, we found that the occupation of the microtubule tip spatially correlates with the occupation along the filament over hundreds of lattice sites. These correlations complicate an analytic approach since standard theories that neglect correlations (mean-field approach) or include them only within a spatially restricted segment (e.g. finite-segment mean-field theory) fail. To this end, we have developed a novel approximation method that accounts for relevant correlations globally. With this approach, we computed the density profiles of particles which, in turn, allowed us

to quantify tip localization. To validate our theory, we showed that it is in excellent quantitative agreement with *in vitro* measurements for the concentration dependence of (de)polymerization velocities of XMAP215 and MCAK. Further, our theory agrees with density profiles measured experimentally for XMAP215. Strikingly, we found that for both proteins, XMAP215 and MCAK, the diffusion and capture mechanism localizes proteins most efficiently at cellular concentrations of these proteins. This finding suggests an important role of the mechanism also *in vivo*.

2.1.3 Publication

This section is based on the publication

Quantifying Protein Diffusion and Capture on Filaments

by

E. Reithmann,[1] L. Reese,[1] and E. Frey[1]
[1]Arnold Sommerfeld Center for Theoretical Physics and Center for NanoScience,
Department of Physics, Ludwig-Maximilians-Universität München,
Theresienstraße 37, 80333 München, Germany

***Biophys. J.* 108 (4), 787–790 (2015).**
DOI: 10.1016/j.bpj.2014.12.053
Also available on arXiv: 1503.00878.

The arXiv preprint of this publication is reprinted on pages 22–27.

Supplemental Material reproduced on pages 28–34.

Quantifying protein diffusion and capture on filaments

Emanuel Reithmann, Louis Reese, and Erwin Frey (frey@lmu.de)

Arnold Sommerfeld Center for Theoretical Physics (ASC) and Center for NanoScience (CeNS), Department of Physics, Ludwig-Maximilians-Universität München, Theresienstraße 37, D-80333 Munich, Germany, and Nanosystems Initiative Munich (NIM), Ludwig-Maximilians-Universität München, Schellingstraße 4, D-80333 Munich, Germany

Abstract

The functional relevance of regulating proteins is often limited to specific binding sites such as the ends of microtubules or actin-filaments. A localization of proteins on these functional sites is of great importance. We present a quantitative theory for a diffusion and capture process, where proteins diffuse on a filament and stop diffusing when reaching the filament's end. It is found that end-association after one-dimensional diffusion is the main source for tip-localization of such proteins. As a consequence, diffusion and capture is highly efficient in enhancing the reaction velocity of enzymatic reactions, where proteins and filament ends are to each other as enzyme and substrate. We show that the reaction velocity can effectively be described within a Michaelis-Menten framework. Together one-dimensional diffusion and capture beats the (three-dimensional) Smoluchowski diffusion limit for the rate of protein association to filament ends.

The catalytic activity of enzymes is often restricted to specific binding sites. The ends of microtubules (MTs) for example are binding sites for a plethora of MT associated proteins (MAPs) [1]. At MT ends, MAPs can catalyze biochemical processes [2], or serve as substrates for other enzymes. This makes an efficient association of MAPs to MT tips important. Recent experiments suggest that one-dimensional diffusion of MAPs on MTs facilitates tip-targeting [3, 4]. This idea goes back to the concept of "reduction in dimensionality" suggested by Adam and Delbrück [5] and has been largely applied [6, 7]. However, a quantitative understanding of tip-binding mediated by diffusion on the filament and subsequent capture at the tip has remained elusive [3, 8–16].

Here we show that capturing at the tip is crucial for tip-localization of proteins. We present a theory where diffusion and capture is accurately quantified with an effective association rate constant and provide a result which depends only on experimentally accessible parameters. For proteins which are enzymatically active at filament ends, our theory predicts that diffusion and capture leads to an enhancement of the enzymatic reaction velocity due to stronger tip-localization. We observe that the reaction velocity in dependence of the enzyme concentration closely follows a Michaelis-Menten curve and quantify the contribution of one-dimensional diffusion to tip-localization and enzymatic processes downstream thereof.

To model the diffusive motion of proteins on a filament we consider a one-dimensional lattice of length l with lattice spacing $a = 8.4\,\mathrm{nm}$ [Fig. 1A]. The lattice corresponds to a single protofilament of a stabilized MT in the absence of dynamic instability. Proteins perform a random walk on the lattice with a hopping rate ϵ; the diffusion constant is $D = \epsilon\, a^2$. Each site can be occupied by only one protein; the system is an exclusion process [17]. Proteins attach to and detach from the lattice at rates $\omega_{\mathrm{on}} c$ and ω_{off},

respectively, where c is the concentration of proteins in solution. The tip of the MT is represented by the first lattice site in our model. To account for its particular structure, different on- and off-rates are assumed there, $k_{\rm on}c$ and $k_{\rm off}$. Proteins that bind to the tip are *captured*, i.e. not allowed to hop on the lattice, but still may detach into solution. This important condition is a critical difference between our model and previous approaches [3, 16], see also the Supporting Material.

A central goal of this letter is to quantify the relative contributions of *diffusion and capture* (tip-attachment after diffusion on the lattice) and *end-targeting* (attachment after diffusion in solution) [Fig. 1B] to tip-localization. To this end we calculated the probability to find a protein at the end of a protofilament (the tip density ρ_+). In the absence of diffusion and capture, the Langmuir isotherm is obtained,

$$\rho_+(c) = \frac{c}{K+c}\,, \tag{1}$$

where $K = k_{\rm off}/k_{\rm on}$ is the dissociation constant of the protein at the tip. However, as noted previously [3, 4], such a model is incomplete as it does not account for the additional protein flux along protofilaments mediated by diffusion and capture. We have analyzed this flux by stochastic simulations of the model [Fig. 1]. Surprisingly, we find that over a broad range of concentrations c, the additional protein current to an unoccupied reaction site J^D effectively obeys first order kinetics, i.e. $J^D = k_{\rm on}^D c$ [Supporting Material Fig. S2]. This observation implies that despite the complexity of the diffusion-reaction process one approximately retains the functional form of the Langmuir isotherm. Accounting for the diffusion-capture contribution to the rate of protein attachment leads to an effective dissociation constant

$$K^{\rm eff} = k_{\rm off}/(k_{\rm on} + k_{\rm on}^D)\,. \tag{2}$$

We have calculated the diffusion-capture rate $k_{\rm on}^D$ analytically, by exploiting the observed approximate linear reaction kinetics. We find

$$k_{\rm on}^D = \frac{\omega_{\rm on} D/a^2}{\omega_{\rm off} + \sqrt{\omega_{\rm off} D/a^2}}\,. \tag{3}$$

Refer to the Supporting Material for a detailed derivation of Eqs. 1-3. Together Eqs. 1-3 comprise an effective theory for the association of proteins to the tip which accounts for direct end-targeting as well as the diffusion-capture process. With Eq. 3 we are able to quantitatively predict the relative contribution of diffusion and capture to tip-binding for different proteins that diffuse on filaments. The results are shown in Fig. 2: $90-99\%$ of molecules bind to the tip through one-dimensional diffusion given they follow diffusion and capture.

Tip-localization due to diffusion and capture as predicted by our theory has important implications for enzymatically active proteins. We extended the model to investigate enzymatic reactions at the MT tip, where the protein-tip complex catalyzes a product at rate $k_{\rm cat}$ [Fig. 1C]. In detail, we assume that the protein does not leave the tip after catalyzing a reaction, but only through detachment into solution. These model assumptions are consistent with filament polymerizing enzymes that act processively, such as XMAP215 for MTs [9, 10], and VASP [15] and formins [18] for actin filaments. The assumption of a constant length l in our model is excellent if the rate of diffusion is fast compared to the polymerization rate. With the above model assumptions the reaction velocity v is determined by the tip density, $v = \rho_+ k_{\rm cat}$. We can apply our previous results, Eqs. 1 -3, to obtain

$$v(c) = k_{\rm cat}\,\rho_+(c) = \frac{k_{\rm cat} c}{K^{\rm eff}+c}\,. \tag{4}$$

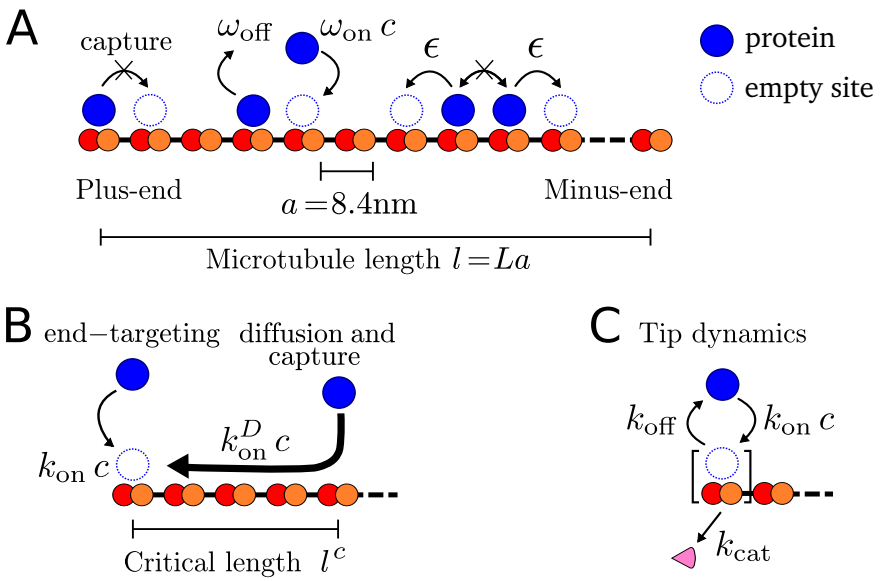

Figure 1: (A) Schematic of a MT with diffusive tip-binding proteins. In the bulk of the lattice, proteins attach to empty sites and detach. Proteins hop to neighboring sites but obey exclusion. At the plus-end, particles are captured. (B) Illustration of direct tip-attachment from solution and via diffusion and capture. (C) Proteins bind reversibly at the plus-end. While a protein is attached there, a reaction is catalyzed at rate $k_{\rm cat}$.

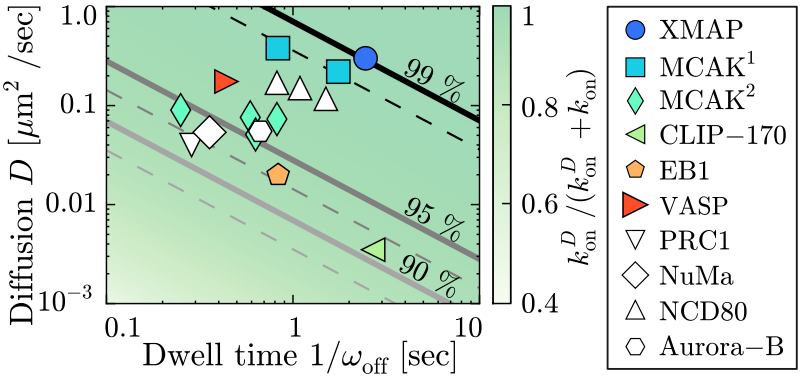

Figure 2: The model predicts the relative contribution to tip localization of proteins due to diffusion and diffusion & capture (color code and solid lines), $k^D_{\rm on}/(k^D_{\rm on}+k_{\rm on})$ with $k_{\rm on} = \omega_{\rm on}$ (dashed for actin: $a = 6\,$nm). Proteins that are captured at the filament end (filled symbols) and proteins where evidence for capturing is lacking (open symbols) are shown. Proteins that in addition have a direct enzymatic activity at the filament end are XMAP215 [9, 10], MCAK^1 [3], and MCAK^2 [8] on MTs, and VASP on actin filaments, see Ref. [15] and personal communicaton [S.D. Hansen and R.D. Mullins, 2014]. There are also proteins that diffuse on MTs without enzymatic activity at MT ends, but with roles downstream of tip-localization, e.g. in the protein network of MT tips [1]: NCD80 [11]; CLIP − 170 [12]; NuMa, PRC1, EB1 [13]; Aurora − B [14].

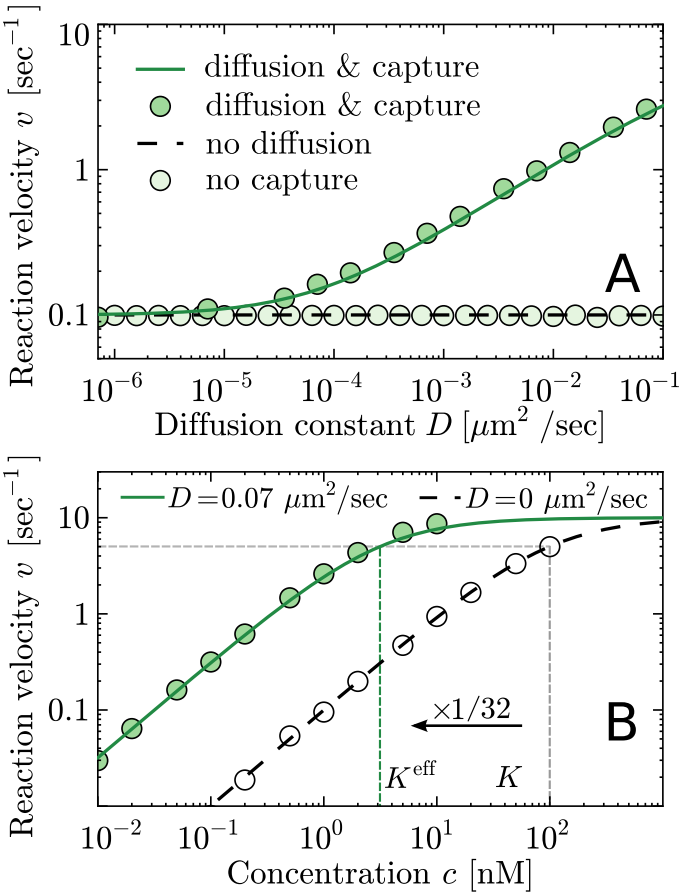

Figure 3: (A) Comparison of the reaction velocity with (solid) and without (dashed) lattice diffusion and with and without capturing at the tip (circles: simulation data; lines: analytic results) (B) shows the reaction velocity $v(c)$. Analytic results (lines) are confirmed by simulation data (circles). Parameters are $L = 1000$, $\omega_{\rm off} = k_{\rm off} = 1\,{\rm sec}^{-1}$, $k_{\rm cat} = 10\,{\rm sec}^{-1}$ $\omega_{\rm on} = k_{\rm on} = 0.01\,{\rm sec}^{-1}\,{\rm nM}^{-1}$ and $c = 1\,{\rm nM}$.

The above equation is reminiscent of a single-molecule Michaelis-Menten equation [19, 20] when $K^{\rm eff}$ is reinterpreted as Michaelis constant and substrate and enzyme concentrations are interchanged. In this way our theory constitutes an effective Michaelis-Menten theory which accounts for end-targeting *and* diffusion and capture; instead of solving a complex many-body problem it suffices to apply a mathematical framework which is analogous to (single-molecule) Michaelis-Menten kinetics; the details of diffusion and caputure are accurately included in the effective on-rate $k_{\rm on}^{\rm eff} = k_{\rm on} + k_{\rm on}^{D}$. This result is in accordance with experimental results for several enzymatically active proteins where Michaelis-Menten curves were observed for the reaction speed depending on the enzyme concentration [8, 9]. Inspired by the processive (de)polymerase activity of (MCAK) XMAP215, we assume that enzyme and substrate are not decomposed in the reaction step. However, it is straightforward to include a decomposition in the theory: the effective dissociation constant would read $K^{\rm eff} = (k_{\rm off} + k_{\rm cat})/k_{\rm on}^{\rm eff}$.

Our analytical results, Eqs. 2-4, agree well with simulation results of the stochastic model, as shown in Fig. 3(A) and (B). We find that the diffusion and capture mechanism dramatically increases $k_{\rm on}^{\rm eff}$ and thereby reduces the effective dissociation constant typically by more than one order of magnitude, e.g. for XMAP215 we find $K^{\rm eff} \approx 10^{-2}K$. In the case of long dwell times $\omega_{\rm off}^{-1}$ and fast diffusion ϵ, $K^{\rm eff}$

reduces to a particularly simple form

$$K^{\text{eff}} = (k_{\text{off}}/\omega_{\text{on}})/\sqrt{\epsilon/\omega_{\text{off}}}\,, \tag{5}$$

where the denominator is the square root of the average number of diffusive steps a protein performs on the filament. Note that one-dimensional diffusion without capturing [16] does not lead to a particle flux on the filament [Supporting Material Fig. S4] and hence the reaction velocity is not increased [Fig. 3A]. Further, the particle flux might be limited by the length of the filament: Below a threshold length l^c (which is smaller than typical *in vivo* lengths of MTs) we observe a length dependent behavior of the reaction velocity [Supporting Material Fig. S3] where our theory is not valid.

Our analysis reveals *diffusion and capture* as an efficient mechanism to circumvent the diffusion limit for the rate of end-targeting: Smoluchowski's theory of three-dimensional diffusion physically limits the rate of direct tip-attachment from solution [21]. As shown here, one-dimensional diffusion along a filament and subsequent capture at the filament end overcomes this limitation. This has been shown experimentally for MCAK [3]. Our work provides an applicable theory for reaction kinetics facilitated by diffusion and capture: specific parameter values for diffusion, tip-association and dwell times can be accounted for, cf. Eqs. 3 and 4. On a broader perspective our results may also be applicable to other systems where one-dimensional diffusion is important [6] including transcription factor binding on DNA [22].

Acknowledgement

The authors thank Scott Hansen and Dyche Mullins for helpful correspondence on diffusing actin binding proteins. This research was supported by the Deutsche Forschungsgemeinschaft (DFG) via project B02 within the SFB 863.

References

[1] Akhmanova, A., and M. O. Steinmetz, 2008. Tracking the ends: a dynamic protein network controls the fate of microtubule tips. *Nat. Rev. Mol. Cell Biol.* 9:309–322.

[2] Howard, J., and A. A. Hyman, 2007. Microtubule polymerases and depolymerases. *Curr. Opin. Cell Biol.* 19:31–5.

[3] Helenius, J., G. J. Brouhard, Y. Kalaidzidis, S. Diez, and J. Howard, 2006. The depolymerizing kinesin MCAK uses lattice diffusion to rapidly target microtubule ends. *Nature* 441:115–9.

[4] Cooper, J. R., and L. Wordeman, 2009. The diffusive interaction of microtubule binding proteins. *Curr. Opin. Cell Biol.* 21:68–73.

[5] Adam, G., and M. Delbrück, 1968. Reduction of dimensionality in biological diffusion processes. *In* Structural chemistry and molecular biology, Freeman, 198–215.

[6] von Hippel, P. H., and O. G. Berg, 1989. Facilitated Target Location in Biological Systems. *J. Biol. Chem.* 264:675–678.

[7] Mirny, L., M. Slutsky, Z. Wunderlich, A. Tafvizi, J. Leith, and A. Kosmrlj, 2009. How a protein searches for its site on DNA: the mechanism of facilitated diffusion. *J. Phys. A: Math. Theor.* 42:434013.

[8] Cooper, J. R., M. Wagenbach, C. L. Asbury, and L. Wordeman, 2010. Catalysis of the microtubule on-rate is the major parameter regulating the depolymerase activity of MCAK. *Nat. Struct. Mol. Biol.* 17:77–82.

[9] Brouhard, G. J., J. H. Stear, T. L. Noetzel, J. Al-Bassam, K. Kinoshita, S. C. Harrison, J. Howard, and A. A. Hyman, 2008. XMAP215 is a processive microtubule polymerase. *Cell* 132:79–88.

[10] Widlund, P. O., J. H. Stear, A. Pozniakovsky, M. Zanic, S. Reber, G. J. Brouhard, A. A. Hyman, and J. Howard, 2011. XMAP215 polymerase activity is built by combining multiple tubulin-binding TOG domains and a basic lattice-binding region. *Proc. Nat. Acad. Sci. USA* 108:2741–6.

[11] Powers, A. F., A. D. Franck, D. R. Gestaut, J. Cooper, B. Gracyzk, R. R. Wei, L. Wordeman, T. N. Davis, and C. L. Asbury, 2009. The Ndc80 Kinetochore Complex Forms Load-Bearing Attachments to Dynamic Microtubule Tips via Biased Diffusion. *Cell* 136:865–875.

[12] Dixit, R., B. Barnett, J. E. Lazarus, M. Tokito, Y. E. Goldman, and E. L. F. Holzbaur, 2009. Microtubule plus-end tracking by CLIP-170 requires EB1. *Proc. Natl. Acad. Sci. USA* 106:492–497.

[13] Forth, S., K.-C. Hsia, Y. Shimamoto, and T. M. Kapoor, 2014. Asymmetric friction of nonmotor MAPs can lead to their directional motion in active microtubule networks. *Cell* 157:420 – 432.

[14] Noujaim, M., S. Bechstedt, M. Wieczorek, and G. J. Brouhard, 2014. Microtubules Accelerate the Kinase Activity of Aurora-B by a Reduction in Dimensionality. *PLoS ONE* 9:e86786.

[15] Hansen, S. D., and R. D. Mullins, 2010. VASP is a processive actin polymerase that requires monomeric actin for barbed end association. *J. Cell Biol.* 191:571–584. & private communication.

[16] Klein, G., K. Kruse, G. Cuniberti, and F. Jülicher, 2005. Filament Depolymerization by Motor Molecules. *Phys. Rev. Lett.* 94:108102.

[17] Krapivsky, P. L., S. Redner, and E. Ben-Naim, 2010. A kinetic view of statistical physics. Cambridge University Press.

[18] Vavylonis, D., D. R. Kovar, B. O'Shaughnessy, and T. D. Pollard, 2006. Model of formin-associated actin filament elongation. *Mol. Cell* 21:455–66.

[19] Kou, S., B. J. Cherayil, W. Min, B. P. English, and X. X. Sunney, 2005. Single-molecule michaelis-menten equations. *J. Phys. Chem. B* 109:19068–19081.

[20] Michaelis, L., and M. L. Menten, 1913. Die Kinetik der Invertinwirkung. *Biochem. Z.* 49:333–369.

[21] von Smoluchowski, M., 1917. Versuch einer mathematischen Theorie der Koagulationskinetik. *Z. Phys. Chem* 92:129–168.

[22] Hammar, P., P. Leroy, A. Mahmutovic, E. G. Marklund, O. G. Berg, and J. Elf, 2012. The lac repressor displays facilitated diffusion in living cells. *Science* 336:1595–1598.

Supporting Material "Quantifying protein diffusion and capture on filaments"

Emanuel Reithmann, Louis Reese, and Erwin Frey (frey@lmu.de)

Arnold Sommerfeld Center for Theoretical Physics (ASC) and Center for NanoScience (CeNS), Department of Physics, Ludwig-Maximilians-Universität München, Theresienstraße 37, D-80333 Munich, Germany, and Nanosystems Initiative Munich (NIM), Ludwig-Maximilians-Universität München, Schellingstraße 4, D-80333 Munich, Germany

A Derivation of Eq. (1), (2), and (4)

In the following we derive the reaction velocity of the model presented in the Main Text. We start by considering the model depicted in Fig. 1 (A): Particles from a reservoir with concentration c can bind reversibly to a single reaction site with rates $k_{\mathrm{on}}c$ for binding and k_{off} for unbinding. As long as the proteins are bound to the tip, they perform a not specified reaction at rate k_{cat}. Inspired by the processive

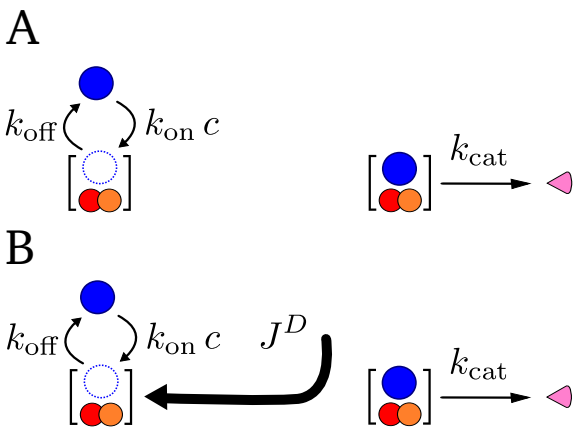

FIGURE S1: Illustration of the chemical reaction considered in this section. Particles (blue circles) from a reservoir with concentration c bind reversibly to an unoccupied (dashed circles) reaction site at rates $k_{\mathrm{on}}c$ for binding and k_{off} for unbinding. Whilst bound, the particles catalyze a (not specified) reaction at rate k_{cat}. In (A) particles can only attach directly via the reservoir. In (B) we have an additional particle flux J^D to the reaction site due to a diffusion and capture mechanism described in the Main Text.

(de)polymerase activity of XMAP215 (MCAK), there is no decomposition of the particle and the reaction site in the reaction step. Including a decomposition in the model would however be straightforward (see also the discussion in the Main Text). Let n_+ denote an occupied ($n_+ = 1$) or vacant ($n_+ = 0$) reaction site. Then, the average velocity of the reaction is given by

$$v = \langle n_+ \rangle k_{\mathrm{cat}}. \tag{S1}$$

Here, the average refers to an ensemble average. Since the reaction site corresponds to the last lattice site of one protofilament, we expect our results to be valid for experimental setups with a sufficiently large

and constant number of protofilaments or (due to ergodicity) for the time average with respect to a single protofilament. In the steady state the equation for the average occupation of the reaction site reads

$$0 = \frac{d}{dt}\langle n_+ \rangle = k_{\text{on}} c(1 - \langle n_+ \rangle) - k_{\text{off}} \langle n_+ \rangle \,. \tag{S2}$$

Solving for $\langle n_+ \rangle$ leads to an equation for the reaction velocity which is analogous to a single molecule Michaelis-Menten equation [1]:

$$v = \frac{k_{\text{cat}} c}{K + c} \tag{S3}$$

with $K = k_{\text{off}}/k_{\text{on}}$. Note that here c is the concentration of the enzyme, not the substrate.

If we now have an additional particle flux J to the reaction site via one-dimensional diffusion, Fig. S1 (B), the dynamics are changed. Including this flux in the equation for the average reaction site occupation leads to

$$0 = \frac{d}{dt}\langle n_+ \rangle = k_{\text{on}} c(1 - \langle n_+ \rangle) + J - k_{\text{off}} \langle n_+ \rangle \tag{S4}$$

$$= \left(k_{\text{on}} c + \frac{J}{1 - \langle n_+ \rangle} \right) (1 - \langle n_+ \rangle) - k_{\text{off}} \langle n_+ \rangle \,. \tag{S5}$$

Note that the term $J^{\text{D}} := J/(1-\langle n_+ \rangle)$ can be interpreted as the conditional particle flux to an unoccupied tip. If the conditional diffusive current can be written as $J^{\text{D}} := k_{\text{on}}^D c$ we conserve the functional form of Eq. S3 but k_{on} is replaced by an effective on-rate for direct binding as well as diffusion and capture: $k^{\text{eff}} = k_{\text{on}} + k_{\text{on}}^D$.

In conclusion, observing a Michaelis-Menten curve for the reaction velocity in dependence of the enzyme concentration c is equivalent to the statement, that the current of particles towards an unoccupied reaction site due to the diffusion and capture mechanism obeys first order kinetics. In Fig. S2 simulation results of our model show that the linearity condition is indeed approximately fulfilled over a broad parameter range. The corresponding parameter values are chosen within the typical parameter range for one-dimensionally diffusing proteins (see Fig. 2 in the Main Text). Note that for high concentrations which imply almost saturated reaction velocities we observe a, in general, non-linear behavior. In such a parameter range extended analytic approaches than the ones presented here would be necessary. For the analysis shown in this work these deviations are, however, not relevant as we are interested in quantities which are almost saturated at such concentrations (tip-occupation and reaction velocity; particle current to the tip).

B Derivation of Eq. (3)

B.1 Mathematical model definition

The mathematical formulation of the model depicted in Fig. 1 of the Main Text relies on a probabilistic description of the lattice site occupations. A basic introduction to lattice gases and related problems can be found in Ref. [2]. The occupation numbers n_i with $i \in \{0, \ldots, L-1\}$ describe the configuration of particles on the lattice, where $n_i = 0$ and $n_i = 1$ stand for an empty or occupied lattice site respectively. The equations of motion for the density on each lattice site are obtained in terms of the mean occupation numbers $\langle n_i \rangle = \rho_i$. Further it is assumed that neighboring lattice sites are occupied independently, which

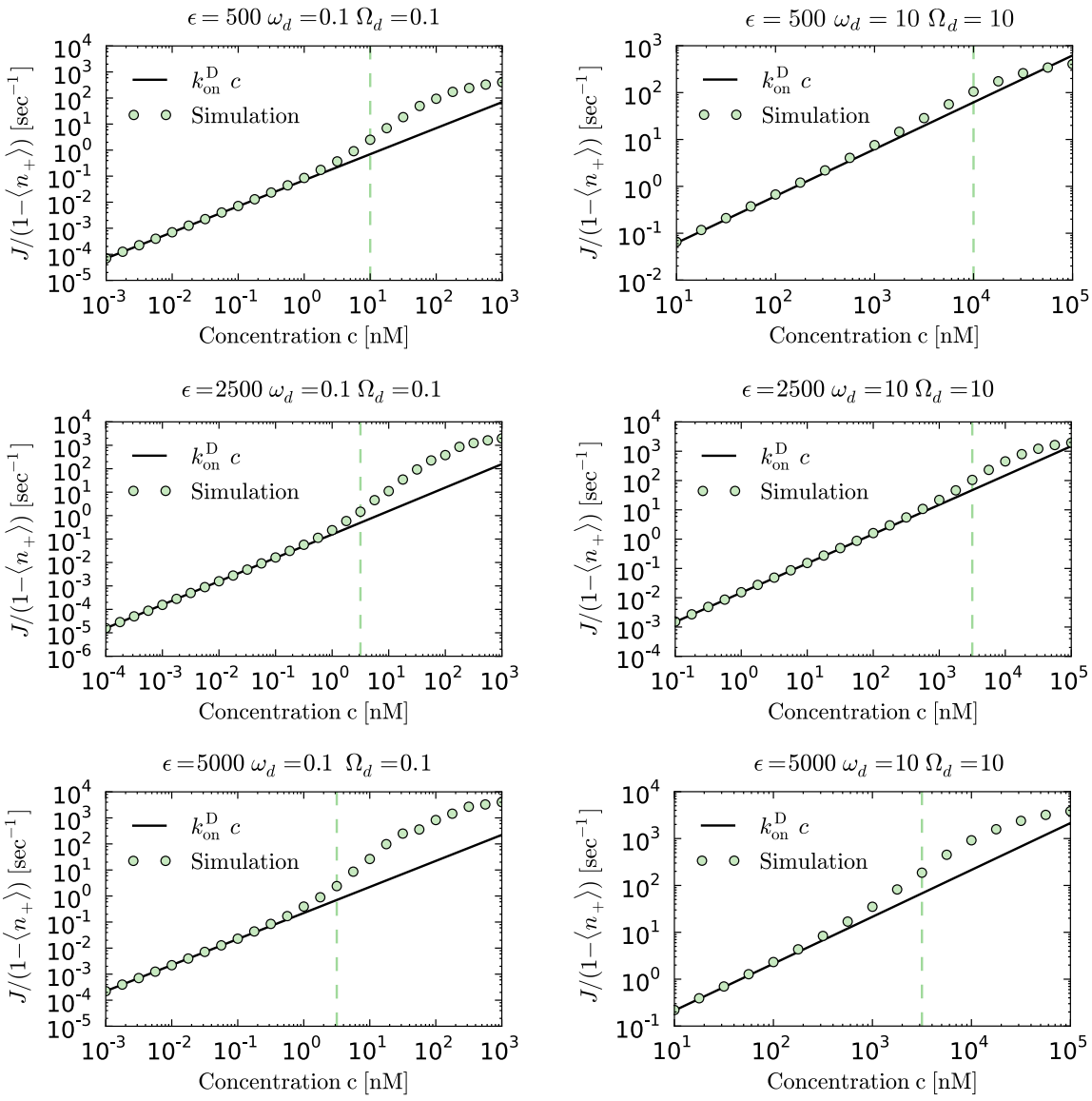

FIGURE S2: The current due to the diffusion and capture mechanism towards an unoccupied reaction site shows linearity in c over a broad parameter range. The dashed line is the concentration, where the reaction velocity is 90% saturated, $v = 0.9\ k_{\mathrm{cat}}$. For concentrations close to the maximum reaction velocity the current differs from the linear behavior. This is, however, largely negligible because v and J are almost saturated.

is a mean-field approximation that reads $\langle n_i n_{i+1} \rangle = \langle n_i \rangle \langle n_{i+1} \rangle$. We will justify later on that this approximation is not a restriction for the computations performed to derive k_{on}^{D}. Given these preliminaries, the equations of motion in the bulk (sites $i = 2, \ldots, L-1$) of the lattice read [3]

$$\frac{d}{dt}\rho_i = \epsilon(\rho_{i-1} - 2\rho_i + \rho_{i+1}) + \omega_{\mathrm{on}} c(1-\rho_i) - \omega_{\mathrm{off}}\rho_i\,, \tag{S6}$$

where particle exclusion as well as attachment and detachment kinetics are accounted for. Particle attachment and detachment define the equilibrium density of particles on the lattice, also called the Langmuir

density,

$$\rho_{\mathrm{La}} = \frac{\omega_{\mathrm{on}} c}{\omega_{\mathrm{on}} c + \omega_{\mathrm{off}}} \,. \tag{S7}$$

Note that we consider the terminal site separately and refer to its average occupation as tip density ρ_+,

$$\rho_+ := \rho_0 = \langle n_0 \rangle \,. \tag{S8}$$

The lattice site next to the tip, $i = 1$, is also considered distinct from the bulk dynamics: It serves as a boundary for the diffusive region. The equations of motion for sites $i = 0, 1$ are

$$\frac{d}{dt}\rho_0 = \epsilon(1-\rho_0)\rho_1 + k_{\mathrm{on}} c(1-\rho_0) - k_{\mathrm{off}}\rho_0 \,, \tag{S9}$$

$$\frac{d}{dt}\rho_1 = \epsilon(\rho_2 - \rho_1) - \epsilon\rho_1(1-\rho_0) + \omega_{\mathrm{on}} c(1-\rho_1) - \omega_{\mathrm{off}}\rho_1 \,. \tag{S10}$$

The density in the bulk is (in leading order of a gradient expansion) governed by the following diffusion equation

$$\partial_t \rho(x,t) = a^2 \epsilon\, \partial_x^2 \rho(x,t) + \omega_{\mathrm{on}} c(1-\rho(x,t)) - \omega_{\mathrm{off}}\rho(x,t) \,, \tag{S11}$$

with $x = ai$. This is a continuous approximation of Eq. S6. The boundary conditions are $\lim_{x\to\infty}\rho(x) = \rho_{\mathrm{La}}$ and $\rho(a) = \rho_1$. The solution is obtained in the steady state $\partial_t\rho(x,t) = 0$ and reads

$$\rho(x) = \rho_{\mathrm{La}} + (\rho_1 - \rho_{\mathrm{La}}) \exp[-(x-a)/\lambda] \,, \tag{S12}$$

with

$$\lambda = \sqrt{\frac{D}{\omega_{\mathrm{on}} c + \omega_{\mathrm{off}}}} \,, \tag{S13}$$

as calculated by Klein et al. [3]. Here we used $D = \epsilon a^2$. This solution is valid for $x \geq a$. At sites $i = 0$ and $i = 1$ the density profile is not continuous and the diffusion equation can not be applied. The remaining task is to determine the values for ρ_0 and ρ_1 in the steady state.

B.2 Low density approximation

To make progress, the particle flux from site $i = 2$ to site $i = 1$ from Eq. S10 is rewritten as a derivative: $(\rho_2 - \rho_1) \approx a\partial_x\rho(x)|_{x=a}$. This corresponds again to a continuous description at the corresponding sites. Using Eq. S12 we see that the (right) derivative at $x = a$ (which is equivalent to $i = 1$) is $\partial_x\rho|_{x=a+} = -(\rho_1 - \rho_{\mathrm{La}})/\lambda$. With this result we can simplify Eq. S10 in the steady state

$$0 \approx -a\frac{\rho_1 - \rho_{\mathrm{La}}}{\lambda} - \rho_1(1-\rho_0) \,, \tag{S14}$$

where attachment and detachment rates have been assumed small. Further, note that we solve Eq. S9 in the steady state for ρ_0 as a function of ρ_1:

$$\rho_0 = \frac{\rho_1\epsilon + k_{\mathrm{on}} c}{\rho_1\epsilon + k_{\mathrm{on}} c + k_{\mathrm{off}}} \,. \tag{S15}$$

The key relation at the basis of our theory is that tip attachment via lattice diffusion obeys first-order reaction kinetics. This is well confirmed by simulations over a broad and biologically relevant parameter region, see Fig. S2. The current to an unoccupied tip is hence approximately given by $J^D = k_{\mathrm{on}}^D c$, where $k_{\mathrm{on}}^{\mathrm{D}}$ is a constant, independent of the enzyme concentration. In the following, we determine the diffusive

current for infinitesimally low enzyme concentrations and thereby determine k_{on}^{D}. In this parameter region correlations become negligible such that the mean-field assumption becomes valid. Further, we assume ρ_1 to be small. This is well justified for low concentrations. Note also that the density along the lattice is minimal at $i = 1$. Up to first order in ρ_1 Eq. S14 reduces to

$$0 = -\frac{a\,\epsilon\,\omega_{\text{on}} c}{\sqrt{\epsilon\,(\omega_{\text{off}} + \omega_{\text{on}} c)}} + \big(a\,\sqrt{\epsilon\,(\omega_{\text{off}} + \omega_{\text{on}} c)} + \frac{\epsilon\,k_{\text{off}}}{k_{\text{on}} c + k_{\text{off}}}\big)\rho_1\,. \tag{S16}$$

The solution of the above equation determines the tip density via Eq. S15. In our low-density approximation and up to first order in c we obtain

$$\rho_0^{\text{low-c}} = \frac{k_{\text{on}} + (\omega_{\text{on}}\,\epsilon)/(\omega_{\text{off}} + \sqrt{\epsilon\,\omega_{\text{off}}})}{k_{\text{off}}}\,c\,. \tag{S17}$$

B.3 Site attachment due to lattice diffusion

The solution of $\rho_+ = \rho_0$ allows us to determine the diffusive current. In Eq. S17 there is an additional term that adds to the direct attachment rate k_{on} which vanishes for $\epsilon = 0$. Identifying this term as the diffusive on-rate the final result reads

$$k_{\text{on}}^{\text{D}} = \frac{\epsilon\,\omega_{\text{on}}}{\omega_{\text{off}} + \sqrt{\epsilon\,\omega_{\text{off}}}}\,. \tag{S18}$$

C XMAP215 parameter values

Model parameters	ϵ s^{-1}	ω_{on} $(\text{nM s})^{-1}$	ω_{off} s^{-1}	k_{cat} s^{-1}	k_{off} s^{-1}	k_{on} $(\text{nM s})^{-1}$
XMAP215	4.7×10^{3}	6×10^{-5}	4.1×10^{-1}	1.3×10^{2}	2.6×10^{-1}	6×10^{-5}

TABLE S1: Parameters used in our simulation for XMAP215. The numbers were derived from experimental data [5, 6].

D Length dependent behavior for short filaments

For filaments shorter than a critical length l_c our model implies a length dependent tip-density, see Fig. S3. Below l_c the particle flux due to diffusion and capture is limited because the filament is shorter than the length scale of free diffusion. For XMAP215 we find $l^c \approx 0.5\,\mu\text{m}$. This means that for typical *in vivo* lengths of MTs, where $l > l^c$, the enhancement of tip association through one-dimensional diffusion and capture is realized. However, below l^c length dependent behavior might occur.

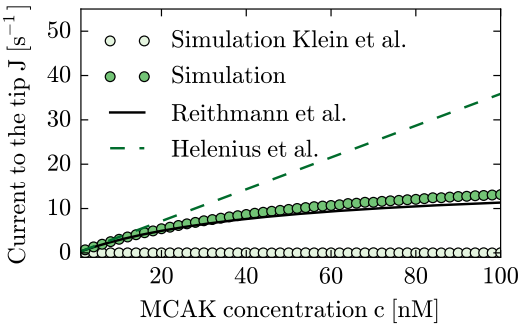

FIGURE S3: Below a critical length l^c (dotted) the reaction velocity v depends on the MT length. The reaction velocity saturates at the value given by Eq. 4 in the Main Text. Parameters are for XMAP215, $c = 300$ nM, see Table S1.

E Differences to work by Helenius et al. [4] and Klein et al. [3]

There are several differences between our work and previous theoretical investigations of the topic. Work by Helenius et al. [4] did not address the question of reaction kinetics and motor occupations at the MT tip. Their approach based on differential equations leads to mathematical inconsistencies when considering a capturing mechanism. This is why we pursued a different approach using a lattice gas. It allows us to account for the capturing mechanism which in turn leads to an explicit expression for the tip density. If the tip is highly occupied, the current saturates at a value which is approximately given by the off-rate at the tip, k_{off}. This saturation effect is not included in the model by Helenius et al. [4], but is accounted for in our model. In Fig. S4 we compare the particle current J obtained by Helenius et al. with our result. For high concentrations, there are large deviations between our model and the approximation in [4]. Work by Klein et al. [3] did not include capturing at the MT tip. Therefore there is a vanishing current to the tip if diffusion is fast compared to the enzymatic reaction at the tip, cf. Fig. S4.

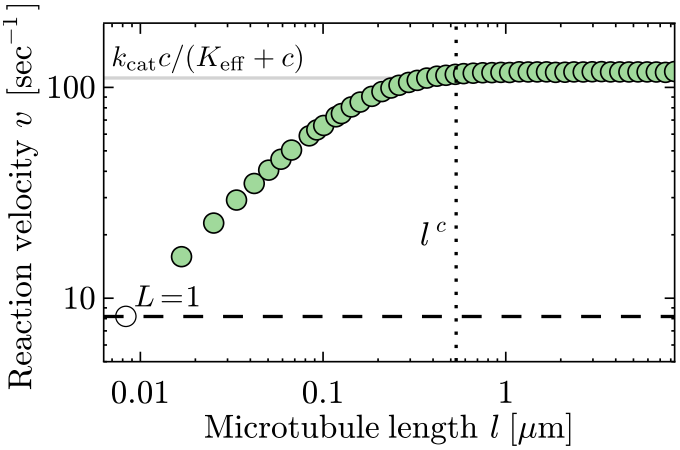

FIGURE S4: Differences in the (total) protein current J to the MT tip between this work and previous theoretical approaches. A continuous diffusion equation with absorbing boundary condition leads to a linear relation $J \propto c$ [4]. A lattice gas without capturing [3] (reflecting boundary condition) has a vanishing current to the tip $J = 0$.

References

[1] Kou, S., B. J. Cherayil, W. Min, B. P. English, and X. X. Sunney, 2005. Single-molecule michaelis-menten equations. *J. Phys. Chem. B* 109:19068–19081.

[2] Krapivsky, P. L., S. Redner, and E. Ben-Naim, 2010. A kinetic view of statistical physics. Cambridge University Press.

[3] Klein, G., K. Kruse, G. Cuniberti, and F. Jülicher, 2005. Filament Depolymerization by Motor Molecules. *Phys. Rev. Lett.* 94:108102.

[4] Helenius, J., G. J. Brouhard, Y. Kalaidzidis, S. Diez, and J. Howard, 2006. The depolymerizing kinesin MCAK uses lattice diffusion to rapidly target microtubule ends. *Nature* 441:115–9.

[5] Brouhard, G. J., J. H. Stear, T. L. Noetzel, J. Al-Bassam, K. Kinoshita, S. C. Harrison, J. Howard, and A. A. Hyman, 2008. XMAP215 is a processive microtubule polymerase. *Cell* 132:79–88.

[6] Widlund, P. O., J. H. Stear, A. Pozniakovsky, M. Zanic, S. Reber, G. J. Brouhard, A. a. Hyman, and J. Howard, 2011. XMAP215 polymerase activity is built by combining multiple tubulin-binding TOG domains and a basic lattice-binding region. *Proc. Nat. Acad. Sci. USA* 108:2741–6.

2.1.4 Publication

This section is based on the publication

Nonequilibrium Diffusion and Capture Mechanism Ensures Tip Localization of Regulating Proteins on Dynamic Filaments

by

E. Reithmann,[1] L. Reese,[1] and E. Frey[1]
[1]Arnold Sommerfeld Center for Theoretical Physics and Center for NanoScience, Department of Physics, Ludwig-Maximilians-Universität München, Theresienstraße 37, 80333 München, Germany

***Phys. Rev. Lett.* 117 (7), 078102 (2016).**
DOI: 10.1103/PhysRevLett.117.078102
Also available on arXiv: 1607.05304.

The arXiv preprint of this publication is reprinted on pages 36–41.[5]

Supplemental Material reproduced on pages 42–50.

5 Note that there is a mistake in the arXiv preprint that we corrected in the final publication. In Eq. (2) it should read $-\delta g_2$ in the last of the three corresponding equations.

A nonequilibrium diffusion and capture mechanism ensures tip-localization of regulating proteins on dynamic filaments

Emanuel Reithmann, Louis Reese,* and Erwin Frey†
Arnold Sommerfeld Center for Theoretical Physics (ASC) and Center for NanoScience (CeNS), Department of Physics, Ludwig-Maximilians-Universität München, Theresienstrasse 37, 80333 München, Germany
(Dated: February 5, 2019)

Diffusive motion of regulatory enzymes on biopolymers with eventual capture at a reaction site is a common feature in cell biology. Using a lattice gas model we study the impact of diffusion and capture for a microtubule polymerase and a depolymerase. Our results show that the capture mechanism localizes the proteins and creates large-scale spatial correlations. We develop an analytic approximation that globally accounts for relevant correlations and yields results that are in excellent agreement with experimental data. Our results show that diffusion and capture operates most efficiently at cellular enzyme concentrations which points to *in vivo* relevance.

The diffusive motion of proteins on filamentous structures in the cell is vital for several cellular functions such as gene regulation [1] and cytoskeletal dynamics [2, 3]: To find their target sites, transcription factors are likely to employ one-dimensional diffusion on the DNA and the dynamics of this process largely determine the kinetics of gene regulation [4, 5]. Similarly, actin and microtubule (MT) binding proteins diffuse on the respective filaments and fulfill regulatory functions primarily at the filament ends. Adam and Delbrück [6] suggested that a reduction in dimensionality of the diffusive motion enhances the effective rate of association of particles with binding sites on the membrane or on DNA and filaments, and this concept has been widely applied and extended [7, 8], see also Refs. [9] for recent reviews on the topic.

With regard to cytoskeletal architectures, efficient association and localization of enzymes to specific sites is relevant for a variety of cellular processes throughout the cell cycle and for cell motility and dynamics [10]. It was recently shown experimentally that one-dimensional diffusion is utilized [2, 5] by two proteins with important roles in the regulation of MT dynamics [12–15], MCAK and XMAP215. These proteins strongly localize at their respective reaction sites and show association rates for these sites that are significantly higher than expected for binding via three-dimensional diffusion [5, 8]. Both proteins carry out vital tasks, with MCAK acting as depolymerase of tubulin protofilaments [17] and XMAP215 as a poylmerase [8] when bound to ends of MTs. Note that similar mechanisms are also assumed to be relevant for actin associated proteins [18]. However, diffusive motion on filaments does not lead to a localization and efficient association of proteins *per se*: As we have shown previously [1], it is crucial to include a *capturing mechanism* at the reaction site, which suppresses the one-dimensional diffusive motion of a protein that reaches this site; without such a capturing mechanism no increase in the effective association rate for the tip occurs. For MCAK and XMAP215 protein capturing is observed in experiments: Diffusive motion stops once the proteins reach the MT tip [5, 8]. Yet, the underlying interactions with the MT tip are still elusive and being studied [20].

Here we present a theoretical description of enzyme diffusion and capture at MT tips where the enzymes catalyze filament polymerization or depolymerization. Previous studies of similar systems have lacked either a capturing mechanism [9, 22] or a dynamic filament [1], although both features are critical. To overcome both limitations, we employ a one-dimensional lattice gas [23, 24] with particle capturing in a dynamic system, in which growth or shrinkage of the filament is triggered by the interactions of particles with the lattice end. Our motivation is twofold: Firstly, we seek for a detailed mathematical understanding of the capturing mechanism. Secondly, based on a fully quantitative model, we wish to elucidate the specific biomolecular mechanisms employed by XMAP215 and MCAK. Our results show that the capturing process induces large-scale spatial correlations in the protein distribution along the filament. We develop a mathematical framework that systematically includes relevant correlations on a global scale. This conceptual advancement allows us to quantitatively explain the results of *in vitro* experiments with XMAP215 and MCAK [4, 8]. We demonstrate that the diffusion and capture mechanism strongly localizes XMAP215 and MCAK at the MT tip and that the process operates optimally under physiological conditions for both proteins, which suggests that it is relevant *in vivo*.

Model definition. We consider a one-dimensional lattice with lattice spacing a and a semi-infinite geometry which corresponds to one protofilament, as depicted in Fig. 1. In the case of MTs, a is the length of a tubulin heterodimer, 8.4 nm. The configuration of enzymes on the lattice is described by occupation numbers n_i, taking values n_i=0 for empty, and n_i=1 for occupied sites. The particles symmetrically hop to neighboring sites at rate ϵ, and interact via hard-core repulsion. We implement Langmuir kinetics to model a surrounding reservoir of particles with a constant concentration c. Particles attach to and detach from the lattice at rates $\omega_a c$ and ω_d,

respectively [27, 28]. Sites $i\geq 3$ are considered as *bulk* sites. There the dynamics differs from that in the bulk as we implement a protein capturing mechanism: Hopping from site $i=1$ to site $i=2$ is disallowed, as suggested experimentally for MCAK and XMAP215 [5, 8]. In this way, detailed balance is broken which leads to strong tip-localization due to a particle flux along the filament; in equilibrium models such a significant localization is absent, see Fig. S1 in the Supporting Material [26]. Particles detach from the first lattice site at a distinct off-rate, $\overline{\omega}_\mathrm{d}\neq\omega_\mathrm{d}$. We refer to site $i=1$ as a *reaction* site at which new lattice sites may be added or removed. For the moment, we specify our discussion to polymerases such as XMAP215 [8]. However, our considerations are largely independent of whether polymerization or depolymerization occurs—an equivalent formulation can also be found for the depolymerase MCAK [26]. For XMAP215, we specify that lattice growth is triggered at rate δ if the protein is bound to the first lattice site. Hence, the average speed of lattice growth v for the MT is proportional to the average particle occupation $\langle n_1\rangle$ and the XMAP215 polymerization rate: $v=\delta a\langle n_1\rangle$. Here we assume one catalyzing protein per protofilament end at saturating conditions [26]. The actual maximum number of catalytically active proteins is unknown; in experimental literature approximately 10 XMAP215 proteins at the MT tip are estimated at 50 nM XMAP215 [8]. As shown in recent experiments, XMAP215 acts *processively*, i.e. one molecule adds multiple tubulin dimers to the growing MT end [8]. To implement such behavior in our model the particle at the tip is transferred to newly incorporated lattice sites. In our analysis we neglect uncatalyzed tubulin addition or removal as typical corresponding experiments [3–5, 8] were performed under conditions where these processes did not occur with a significant rate. An extension is, however, possible in a straightforward fashion and does not affect tip-localization significantly; see Fig. S5 and S6 in the Supporting Material [26]. Therefore we expect validity of our further considerations also with

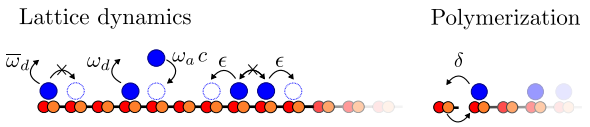

FIG. 1. Illustration of the model for XMAP215. Particles bind to empty lattice sites with rate $\omega_\mathrm{a}c$, where c is the particle concentration in solution, and detach with rate ω_d. The proteins hop symmetrically to neighboring sites at rate ϵ but exclude each other. We assume a distinct off-rate $\overline{\omega}_\mathrm{d}$ at the first site. Particles bound there cease hopping but add new lattice sites at rate δ. The particle which stimulates polymerization moves with the tip. An analogous model can be defined for MCAK, where depolymerization occurs if the lattice end is occupied, see Supporting Material for details [26].

intrinsic MT dynamics, for example as a consequence of hydrolysis of tubulin bound GTP which was studied extensively in previous models [6].

Mathematical analysis. We set up the equations of motion for the average occupation numbers of the stochastic process defined above. All equations will be formulated in the frame of reference comoving with the dynamic lattice end. In the bulk of the lattice, $i\geq 3$, we obtain

$$\begin{aligned}\tfrac{\mathrm{d}}{\mathrm{d}t}\langle n_i\rangle = \epsilon\big(\langle n_{i+1}\rangle - 2\langle n_i\rangle + \langle n_{i-1}\rangle\big) + \delta\big(\langle n_1 n_{i-1}\rangle - \langle n_1 n_i\rangle\big)\\ + \omega_\mathrm{a} c\big(1-\langle n_i\rangle\big) - \omega_\mathrm{d}\langle n_i\rangle\,. \end{aligned} \tag{1}$$

This equation comprises contributions from hopping while obeying the exclusion principle [2] (terms proportional to ϵ) and a displacement current due to polymerization (terms proportional to δ) as well as particle attachment and detachment (terms proportional to ω_a and ω_d, respectively). The tip occupations complement these bulk dynamics in the following manner:

$$\begin{aligned}\tfrac{\mathrm{d}}{\mathrm{d}t}\rho_1 &= \epsilon(\rho_2-g_2) + \omega_\mathrm{a} c(1-\rho_1) - \overline{\omega}_\mathrm{d}\rho_1\,, \\ \tfrac{\mathrm{d}}{\mathrm{d}t}\rho_2 &= \epsilon(\rho_3-2\rho_2+g_2) - \delta g_2 + \omega_\mathrm{a} c(1-\rho_2) - \omega_\mathrm{d}\rho_2\,, \\ \tfrac{\mathrm{d}}{\mathrm{d}t}g_2 &= \epsilon(g_3-g_2) + \delta g_2 + \omega_\mathrm{a} c(\rho_1+\rho_2-2g_2) - (\omega_\mathrm{d}+\overline{\omega}_\mathrm{d})g_2\,. \end{aligned} \tag{2}$$

Here we have defined the average density, $\rho_i{:=}\langle n_i\rangle$, and the correlation function, $g_i{:=}\langle n_1 n_i\rangle$. Moreover, since the polymerization process facilitated by XMAP215 is processive, an empty lattice site at $i=2$ is created and site $i=1$ remains occupied each time a new site is added. We fully quantify our model with the experimental data available for XMAP215 [3, 8]; see Supporting Material for parameter values [26].

In the first step we test the quality of standard approximation techniques for driven lattice gases against stochastic simulation data obtained from Gillespie's algorithm [32]. The set of equations which determines the lattice occupations (Eq. 1 and Eqs. 2) is not closed; the dynamics of the density ρ_i and the correlation functions $g_i{=}\langle n_1 n_i\rangle$ are coupled. In fact, there is a hierarchy of equations, which, in general, precludes the derivation of an exact solution for many driven lattice gas systems. A common and often quite successful approximation scheme for exclusion processes is to assume that there are no correlations and that one may factorize all correlation functions, $\langle n_1 n_i\rangle{\approx}\langle n_1\rangle\langle n_i\rangle$. In this *mean-field* (MF) approximation one obtains a closed set of differential equations for the particle density ρ_i which may be solved subject to proper boundary conditions; see Supporting Material for details. Fig. 2 shows the average occupation number of the first site, $\langle n_1\rangle$, as a function of the protein concentration in solution c. A comparison with our stochastic simulation data shows that the MF solution strongly overestimates $\langle n_1\rangle$ and thus the average polymerization speed v.

One possible reason for the failure of the MF calculation lies in correlations that arise close to the reaction

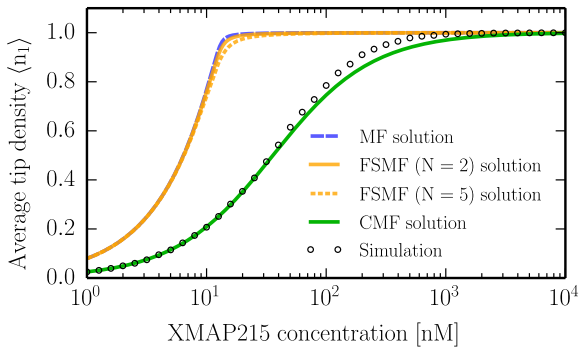

FIG. 2. Average occupation of the first lattice site $\langle n_1\rangle$. The MF approach as well as the FSMF approximation for segment sizes of $N{=}2,5$ deviate strongly from stochastic simulation data (open circles), in complete contrast to the CMF approximation. Parameter values are detailed in the Supporting Material [26].

site. Local correlations can efficiently be accounted for by employing a *finite segment mean-field* (FSMF) theory [33, 34]. Here, the idea is to retain all correlations close to the catalytic site by solving the full master equation for the first N sites and to use the MF assumption only outside of this segment. The density profile is then obtained by matching the tip solution and the MF solution [9, 35]; see Supporting Material [26]. While the results show the right trend towards the numerical data, the improvement over the MF results is insignificant. These observations suggest that correlations extend far beyond the immediate vicinity of the reaction site.

To account for such correlations we extend the MF theory by retaining both the density and the correlation function as dynamic variables. In order to close the set of equations we employ the following factorization scheme: $\langle n_1n_2n_i\rangle{\approx}\langle n_1n_2\rangle\langle n_i\rangle$, and $\langle n_2n_i\rangle{\approx}\langle n_2\rangle\langle n_i\rangle$ for $i{\geq}3$, i.e. we retain correlations with respect to the reaction site but neglect them within the bulk of the lattice. We confirmed this approximation scheme for typical biological parameter values by stochastic simulations; see Fig. S2 in the Supporting Material [26]. With the above closure relations one obtains for the bulk dynamics in a continuous description

$$\partial_t\rho(x,t) = D\partial_x^2\rho - v_0\partial_x g + \omega_{\rm a}c(1{-}\rho) - \omega_{\rm d}\rho\,, \quad \text{(3a)}$$

$$\partial_t g(x,t) = D\partial_x^2 g - v_0\partial_x g + \epsilon\rho\,(\rho_2{-}g_2) + \omega_{\rm a}c\,(\rho{+}\rho_1{-}2g) - (\omega_{\rm d}{+}\overline{\omega}_{\rm d})g\,, \quad \text{(3b)}$$

where we defined $\rho(x,t){=}\langle n_{i+1}\rangle$ and $g(x,t){=}\langle n_1n_{i+1}\rangle$ with $x{=}a(i{-}1)$ for $i{\geq}3$. We have further introduced the macroscopic diffusion constant $D{=}\epsilon a^2$ and the maximum polymerization speed $v_0{=}\delta a$. Equations 3 can be derived from the discrete equations for the density ρ_i, Eq. 1, and the correlation function g_i; for details see the Supporting Material [26]. Due to the capturing mechanism a continuous description is not valid at sites $i{=}1,2$, and we retain the local dynamics there, Eqs. 2. These equations constrain the boundary conditions of $\rho(x)$ and $g(x)$ at $x{=}a$. We further impose that the density equilibrates asymptotically at the Langmuir isotherm, $\lim_{x\to\infty}\rho(x){=}\rho_{\rm La}{=}\omega_{\rm a}c/(\omega_{\rm a}c{+}\omega_{\rm d})$, and that correlations vanish, $\lim_{x\to\infty}g(x){=}\langle n_1\rangle\rho_{\rm La}$. Solving the equations of this *correlated MF* (CMF) theory for the steady state tip density we obtain the results shown in Fig. 2, which are in excellent agreement with the stochastic simulation data. We therefore conclude that there are long-ranged correlations along the MT and that they are essential in explaining the observed average tip density and the ensuing polymerization speed.

Fig. 3(a) shows the density profile along the lattice obtained by stochastic simulations and the CMF approach. The particle occupation is obtained with high precision within the CMF framework along the whole lattice. The density profiles also agree with recent data from time and ensemble averaged high resolution fluorescence intensity profiles for XMAP215 [36]. Notably, there is a discontinuity at sites $i{=}1,2$, which is due to particle capture and which demonstrates the strong tip-localization of the proteins.

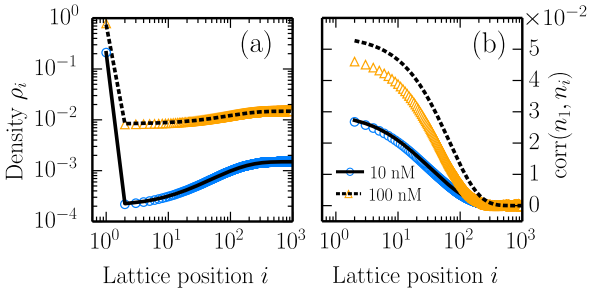

FIG. 3. Comparison of density and tip-bulk correlation profiles obtained by the CMF approximation (lines) and stochastic simulations (symbols) for XMAP215 concentrations of 10 and 100 nM (see Supporting Material [26] for parameter values [3, 8]). (a) XMAP215 strongly localizes to the MT tip and the density profile drops abruptly at sites $i{=}1,2$. (b) The correlation coefficient $\mathrm{corr}(n_1,n_i)$ (see Eq. (4)) along the lattice shows the significance of tip-bulk correlations over hundreds of lattice sites.

In Figure 3(b), the Pearson product-momentum correlation coefficient

$$\mathrm{corr}(n_1,n_i) = \frac{\mathrm{cov}(n_1,n_i)}{\sigma(n_1)\sigma(n_i)}, \quad (4)$$

which quantifies the correlations between the tip site $i{=}1$ and sites $i{\geq}2$ in the bulk, is plotted against lattice position. Here $\mathrm{cov}(\cdot,\cdot)$, and $\sigma(\cdot)$ signify the covariance and the standard deviation, respectively. The correlation coefficient decays very slowly over a broad region at the tip. The capturing mechanism and the resulting particle

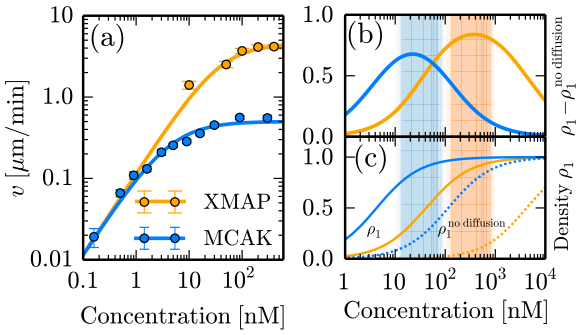

FIG. 4. Panel (a) demonstrates excellent agreement of polymerization and depolymerization velocities obtained from our theoretical analysis (CMF approximation) with existing experimental data for XMAP215 [3, 8] and MCAK [4], respectively. Panel (b) depicts the difference between the occupation density at the tip ρ_1 with and without diffusion on the MT, where $\rho_1^{\text{no diffusion}} = \omega_a c/(\overline{\omega}_d + \omega_a c)$, and shows the impact of diffusion and capture on tip localization of MCAK (blue) and XMAP (orange). The concentration range for maximum efficiency coincides with the physiological concentration range for each protein: $100 - 1000\,$nM for XMAP215 [13] and $10 - 100\,$nM for MCAK [37] (shaded areas). In (c) the reaction site density with lattice diffusion (ρ_1, solid lines) and without lattice diffusion ($\rho_1^{\text{no diffusion}}$, dashed lines) is depicted. Kinetic parameters are given in the Supporting Material [26].

flux towards the filament tip ensue strong positive correlations with respect to the first lattice site and sites in its vicinity. This effect is antagonized by weak negative correlations caused by the creation of empty lattice sites due to polymerization. With diffusion taking place on a faster time scale than polymerization, the positive correlations dominate. This is confirmed by stochastic simulations where either capturing or growth is switched off: We find anti-correlations if capturing is turned off, and positive correlations if there is no growth of the lattice; see Fig. S3 in the Supporting Material [26]. Note that for higher growth rates the correlation profile can also become negative. We conclude that the spatial correlations which emerge over several hundred lattice sites are a direct consequence of protein capture and processive growth. Further, it becomes evident why the MF and the FSMF approaches do not lead to the correct tip density: Correlations extend into the system on a length-scale which exceeds the scope of these and other previous approaches [1, 9, 22]. In contrast the CMF approximation captures and quantifies significant correlations and successfully reproduces simulation data. Note that also higher order correlations of the form $\langle n_1 n_j n_k \rangle$ and $\langle n_j n_k \rangle$ with $j, k \geq 2$ and $k > j$, which are neglected in the CMF approximation, might be of relevance when particle interactions become important for lattice diffusion. This explains the deviations in the computed correlation profile, Fig 3(b). As the CMF method is based on a non-perturbative ansatz there is no analytic expression that exactly quantifies its error. However, we observe very good agreement with our Gillespie algorithm based simulations over a very broad parameter range and, importantly, for typical biological parameters, see Fig. S4 in the Supporting Material [26].

Comparison with experimental data. We now turn to a comparison with experimental data for the polymerization velocity [3, 8] and, to supplement the results for XMAP215, we apply our methods to an analogous model for MCAK particles which depolymerize MTs [4, 5]. In essence, we adapt the above model to account for lattice shrinkage triggered by an occupied reaction site, see Supporting Material for details [26]. Similar to the processive polymerization of XMAP215 also MCAK is assumed to depolymerize processively [4, 5]. The parameters employed in the model are again drawn from available experimental data [4]. For both MCAK and XMAP215, we find excellent quantitative agreement between our theoretical approach and experimentally determined polymerization and depolymerization velocities; see Fig. 4(a). This quantitative agreement is achieved without an adjustable parameter; see Supporting Material [26]. We then used the quantified models to investigate the impact of the diffusion and capture process for XMAP215 and MCAK. Fig. 4(b) shows the increase of protein localization at the reaction site due to diffusion and capture on the filament: We plot the difference between tip densities in the presence (ρ_1^{CMF}) and absence of diffusion on filaments ($\rho_1^{\text{no diffusion}} = \omega_a c/(\overline{\omega}_d + \omega_a c)$). For both enzymes, diffusive motion and subsequent capturing at the MT lattice strongly increases the occupation density at the tip and therefore constitutes a highly efficient means of increasing the effective attachment rate to the reaction site. Moreover, the ensuing curve shows a pronounced maximum, indicating an optimal concentration range at which the enhancement of tip occupancy due to diffusion on the MT reaches its peak. Strikingly, this maximum coincides with the physiological concentration range for each protein: $100-1000\,$nM for XMAP215 [13] and $10-100\,$nM [37] for MCAK. This strongly supports the importance of diffusion and capture for MCAK and XMAP215 *in vivo*.

It is interesting to speculate about possible biomolecular mechanisms that could generate particle capturing at the MT tip as such a mechanism would probably require an energy source to drive the system out of equilibrium. Concerning MCAK, it was recently hypothesized, that an ATP is required to stop its diffusive motion at the MT tip [20] which is consistent with our proposed non-equilibrium model. Since XMAP215 does not bind nucleotides such as ATP or GTP itself [8], one might speculate that a non-equilibrium capturing mechanism relies on tubulin polymerization or depolymerization. Possibly, a conformational change of XMAP215 coupled to

processes involved in MT depolymerization or polymerization could lead to protein capture.

Summary and Conclusion. In this work, we studied the regulatory influence of an explicit capture process on the distribution of MT polymerases and depolymerases that are subject to one-dimensional diffusion on MTs. To model these biologically relevant situations we employed a model based on a *symmetric simple exclusion process* [24] extended by a detailed balance breaking capturing process at the lattice end, which acts as a biasing mechanism. Our results show that the occupation of the MT tip with a protein spatially correlates with the occupation of the MT lattice. This is a direct consequence of protein capturing which in turn strongly localizes the proteins at the MT tip. Correlations decay slowly along the lattice and have a large impact on the occupation of the MT tip. This is of relevance as the latter quantity determines the velocity of enzyme-dependent MT growth or shrinking. We derive a generalized set of hydrodynamic equations which couple the evolution of the particle density with the evolution of relevant correlations. In that way it is possible to account for those correlations on a global scale. Similar correlations have been identified in two-dimensional diffusive systems [38] or in diffusive systems with a small, local drive [39].

Our findings are not limited to MTs and their associated enzymes, but might also be applicable to other enzymatic processes with spatial degrees of freedom and, quite generally, non-equilibrium physics.

We thank Linda Wordeman, Gary Brouhard and their respective co-workers for sharing data points of XMAP215 and MCAK induced MT growing and shrinking velocities, respectively, as shown in Fig. 4(a). This research was supported by the German Excellence Initiative via the program "NanoSystems Initiative Munich" (NIM) and the Deutsche Forschungsgemeinschaft (DFG) via project B02 within the Collaborative Research Center (SFB 863) "Forces in Biomolecular Systems".

* Present address: Department of Bionanoscience, Delft University of Technology, Delft, Netherlands.
† frey@lmu.de

[1] P. H. von Hippel and O. G. Berg, J. Biol. Chem. **264**, 675 (1989).
[2] J. R. Cooper and L. Wordeman, Curr. Opin. Cell Biol. **21**, 68 (2009).
[3] J. Howard and A. A. Hyman, Curr. Opin. Cell Biol. **19**, 31 (2007).
[4] A. D. Riggs, H. Suzuki, and S. Bourgeois, J. Mol. Biol. **48**, 67 (1970).
[5] P. Hammar, P. Leroy, A. Mahmutovic, E. G. Marklund, O. G. Berg, and J. Elf, Science **336**, 1595 (2012).
[6] G. Adam and M. Delbrück, in *Structural chemistry and molecular biology* (Freeman, 1968) pp. 198–215.
[7] P. H. Richter and M. Eigen, Biophys. Chem. **2**, 255 (1974); O. G. Berg, R. B. Winter, and P. H. Von Hippel, Biochemistry **20**, 6929 (1981).
[8] L. Bintu, N. E. Buchler, H. G. Garcia, U. Gerland, T. Hwa, J. Kondev, and R. Phillips, Curr. Opin. Genet. Dev. **15**, 116 (2005).
[9] L. Mirny *et al.*, J. Phys. A: Math. Theor. **42**, 434013 (2009); A. B. Kolomeisky, Phys. Chem. Chem. Phys. **13**, 2088 (2011); O. Bénichou *et al.*, Rev. Mod. Phys. **83**, 81 (2011); M. Sheinman *et al.*, Rep. Prog. Phys. **75**, 026601 (2012).
[10] C. G. Dos Remedios *et al.*, Physiol. Rev. **83**, 433 (2003); A. Akhmanova and M. O. Steinmetz, Nat. Rev. Mol. Cell Biol. **9**, 309 (2008).
[5] J. Helenius, G. J. Brouhard, Y. Kalaidzidis, S. Diez, and J. Howard, Nature **441**, 115 (2006).
[12] R. Tournebize *et al.*, Nat. Cell Biol. **2**, 13 (2000).
[13] K. Kinoshita, I. Arnal, A. Desai, D. N. Drechsel, and A. A. Hyman, Science **294**, 1340 (2001).
[14] J. D. Wilbur and R. Heald, eLife **2**, e00290 (2013).
[15] S. B. Reber *et al.*, Nat. Cell Biol. **15**, 1116 (2013).
[8] G. J. Brouhard, J. H. Stear, T. L. Noetzel, J. Al-Bassam, K. Kinoshita, S. C. Harrison, J. Howard, and A. A. Hyman, Cell **132**, 79 (2008).
[17] A. Desai, S. Verma, T. J. Mitchison, and W. C. E., Cell **96**, 69 (1999).
[18] S. Romero *et al.*, Cell **119**, 419 (2004); D. Vavylonis *et al.*, Mol. Cell **21**, 455 (2006); S. D. Hansen and R. D. Mullins, J. Cell Biol. **191**, 571 (2010); H. Mizuno *et al.*, Science **331**, 80 (2011).
[1] E. Reithmann, L. Reese, and E. Frey, Biophys. J. **108**, 787 (2015).
[20] C. T. Friel and J. Howard, EMBO J. **30**, 3928 (2011); A. Ritter, N. Kreis, F. Louwen, L. Wordeman, and J. Yuan, Crit. Rev. Biochem. Mol. Bio. **51**, 228 (2016).
[9] G. A. Klein, K. Kruse, G. Cuniberti, and F. Jülicher, Phys. Rev. Lett. **94**, 108102 (2005).
[22] M. Schmitt and H. Stark, Europhys. Lett. **96**, 28001 (2011).
[23] T. Chou, K. Mallick, and R. K. P. Zia, Rep. Prog. Phys. **74**, 116601 (2011).
[24] B. Derrida, Phys. Rep. **301**, 65 (1998).
[4] J. R. Cooper, M. Wagenbach, C. L. Asbury, and L. Wordeman, Nat. Struct. Mol. Biol. **17**, 77 (2010).
[26] See Supplemental Material.
[27] R. Lipowsky, S. Klumpp, and T. M. Nieuwenhuizen, Phys. Rev. Lett. **87**, 108101 (2001).
[28] A. Parmeggiani, T. Franosch, and E. Frey, Phys. Rev. Lett. **90**, 086601 (2003); Phys. Rev. E **70**, 046101 (2004).
[3] P. O. Widlund, J. H. Stear, A. Pozniakovsky, M. Zanic, S. Reber, G. J. Brouhard, A. A. Hyman, and J. Howard, Proc. Nat. Acad. Sci. USA **108**, 2741 (2011).
[6] T. Antal, P. L. Krapivsky, S. Redner, M. Mailman, and B. Chakraborty, Phys. Rev. E **76**, 041907 (2007); R. Padinhateeri, A. B. Kolomeisky, and D. Lacoste, Biophys. J. **102**, 1274 (2012); T. Niedermayer and R. Lipowsky, Phys. Rev. E **92**, 052137 (2015).
[2] B. Derrida, J. Stat. Mech. Theor. Exp. **2007**, P07023 (2007).
[32] D. T. Gillespie, Annu. Rev. Phys. Chem. **58**, 35 (2007).
[33] T. Chou and G. Lakatos, Phys. Rev. Lett. **93**, 198101 (2004).
[34] G. Lakatos, T. Chou, and A. Kolomeisky, Phys. Rev. E **71**, 011103 (2005).
[35] S. A. Nowak, P.-W. Fok, and T. Chou, Phys. Rev. E **76**,

031135 (2007).
[36] S. P. Maurer, N. I. Cade, G. Bohner, N. Gustafsson, E. Boutant, and T. Surrey, Curr. Biol. **24**, 372 (2014).
[37] A. W. Hunter, M. Caplow, D. L. Coy, W. O. Hancock, S. Diez, L. Wordeman, and J. Howard, Mol. Cell **11**, 445 (2003).
[38] D. C. Markham, M. J. Simpson, and R. E. Baker, Phys. Rev. E **87**, 062702 (2013); D. C. Markham, M. J. Simpson, P. K. Maini, E. A. Gaffney, and R. E. Baker, Phys. Rev. E **88**, 052713 (2013).
[39] T. Sadhu, S. N. Majumdar, and D. Mukamel, Phys. Rev. E **90**, 012109 (2014).

Supplemental Material: A nonequilibrium diffusion and capture mechanism ensures tip-localization of regulating proteins on dynamic filaments

Emanuel Reithmann, Louis Reese, and Erwin Frey
Arnold Sommerfeld Center for Theoretical Physics (ASC) and Center for NanoScience (CeNS), Department of Physics, Ludwig-Maximilians-Universität München, Theresienstrasse 37, 80333 München, Germany

TIP LOCALIZATION DUE TO PARTICLE CAPTURING

In this work, we investigate a model where the diffusive motion of particles on a filament ceases as soon as they arrive at a reaction site. This feature, which we refer to as particle capturing, is a key element of our model, as it drives the system out of thermal equilibrium. In order to investigate the impact of particle capture on tip localization of particles, we also investigated a model where particles are not captured at the tip, but where a hopping from the tip into the bulk occurs such that detailed balance is not broken. In detail, we introduce a release rate $\overline{\epsilon}$, at which particles hop from site $i = 1$ to site $i = 2$. Then, to implement equilibrium conditions for particle hopping (i.e. with respect to a system without lattice growth or shrinkage), we impose $\epsilon/\overline{\epsilon} = \omega_d/\overline{\omega}_d$. This condition ensures detailed balance in a static system and for a constant on-rate along the lattice. Since we also implement lattice growth, detailed balance is still broken, which manifests itself in a net particle drift away from the tip in the comoving frame of reference. In Fig. S1 we compare density profiles of the hopping-equilibrium model and the one with strict (i.e. irreversible) particle capturing as defined in the main text with parameters as for XMAP215. In the equilibrium model, the density profile is almost constant whereas in the model with capturing a strong tip-localization occurs (1-2 orders of magnitude increase in the tip-density). Although an irreversible capturing is, of course, a simplification, we expect similar effects to occur for release rates much smaller than the equilibrium release rate, $\overline{\epsilon} \ll \overline{\epsilon}_{\mathrm{eq}} := (\epsilon\,\overline{\omega}_d)/\omega_d$. In this case, capturing generates a particle current towards the MT tip which conversely leads to spatial correlations subject of this work.

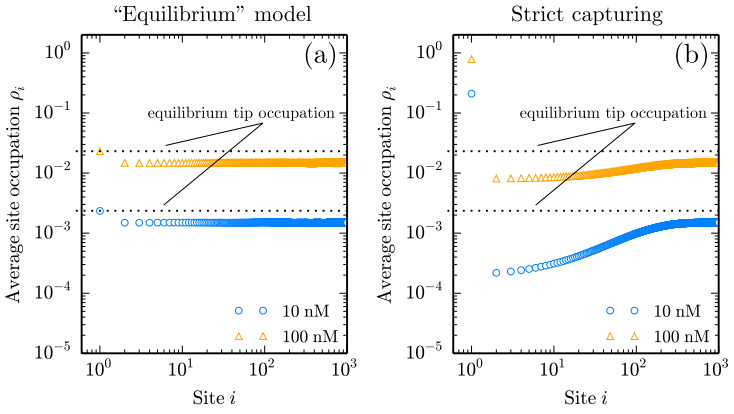

FIG. S1. Diffusion and capture ensures tip-localization. Density profiles from MC simulations (open symbols) of (a) a model where particle hopping obeys detailed balance with respect to a static lattice and (b) the model from the main text. In an "equilibrium" model no localization occurs and the density profile is almost constant due to fast diffusion. With strict (i.e. irreversible capturing), the tip is highly occupied as compared to its equilibrium occupation (dotted lines). Note that in both models we implement off-rates which differ at the tip and lattice growth which results in non-constant density profiles also when particle hopping obeys detailed balance. Further, also the "equilibrium" model is out of equilibrium due to lattice growth. In (a) $\overline{\epsilon} = 3.0 \times 10^3\,\mathrm{s}^{-1}$, in (b) $\overline{\epsilon} = 0$. Other parameters as for the XMAP215 model, see Table I.

MEAN-FIELD (MF) APPROXIMATION

In the mean-field approximation all correlations are neglected; we set $\langle n_i n_j\rangle = \langle n_i\rangle\langle n_j\rangle$. This closes the hierarchy of equations stated in the main text:

$$\frac{\mathrm{d}}{\mathrm{d}t}\langle n_i\rangle = \epsilon(\langle n_{i+1}\rangle - 2\langle n_i\rangle + \langle n_{i-1}\rangle) + \delta(\langle n_1\rangle\langle n_{i-1}\rangle - \langle n_1\rangle\langle n_i\rangle) + \omega_\mathrm{a} c(1-\langle n_i\rangle) - \omega_\mathrm{d}\langle n_i\rangle \text{ for } i \geq 3 \tag{S1}$$

$$\frac{\mathrm{d}}{\mathrm{d}t}\langle n_1\rangle = \epsilon(\langle n_2\rangle - \langle n_1\rangle\langle n_2\rangle) + \omega_\mathrm{a} c(1-\langle n_1\rangle) - \overline{\omega}_\mathrm{d}\langle n_1\rangle \tag{S2}$$

$$\frac{\mathrm{d}}{\mathrm{d}t}\langle n_2\rangle = \epsilon(\langle n_3\rangle - 2\langle n_2\rangle + \langle n_1\rangle\langle n_2\rangle) - \delta\langle n_1\rangle\langle n_2\rangle + \omega_\mathrm{a} c(1-\langle n_2\rangle) - \omega_\mathrm{d}\langle n_2\rangle\,. \tag{S3}$$

Instead of solving the recurrence relation, we use a continuous description for Eq. S1. At sites $i = 1, 2$ such an approximation is not valid due to a discontinuity in the density profile. Performing a Taylor expansion for small lattice spacings a up to second order we obtain

$$\partial_t \rho(x,t) = \epsilon a^2 \partial_x^2 \rho(x,t) - \delta a \partial_x \rho(x,t)\langle n_1\rangle + \omega_\mathrm{a} c(1-\rho(x,t)) - \omega_\mathrm{d}\rho(x,t)\,. \tag{S4}$$

In the above equation the continuous labeling $x = a(i-1)$ is used for $\rho(x,t) = \langle n_{i+1}\rangle$. Further, we use that for typical biological systems $\epsilon \gg \delta$ holds true and neglect the second order term due to the particle drift in the comoving frame, $\frac{1}{2}\delta a^2 \partial_x^2 \rho(x)$. Since we are only interested in the steady state solution we set the time derivative to zero. As boundary condition, we impose that the density equilibrates at the Langmuir density for large distances to the tip, $\lim_{x\to\infty}\rho(x) = \rho_\mathrm{La} = \omega_a c/(\omega_a c + \omega_d)$. The boundary condition at $x = a$ has to be consistent with the solution of Eqs. S2 and S3, $\rho(a) = \langle n_2\rangle$. We can use the continuous solution to express $\langle n_3\rangle = \rho(2a)$ and solve Eqs. S2 and S3. This self-consistent solution can be obtained numerically and determines the MF density profile along the whole lattice.

THE FINITE SEGMENT MEAN-FIELD (FSMF) APPROXIMATION

The finite segment mean-field approach is based on the idea to account for correlations locally within a small segment. In detail, all correlations within this segment are retained whereas outside the segment correlations are neglected. An efficient implementation is achieved by using the transition matrix corresponding to the master equation for occupations of the segment. Since in our model correlations are strongest close to the tip, we choose to keep correlations with respect to the first N sites. For example, for $N = 2$ the corresponding transition matrix M_{ij} with $i, j \in \{0, \ldots, 3\}$ reads

$$M = \begin{pmatrix} -2\omega_a c - \epsilon\langle n_3\rangle & \omega_d + \epsilon\langle \overline{n}_3\rangle & \overline{\omega}_d & 0 \\ \omega_a c + \epsilon\langle n_3\rangle & -\omega_d - \omega_a c - \epsilon(1+\langle \overline{n}_3\rangle) & 0 & \overline{\omega}_d \\ \omega_a c & \epsilon & -\overline{\omega}_d - \omega_a c - \epsilon\langle n_3\rangle & \delta + \epsilon\langle \overline{n}_3\rangle + \omega_d \\ 0 & \omega_a c & \omega_a c + \epsilon\langle n_3\rangle & -\omega_d - \overline{\omega}_d - \epsilon\langle \overline{n}_3\rangle - \delta \end{pmatrix}.$$

Here we introduced $\langle \overline{n}_3\rangle = (1 - \langle n_3\rangle)$. Further, the enumeration of states is chosen such that it corresponds to the respective binary number, e.g. M_{01} describes transitions from state $(n_1 = 0, n_2 = 1)$ to state $(n_1 = 0, n_2 = 0)$. Note that correlations with respect to n_{N+1} are already neglected. The eigenvector of M with eigenvalue 0 is then computed, which yields steady state occupations within the segment in dependence of $\langle n_{N+1}\rangle$. A self-consistent solution of these occupations and those for sites $i > N$ is obtained in analogous fashion to the MF procedure: We use the continuous MF solution for densities with $i > N$ and the discrete solutions for sites in the segment to express all densities in terms of $\langle n_{N+1}\rangle$. The master equation for $\langle n_{N+1}\rangle$ (given by Eq. S1) is then solved numerically in the steady state to compute the complete density profile. This procedure is, however, strongly limited by the size of the finite segment as the corresponding transition matrix is of size $2^N \times 2^N$.

THE CORRELATED MEAN-FIELD (CMF) APPROXIMATION

In the following we will show how to perform the CMF approximation for the model presented in the main text. This approach systematically includes the relevant correlations arising due to the capturing mechanism.

The CMF calculations can be separated in three steps: a) Computation of the continuous solution for the density $\rho(x)$ and correlation profile $g(x)$ in the bulk, $i \geq 2$. b) Computation of the discrete solution for $i = 1$. c) Matching of the continuous solution and the discrete solution.

We start with deriving the continuous bulk solutions. The density profile is governed by Eq. 1 of the main text:

$$\begin{aligned}\tfrac{\mathrm{d}}{\mathrm{d}t}\langle n_i\rangle &= \epsilon\big(\langle n_{i+1}(1-n_i)\rangle - \langle n_i(1-n_{i+1})\rangle + \langle n_{i-1}(1-n_i)\rangle - \langle n_i(1-n_{i-1})\rangle\big) + \delta\big(\langle n_1 n_{i-1}\rangle - \langle n_1 n_i\rangle\big)\\ &\quad + \omega_\mathrm{a} c\big(1-\langle n_i\rangle\big) - \omega_\mathrm{d}\langle n_i\rangle\\ &= \epsilon\big(\langle n_{i+1}\rangle - 2\langle n_i\rangle + \langle n_{i-1}\rangle\big) + \delta\big(\langle n_1 n_{i-1}\rangle - \langle n_1 n_i\rangle\big) + \omega_\mathrm{a} c\big(1-\langle n_i\rangle\big) - \omega_\mathrm{d}\langle n_i\rangle\,. \end{aligned} \tag{S5}$$

Here, we account for particle hopping with exclusion (terms $\propto \epsilon$), lattice growth (terms $\propto \delta$), particle attachment (terms $\propto \omega_\mathrm{a}$), and particle detachment (terms $\propto \omega_\mathrm{d}$). In the main text we show that it is essential to account for tip-bulk correlations on a large scale. In the CMF approach this is achieved globally by coupling the evolution of the density with the one for tip-bulk correlations. The discrete equation governing the evolution of correlations with respect to the reaction site reads

$$\begin{aligned}\tfrac{\mathrm{d}}{\mathrm{d}t}\langle n_1 n_i\rangle &= \epsilon(\langle n_1 n_{i-1}\rangle - 2\langle n_1 n_i\rangle + \langle n_1 n_{i+1}\rangle + \langle n_2 n_i\rangle - \langle n_1 n_2 n_i\rangle) + \delta(\langle n_1 n_{i-1}\rangle - \langle n_1 n_i\rangle)\\ &\quad + \omega_\mathrm{a} c(\langle n_1\rangle + \langle n_i\rangle - \langle n_1 n_i\rangle) - (\overline{\omega}_\mathrm{d} + \omega_\mathrm{d})\langle n_1 n_i\rangle. \end{aligned} \tag{S6}$$

The above equation, which follows from the master equation, describes changes of the joint probability for a simultaneous occupation of the first and the i-th site: All probabilities for processes that lead to a simultaneous occupation of both lattice sites multiplied with the respective rate are added and all probabilities for processes where one of the two sites is emptied multiplied with the respective rate are subtracted. Again, contributions arise from particle hopping with exclusion (terms $\propto \epsilon$), lattice growth (terms $\propto \delta$), particle attachment (terms $\propto \omega_\mathrm{a}$), and particle detachment (terms $\propto \omega_\mathrm{d}$), respectively. For example, for particle hopping we have contributions from hopping processes with respect to the i-th site ($\langle n_1 n_{i-1}\rangle - 2\langle n_1 n_i\rangle + \langle n_1 n_{i+1}\rangle$) as well as the capturing of a particle at the first site ($\langle n_2 n_i\rangle - \langle n_1 n_2 n_i\rangle$). Note that higher order correlators can be obtained in complete analogy. In order to close the hierarchy of moments, we use the factorization scheme stated in the main text: $\langle n_1 n_2 n_i\rangle \approx \langle n_1 n_2\rangle\langle n_i\rangle$ and $\langle n_2 n_i\rangle \approx \langle n_2\rangle\langle n_i\rangle$ for $i \geq 3$. Fig. S2 shows that this is justified, as the corresponding correlation coefficients are one to two orders of magnitude lower than $\mathrm{corr}(n_1, n_i)$. In the continuous limit $a \to 0$ the recurrence relations given by the dynamic equations for $\langle n_i\rangle$ and $\langle n_1 n_i\rangle$ translate into a set of coupled differential equations. Up to a second order Taylor expansion we obtain

$$\partial_t \rho(x,t) = \epsilon a^2 \partial_x^2 \rho(x,t) - \delta a \partial_x g(x,t) + \omega_\mathrm{a} c(1-\rho(x,t)) - \omega_\mathrm{d}\rho(x,t) \tag{S7}$$

$$\begin{aligned}\partial_t g(x,t) &= \epsilon(a^2\partial_x^2 g(x,t) + \langle n_2\rangle(t)\rho(x,t) - \langle n_1 n_2\rangle(t)\rho(x,t)) - \delta a\partial_x g(x,t) + \omega_\mathrm{a} c(\langle n_1\rangle(t) + \rho(x,t) - 2g(x,t))\\ &\quad -(\omega_\mathrm{d} + \overline{\omega}_\mathrm{d}) g(x,t)\,. \end{aligned} \tag{S8}$$

Here, we used again a continuous labeling $x = a(i-1)$ and neglected second order terms due to lattice growth ($\propto \frac{1}{2}\delta a^2 \partial_x^2 g(x)$) since $\epsilon \gg \delta$ for typical biological situations. In this work, we are interested in the steady state properties of the system, $\partial_t \rho(x,t) = 0$ and $\partial_t g(x,t) = 0$. Under this condition, Eqs. S7 and S8 are solved for the continuous solutions $\rho(x)$ and $g(x)$. Further, we impose the following boundary conditions to obtain a meaningful solution: $\lim_{x\to\infty}\rho(x) = \rho_\mathrm{La} = \omega_\mathrm{a} c/(\omega_\mathrm{a} c + \omega_\mathrm{d})$, $\lim_{x\to\infty} g(x) = \langle n_1\rangle\rho_\mathrm{La}$, $\rho(a) = \langle n_2\rangle$ and $g(a) = \langle n_1 n_2\rangle$. Note that the solutions depend on the yet unknown variables $\langle n_1\rangle$, $\langle n_2\rangle$ and $\langle n_1 n_2\rangle$.

In the second step, we solve the equation for the occupancy of the reaction sites, $i = 1$,

$$\tfrac{\mathrm{d}}{\mathrm{d}t}\langle n_1\rangle = 0 = \epsilon(\langle n_2\rangle - \langle n_1 n_2\rangle) + \omega_\mathrm{a} c(1-\langle n_1\rangle) - \overline{\omega}_\mathrm{d}\langle n_1\rangle\,, \tag{S9}$$

to express $\langle n_1\rangle$ in terms of $\langle n_2\rangle$ and $\langle n_1 n_2\rangle$.

Lastly, we self-consistently match the discrete and continuous solutions in that we determine the values of $\langle n_2\rangle$ and $\langle n_1 n_2\rangle$. To this end we employ the "master equations" for the latter variables.

$$\tfrac{\mathrm{d}}{\mathrm{d}t}\langle n_2\rangle = 0 = \epsilon(\langle n_3\rangle - 2\langle n_2\rangle + \langle n_1 n_2\rangle) - \delta\langle n_1 n_2\rangle + \omega_\mathrm{a} c(1-\langle n_2\rangle) - \omega_\mathrm{d}\langle n_2\rangle \tag{S10}$$

$$\tfrac{\mathrm{d}}{\mathrm{d}t}\langle n_1 n_2\rangle = 0 = \epsilon(\langle n_1 n_3\rangle - \langle n_1 n_2\rangle) + \delta\langle n_1 n_2\rangle + \omega_\mathrm{a} c(\langle n_1\rangle + \langle n_2\rangle - 2\langle n_1 n_2\rangle) - (\omega_\mathrm{d} + \overline{\omega}_\mathrm{d})\langle n_1 n_2\rangle. \tag{S11}$$

We insert the continuous bulk solutions derived in the first step for $\langle n_3\rangle = \rho(2a)$ and $\langle n_1 n_3\rangle = g(2a)$. Finally, the discrete solution for $\langle n_1\rangle$ is used to express all variables in terms of $\langle n_2\rangle$ and $\langle n_1 n_2\rangle$. This allows us to solve Eqs. S10 and S11 numerically which, as a consequence, fixes the entire density and correlation profile.

The behavior of correlations is also demonstrated in Fig S3: Without a capturing mechanism, correlations are purely negative due to the creation of empty sites resulting from the processive polymerization scheme. Opposed to that, purely positive correlations arise in a static lattice with capturing.

The CMF approach neglects correlations within the diffusive compartment (i.e. we assume $\langle n_i n_j\rangle = \langle n_i\rangle\langle n_j\rangle$ and $\langle n_1 n_i n_j\rangle = \langle n_1 n_i\rangle\langle n_j\rangle$ for $i, j \geq 3$ and $i < j$). As this approximation is a non-perturbative ansatz, it is in general not

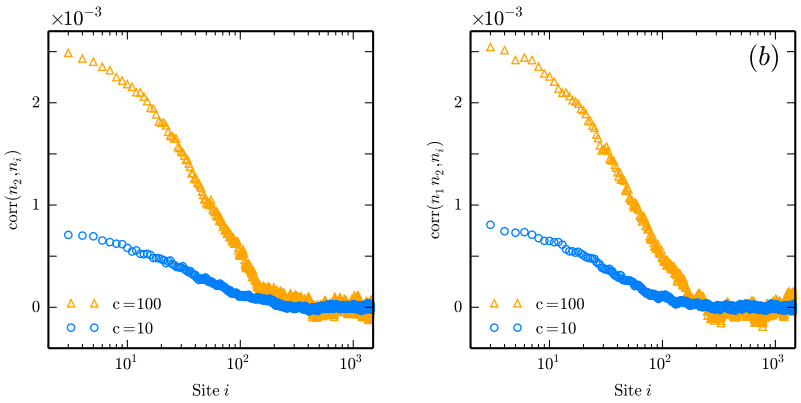

FIG. S2. In panel (a) and (b) we show that correlations $\mathrm{corr}(n_2, n_i)$ and $\mathrm{corr}(n_1 n_2, n_i)$ for $i \geq 3$ are negligible since they are one to two orders of magnitude smaller than the tip bulk correlations, $\mathrm{corr}(n_1, n_i)$. Parameters as for the XMAP215 model.

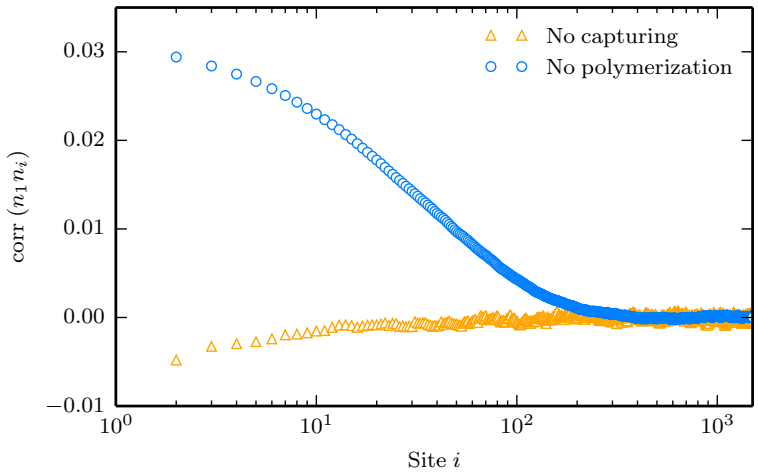

FIG. S3. Tip-bulk correlation profile obtained from stochastic simulations. Without particle capturing (orange data points) correlations are negative due to the processive growth of the lattice and the resulting creation of empty lattice sites. Correlations are positive in a static system with a capturing mechanism (blue points). Parameter values are equal to the ones used for the XMAP215 model; concentrations are $c = 10$ nM for the case without polymerization and $c = 5000$ nM for the case without capturing.

possible to quantify its error. In order to ensure the validity over a broad and biologically relevant parameter range, we performed extensive MC simulations and compared the result with CMF computations. In detail, we performed parameter sweeps for ϵ (from $300 - 10000$ s^{-1}), ω_d (from $0.1 - 10$ s^{-1}), δ (from $5 - 95$ s^{-1}) and c (for each parameter point at five equidistant values between c_1 and c_5, such that $\rho_1^{\mathrm{CMF}}(c_1) = 0.1$ and $\rho_1^{\mathrm{CMF}}(c_5) = 0.9$). The results are shown in Fig. S4. The CMF approximation delivers good results over this very broad parameter range; the maximum relative deviation for ρ_1 over the 1000 different tested parameter sets is 6.5%.

In a previous publication, we derived an effective theory that allows for the calculation of reaction site occupations that are subject to a diffusion and capture mechanism in a static lattice (i.e. without lattice growth or shrinkage) [S1]. While both approaches consider protein diffusion and capture on filaments, they differ significantly on a conceptual level and with respect to the scope of their predictions: Whereas the previous approach is based an on a heuristic theory and *a priori* only valid in the absence of polymerization and depolymerization, respectively, the CMF approach specifically accounts for lattice growth and shrinkage. Further, the CMF approximation is derived from more conceptual considerations: It assumes that diffusion and capture creates correlations which primarily affect the tip

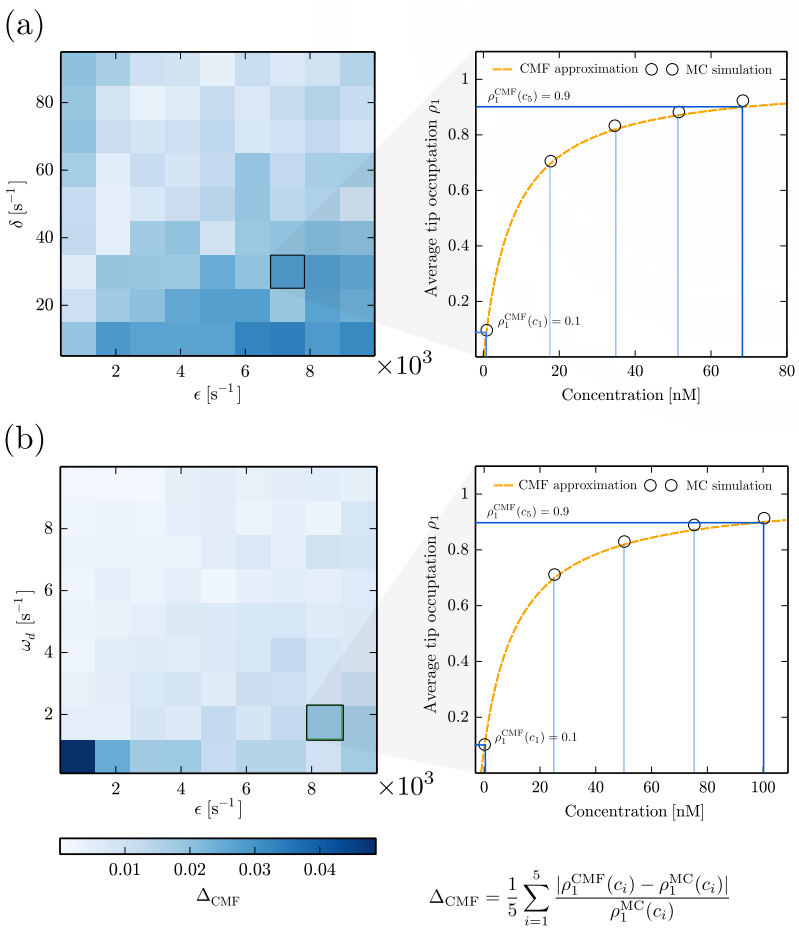

FIG. S4. Error of CMF approximation. We compared results for the tip density obtained from the CMF approximation (ρ_1^{CMF}) and MC simulations (ρ_1^{MC}) for 1000 different parameter sets. For each set $\{\epsilon,\ \delta,\ \omega_a,\ \omega_d,\ \overline{\omega}_d\}$ we determined five equidistant concentrations between c_1 and c_5, such that $\rho_1^{\mathrm{CMF}}(c_1) = 0.1$ and $\rho_1^{\mathrm{CMF}}(c_5) = 0.9$. For these concentrations, we computed the average relative deviation between simulation results and analytic approximation to get an estimate Δ_{CMF} of the error along a $\rho_1 - c$ curve (right side). Note that we expect the error to vanish for very low and very high occupations. We performed sweeps with respect to ϵ and δ (a), and ϵ and ω_d (b). Deviations are small, with the maximal c-averaged deviation being 5% and the maximal relative deviation being 6.5%. Color encodes the c-averaged deviations Δ_{CMF} with white denoting 0% deviation and dark blue denoting more significant deviations. As expected, we observe a small trend of increasing errors whenever interactions in the lattice bulk become more frequent, i.e. for high ϵ, small δ and small ω_d. Opposed to Eq. S8 we include the second order term that arises due to lattice polymerziation, $\frac{1}{2}\delta a^2 \partial_x^2 g(x)$, as $\epsilon \gg \delta$ does not necessarily hold true any more.

occupation while the diffusive motion of proteins on the MT depends less significantly on mutual correlations [S2]. As a consequence, the CMF approach yields density and tip-bulk correlation profiles for protein occupations along the MT, which are beyond the scope of our previous approach. As shown in the main text, the latter quantities are key to a quantitative understanding of tip-localization due to diffusion and capture and related processes.

UNCATALYZED GROWTH AND SHRINKAGE OF MTS

The model described in the main text does not account for MT growth or shrinkage in the absence of depolymerziation or polymerization factors like MCAK or XMAP215. The reason for this assumption is twofold: a) In the experiments with XMAP215 [S3] and MCAK [S4] low concentrations of free tubulin were used such that no spon-

taneous MT growth was observed. Also, the measurements in Widlund et al. [S3] suggest that the rate of tubulin detachment in the corresponding experiments is negligible. b) Concerning MT depolymerization, we aim for a description of protein induced tubulin removal from stabilized MTs in analogy to *in vitro* experiments with MCAK [S4, S5]. In this way, our model neglects the dynamic instability seen for unstabilized MTs [S6, S7], but provides a description how a stabilizing structure at the MT tip (e.g. GTP-tubulin) can be removed by regulatory enzymes.

That being said, let us emphasize that an extension towards uncatalyzed tubulin attachment and detachment is feasible based on the model described in the main text. To this end we include further processes in the model: If the terminal lattice site is unoccupied, a new site can be added at rate $\delta_{\text{spont}}^{\text{poly}}$ or removed at rate $\delta_{\text{spont}}^{\text{depoly}}$. For completeness, we also include catalyzed (processive) growth *and* shrinkage with corresponding rates $\delta_{\text{cat}}^{\text{poly}}$ and $\delta_{\text{cat}}^{\text{depoly}}$, respectively. The resulting equations for the CMF framework then read

$$\begin{aligned}
\partial_t\rho(x,t) = 0 = {} & (\delta_{\text{spont}}^{\text{depoly}} - \delta_{\text{spont}}^{\text{poly}})a\partial_x\rho(x,t) + (\epsilon + \frac{1}{2}\delta_{\text{spont}}^{\text{depoly}} + \frac{1}{2}\delta_{\text{spont}}^{\text{poly}})a^2\partial_x^2\rho(x,t) \\
& + (\delta_{\text{cat}}^{\text{depoly}} - \delta_{\text{cat}}^{\text{poly}} + \delta_{\text{spont}}^{\text{poly}} - \delta_{\text{spont}}^{\text{depoly}})a\,\partial_x g(x,t) + \frac{1}{2}(\delta_{\text{cat}}^{\text{poly}} + \delta_{\text{cat}}^{\text{depoly}} - \delta_{\text{spont}}^{\text{poly}} - \delta_{\text{spont}}^{\text{depoly}})a^2\partial_x^2 g(x,t) \\
& + \omega_{\text{a}}c(1-\rho(x,t)) - \omega_{\text{d}}\rho(x,t)\,, \qquad \text{(S12)} \\
\partial_t g(x,t) = 0 = {} & (\delta_{\text{spont}}^{\text{depoly}} + \epsilon)(\langle n_2\rangle(t) - \langle n_1 n_2\rangle(t))\rho(x,t) + \delta_{\text{spont}}^{\text{depoly}}(\langle n_2\rangle(t) - \langle n_1 n_2\rangle(t))(a\partial_x\rho(x,t) + \frac{1}{2}a^2\partial_x^2\rho(x,t)) \\
& + (\delta_{\text{cat}}^{\text{depoly}} - \delta_{\text{cat}}^{\text{poly}})a\partial_x g(x,t) + (\epsilon + \frac{1}{2}\delta_{\text{cat}}^{\text{poly}} + \frac{1}{2}\delta_{\text{cat}}^{\text{depoly}})a^2\partial_x^2 g(x,t) + \omega_{\text{a}}c(\langle n_1\rangle(t) - \rho(x,t) - 2g(x,t)) \\
& - (\omega_{\text{d}} + \overline{\omega}_{\text{d}})g(x,t)\,, \qquad \text{(S13)} \\
\tfrac{\text{d}}{\text{d}t}\langle n_1\rangle(t) = 0 = {} & \epsilon(\langle n_2\rangle(t) - \langle n_1 n_2\rangle(t)) + \delta_{\text{spont}}^{\text{depoly}}(\langle n_2\rangle(t) - \langle n_1 n_2\rangle(t)) + \omega_{\text{a}}c(1 - \langle n_1\rangle(t)) - \overline{\omega}_{\text{d}}\langle n_1\rangle(t)\,, \qquad \text{(S14)} \\
\tfrac{\text{d}}{\text{d}t}\langle n_2\rangle(t) = 0 = {} & \epsilon(\langle n_3\rangle(t) - 2\langle n_2\rangle(t) + \langle n_1 n_2\rangle(t)) - \delta_{\text{cat}}^{\text{poly}}\langle n_1 n_2\rangle(t) + \delta_{\text{cat}}^{\text{depoly}}(\langle n_1 n_3\rangle(t) - \langle n_1 n_2\rangle(t)) \\
& - \delta_{\text{spont}}^{\text{poly}}(\langle n_2\rangle(t) - \langle n_1 n_2\rangle(t)) + \delta_{\text{spont}}^{\text{depoly}}(\langle n_1 n_2\rangle(t) - \langle n_1 n_3\rangle(t) + \langle n_3\rangle(t) - \langle n_2\rangle(t)) + \omega_{\text{a}}c(1 - \langle n_2\rangle(t)) - \omega_{\text{d}}\langle n_2\rangle(t)\,, \\
& \qquad \text{(S15)} \\
\tfrac{\text{d}}{\text{d}t}\langle n_1 n_2\rangle(t) = 0 = {} & \epsilon(\langle n_1 n_3\rangle(t) - \langle n_1 n_2\rangle(t)) - \delta_{\text{cat}}^{\text{poly}}\langle n_1 n_2\rangle(t) + \delta_{\text{cat}}^{\text{depoly}}(\langle n_1 n_3\rangle(t) - \langle n_1 n_2\rangle(t)) \\
& + \delta_{\text{spont}}^{\text{depoly}}(\langle n_2\rangle(t)\langle n_3\rangle(t) - \langle n_1 n_2\rangle(t)\langle n_3\rangle(t)) + \omega_{\text{a}}c(\langle n_1\rangle(t) + \langle n_2\rangle(t) - 2\langle n_1 n_2\rangle(t)) - (\omega_{\text{d}} + \overline{\omega}_{\text{d}})\langle n_1 n_2\rangle(t). \qquad \text{(S16)}
\end{aligned}$$

The equations are solved in analogy to the case without spontaneous lattice dynamics.

As mentioned above, our models neglect intrinsic MT dynamics such as dynamic instability. However, we expect validity of our results for tip-localization also under such circumstances. We studied the extended model with spontaneous growth and shrinkage rates over a variety of parameter values (up to spontaneous growth and shrinkage rates of 24 μm/min). For a comparison, we estimated the rate of spontaneous MT growth ($v_{\text{spont}} = a(\delta_{\text{spont}}^{\text{poly}} - \delta_{\text{spont}}^{\text{depoly}})$) at tubulin concentrations slightly above 5 μM from the experiments performed by Widlund et al. [S3]. At such tubulin concentrations, MTs were observed to start growing also without the presence of XMAP215 at a speed of approximately $v_{\text{spont}} = 0.5$ μm/min. Given this resulting spontaneous MT growth rate, we compared a model with and without fast intrinsic MT dynamics ($\delta_{\text{spont}}^{\text{poly}} = 1\,s^{-1}$ and $\delta_{\text{spont}}^{\text{depoly}} = 0$ for a stable lattice; $\delta_{\text{spont}}^{\text{poly}} = 51\,s^{-1}$ and $\delta_{\text{spont}}^{\text{depoly}} = 50\,s^{-1}$ for a dynamic lattice). The results are shown in Figs. S5 and S6. They show the robustness of the protein distribution $\rho(x)$ and, in particular, the tip occupation against changes in the lattice growth or shrinkage rates. Moreover, the CMF approximation is also applicable for rapidly fluctuating MT lengths. Note that XMAP215 also catalyzes tubulin removal under certain conditions [S8] which could readily be accounted for in the above approach.

MCAK MODEL

Similar to the model for XMAP215 stated in the main text we can set up a model for the depolymerase activity of MCAK, see Fig. S7. The ensuing set of equations corresponding to the CMF approach in the bulk are a special case of Eqs. S12-S16 with $\delta_{\text{spont}}^{\text{poly}} = \delta_{\text{spont}}^{\text{depoly}} = \delta_{\text{cat}}^{\text{poly}} = 0$. We implement a processive depolymerization scheme [S4, S5, S9]. In detail, MCAK particles stay at the terminal site during depolymerization (i.e. move along with the tip) whenever the neighboring site is empty. Otherwise, they dissociate from the tip during depolymerization. This means that MCAK particles fall off the MT tip whenever they hit another particle during the depolymerization process. The results of the CMF approach for the MCAK model agree excellently with simulation data, as shown in Fig. S8. Further, also for the MCAK model the MF approximation and FSMFT produce results that deviate from simulation data at intermediate concentrations.

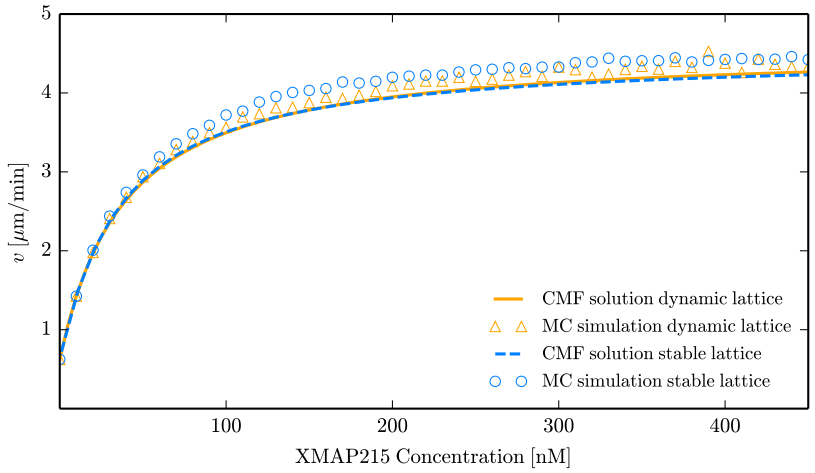

FIG. S5. Extended model that accounts for uncatalyzed growth and shrinkage of MTs. We compare diffusion and capture on a slowly growing lattice ($\delta^{\text{poly}}_{\text{spont}} = 1\,s^{-1}$, $\delta^{\text{depoly}}_{\text{spont}} = 0$, $\delta^{\text{depoly}}_{\text{cat}} = 0$, $\delta^{\text{poly}}_{\text{cat}} = 9.5\,s^{-1}$, blue) with diffusion and capture on a lattice with fast intrinsic dynamics but the same average growth speed ($\delta^{\text{poly}}_{\text{spont}} = 51\,s^{-1}$, $\delta^{\text{depoly}}_{\text{spont}} = 50\,s^{-1}$, $\delta^{\text{depoly}}_{\text{cat}} = 50\,s^{-1}$, $\delta^{\text{poly}}_{\text{cat}} = 59.5\,s^{-1}$, orange). The average MT growing velocity, and therefore also the tip density, deviate little which implies the validity of our results also on dynamic lattices. MC simulations (symbols) agree well with solutions of the CMF approximation (lines). Other parameter values are as for the XMAP215 model, see Table I.

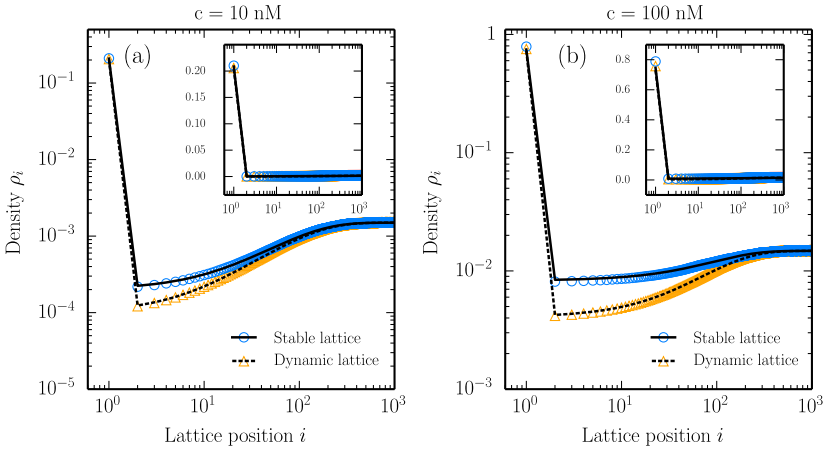

FIG. S6. Density profiles of an adapted model with an intrinsically dynamic lattice (orange) in comparison to the model presented in the main text (blue) for $c = 10\,\text{nM}$ and $c = 100\,\text{nM}$. Tip-localization occurs also on a lattice with fast spontaneous growth and shrinkage. The tip-density is almost unaffected by rapid fluctuations of the MT length, suggesting the validity of our results also for dynamic MTs. The results of our simulations (symbols) agree well with the CMF results (lines). Model parameters are $\delta^{\text{poly}}_{\text{spont}} = 51\,s^{-1}$, $\delta^{\text{depoly}}_{\text{spont}} = 50\,s^{-1}$, $\delta^{\text{depoly}}_{\text{cat}} = 50\,s^{-1}$, $\delta^{\text{poly}}_{\text{cat}} = 59.5\,s^{-1}$ for the dynamic lattice. Other parameters and parameters for the stable lattice as for the XMAP215 model.

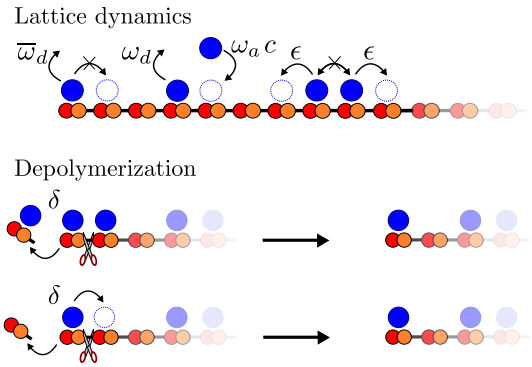

FIG. S7. Illustration of the MCAK model. Particle movement is identical to the XMPAP215 model. Depolymerization occurs whenever the first lattice site is occupied. Particles depolymerize processively in that they move along with the shrinking tip. When the second site is occupied, a particle on the tip that simulates shrinkage falls off together with the first lattice site.

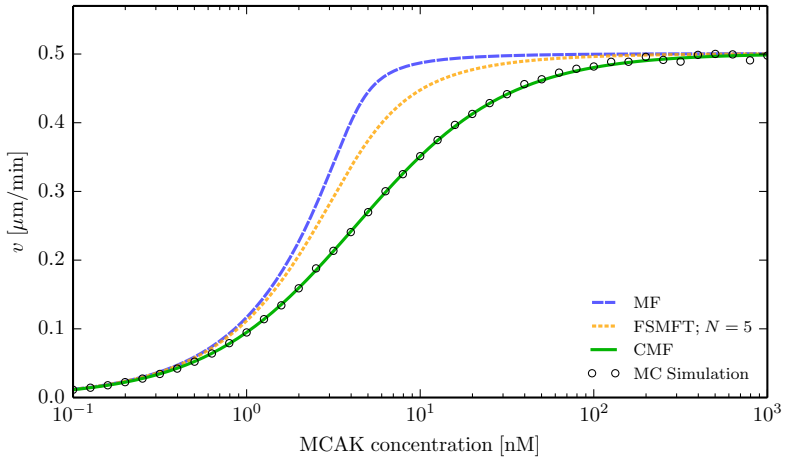

FIG. S8. Comparison of different analytic approaches (lines) with simulations of the MCAK model (circles). Whereas the MF and FSMFT approaches (dashed lines) predict the depolymerization velocity insufficiently, the CMF approximation (solid line) delivers results which are in excellent agreement with simulation data. Model parameters are given in Table I.

PARAMETER VALUES

The parameter values used for the XMAP215 and MCAK model were extracted from experimental data [S3, S4, S8]. Model parameters were computed based on measured diffusion coefficients (for ϵ), particle dwell times on the MT tip (for $\overline{\omega}_d$) and bulk (for ω_d), attachment rates (for ω_a), and maximal (de)polymerization velocities at saturated (de)polymerase concentrations (for δ). A conversion factor n_{tubulins} from μm into tubulin subunits was adapted to the assumed protofilament numbers $n_{\text{protofilaments}}$ of the MTs used in the respective experiments: 1625 tubulin dimers/μm for XMAP215 [S3] and 1750 tubulin dimers/μm for MCAK [S4]. Note that the polymerization velocity refers to one MT tip [S3, S8], wheres the depolymerization rate refers to the average shrinkage rate of both ends [S4]. Opposed to the measurements for MCAK, where the maximal depolymerization velocity was determined [S4], Widlund et al. do not directly state the maximal MT polymerization velocity due to XMAP215 induced growth [S3]. To get a good estimate for the maximal growing velocity $v_{\max}$ of MTs at saturating polymerase (XMAP215) concentrations, we fitted a Michaelis-Menten curve to the experimental data. The rate of tubulin attachment and detachment per regulating

Experiment

	D $(\mu\text{m})^2\ \text{s}^{-1}$	k_{on} events /(s μm nM)	k_{off} events/s	v_{max} μm/min	K_M μm/(min nM)
MCAK-FL	7.6×10^{-2}	4.56×10^{-1}	1.70	5.0×10^{-1}	4.3
	D $(\mu\text{m})^2\ \text{s}^{-1}$	k_{on} events /(s μm nM)	k_{off} events/s	v_{max} μm/min	K_{off} s^{-1}
XMAP215	3.0×10^{-1}	1×10^{-1}	4.1×10^{-1}	4.6	2.6×10^{-1}

Theory

	ϵ s^{-1}	ω_{a} $(\text{nM s})^{-1}$	ω_{d} s^{-1}	δ s^{-1}	$\overline{\omega}_{\text{d}}$ s^{-1}
MCAK-FL	1.2×10^{3}	2.61×10^{-4}	1.70	5.2×10^{-1}	3.0×10^{-2}
XMAP215	4.7×10^{3}	6×10^{-5}	4.1×10^{-1}	9.5	2.6×10^{-1}

TABLE I. Rate constants for MCAK-FL [S4] and XMAP215 [S3, S8]. The diffusion constant D and the on- and off-rates of enzymes to the MT lattice, k_{on} and k_{off}, were measured directly. The measured depolymerization and polymerization profiles yield the maximal depolymerization and polymerization velocities v_{max} and the effective Michaelis constant K_M. Conversion to the theoretical values was achieved by translating k_{on}, k_{off}, and v_{max}, into appropriate lattice units. The hopping rate is related to the diffusion coefficient by $\epsilon = D/a^2$. The off-rate at the first site for MCAK was, in contrast to the one for XMAP215, not measured directly. It can, however, be estimated from K_M by using the depolymerization behavior at low concentrations and a MF argument which exploits the fact that the system is uncorrelated at asymptotically low occupations [S1].

protein δ depends on the maximal number of catalytically active proteins at the MT tip n_{tip}: $v_{\text{max}} = \delta\, n_{\text{tip}}\, n_{\text{tubulins}}^{-1}$. Since the specific number for n_{tip} is elusive (there are estimates for approximately 10 XMAP215s at the MT tip at 50 nM XMAP215. [S8]), we have to make an assumption. Here, we choose one protein per protofilament, $n_{\text{tip}} = n_{\text{protofilaments}}$. In doing so the MT tip velocity then reduces to $v = \langle n_1\rangle\, \delta\, n_{\text{protofilaments}}\, n_{\text{tubulins}}^{-1} = \langle n_1\rangle\, \delta\, a$, where a is the length of a tubulin dimer.

As the dwell time of proteins on the tip (i.e. $1/\overline{\omega}_d$) was not measured for MCAK particles, we used the measured Michaelis constant K_M to estimate this value: Since the Michaelis constant determines the linear increase in the depolymerization velocity for asymptotically low MCAK concentrations, $v_{\text{low } c} = 1/K_M \times c + \mathcal{O}(c^2)$, we can use it to estimate the tip-dwell time for MCAK particles. In detail, we analytically computed the depolymeriztion velocity for asymptotically low concentrations using a MF and low-density approximation of our model up to first order in c [S1]. As correlations vanish under these conditions, we expect the result to be exact which allows us to infer the MCAK off-rate at the tip $\overline{\omega}_d$. The list of ensuing parameters is given in Table I.

* Present address: Department of Bionanoscience, Delft University of Technology, Delft, Netherlands.
† frey@lmu.de

[S1] E. Reithmann, L. Reese, and E. Frey, Biophys. J. **108**, 787 (2015).
[S2] B. Derrida, J. Stat. Mech. Theor. Exp. **2007**, P07023 (2007).
[S3] P. O. Widlund, J. H. Stear, A. Pozniakovsky, M. Zanic, S. Reber, G. J. Brouhard, A. A. Hyman, and J. Howard, Proc. Nat. Acad. Sci. USA **108**, 2741 (2011).
[S4] J. R. Cooper, M. Wagenbach, C. L. Asbury, and L. Wordeman, Nat. Struct. Mol. Biol. **17**, 77 (2010).
[S5] J. Helenius, G. J. Brouhard, Y. Kalaidzidis, S. Diez, and J. Howard, Nature **441**, 115 (2006).
[S6] T. Antal, P. L. Krapivsky, S. Redner, M. Mailman, and B. Chakraborty, Phys. Rev. E **76**, 041907 (2007); R. Padinhateeri, A. B. Kolomeisky, and D. Lacoste, Biophys. J. **102**, 1274 (2012); T. Niedermayer and R. Lipowsky, Phys. Rev. E **92**, 052137 (2015).
[S7] P. Zakharov, N. Gudimchuk, V. Voevodin, A. Tikhonravov, F. I. Ataullakhanov, and E. L. Grishchuk, Biophys. J. **109**, 2574 (2015).
[S8] G. J. Brouhard, J. H. Stear, T. L. Noetzel, J. Al-Bassam, K. Kinoshita, S. C. Harrison, J. Howard, and A. A. Hyman, Cell **132**, 79 (2008).
[S9] G. Klein, K. Kruse, G. Cuniberti, and F. Jülicher, Phys. Rev. Lett. **94**, 108102 (2005).

2.2 Two-species transport and topological hindrance

In this section, we focus on the collective dynamics two species of molecular motors along a microtubule. The two species are distinguished by different gaits that are motivated by recent experimental observations: One species of molecular motors moves straight ahead along the cylindrical geometry of a microtubule while the other one follows a helical path. In the corresponding research project, we found that such systems are characterized by a fundamentally different phenomenology as compared to collective transport in the presence of a single species. This can be explained by a change in the network topology of the underlying stochastic process when adding a second species to the system: A single lattice site may then be accessed from two directions which increases the impact of steric interactions between particles. This *topological hindrance* has far-reaching consequences: Jamming of molecular motors occurs already at comparably low densities and depends not only on the total density but also on the fraction of particles from each of the respective species. Our findings show that jamming might be more relevant than previously thought and might indeed occur at cellular concentrations of motor proteins. Results related to this research project were published in the manuscript *"Two-Species Active Transport along Cylindrical Biofilaments is Limited by Emergent Topological Hindrance"* [62] in the journal *Physical Review X*. To this work, I contributed as shared first author (together with Patrick Wilke). The following section provides an introduction and the scientific background related to this publication. The corresponding publication is reprinted in section 2.2.3 of this thesis.

2.2.1 Background

2.2.1.1 Active motion along cytoskeletal filaments

Every living cell constitutes a system far from thermal equilibrium and keeping a cell alive demands for permanent active reorganization and relocation of many of its components [20, 22, 85, 100]. To this end, the cell constantly transforms chemical energy into translocation and (re)assembly of proteins [17]. In the last section we have already encountered regulating proteins that actively remodel and reshape the cytoskeleton. But besides the dynamics of the cytoskeleton itself also active motion along the cytoskeleton is vital for cell biology [45]. This task is fulfilled by another example of the cell's remarkable biomolecular "engineering skills": kinesins [42, 43,

46, 101]. Kinesins are molecular motors that associate with microtubules to move processively and (in most cases) unidirectionally over micrometer distances towards the microtubule ends [102, 103]. In doing so, they contribute to essential processes such as organelle transport [52], mitosis [104], and intracellular organization [17, 105]. Since the discovery of kinesin [106] many different experimental studies have focused on elucidating the behavior of individual molecular motors and, in particular, their stepping mechanism [101, 107, 108]. While the details certainly depend on the respective kinesin class, the general model for the motion of kinesins is an ATP driven hand-over-hand mechanism with a step size that equals the size of a tubulin dimer [101, 108–110].[6] Moreover, for probably the most prominent kinesin involved in intracellular transport—kinesin-1—it was shown that motion occurs along a single protofilament [111], which is one of typically 13 linear arrays of tubulin dimers that compose a microtubule. Phrased differently, a protofilament was long thought to act as a lane for kinesin transport along a microtubule.

In addition to elucidating the mechano-chemical mechanisms of *single kinesins* also understanding their *collective behavior* remains an open question of at least comparable scientific reach. In this respect, concepts from statistical physics have significantly advanced our understanding as they offer general tools to bridge from microscopic to macroscopic properties. Based on the experimental work on molecular details of kinesins, a plethora of theoretical studies has by now established a comprehensive picture for the corresponding many-body system. Foremost, the totally asymmetric exclusion process (TASEP) [14, 112–115] and extended versions of it have been widely applied to model collective motion of kinesins. In the limelight of many theoretical studies of the TASEP and extended versions thereof is an abrupt transition of collective particle dynamics into a jammed state. This jamming transition has not only stimulated a multitude of theoretical studies that aim for a mathematical description of the problem but also the question whether particle jams are of relevance for cell biology. To provide a background for the remainder of this section we therefore briefly review particle jamming in theory and experiment.

2.2.1.2 Molecular crowding in theory and experiment

We begin our overview of molecular crowding and jamming with an excursion to the probably most central model in this context, the TASEP. In its easiest formulation, the TASEP describes the stochastic and unidirectional motion of point-like particles which exclude each other on a one-dimensional lattice. In this way, it serves a prototypical

6 In general, the way kinesins move along microtubules differs significantly among the kinesins classes. Two particularly "exotic" exceptions to a classical stepping mechanism are addressed in other sections of this thesis: MCAK (see Section 2.1) is a kinesin-13 that has been shown to diffuse on microtubules and to use its ATPase cycle to depolymerize microtubules [87]. In Section 2.3, we discuss biomolecular properties of Cin8—a yeast kinesin-5—which was shown to exhibit a context-dependent directionality.

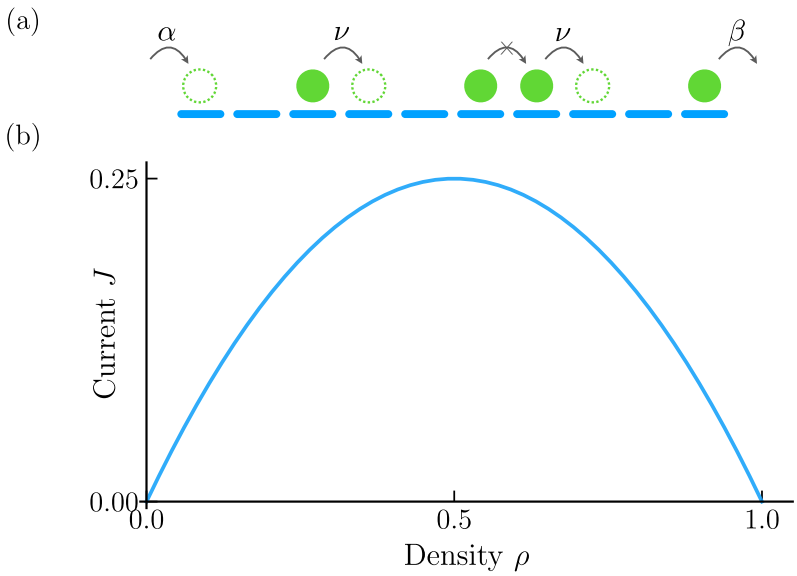

Figure 2.8 Dynamics and current-density relation of the TASEP. (a) Illustration of the particle dynamics of the TASEP. Particles populate a one-dimensional lattice where they exclude each other. A particle hops to the neighboring lattice site on the right at rate ν given that the target site is vacant. On the left, new particles enter the system at rate α when the first site is empty. On the right, particles leave at rate β. **(b)** Current-density relation of the TASEP. For any given set of α and β, the emerging average particle current and density in the steady state fulfill the unique relation $J = \rho(1-\rho)$. The current vanishes either for zero density or at full occupation of the lattice (density equal to one).

model for the collective motion of unidirectionally moving particles on a filamentous structure, such as the collective motion of kinesins along a microtubule. In the TASEP, particles hop stochastically at a rate $\nu = 1$ to the neighboring lattice site on their right, given that the respective target site is vacant.[7] The TASEP has been studied with different boundary conditions, of which open boundary conditions may well be the most important ones [14]. When implementing open boundary conditions, particles enter the lattice at a rate α on the left end of the lattice (given that the respective site is vacant) and leave the last lattice site at a rate β. Open boundary conditions may be interpreted as connecting the lattice to two particle reservoirs at fixed densities $\rho_L = \alpha$ on the left and $\rho_R = 1-\beta$ on the right. An illustration of the model is shown in Fig. 2.8(a).

Two central macroscopic observables of the TASEP are (a) the average particle density ρ and (b) the average particle current J that emerge in the stationary state

7 Without loss of generality, we can set $\nu = 1$ by rescaling time.

of the system for a given set of input parameters α and β.[8] For the TASEP and many corresponding extended models, these two observables are connected by a unique relation, the so-called current-density relation $J(\rho)$, that is at the heart of most phenomenological theories. Intuitively, it should be clear that the current vanishes for (a) vanishing densities ($\rho = 0$) or (b) at full occupation ($\rho = 1$) because of a lack of particles and particle jamming, respectively. Moreover, the current-density relation is expected to exhibit two qualitatively different regimes: A regime where the current is limited by a lack of particles and where J increases monotonically with ρ as well as a regime where the current is limited by jamming and where J decreases monotonically with ρ. A naïve guess is $J = \nu\rho(1-\rho)$. This relation reflects the motion of particles [effective rate $\nu\rho$] to empty sites [present with probability $(1-\rho)$]. It turns out that this educated guess is indeed the exact current-density relation of the TASEP in the stationary state [14, 116]; For an illustration of the current-density relation, see Fig. 2.8(b). In particular, the relation exhibits the two anticipated roots for vanishing densities and full occupation.

The importance of open boundary conditions is highlighted by the observation that they give rise to a surprising phenomenology: boundary induced phase transitions [117]. This can be understood as follows: If the influx of particles is small but the potential maximal outflux of particles is high, the limiting determinant of particle transport along the lattice will be the rate at which particles enter the system. In this case, the macroscopic behavior will be solely determined by the density of the reservoir on the left, $\rho = \rho_L = \alpha$. If, on the other hand, the outflux of particles is small while there is a strong influx of particles, particles will jam due to steric interactions. Then, the rate at which particles leave the system, and therefore the density of the reservoir on the right, will be the sole determinant of collective dynamics, $\rho = \rho_R = 1-\beta$. In a third scenario, when particles enter and leave the system at high rates, the limiting factor of transport will be the maximal rate at which particles move along the lattice, $\rho = \rho_{MC} = 1/2$. Indeed, a detailed analysis of the TASEP reveals the existence of all of these three scenarios. A striking observation for the TASEP is that—upon varying the rates for particle in- and outflux—a phase transition between the three scenarios occurs [116–119]. It is probably for this observation together with the much-celebrated exact solution of the TASEP [116, 118, 119] that the TASEP is considered as a hallmark model of nonequilibrium physics. Fig. 2.9 summarizes the phase behavior of the TASEP and shows the response of the average system density

8 Mathematically, the particle density ρ and current J are defined as follows: $\rho_i = \langle n_i \rangle$ denotes the particle density at lattice site i and $J_i = \nu\langle n_{i-1}(1-n_i)\rangle$ the particle current to site i. Here, $n_i \in \{0,1\}$ is the occupation number of site i that equals one in the presence of a particle and zero otherwise. Further, angle brackets denote the (ensemble) average. For simplicity, we neglect the spatial dependency in the introductory text above since—for the purpose of this section—we can assume a spatially constant current and density.

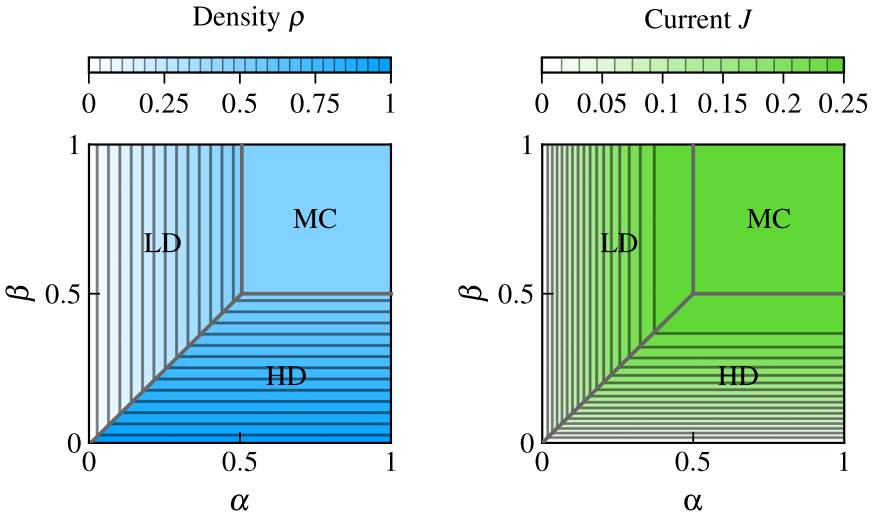

Figure 2.9 Phase diagram of the TASEP. The figure shows the emerging (spatially constant) average particle density ρ (left panel) and current J for different parameter values α (in rate) and β (out rate). The TASEP exhibits a phase transitions between the low-density (LD), high-density (HD), and maximal-current (MC) phase. The functional dependency of the density on the system parameters in the three phases is $\rho_{\mathrm{LD}} = \alpha$, $\rho_{\mathrm{HD}} = 1 - \beta$ and $\rho_{\mathrm{MC}} = 1/2$. The respective values for the current are related to the density via $J = \rho(1 - \rho)$. Without loss of generality, values refer to $v = 1$.

ρ and the average particle current J to the model parameters α and β.[9] The three different phases are termed as follows: Low-density (LD) phase for the case where the system is determined by the particle reservoir on the left [$\rho_{\mathrm{LD}} = \alpha$, $J_{\mathrm{LD}} = \alpha(1 - \alpha)$], high-density phase when the system is determined by the particle reservoir on the right [$\rho_{\mathrm{HD}} = 1 - \beta$, $J_{\mathrm{HD}} = \beta(1 - \beta)$], and maximal-current (MC) phase when the system establishes the maximal flow of particles [$\rho_{\mathrm{MC}} = 1/2$, $J_{\mathrm{MC}} = 1/4$].

Having addressed a first prototypical model for the collective motion of unidirectionally moving particles raises the question if the collective motion of kinesins is indeed subject to a similar phenomenology as predicted by the TASEP. In principle, the results of the TASEP imply that molecular motors that move along a filament might abruptly start to jam above a certain threshold density. Nevertheless, many of the TASEP's basic assumptions are certainly oversimplifications of the biological situation. Especially particle conservation along the lattice and particle injection

9 Note that both observables ρ and J are spatially constant along the lattice. For the particle current this is a trivial consequence from current conservation in the steady state. For the average particle density this statement only holds true in the thermodynamic limit and can, for example, be shown by mean-field methods and the exact solution [14].

only at the front of the lattice are assumptions that are not compatible with the motion of molecular motors. Those may, in general, attach and detach along the whole microtubule lattice. To tackle this problem, the TASEP has been extended to account for Langmuir kinetics (TASEP-LK) [120–122], that means the random attachment and detachment of particles along the lattice. The TASEP-LK is defined as follows. In addition to the original TASEP dynamics, the particles may attach to an empty lattice site at rate ω_a and detach at rate ω_d. This choice of dynamics can be interpreted as connecting the whole lattice to a reservoir with a spatially and temporally constant particle density. Such an implementation would find its experimental equivalence in a large and well-mixed solution of molecular motors. Without active motion on the filament the system would be in thermal equilibrium and the density would homogeneously equilibrate at the Langmuir isotherm, $\rho_{\mathrm{La}} = \omega_a/(\omega_a + \omega_d)$. Adding TASEP dynamics will, however, redistribute the particles and thereby lead to a competition of the equilibrium dynamics of attaching and detaching particles with the nonequilibrium dynamics of the TASEP. In essence, the main difference of the TASEP-LK as compared to the original TASEP is a lacking particle conservation. Lacking particle conservation, in turn, allows for a spatially varying particle current and thus also for density profiles with a spatial dependency. While the current does not have to be spatially constant anymore, it is still expected to be continuous [121]. Valid solutions for the density profile can therefore be constructed by adding different domains in which different phases are realized. The spatial transition from one phase to another one occurs at the point where the currents match locally. Indeed such mixed phases are observed in the TASEP-LK and a phase separation along the lattice as well as the coexistence of phases are well-known features of this model. In fact, this behavior is a key difference of the TASEP-LK as compared to the original TASEP, where always a single phase dominates the whole system.[10]

With this simple but powerful model extension at hand, the leap towards a quantitative comparison of theory and experiment was made. *In vitro* experiments with the yeast kinesin-8 Kip3 unraveled that—under appropriate conditions—the particle density along the microtubule phase separates into a low-density region (characterized by a sparse occupation and large particle velocity) and a high-density region (characterized by a dense particle occupation and low velocities) [124]. Moreover, it could be shown that the velocity v of single motors slows down linearly with increasing motor densities on a microtubule. This is in accordance with TASEP based models, where the linear relation $v = v(1-\rho)$ gives rise to the current-density relation $J = v\rho(1-\rho)$. Despite these *in vitro* measurements that proved the existence of jams of molecular motors it remained an open question whether such phenomena occur

10 A noteworthy subtlety in this context is the LD-HD transition line of the original TASEP. There, for $\alpha = \beta < 1/2$, a domain wall separates the system into a high and low density regime. The domain wall is, however, unstable and performs a random walk, yielding an overall linear profile for the average particle density in the stationary state [123].

under physiological conditions or cellular concentrations and are thus of relevance *in vivo*. In the same study, it was argued that the central transport kinesins, kinesin-1 and kinesin-2, are optimized in a way to prevent particle jams: They are characterized by a (in comparison to, for example, Kip3) moderate processivity of motion (approximately one micrometer) and exhibit short dwell times at the microtubule end. Furthermore, the independence of the motor's detachment rate of the local density of motors—as it is assumed for most TASEP-like models—is most likely an oversimplification which increases the probability to form jams.[11] Opposing these arguments against an important potential role of traffic jams in biological systems there are, however, also arguments that support the notion that traffic jams occur *in vivo*: Cargo transport *in vivo* is typically carried out by multiple motors, which has been shown to increase the processivity by orders of magnitude [103, 127]. Moreover, for Kip3 it was suggested that results from the TASEP-LK may actually be of relevance for its regulatory function [128]: Kip3 is a highly processive microtubule depolymerase that depolymerizes microtubules in a length-dependent manner. This is the result of the linearly growing "antenna" density profile predicted by the TASEP-LK. So, taken together, while *in vitro* experiments have confirmed the existence of traffic jams of motor proteins, the role of these jams *in vivo* is currently still unclear.

2.2.1.3 Helically moving molecular motors

To apply TASEP-like models to the collective motion of kinesins, they should account for all of the relevant biomolecular details of these motor proteins. One of the key assumptions of the previously discussed TASEP and TASEP-LK models is that particles move along one dimension. Thus, it is important to ask whether such a simplification adequately describes to motion of molecular motors. Indeed, it was thought for a long time that one-dimensional motion characterizes the dynamics of molecular motors on microtubules. As mentioned above, experimental studies for kinesin-1, one of the central players of intracellular transport [45], have shown that this motor protein indeed follows a single protofilament of the microtubule, i.e. a single lane [111]. As the microtubule is typically composed of 13 of these lanes [129], the fact that lane switching doesn't occur for kinesin-1 suggested that transport along each of the lanes is basically independent of the transport on neighboring lanes. But while motion along a single lane is well established for kinesin-1, recent experimental studies have by now unraveled an ever growing number of exceptions to this behavior for all superfamilies of molecular motors: kinesin[130–133], dynein [134], and myosin [135]. Specifically, multiple molecular motors have, for example, been shown to rotate microtubules in gliding assays where filaments are propelled over a cover slip coated

11 Detachment rates that are increased by interactions of molecular motors with obstacles or other molecular motors have also been addresses experimentally [125] and recently in a comprehensive theoretical work [126].

with molecular motors. This behavior has been observed for single headed kinesin-1 monomers [131], kinesin-2 [132], kinesin-5 [133], kinesin-8 [136], dynein [134], and heavy meromyosin [135]. While these experiments clearly show the capability of motors to generate torque when acting in teams, the molecular origin of this behavior has long been unclear. In this respect, progress was made recently by the usage of optical traps [137], three-dimensional tracking [138, 139] and super-resolution methods [140]. Based on these experimental methods, it was shown that also, for example, single kinesin-2 and kinesin-8 proteins follow helical tracks, most likely due to a side-stepping mechanism that allows them to switch protofilaments.

These observations further complicate theoretical analyses of molecular transport as the dynamics on different protofilaments are likely coupled due to the sidesteps of motor proteins. This consideration suggests to extend models to two dimensions to properly account for multiple lanes on which molecular transport may occur. The problem of multi-lane driven systems has been addressed in a very general setup by a recent theoretical study by Curatolo et al. [141]. In the corresponding model, particles move in a biased fashion on multiple lanes that connect two reservoirs on the left and on the right in analogy to the one-dimensional TASEP. The model by Curatolo et al. explicitly allows for transverse currents as they emerge in the collective motion of molecular motors that switch lanes with a bias towards one side. In this way, Curatolo et al. established a comprehensive framework for such problems that can readily be applied to a single species of molecular motors which follows helical paths on a microtubule. One of the main findings of this study was that—in most cases—these multi-lane systems with transverse particle currents can indeed be reduced to a one-dimensional system. Overall, this finding hence legitimizes applying results of the TASEP to the collective motion of motor proteins that move helically along a microtubule.

Yet, within each single cell a multitude of molecular motors from different species is present and simultaneously involved in intracellular transport. And, as detailed above, a multitude of molecular motors is likely to switch protofilaments in a biased fashion, thus giving rise to helical trajectories. This raises the question if the phenomenology of molecular transport changes significantly in the presence of two species of molecular motors that are characterized by different gaits on the filament. Here, we address this question with a simplistic but generic multi-lane and multi-species extension of the paradigmatic TASEP model.

2.2.2 Key results

The following section summarizes the key results of the publication “Two-Species Active Transport along Cylindrical Biofilaments is Limited by Emergent Topological Hindrance” [62] to which I contributed as shared first author (together with Patrick Wilke). The corresponding manuscripts are reprinted in Section 2.2.3 of this

thesis. Detailed author contributions are listed in the "Abstracts of the projects and contribution" section at the beginning of this thesis.

Our study addressed a model for two species of molecular motors that move between two particle reservoirs on a variable number of lanes oriented in a cylindrical fashion. The species were distinguished by different ways to move: One species moved straight ahead and followed a single lane while the other one followed a helical pathway as a result of switching the lane in a biased fashion. In the presence of both species, a specific lattice site can be accessed from two directions by two different particles. Therefore, a single particle can block the motion of up to two other particles in this model. The result of this simple change in the network topology of possible particle motions has two far-reaching consequences: (a) The existence of lattice sites that are empty but inaccessible. (b) The creation of intrinsic bottlenecks in the motion of particle trajectories that force particles to hop sequentially. As it is the network topology that amplifies and extends the impact of steric hindrance in our model, we termed the corresponding type of interaction *topological hindrance*. Topological hindrance led to a significantly new phenomenology as compared to previous models for molecular transport and could—to the best of our knowledge—not be characterized by standard analytic methods.

Importantly, two-species transport in the way described above is characterized by a jamming transition below a full occupation of the system by particles. While jamming in the TASEP and similar models is driven by overcrowding, the central determinant of jamming in our two-species model is particle arrangement. The result is that even a completely jammed state, where the motion of every particle is blocked, exhibits lattice sites which are inaccessible but vacant. Moreover, in the presence of both species, the overall average particle current is strictly smaller than the one in the presence of a single species at identical average particle densities. We found out that the impact of topological hindrance critically depends on two factors: First, the fraction of the relative particle species in the system. Second, the number of lanes composing the system. Strikingly, already a small fraction (approximately 5%) of a second species sufficed to induce strong topological hindrance. Moreover, increasing the number of lanes rapidly decreased the maximal particle density reachable in the stationary state. For example, for a system with 13 lanes (the typical number of protofilaments of a microtubule) and equal fractions of the two species, the maximal density we obtained in our simulations was as low as $\rho_{\max} \approx 0.2$. A naïve estimate suggested a scaling of the maximal reachable density as $\rho_{\max} \to \ln(W)/W$ in the limit of large numbers of lanes, where W denotes the number of lanes.

Another novel phenomenon of our model where the relevance of the arrangement of particles for the collective dynamics of our model became evident was pattern formation. For systems that are characterized by small aspect ratios (length to width), i.e. either for short systems or for systems with many lanes, particles self-organized

in a way such that the density profile in the stationary state showed an oscillatory behavior.

While the aim of our work was to study the novel physical aspects of two-species transport in an isolated fashion, we also tested extended versions of our model inspired by biomolecular details of kinesins: Since several assumptions of the original model certainly simplified the dynamics of motor proteins, we studied several extended model versions with more realistic particle dynamics and interactions. In all cases, however, the key phenomenology remained unchanged: We still observed a significantly increased impact of jamming in the presence of two-species of motor proteins. Importantly, this led us to the conclusion that—in multi-species systems—jamming may take place at much lower densities than previously thought. Therefore, molecular crowding may indeed be relevant at cellular concentrations of kinesins.

2.2.3 Publication

Two-Species Active Transport along Cylindrical Biofilaments is Limited by Emergent Topological Hindrance

by

P. Wilke,*,[1], E. Reithmann,*,[1] and E. Frey[1]
*equal contribution,
[1]Arnold Sommerfeld Center for Theoretical Physics and Center for NanoScience,
Department of Physics, Ludwig-Maximilians-Universität München,
Theresienstraße 37, 80333 München, Germany

reprinted on pages 62–86

from

Phys. Rev. X **8(3), 031063 (2018).**
DOI: 10.1103/PhysRevX.8.031063

Also available on arXiv: 1807.02410.

Two-Species Active Transport along Cylindrical Biofilaments is Limited by Emergent Topological Hindrance

Patrick Wilke,[*] Emanuel Reithmann,[*] and Erwin Frey[†]

Arnold Sommerfeld Center for Theoretical Physics and Center for NanoScience, Department of Physics, Ludwig-Maximilians-Universität München, Theresienstrasse 37, D-80333 Munich, Germany

(Received 20 December 2017; revised manuscript received 21 June 2018; published 11 September 2018)

Active motion of molecules along filamentous structures is a crucial feature of cell biology and is often modeled with the paradigmatic asymmetric simple exclusion process. Motivated by recent experimental studies that have addressed the stepping behavior of kinesins on microtubules, we investigate a lattice gas model for simultaneous transport of two species of active particles on a cylinder. The species are distinguished by their different gaits: While the first species moves straight ahead, the second follows a helical path. We show that the collective properties of such systems critically differ from those of one-species transport in a way that cannot be accounted for by standard models. This is most evident in a jamming transition far below full occupation, as well as in nonequilibrium pattern formation. The altered behavior arises because—unlike the case in single-species transport—any given position may be targeted by two particles from different directions at the same time. However, a particle can leave a given position only in one direction. This simple change in connectivity significantly amplifies the impact of steric interactions and thus becomes a key determinant of mixed species transport. We computationally characterize this type of hindrance and develop a comprehensive theory for collective two-species transport along a cylinder. Our observations show high robustness against model extensions that account for additional biomolecular features and demonstrate that even small fractions of a second species can significantly alter transport. This suggests that our analysis is also relevant in a biological context.

DOI: 10.1103/PhysRevX.8.031063

Subject Areas: Biological Physics, Statistical Physics

I. INTRODUCTION AND MOTIVATION

Efficient collective molecular transport is a vital prerequisite for a multitude of processes in cell biology on many different levels. Examples range from messenger RNA (mRNA) translation to organelle transport. Typically, highly functional molecular motors that transform chemical energy into stepwise mechanical translation perform this complex task by moving along filamentous structures such as the cytoskeleton or mRNA [1,2]. Of particular importance for intracellular organization are the cylindrically shaped and polarized microtubules. Kinesins—the molecular motors associated with microtubules—exhibit distinct efficient motility, as they are capable of "walking" processively over micrometer distances towards the microtubule end [1]. Many experimental studies have focused on elucidating the microscopic working mechanisms of molecular motors [3–5], but understanding their collective behavior [6] remains a challenging task. For this reason, concepts drawn from statistical physics and modeling have proven to be of much relevance, as they offer a means of linking the microscopic to macroscopic behavior. In this context, the totally asymmetric exclusion process (TASEP) [7,8] and extensions thereof have proven particularly fruitful. In its simplest formulation, the TASEP accounts for two central aspects of transport: active motion and steric interactions. It describes the motion of point particles along a one-dimensional lattice and therefore serves as an ideal basis to study collective transport of one-particle species along a single track. Despite its simplicity, this model shows a surprisingly rich phenomenology and captures many essential features of transport processes. Indeed, by now it has acquired the status of a paradigmatic model, not only for transport [8,9] but also for nonequilibrium physics, in general, comparable to that of the Ising model for equilibrium physics.

Motion of kinesins was initially thought to occur mostly along the so-called protofilaments—separate lanes oriented parallel to the axis of the cylindrical microtubule

[*]P. W. and E. R. contributed equally to this work.
[†]frey@lmu.de

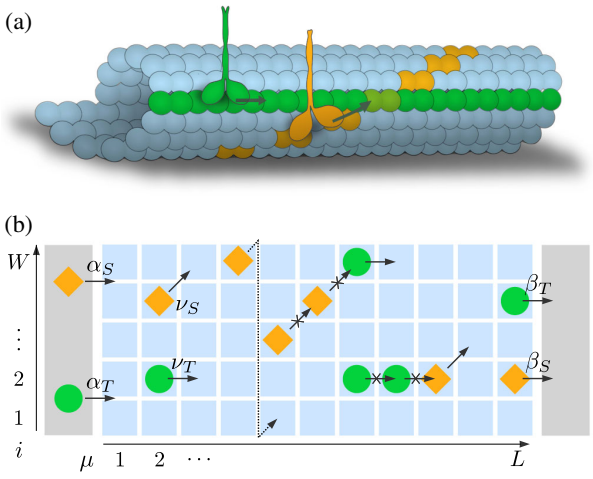

FIG. 1. Active transport by two species along a cylindrical structure. (a) Kinesins (e.g., kinesin-1, green) may track a single lane of a microtubule (protofilament), but many molecular motor species have also been reported to regularly switch protofilaments in a biased fashion and thereby effectively undergo a helical motion (e.g., kinesin-2, orange). (b) Model implementation to study collective two-species transport along cylindrical structures. We consider a lattice with length L and width W. Periodic boundary conditions are employed along the transversal direction to account for a cylindrical geometry (e.g., microtubule). Particles of species T (lane tracking, green) hop to the neighboring lattice site on the right at rate ν_T, and particles of species S (lane switching, orange) hop to the neighboring lattice site on the upper-right at rate ν_S. All particles exclude each other. Particles enter the system with rates α_T and α_S at the left boundary and exit the system at the right boundary with rates β_T and β_S, respectively. Gray areas denote system boundaries.

(see Fig. 1, green kinesin). While this motion along a single protofilament is a well-studied feature of one of the most prominent kinesins involved in intracellular transport, kinesin-1 [10], several *in vitro* studies have revealed notable exceptions to this behavior. Members of all three superfamilies of molecular motors—kinesin [11–14], dynein [15], and myosin [16]—have been shown to produce torsional force during their axial translation. While the precise basis for this observation has remained unclear, recent studies of kinesin-2 [17] and the microtubule depolymerizing kinesin-8 [18,19] strongly suggest that these molecular motors regularly switch protofilaments and show a bias towards one side. This effectively results in a helical motion along the microtubule [17,20,21] (see Fig. 1, orange kinesin). On a theoretical level, systems with a single species of kinesins that stochastically switch protofilaments have been studied recently by employing extended TASEP-like models with multiple lanes [22]. In that case, the qualitative behavior of collective transport along the cylindrical microtubule was reported to be widely conserved as compared to models for kinesins that track protofilaments. However, many different types of molecular motors are present in a single cell and, as lane switching is likely to be the rule rather than the exception, the general scenario is that several different molecular motor species should interact on a single cytoskeletal filament. This raises the question of how the interplay of distinct molecular motor species that show different gaits alters collective transport along a cylindrical structure.

Inspired by molecular transport on microtubules, we employ lattice gas models to find generic principles of collective transport by two species of particles that are distinguished by different gaits on a cylinder. Here, we demonstrate that the emerging behavior of such systems critically differs from collective behavior in the presence of a single species only. The simultaneous presence of molecular motors that follow a straight and a helical course, respectively, inevitably leads to crossings between their trajectories: A certain lattice site may be targeted from two different directions but, once occupied, can only be vacated in a single direction. This modification of connectivity in the network topology of potential particle movements amplifies the impact of steric interactions globally and thus hinders particle motion—an effect we call topological hindrance. Topological hindrance produces highly nontrivial correlations between the dynamics of particles of the different species. Specifically, the particle current and distribution on the filament are now dependent not only on the total number of particles but also on the fraction of the respective species. The impact of topological hindrance is most evident in the jamming of particle flows at densities far below full occupation. We present an analytical framework that quantifies topological hindrance and provides a theoretical basis for understanding two-species transport along cylinders, much as the TASEP does for transport by a single motor species. Moreover, our model predicts nonequilibrium patterns in the particle distribution that have not been observed in classical models for single-species transport. To specifically target the robustness and biological relevance of topological hindrance, we further investigate extended models that account for specific biomolecular features. We find that topological hindrance still plays a key role for collective transport properties in these cases. While the extended models are too complicated for an analytic investigation, we can understand their behavior on the basis of our idealized model and our theory for topological hindrance.

This paper is organized as follows: We begin with a review of the collective transport by a single species in Sec. II. Our model for collective transport by two species on a cylindrical structure is presented in Sec. III. The phenomenology of our model and the key differences to transport with a single species are discussed in Sec. IV, which also provides a qualitative explanation of topological hindrance. Furthermore, we address how the system dimensions influence topological hindrance. We then develop a theory to quantify the strength of topological

hindrance for arbitrary particle densities in Sec. V, which yields the current-density relation for an arbitrary number of lanes and species fractions. This allows us to compute the complete phase diagram of our model, i.e., the particle density and current emerging in the system as a function of the control parameters. In Sec. VI, we discuss the robustness of our results against model modifications and their biological relevance, and provide a guideline for potential experimental verification. Finally, in Sec. VII, we relate our work to existing mathematical theories of driven systems and discuss its applicability and possible relevance in the biological context.

II. REVISITING ONE-SPECIES TRANSPORT

We start with a summary of the TASEP, which is one of the most fundamental models used to describe active transport of sterically interacting agents along defined pathways. While exact results relating to its properties have had a major impact on the field of nonequilibrium physics, in general [23–27], its applications cover a vast variety of transport processes, such as ion channels [28,29], spin transport [30,31], traffic flow [32], mRNA translation [33], and intracellular transport [8]. Here, the TASEP will serve as the starting point to treat molecular transport along cytoskeletal structures in the presence of a single motor species.

The model is defined as follows: Point particles populate a one-dimensional lattice along which they can hop stochastically at a rate ν to the neighboring lattice site on their right. To account for steric interactions, the particles exclude each other, such that a lattice site can only be occupied by a single particle. The particles enter the lattice from the left at a rate α and leave the lattice on the right at a rate β. This can be interpreted as connecting the lattice with two particle reservoirs with fixed densities $\rho_{\mathrm{L}} = \alpha$ on the left and $\rho_{\mathrm{R}} = 1 - \beta$ on the right.

With these definitions, the TASEP allows one to study macroscopic properties that emerge in transport processes. Two central observables are the average particle density $\rho(x,t)$ (average particle distribution) and the average particle flux $J(x,t)$, where x denotes the position in the system and t the time. Particles cannot be created or annihilated within the lattice. Therefore, a spatial difference in the particle flux must lead to a temporal change in the particle distribution in the ensemble average. This is reflected by a continuity equation that describes the system's temporal evolution on a macroscopic scale [34],

$$\partial_t \rho(x,t) + \partial_x J(x,t) = 0. \tag{1}$$

Both the TASEP and the model considered in this paper are ergodic, and the Perron-Fobenius theorem holds true [35]. This means that they will evolve into a unique nonequilibrium steady state, on which we focus from now on.

For the TASEP and many other transport models, there is a unique connection between the current and the density, the current-density relation $J(\rho)$. The existence of this unique function means that the local current J is completely determined by the density ρ; J depends on the in rate α and out rate β only implicitly via the density. This phenomenological approach based on a unique current-density relation goes back to the work of Lighthill and Whitham [36] and is at the heart of many theories for various transport models [22,37–39]. For the TASEP, the current-density relation is given by [23,24]

$$J(\rho) = \nu\rho(1-\rho). \tag{2}$$

This equation reflects the fact that particles may only move to empty lattice sites: Neglecting correlations, the probability of finding a particle (given by ρ) must be multiplied by the probability that a lattice site is empty (given by $1-\rho$) to obtain the current. Although this is just a heuristic mode of argumentation, it can be proven that the corresponding Eq. (2) is an exact relation for the TASEP on an infinite-dimensional lattice [23–25]. This relation also implies that the particle current vanishes if the density is either zero (no particles) or one (full occupation). In the latter case, the motion of every particle except for the last one is blocked, and consequently, no hopping within the lattice can occur. We refer to such a system as jammed.

Based on the current-density relation, it is possible to describe the complete macroscopic behavior in terms of the control parameters of the TASEP in the stationary state. Specifically, it uniquely determines the average density and particle current of the stationary state associated with a specific choice of control parameters α and β. A very successful theoretical concept in this context is the extremal current principle [37,38,40]. It states that, given a set of possible densities, the system will always realize the one corresponding to the extremal current. As explained above, the lattice boundaries are effectively connected to particle reservoirs of density $\rho_{\mathrm{L}} = \alpha$ and $\rho_{\mathrm{R}} = 1-\beta$ on the left and right ends, respectively. According to the extremal current principle, the steady-state density and current are then given by

$$J = \begin{cases} \max\limits_{\rho\in[\rho_R,\rho_L]} J(\rho) & \text{if } \rho_L > \rho_R \\ \min\limits_{\rho\in[\rho_L,\rho_R]} J(\rho) & \text{if } \rho_L < \rho_R. \end{cases} \tag{3}$$

The current-density relation of the TASEP, Eq. (2), exhibits only a single maximum. Consequently, the extremal current principle predicts boundary-induced transitions between three different phases: Eq. (3) implies that either the left reservoir density ρ_L, the right reservoir density ρ_R, or the density corresponding to the sole maximum in the current-density relation, $\rho_{\mathrm{MC}} = 0.5$, is a valid solution and therefore realized in the system. On an intuitive level, when the left

reservoir density is realized, a lack of particles determines the system's behavior, as the in rate is too small to create large particle jams. The corresponding phase is called the low-density (LD) phase. When the out rate is so small that it is the factor that limits transport, particles start to jam at the lattice end. Ultimately, the corresponding outflux will determine the overall particle current. The system then realizes the right reservoir density. This phase is called the high-density (HD) phase. Third, if neither a lack of particles nor the out rate is limiting transport, the particles' motion itself and thus the maximal possible current and the corresponding density constitute a constraint. This phase is the maximal-current (MC) phase.

It is worth noting that the above derivation of phase transitions is independent of the microscopic rules of a system and has also been applied successfully to driven-lattice-gas models other than the TASEP [40,41]. Therefore, the extremal current principle suggests that the phase behavior of a driven lattice gas is qualitatively identical to that of the TASEP as long as the curve characteristics of the current-density relation are conserved: a region where the current shows a monotonic increase with increasing density, a region where the current monotonically decreases with increasing density, and a single maximum.

The TASEP has been generalized in various ways. Several studies investigated systems with a more involved geometry such as two lanes [30,31,42–44], junctions [45–51], or networks [52–56]. In particular, Curatolo *et al.* [22] treated TASEPs with an arbitrary number of parallel lanes on a cylinder, where particles are also allowed to switch lanes. The authors find that, in this case, the system reduces in many ways to the single-lane TASEP, which justifies its application for the case of a single species of lane-switching molecular motors on a microtubule. Besides these studies addressing more complicated geometries, several authors have treated multiple species of particles, typically in opposite directions [39,57–62]. Yet, how a mixture of different species of molecular motors—that naturally may move with different gaits—behave collectively on the cylindrical microtubule structure remains elusive.

III. MODELING TWO-SPECIES TRANSPORT

As discussed in the previous section, the TASEP adequately describes molecular transport along a cylinder in the presence of a single species of molecular motors. We now turn to a mixture of two species of molecular motors that are distinguished by different gaits. Specifically, we address the question of how to describe collective transport in the presence of molecular motors that move parallel to the cylinder axis *and* molecular motors that follow a helical path as suggested by experiments [17–19]. To this end, we study the stochastic model with Markovian dynamics illustrated in Fig. 1. We consider a two-dimensional lattice composed of W parallel lanes, each with a length of L lattice sites. The system is populated by two different particle species: a lane-tracking species (T species) and a lane-switching species (S species). Particles of the lane-tracking species stochastically hop at rate ν_T to the neighboring lattice site on the right while staying on the same lane. In detail, using Latin letters to denote the lane index and Greek letters to denote the site index, hopping of T particles is described by $i \to i$ and $\mu \to \mu + 1$. They represent, for example, molecular motors that track a single protofilament. Particles of the S species change lanes with every hopping event and stochastically move at rate ν_S to the neighboring lattice site on the upper-right, i.e., $i \to i + 1$ and $\mu \to \mu + 1$. To implement a cylindrical structure, periodic boundary conditions in the transversal direction are imposed. Thus, members of the S species hop from the uppermost to the lowermost lane. In this way, the lane-switching particles represent molecular motors that move in spirals around the microtubule. Furthermore, particles are subject to steric interactions. In the model, they exclude each other, and hopping events can only occur if the corresponding lattice site is empty. At the left boundary, an empty site is filled with a particle of the respective species at rates α_T and α_S. Conversely, at the right boundary, particles of the T and S species leave the lattice at rates β_T and β_S.

Note that the assumptions of lane switching in each step and the absence of random particle attachment and detachment (Langmuir kinetics) are simplifications from a biological point of view. Their aim is to isolate the basic principles of two-species transport along a cylinder, which, in turn, allows us to develop an analytic theory for topological hindrance. To bridge back to biological systems and prove the relevance of our concepts, we discuss extended models in Sec. VI.

To describe the state of the system, we use occupation numbers $n^T_{i,\mu}, n^S_{i,\mu} \in \{0, 1\}$ for lattice site μ on lane i. Here, 1 indicates that the lattice site is occupied by a T or S particle, whereas 0 stands for the absence of the respective species. We focus our analysis on the average particle distribution (density) ρ and the average particle current J that emerge in the system with the above stochastic rules. More specifically, we define $\rho^X_{i,\mu} \coloneqq \langle n^X_{i,\mu} \rangle$ as the ensemble averaged occupation of site μ on lane i by a particle of type $X \in \{T, S\}$. The current of S particles at site μ on lane i is defined as the average number of S particles hopping onto this site per unit time: $J^S_{i,\mu} \coloneqq \nu_S \langle n^S_{i-1,\mu-1}(1 - n^T_{i,\mu} - n^S_{i,\mu}) \rangle$. Equivalently, the current for the T species J^T is defined as $J^T_{i,\mu} \coloneqq \nu_T \langle n^T_{i,\mu-1}(1 - n^T_{i,\mu} - n^S_{i,\mu}) \rangle$. Because of periodic boundary conditions along the transversal direction, we implicitly use the identification $i = W + 1 \equiv 1$ and $i = 0 \equiv W$ in these relations and in the following. For later convenience, we also define the occupation number irrespective of the particle species, $n_{i,\mu} \coloneqq n^T_{i,\mu} + n^S_{i,\mu}$. The temporal evolution of average occupations in the bulk of the system ($\mu \neq 1, L$) is then given by the master equations

$$\frac{d}{dt}\langle n^T_{i,\mu}\rangle = \nu_T\langle n^T_{i,\mu-1}(1-n_{i,\mu})\rangle - \nu_T\langle n^T_{i,\mu}(1-n_{i,\mu+1})\rangle = J^T_{i,\mu} - J^T_{i,\mu+1}, \tag{4a}$$

$$\frac{d}{dt}\langle n^S_{i,\mu}\rangle = \nu_S\langle n^S_{i-1,\mu-1}(1-n_{i,\mu})\rangle - \nu_S\langle n^S_{i,\mu}(1-n_{i+1,\mu+1})\rangle = J^S_{i,\mu} - J^S_{i+1,\mu+1}. \tag{4b}$$

At the boundary sites $\mu = 1, L$, the equations read

$$\frac{d}{dt}\langle n^T_{i,1}\rangle = \alpha_T(1-\langle n_{i,1}\rangle) - J^T_{i,2}, \tag{5a}$$

$$\frac{d}{dt}\langle n^S_{i,1}\rangle = \alpha_S(1-\langle n_{i,1}\rangle) - J^S_{i+1,2}, \tag{5b}$$

$$\frac{d}{dt}\langle n^T_{i,L}\rangle = J^T_{i,L} - \beta_T\langle n^T_{i,L}\rangle, \tag{5c}$$

$$\frac{d}{dt}\langle n^S_{i,L}\rangle = J^S_{i,L} - \beta_S\langle n^S_{i,L}\rangle. \tag{5d}$$

By rescaling time, it is possible to set one hopping rate equal to $\nu_X = 1$ without loss of generality. For simplicity, we focus on identical hopping rates $\nu_S = \nu_T = 1$ throughout this paper.

IV. PHENOMENOLOGY OF TOPOLOGICAL HINDRANCE

A. Two-species transport cannot be reduced to one-dimensional or single-species transport

In this work, we focus on steady-state properties, i.e., $d\langle n^X_{i,\mu}\rangle/dt = 0$ and likewise for other moments. Equations (4) show that the average occupation of a lattice site depends on higher moments, which ultimately leads to an unclosed hierarchy of equations. This typically precludes an exact solution. The simplest analytic approach to treat Eqs. (4) and (5) is the mean-field approximation [8], where correlations are neglected by factorizing (second) moments, $\langle n^X_{i,\mu}n^Y_{j,\nu}\rangle = \langle n^X_{i,\mu}\rangle\langle n^Y_{j,\nu}\rangle$, which closes the hierarchy. The mean-field approximation works successfully for the TASEP and various similar models, and it therefore has acquired the status of a standard method for the analytical treatment of driven lattice gases [8]. We employ this factorization scheme for the total current $J_{i,\mu} \coloneqq J^S_{i,\mu} + J^T_{i,\mu}$. Furthermore, our system is irreducible [63]. For a continuous-time Markov process, this suffices to show that the stationary state is unique [64]. Since there is only one stationary state, it has to adapt the symmetry of the system. Thus, all macroscopic quantities have to be independent of the lane number, and we therefore omit the lane index i in the following. This reasoning is further validated by stochastic simulations as shown in Appendix D 1. The mean-field current-density relation then reads

$$J_\mu = \rho^T_{\mu-1}(1-\rho^T_\mu-\rho^S_\mu) + \rho^S_{\mu-1}(1-\rho^T_\mu-\rho^S_\mu) = \rho_{\mu-1}(1-\rho_\mu). \tag{6}$$

Here, we also define the total particle density $\rho_\mu \coloneqq \rho^T_\mu + \rho^S_\mu$ at site μ. Equation (6) is identical to the current-density relation of the TASEP, Eq. (2). In particular, it predicts that the current is independent of the fraction of spiraling molecular motors and depends only on the total density. To relate the current and density to the system's control parameters, it is useful to introduce new quantities. First, the total in rate is given by $\alpha \coloneqq \alpha_T + \alpha_S$. Second, since particles enter the system independently, the fraction of the current contributed by lane-switching particles is $\delta \coloneqq \alpha_S/(\alpha_T+\alpha_S)$. Because of current conservation, this current fraction is spatially constant. In the mean-field analysis, $J_S/J = \rho_S/\rho$ holds true, such that the current fraction δ of the S species also equals the density fraction of S particles. Therefore, we can consider ρ, J instead of ρ_S, ρ_T, J_S, and J_T, and use δ to compute the respective fraction in the mean-field analysis. Third, we can identify an effective out rate β of particles irrespective of their species. The average dwell time of a particle at the last site is $T = \delta/\beta_S + (1-\delta)/\beta_T$, and therefore, $\beta \coloneqq T^{-1} = (\beta_T\beta_S)/[\delta\beta_T + (1-\delta)\beta_S]$. With these definitions of α and β, we then obtain the full phase-diagram predicted by a naïve mean-field approximation, which recovers all TASEP relations.

To test this mean-field analysis, we perform stochastic simulations based on Gillespie's algorithm [65] for a system with two lanes. Irrespective of the initial conditions, the dynamics converge to a unique stationary state that is characterized by a particle density ρ averaged over the whole system and a particle flux J that we numerically computed for various values of α, β, and δ. The result for a system composed of two lanes is shown in Figs. 2(a) and 2(b). In clear contradiction to the mean-field analysis, Eq. (6), we observe a strong dependence of the average current and density of particles on the fraction of spiraling molecular motors in the system. These findings falsify the mean-field approximation and show that the current is not uniquely determined by the density but carries an explicit dependence on the species fraction δ. For fixed δ, however, a unique current-density relation $J(\rho(\alpha,\beta,\delta),\delta)$ can still be found, as shown in Fig. 2(a). Unlike the species fraction δ, the in rate α and out rate β of particles are parameters that change the density only locally and therefore the current only implicitly. The resulting current-density relation $J(\rho(\alpha,\beta,\delta),\delta)$, as shown for $W = 2$ lanes in Fig. 2(a), exhibits a symmetry upon exchanging the species. This is explained by an invariance of particle dynamics when lattice sites are relabeled [66]. For $\delta = 0$ and $\delta = 1$, i.e., in the presence of a single species only, we recover the TASEP current-density relation. If both particle species are present, the relation changes and the current is always less than in a single-species setup. Most interestingly, in a mixed system,

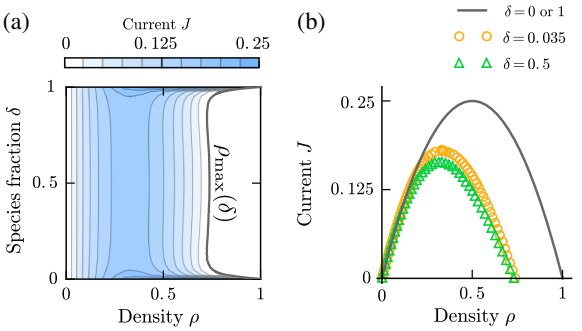

FIG. 2. Current-density relation obtained from stochastic simulations with $W = 2$ lanes and $L = 4096$ sites. (a) The emerging current J of an arbitrary lane (blue color) shows a dependence not only on the average system density ρ but also on the fraction of lane-switching particles, δ. The system jams at a maximal density $\rho_{\max}(\delta)$ (bold gray line); densities between $\rho_{\max}$ and full occupation are not realized in any stationary state. (b) Current-density relation for mixed species ($\delta = 0.5$, $\delta = 0.035$, symbols) and single species ($\delta = 0$ or 1, line). For the latter cases, we recover the TASEP current-density relation.

the current vanishes already at densities below full occupation [Fig. 2(a), white area]; densities above a maximal value of $\rho_{\max}(\delta)$ (bold gray line) are not realized in the steady state. Moreover, a very small fraction of lane-switching particles already cause this effect: Approximately 2%–5% of a second species (see Fig. 2) is sufficient to cause significant deviations from the single-species and mean-field results. Besides this critical difference in the maximum density of a mixed and a one-species system, the qualitative shape of the current-density relation remains unchanged when the species fraction is varied. As shown in Fig. 2 for the special case of $W = 2$ lanes, we observe the same curve characteristics as for the TASEP. These are a single maximum corresponding to the MC phase, a LD region where the current monotonically increases with increasing density, and a HD region where the current monotonically decreases with increasing density. The extremal current principle, Eq. (3), then suggests that the phase diagram of our model and the TASEP are topologically equivalent, although the positions of the phase boundaries might differ.

As the mean-field approximation fails to describe two-species transport, the species current fraction δ cannot be equated with the species density fraction. This complicates any further discussion as ρ_S and ρ_T have to be treated separately. However, as shown in Appendix D 2, in the context of this paper, no significant deviations of the density species fraction from the current species fraction occur. Therefore, for the remainder of this work, we mostly use ρ and implicitly assume a conversion to ρ_S and ρ_T via δ. Furthermore, we refer to δ simply as a species fraction.

In summary, our simulation data show that, first, the dynamics of the two species are correlated, as manifested by the failure of the mean-field approach and the dependence of the current and density on the species fraction δ. Second, correlations of the species dynamics always lead to a reduction of the average particle current; hence, the presence of a second species always hinders transport. We conclude that our model cannot be reduced to the TASEP and that naïve mean-field approaches are incapable of capturing the emerging macroscopic transport behavior.

B. Topological hindrance

To obtain insight into the interactions that reduce the particle flux in the presence of both particle species, we take a qualitative look at particle configurations that might arise in our model. First, we consider jammed configurations where all particles (except for the very last one) are blocked and where, consequently, the average particle current vanishes. As discussed in Sec. II, for one species transport, a jammed system can only arise trivially if every lattice site is occupied. In contrast, our model exhibits jamming at densities below full occupation. A possible jammed configuration of a mixed system is shown in Fig. 3(a). Although the system is jammed, there exist lattice sites that are not occupied. These sites are inaccessible to any particle of this configuration [Fig. 3(a), crosses] and ultimately lead to jamming below the full occupation. In our model, two particles from different species can simultaneously target a single site. Consequently, if that site is occupied, a single particle can block the motion of two other particles [Fig. 3(b), configuration 1]. This, in turn, can create sites that are empty but nevertheless inaccessible. Moreover, if particles of both species try to access a single site that is empty and accessible [Fig. 3(b), configuration 2], their motion is restricted insofar as either one of them, but not both,

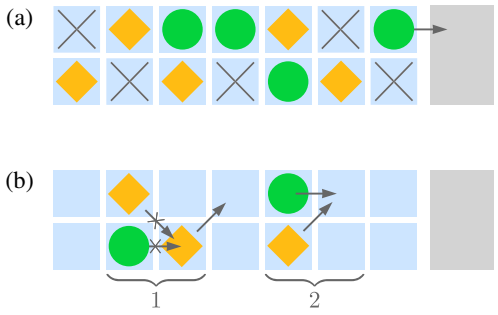

FIG. 3. Illustration of topological hindrance for a system with $W = 2$ lanes at the right lattice end. (a) State where the motion of each particle in the bulk is blocked (jammed state) and only the rightmost particle is allowed to move (arrow). Empty lattice sites (crosses) are present, which lead to average densities below the full occupation for jammed systems. (b) The second species, which changes the connectivity of the network of possible particle motions, amplifying the impact of steric hindrance in our model. Bracketed area 1 shows how a single particle can now block up to two other particles. Area 2 shows how particles might align such that motion has to occur sequentially. The same symbols as in Fig. 1 are used to illustrate the system and particles.

can hop at a time. These configurations hence act as an intrinsic bottleneck and will further reduce the particle current on average. To assess these considerations also quantitatively, we specifically compute the number of inaccessible lattice sites and, with it, the maximal density $\rho_{\max}$ as a proof of principle for a system with $\delta = 1/2$ and $W = 2$ lanes. The detailed computations are shown in Appendix A and lead to a value of $\rho_{\max}^{\text{theory}} = 0.74$. This is in very good agreement with simulations that yield $\rho_{\max}^{\text{sim}} = 0.73$, which validates the qualitative arguments given above.

In summary, when the lane-switching species is added to the system, the network topology of possible particle motions is changed. Any given site is now potentially connected to two other sites, although leaving a site is only possible in one direction at a time. This creates a two-to-one connectivity. The single-species model, on the other hand, shows one-to-one connectivity or, for the general case of particles that may stochastically switch lanes, n-to-n connectivity. The two-to-one connectivity of our model amplifies the impact of steric interactions relative to single-species transport and therefore hinders motion. First, steric interactions may now occur at more points in space as compared to single-species transport, and thus give rise to inaccessible lattice sites [see Fig. 3(b), group 1]. Second, at intrinsic bottlenecks, steric interactions can now act at more points in time, as particles may have to hop one after the other [see Fig. 3(b), group 2]. Throughout this paper, we refer to these phenomena as topological hindrance.

C. Influence of the number of lanes

The first important question to address is how the density of a jammed system $\rho_{\max}$ is influenced by the number of lanes W. Our analytic approach for $W = 2$ lanes, however, is not feasible for large numbers of lanes as the complexity of the underlying mathematical problem increases rapidly. Figure 4 shows numeric results for the maximal system density obtained from stochastic simulations of systems with up to $W = 50$ lanes. Strikingly, the maximal density $\rho_{\max}$ decreases rapidly with an increasing number of lanes. Therefore, the overall impact of topological hindrance grows accordingly and becomes the major determinant of the system's dynamics. This is of importance as large numbers of lanes are often encountered in biological contexts. For example, microtubules are typically composed of 13 lanes, where our model already exhibits a maximal density of $\rho_{\max} \approx 0.2$. Let us also emphasize that, in analogy to the two-lane system, current reduction and, likewise, jamming due to topological hindrance practically saturate at low fractions of the second species (see Appendix D 3).

To improve our conceptional understanding of the decrease of the maximal density with increasing numbers of lanes, we can estimate the jamming density $\rho_{\max}(W)$. To this end, we consider groups of lattice sites with equal site index μ but different lane index i, which corresponds to a column of our two-dimensional lattice. Those columns can be occupied by

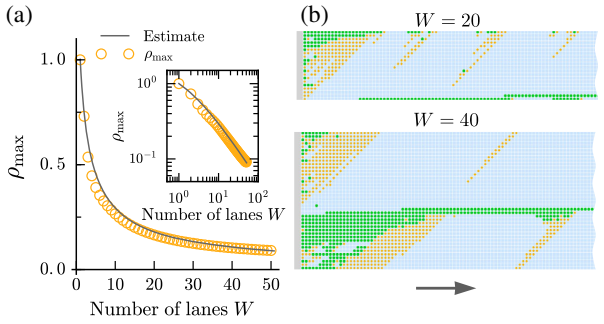

FIG. 4. Dependence of the maximal density $\rho_{\max}$ on the number of lanes W for the special case $\delta = 1/2$ and $L = 16384$. (a) Rapidly decreasing $\rho_{\max}$ with increasing numbers of lanes W. The decrease can be estimated by a maximum entropy argument leading to $\rho_{\max}(W) \approx \mathrm{Hm}(W)/W$ (solid line). (b) Snapshots of particle distributions in systems with $W = 20$ and $W = 40$ to illustrate the maximal density. Although the system is almost fully occupied at the left lattice end, the degree of occupation successively decreases and converges to the maximal density. Larger numbers of lanes exhibit more inaccessible sites and therefore a lower maximal density. In panel (b), the same symbols as in Fig. 1 are used to plot the system and particles. Only the leftmost part of the system is shown for illustrative purposes.

one up to W particles. The respective probabilities in a jammed system are unknown. A rough estimate is given by a maximum entropy approach, which assumes that all numbers (up to W) are equally likely to occur. Then, the maximal density for a system with W lanes can be estimated as

$$\rho_{\max}(W) = \frac{1}{W}\sum_{k=1}^{W}\frac{1}{k} = \frac{\mathrm{Hm}(W)}{W} \overset{1\ll W}{\longrightarrow} \frac{\ln(W)}{W}, \qquad (7)$$

where $\mathrm{Hm}(W)$ denotes the Wth harmonic number. This scaling argument, despite its simple nature, turns out to be very accurate for the case of symmetric particle mixtures $\delta = 1/2$. While simulations show that the assumption of uniformly distributed numbers of particles per column is *per se* incorrect, deviations from the uniform distribution for highly and sparsely occupied columns seem to cancel out, leading to a correct mean value. An intuitive justification for this is that, for example, a completely filled column is compatible with all configurations to its left. Nonetheless, it is very unlikely to occur because only a very restricted number of states may appear to its right. On the other hand, a column with a single particle in it can occur to the right of any other state, but it is only compatible with a few configurations to its left. Hence, this state is very rare as well. On average, high and low occupancies are both suppressed. The effects balance out, making the mean a good approximation.

Note here that the jamming of particles below full occupation shows strong similarities with the jamming transition observed in the Biham-Middleton-Levine model [67]. The latter is a (often deterministically described) model of two perpendicularly crossing pedestrian flows

that exhibits a sharp transition from a phase with finite flow to jamming. A rigorous mathematical treatment of this transition is, however, lacking for the Biham-Middleton-Levine model [68].

In summary, our analysis suggests that topological hindrance becomes much more significant for large numbers of lanes, where we expect it to dominate the complete dynamics. In the Sec. V, we use a novel analytic method to construct the complete current-density relation and, thus, relate the impact of topological hindrance to arbitrary densities. For this theory, the maximal density is also a key parameter as it incorporates the full impact of the number of lanes into the relation.

V. A THEORY FOR TOPOLOGICAL HINDRANCE

In the following, we present an approximation method that is designed to quantify the impact of topological hindrance for arbitrary densities. This will enable us to derive the current-density relation of our model, which successfully takes those correlations into account that lead to the failure of mean-field arguments. To do so, we show that the current-density relation can be split into a mean-field contribution, as derived in Sec. IV, and a correction term that depends on the local density. This correction term can be associated with the inaccessibility of an empty lattice site and therefore quantifies topological hindrance at a certain density. We present a construction method for this hindrance function that, in turn, allows us to compute the current-density relation.

A. The hindrance function

First, we split the particle currents into a mean-field contribution and a correction term. The particle density is independent of the lane index i, such that we find $J^S_\mu = \rho^S_{\mu-1}(1-\rho_\mu) - \mathrm{cov}(n^S_{i-1,\mu-1}, n_{i,\mu})$ and $J^T_\mu = \rho^T_{\mu-1}(1-\rho_\mu) - \mathrm{cov}(n^T_{i,\mu-1}, n_{i,\mu})$. Here, $\mathrm{cov}(n^X_{i,\mu}, n^Y_{l,\nu}) = \langle n^X_{i,\mu} n^Y_{l,\nu}\rangle - \langle n^X_{i,\mu}\rangle\langle n^Y_{l,\nu}\rangle$ denotes the covariance of two occupation numbers. According to the master equations, Eqs. (4) and (5), the particle currents J^S and J^T must be conserved on each lane in the stationary state. In addition, the current must be independent of the lane index i due to the rotational invariance imposed by the system's cylindrical symmetry. Hence, the total current $J = J^S + J^T$ is conserved within the whole system:

$$J = \rho_{\mu-1}(1-\rho_\mu) - \mathrm{cov}(n^S_{i-1,\mu-1}, n_{i,\mu}) - \mathrm{cov}(n^T_{i,\mu-1}, n_{i,\mu}) = \text{const}, \tag{8}$$

for arbitrary lanes $i \in \{1, \ldots, W\}$. The first summand is identical to the mean-field current derived in Sec. IV, whereas the covariances account for correlations. We define the hindrance function H at site μ as

$$H_\mu := \frac{\mathrm{cov}(n^S_{i-1,\mu-1}, n_{i,\mu}) + \mathrm{cov}(n^T_{i,\mu-1}, n_{i,\mu})}{\rho_{\mu-1}}. \tag{9}$$

Then, using definition (9), the current can be rewritten as

$$J = \rho_{\mu-1}(1 - H_\mu - \rho_\mu). \tag{10}$$

Note that no approximations have been made so far. Only symmetries and conservation laws have been employed. Considering the current-density relation of the TASEP, $J = \rho(1-\rho)$, we find that strict accessibility of empty lattice sites is reflected by the 1 in the second factor. In contrast, Eq. (10) reveals that, in our model, an empty lattice site can be accessed only with probability $1 - H_\mu$. Thus, the hindrance function H can be viewed as a correction to the accessibility of empty lattice sites and reflects topological hindrance in the system.

As the current-density relation, Eq. (10), defines an unclosed set of difference equations, we have to employ approximation methods to proceed with our analysis. Often, moment closure techniques are applied to get an approximation for higher moments and thus the covariances. This would, in our case, also fix the hindrance function that depends on them. However, based on our discussion of topological hindrance and the maximal density in Sec. IV, we expect correlations to be long-ranged and not constrained to certain subsegments of the lattice. Therefore, such methods do not seem promising, especially for large numbers of lanes. Instead, we derive a theory similar to the considerations of Lighthill and Whitham [36,39] for our model based on Eq. (10). Specifically, we consider the limit of large system lengths $L \gg 1$. Then, we can replace the discrete site index μ by a continuous spatial variable $x := \mu/L \in (0, 1]$. We perform a Taylor expansion in x, which we truncate at first order in the lattice spacing $\epsilon := 1/L \ll 1$. This is justified for small spatial variations of the density profile [69]. Indeed, our stochastic simulations confirm this assumption for large aspect ratios L/W [see Fig. 8(b) and Sec. V D]. Taking everything together, the result is a current-density relation that depends on the local density but not on its gradient,

$$J = \rho(x)[1 - H(x) - \rho(x)]. \tag{11}$$

The current is spatially conserved (and therefore does not explicitly depend on x), and hence the dependence of the hindrance function H on the lattice position must be implicit via the local density ρ. Thus, our current-density relation can be written as

$$J = \rho[1 - H(\rho) - \rho]. \tag{12}$$

At this point, the explicit dependence of H on ρ is still unknown. To make progress, we derive an approximating function for the hindrance function H that captures its physical properties. This function can then be used to predict the current [70].

B. Constructing the current-density relation

Since the current-density relations of the TASEP and our model show similar curve characteristics, we expect their qualitative phase behavior to be comparable because of the extremal current principle. We split the approximating function for topological hindrance H into two corresponding regimes: H_{LD} is associated with the monotonically increasing part of the current-density relation, and H_{HD} with its monotonically decreasing part. These two functions can be expanded independently around extremal density values for which the behavior of H can be derived using mean-field arguments. Each extremal case isolates one central aspect of transport limitation: first, the lack of particles for $\rho \to 0$, and second, jamming in the case of $\rho \to \rho_{\max}$. In the intermediate regime, both transport limiting factors come into play.

For vanishing densities $\rho \to 0$, particles do not interact and are thus uncorrelated. In this limit, we do not expect any topological hindrance, and therefore, the hindrance function H vanishes. Furthermore, we can compute the derivative of H by calculating the change in current due to the addition of particles in the mean-field approximation (see Appendix B). These two conditions allow us to determine the coefficients of an expansion of the function H_{LD} up to linear order in ρ:

$$H_{\mathrm{LD}}(0) = 0, \tag{13a}$$

$$\frac{d}{d\rho} H_{\mathrm{LD}}(\rho)\Big|_{\rho=0} = \delta(1-\delta). \tag{13b}$$

Interestingly, the result is independent of the number of lanes W and depends on the species fraction δ in the simplest nontrivial way that fulfills the species exchange symmetry $\delta \to 1-\delta$.

In contrast to the low-density limit, particles are totally correlated for $\rho \to \rho_{\max}$. A particle can only be located at a certain lattice site if the respective target site is occupied. For this limit, we can again find the corresponding derivative of the hindrance function using mean-field arguments (see Appendix B). Note that $H(\rho_{\max})$ is known from the definition of the maximal density $\rho_{\max}$ itself. Again, we can determine the coefficients of an expansion up to linear order:

$$1 - H_{\mathrm{HD}}(\rho_{\max}) \overset{!}{=} \rho_{\max}, \tag{14a}$$

$$\frac{d}{d\rho} H_{\mathrm{HD}}(\rho)\Big|_{\rho=\rho_{\max}} = -\delta(1-\delta)\rho_{\max}. \tag{14b}$$

Since the maximal density depends on the number of lanes, as discussed in Sec. IV, the same holds true for the high-density approximation of the hindrance function. This is a major difference compared to the low-density limit. However, the low- and high-density components both show the simple dependence on $\delta(1-\delta)$.

A closer look reveals that linear approximations for the low- and high-density regimes do not, in general, intersect on the interval $[0, \rho_{\max}]$. This would result in a discontinuous current-density relation that is unreasonable. We conclude that an expansion up to at least second order in ρ is necessary. Therefore, we have to look for further physical conditions to uniquely determine the additional coefficients of the expansion. This can be achieved by imposing a differentiable transition between the high-density and low-density regimes. At this intersection point, neither a lack of particles nor jamming is the limiting factor for transport, and hence, the transition should take place at the density ρ_{MC}, which corresponds to the maximal current. Furthermore, both derivatives must vanish at ρ_{MC}. This can be translated into three conditions:

$$H_{\mathrm{LD}}(\rho_{\mathrm{MC}}) = H_{\mathrm{HD}}(\rho_{\mathrm{MC}}), \tag{15a}$$

$$\frac{d}{d\rho}\rho(1 - H_{\mathrm{LD}}(\rho) - \rho)\Big|_{\rho=\rho_{\mathrm{MC}}} = 0, \tag{15b}$$

$$\frac{d}{d\rho}\rho(1 - H_{\mathrm{HD}}(\rho) - \rho)\Big|_{\rho=\rho_{\mathrm{MC}}} = 0. \tag{15c}$$

Combining all properties derived for the hindrance function, we can uniquely approximate H_{LD} and H_{HD} up to second order in the bulk density [71]. The resulting hindrance function is shown in Fig. 6(a) for a system with two lanes and species fraction $\delta = 1/2$; the corresponding current-density relations for multiple numbers of lanes W are shown in Fig. 5. As can be seen, the results of our approximations are in very good agreement with the stochastic simulations and capture the main characteristics of the current-density relation. At this point, let us also emphasize that the theory can be applied for general δ and W. It does not involve any explicit dependence on the number of lanes W but depends on $\rho_{\max}$, which, in turn, depends on W and also on δ. Therefore, $\rho_{\max}$ is a key quantity in our theory, which determines the current-density relation and hindrance function and thus quantifies topological hindrance in general.

Since the current is very well approximated with this method, the exact relation given by Eq. (9) allows us to infer the underlying correlations. This leads to a prediction for the covariances,

$$\mathrm{cov}(n^S_{i-1,\mu-1} + n^T_{i,\mu-1}, n_{i,\mu}) \approx \rho H(\delta, W; \rho), \tag{16}$$

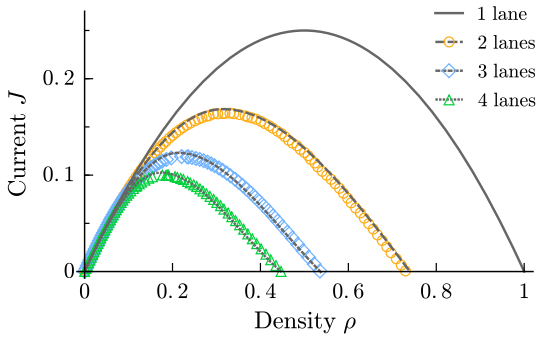

FIG. 5. Current-density relation for different numbers of lanes W with $L = 16384$ and $\delta = 1/2$. The theory for the current-density relation (dashed lines) agrees very well with simulation data (symbols). Although deviations from the TASEP current-density relation (solid line) increase with a growing number of lanes, the three regimes of the current-density relation are preserved: the low-density regime (positive derivative with respect to ρ), the high-density regime (negative derivative), and a unique maximum. Note that the theory depends on $\rho_{\max}$, which in turn depends on W and δ. For the theoretical lines, a fit-free approach based on the analytic result for $\rho_{\max}$ (see Appendix A) was employed for two lanes. For three and four lanes, results were taken from the simulations to ensure that deviations originate from the theory itself not the estimate of $\rho_{\max}$. The particle current refers to an arbitrary lane of the system in order to allow for a comparison to the TASEP.

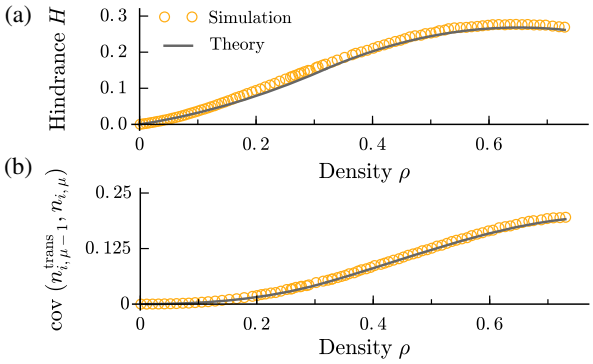

FIG. 6. Comparison of the developed theory for the strength of topological hindrance with simulations for $W = 2$, $L = 4096$, and $\delta = 1/2$. (a) Hindrance function H in the bulk as a function of the density ρ. Results from simulations (symbols) verify the continuous approximation of the hindrance function (lines). (b) The construction of H can be used for an accurate prediction of correlations of occupations between neighboring sites in the bulk. The prediction for the covariance $\mathrm{cov}(n^{\mathrm{trans}}_{i,\mu-1}, n_{i,\mu})$ in the bulk agrees well with simulation results. Here, $n^{\mathrm{trans}}_{i,\mu} \coloneqq n^{T}_{i,\mu} + n^{S}_{i-1,\mu}$ is the total occupation of S and T particles of two neighboring lattice sites in the transversal direction. For the theory, $\rho_{\max}$ was taken from our analytic approach (see Appendix A).

where we have accounted explicitly for the dependence of the hindrance function on the control parameters W and δ. This prediction of the covariances is confirmed by the stochastic simulation shown in Fig. 6(b), as expected from the method's accurate prediction of the current.

In summary, our analysis shows that modifications of the current-density relation in our system are caused by particle correlations. These correlations are accounted for by a hindrance function H, which quantifies the degree of inaccessibility of empty lattice sites and therefore quantitatively characterizes topological hindrance. We construct the hindrance function in terms of a gradient expansion. This expansion is determined by physical constraints with respect to the high- and low-density limits, as well as the transition to the maximal-current phase. Numerical simulations validate our method.

C. Phase behavior of collective two-species transport

So far, we have computed the relation between the average density and particle current but have not addressed how these observables are connected to the system's control parameters. In this section, we determine the response of the current and density to a change in the control parameters α and β and thereby derive the complete phase diagram. As mentioned above, the extremal current principle implies the existence of the three phases as in the TASEP (low-density, high-density, and maximal-current phase), due to the similarity in the form of the current-density relation. Then, for various driven lattice gas systems, current conservation at the respective boundary is used to relate the system's current and density to in and out rates. Because of nontrivial correlations in our system, it is, however, not possible to simply treat the boundaries as reservoirs with density $\rho_L = \alpha$ and $\rho_R = 1 - \beta$ as is done for the TASEP. In Appendix C, we present ways to account for correlations at the edges of the system. This involves determining the response of the current and density to the in rate α in the low-density phase and to the out rate β in the high-density phase.

The LD-MC and HD-MC transitions take place when the respective current matches the maximal bulk current. The latter can be computed with the methods outlined in the previous section. Analogously, the LD-HD transition takes place when both currents are identical. The resulting phase diagram for the special case of two lanes and a species fraction of $\delta = 1/2$ is shown in Fig. 7. The theoretical boundaries are calculated based on the analytically determined value for the maximal density for this choice of parameters (see Appendix A) and hence are derived without any free parameter. The results agree very well with the data obtained from stochastic simulations. Changing δ does not affect the existence of phases but interpolates between the boundaries known for the TASEP and those presented in Fig. 7. Increasing the number of lanes W lowers the maximal density (see Fig. 4) and increases the parameter range of the maximal-current

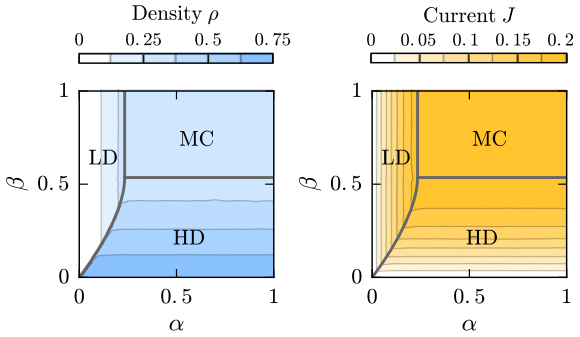

FIG. 7. Phase diagram for the special case $W = 2$, $L = 4096$, and $\delta = 1/2$. Colors denote density (left panel, blue) and current (right panel, orange) obtained from stochastic simulations. Three different phases can be identified: the LD phase where current and density only depend on the in rate, the HD phase where current and density only depend on the out rate, and the MC phase that is independent of both boundary parameters. The theory (bold lines) accurately predicts the phase boundaries and is valid for general δ and W as soon as the maximal density is known. Here, $\rho_{\max}$ was taken from the analytic approach (see Appendix A).

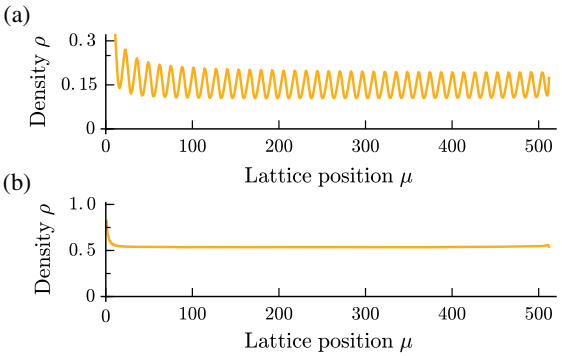

FIG. 8. Density profiles ρ_μ for large and small system widths W compared to the length $L = 512$. (a) The stationary density distribution for $W = 13$ lanes shows an oscillatory pattern with a wavelength equal to the number of lanes. The system exhibits a constant current despite the density oscillations. (b) Stationary density distribution for $W = 2$ lanes. The system exhibits a flat density profile within the bulk. Other parameter values include $\alpha = 0.6$, $\beta = 0.2$, and $\delta = 1/2$ in both simulations.

phase, while the corresponding current is reduced. Hence, as predicted by the extremal current principle, given the number of lanes and species ratio, the phase diagram is topologically equivalent to the one obtained for the normal TASEP [72]. Note that our theory holds for general values of the system width W and the species fraction δ.

D. Nonequilibrium pattern formation

The construction of the hindrance function shown above relies on an expansion of the density ρ in terms of the spatial variable $x = \mu/L$. Specifically, we assume that gradients in the density are negligible, which is justified for slowly varying density profiles. While this assumption as illustrated in Fig. 8(b) leads to accurate results in most cases, we observe surprising exceptions to this behavior for systems with a small aspect ratio L/W: If we sufficiently decrease the system length L or increase the system width W, our stochastic simulations reveal spatial oscillations of the stationary average particle distribution. As shown in Fig. 8(a), the density $\rho_{i,\mu} = \langle n_{i,\mu} \rangle$ oscillates along the longitudinal direction (Greek index μ) with a wavelength equal to the width of the system W. Because of rotational symmetry, these wavelike patterns of the density profile are equally present for each lane i. Furthermore, oscillations are sustained for thousands of lattice sites almost without any decay; therefore, they show remarkable robustness. This behavior is in stark contrast to the TASEP, which (except for boundary layers) exhibits a constant density profile. In general, pattern formation is rarely observed in lattice gas models and has so far been found predominantly in the form of segregation or localization effects [62,73–75].

As stated above, the continuous approximation Eq. (12) is, by virtue of its construction, incapable of describing these varying density profiles. Also, the species current fraction δ may, in this case, significantly differ from the species density fraction (see Appendix D 2). It is, however, worth noting that our theory still provides a good approximation for the current-density relation in terms of the *total* system density (i.e., when averaging over an oscillating density profile) for symmetric species fraction $\delta = 1/2$. To describe the density profile itself, it is necessary to include a dependence not only of the local density but also its spatial change in the hindrance function H. The problem is comparable to the boundary layers of the TASEP, which cannot be captured by a first-order continuous theory but are predicted by exact or higher order solutions [8,44,76]. In future work, it would be interesting to address if such a construction or some alternative analytic method is capable of reproducing these intriguing patterns.

VI. ROBUSTNESS AND BIOLOGICAL RELEVANCE

To establish a generic theory for two-species transport and to enable an analytic study of topological hindrance, we previously made several assumptions that do not necessarily hold in a physical or biological context. To probe the robustness of our results and the relevance of topological hindrance further, we now turn to extended versions of our model that account for biomolecular features of molecular motors.

First, kinesins are not likely to strictly follow a unique pathway; i.e., lane switching does not occur at every step but stochastically. Adding this modification to our model mitigates effects such as a strict maximal density and phase

transitions since any inaccessible site of the original model can now be accessed, in principle, on long timescales. Nonetheless, topological hindrance also has a significant impact in this case. To demonstrate this, we perform simulations with a four-lane system in which lane-switching particles switch lanes with a probability of $\theta = 0.2$ and track their respective lane otherwise. The results are shown in Fig. 9. While this system does not strictly follow the current-density relation as predicted by our theory, it demonstrates that topological hindrance has a strong influence on collective transport as the particle current is heavily suppressed: For example, the average particle current is reduced by more than 50% at densities around the maximal density of the original model. For higher lane numbers, current reduction is even more pronounced. This shows that topological hindrance can also have substantial influence on systems where particles rarely switch lanes but that are composed of many lanes.

To challenge our results further, we perform stochastic simulations of an extended model that accounts for other important biomolecular features of molecular motors: In addition to the stochastic lane switching described above, particles may attach (rate ω_a^X) and detach (rate ω_d^X) randomly

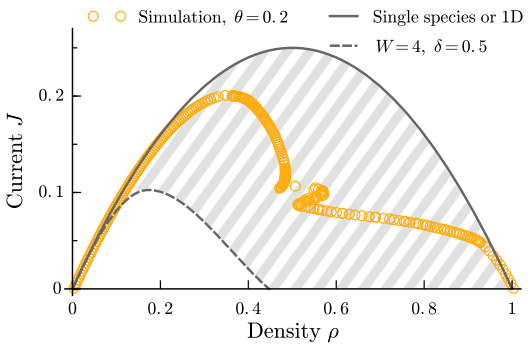

FIG. 9. Current-density relation of a model with nonstrict lane hopping on a system composed of $W = 4$ lanes. Simulation results (symbols) for the current and density of a model where the lane-switching species switches the lane only with probability $\theta = 0.2$ in each step; with probability $1 - \theta$, the second species follows its current lane. Topological hindrance significantly suppresses current and density for this model also, where lane switching seldomly occurs. The resulting data points are in the area between the current-density relation of the single-species case or one-dimensional model (solid line) and the one of our model (dashed line). For models similar to the one presented in this work but with more realistic particle dynamics (e.g., random particle attachment or detachment, nonstrict lane hopping, dimeric particles), we expect current suppression due to topological hindrance to be stronger for parameters that lead to bigger differences in both curves (shaded area). Thus, our theory provides qualitative insights in more complex models also. Note that the simulations suggest a noninjective current-density relation at the onset of jamming of the original model. Other parameter values are $\delta = 1/2$, $L = 16\,384$.

along the lattice (Langmuir kinetics) [77,78] and occupy two lattice sites to account for a dimeric structure [79] of most molecular motors (see illustration in Fig. 10). In analogy to our analysis of the minimal model shown in Fig. 2, we increase the particle attachment rate ω_a^S of the spiraling motor species while keeping the attachment rate of the tracking species ω_a^T constant. An example for the corresponding average particle current per lane is depicted in Fig. 10. Even in this greatly expanded model, topological hindrance causes a significant decrease in the particle current already at low fractions of the second species. In particular, the impact of topological hindrance follows the same principles as discussed in Sec. IV: It increases rapidly with an increasing number of lanes, and it sets at already small fractions of a second species. Taking all results together, we conclude that topological hindrance is most likely also of relevance in biological contexts, and the theory described here allows one to estimate its impact. Another interesting question in this context is whether a phenomenon similar to the density patterns that we observe in the main model exists in a biological context. As this strongly depends on the system considered, at this stage, we cannot provide a complete analysis. Nevertheless, to give an outlook on the impact of model extensions on pattern formation, a brief discussion is given in Appendix D 4.

Moreover, we would like to add that random particle attachment and detachment may, in general, modify our results. In particular, we expect that adding Langmuir kinetics to our model will lead to the emergence of additional phases [77,78] such that our results—while providing a mathematical foundation—cannot be transferred directly [80]. Whereas a complete analysis of the jamming behavior is out of scope of this work, the analysis of our fully extended model (Fig. 10) strongly suggests that whenever transport occurs over significant length scales, topological hindrance can be expected to significantly impact the particle current, in general.

To provide a further link from our theoretical work to biological systems, we finally address how our results could be tested experimentally. Two central predictions that our model makes in this context are (1) current reduction and (2) periodic particle jams. In case (1), the average particle current in the system with two species is expected to be significantly smaller compared to a single-species system (see Fig. 10). This could be measured experimentally using time-resolved single-molecule techniques. In case (2), topological hindrance is related to spatial correlations in the particle arrangement and movement, which may lead to patterns in the particle density. These could be resolved experimentally using techniques described previously, for example, by Maurer *et al.* [81]. One hurdle to overcome is to construct suitable total internal reflection fluorescence (TIRF) microscopy setups that do not obstruct the helical pathways of the spiraling motor species, similar to those described in Refs. [20,82].

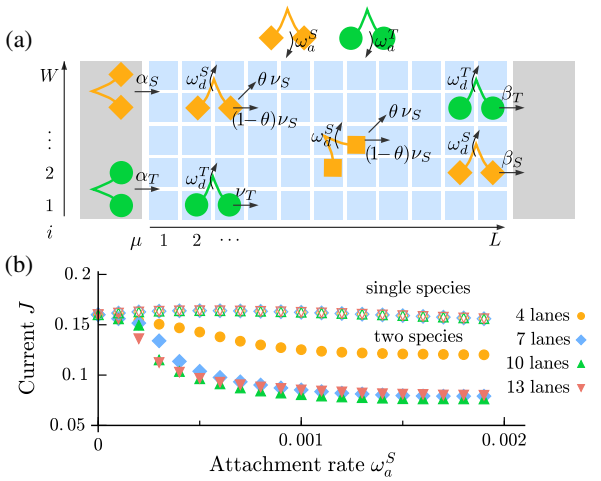

FIG. 10. Illustration of the extended model and current reduction for different numbers of lanes. (a) Dimers populate a lattice of width W and length L. Periodic boundary conditions are employed along the transversal direction. Dimers of species T move their rear legs to the neighboring lattice site on the right of their front legs at a rate ν_T. Dimers of species S move their rear legs to the neighboring lattice site on the right of the front legs at a rate $(1-\theta)\nu_S$ and to the neighboring lattice site on the upper-right of the front legs at a rate $\theta\nu_S$. All particles exclude each other. Dimers either enter the system at the left boundary at rates α_S and α_T or randomly attach to the lattice at respective rates ω_a^S and ω_a^T. Lane-switching particles may either attach with both legs in the same lane at rate $(1-\theta)\omega_a^S$ or, alternatively, with feet in neighboring lanes at rate $\theta\omega_a^S$. Particles exit the system at the right boundary at rates β_S and β_T or stochastically detach from the lattice at rates ω_d^S and ω_d^T. (b) Simulation results show the current for systems with different numbers of lanes W without any spiraling motion (empty symbols) and with rare stochastic lane switching (filled symbols) of $\theta = 0.1$. If no lane switching is possible, the current is not affected by the number of lanes, and it reduces to the single-species TASEP with Langmuir kinetics and dimeric particles [77–79], as identical hopping rates for both species are chosen. However, if the second species is allowed to switch lanes, a rapid current reduction similar to the one described above for the main model can be observed. Note that the current is no longer conserved within the system, such that a spatial average over a lane is taken. Other parameter values include $\omega_d^S = \omega_d^T = \omega_a^T = 0.001$, $\nu_S = \nu_T = 1$, $\alpha = 0$, $\beta = 0.5$, $L = 2048$.

VII. SUMMARY AND CONCLUSION

In this work, we have studied collective transport of two particle species with distinct gaits and therefore different directions of motion on a cylinder. As a key result, we found that the presence of different stepping modes enhances steric interactions and compromises particle dynamics in ways not seen in single-species systems. This additional hindrance changes the macroscopic transport behavior in a way that—to the best of our knowledge—cannot be accounted for by previous models or analyses. The combination of a lane-tracking and a lane-switching species gives rise to unexpected phenomenology in the following fashion:

(1) Systems with a mixed population of both species always jam at densities far below full occupation.
(2) Closely related to that, a system with a mixed population is always characterized by a lower average particle current at a given total system density.
(3) The proportion of the second species present has a crucial influence on this behavior: Current reduction sharply sets in at very small fractions of the second species and practically saturates for fractions larger than $\delta \approx 5\%$.
(4) In contrast to single-species transport, the system width W is an important determinant of collective dynamics. Increasing W rapidly decreases the density at which particles jam and also rapidly increases the degree of current reduction.
(5) The average particle distribution (density profile) shows wavelike patterns for small aspect ratios L/W of the system. This again contrasts with single-species transport and many transport models, as those typically exhibit a spatially constant or linear density profile.

The above observations can be traced back to the following microscopic origin: While for transport with a single species each position can be equally accessed and vacated from a certain number of directions, our model shows a more intricate connectivity. A single lattice site may now be accessed from two different directions but can be vacated in one direction only. This simple change in the network topology has substantial influence on collective behavior. It creates inaccessible lattice sites and slows down particle motion due to intrinsic bottlenecks at points where trajectories intersect. This concept, that steric interactions are amplified by the network topology, forms the basis of our theoretical approaches, which sheds light on the following issues.

(1) We provide a detailed analysis of the jamming process. The decrease of the jamming density with increasing system width W is well approximated by $\rho_{\max} \to \ln(W)/W$ for large W and symmetric species mixtures $\delta = 1/2$. This explains the relevance of the system width W for topological hindrance and suggests convergence to a vanishing jamming density for large system widths. We specifically compute the jamming density in the case $\delta = 1/2$ and $W = 2$, which validates our understanding of the jamming process.
(2) Even at densities well below the jamming transition, many lattice sites are inaccessible. We show that inaccessibility is quantified by a hindrance function, which naturally arises from particle correlations. In doing so, we obtain the current-density relation for arbitrary species fractions and system widths. This method is not restricted to our specific system. It reproduces the correct current-density relation of the TASEP, and we expect it to be applicable to other TASEP-like systems that exhibit cylindrical symmetry.

(3) The current-density relation is used to compute the phase diagram of our model. In this way, we globally relate central macroscopic observables, namely, the average particle current and distribution, to the model's control parameters—the particle in and out rates.

An important conclusion of our study is that the reduction to one dimension is *a priori* not possible for collective transport of differently moving agents along a cylinder. Although dynamics for each species alone are effectively one dimensional and are successfully described by mean-field methods, the joint system deviates from this behavior. Our analysis overcomes this limitation and establishes a framework for mixed populations comprising distinct particle species. It further identifies topologically amplified hindrance as a central determinant in this context. The derivation of the hindrance function not only quantifies the strength of topologically amplified hindrance but also implements an *effective* mapping to a one-dimensional system. This mapping is useful in two ways. First, it reduces the complexity of the mathematical problem by integrating out the transversal spatial dimension. Second, it allows one to infer possible microscopic interactions whenever only a one-dimensional projection is visible. For example, in a biological context, it is still technically challenging to resolve the motion of molecular motors below the diameter of their respective filament. Hence, the projection of particle positions on the filament contour is the standard information accessible in experiments. This holds particularly true in experimental setups with a multitude of moving particles, where super-resolution techniques are not always feasible. As our work shows, it is a highly nontrivial task to relate macroscopic information back to individual microscopic interactions, and our theory might yield valuable insights in this respect. But our considerations also raise the question of how much actual biological systems, such as molecular transport along microtubules, are affected by topological hindrance. While some of our specific results (e.g., a strict maximal density or phase transitions) are weakened by processes like random particle attachment or detachment and nonstrict lane hopping, we still expect topologically amplified interactions to play a critical role. Our analysis regarding model modifications in Sec. VI suggests that, whenever transport occurs over significant length scales and timescales, topological hindrance most likely changes collective behavior substantially. An important conclusion in the biological context is that particle jamming due to topological hindrance takes place at significantly lower particle densities as compared to single-species transport: Figure 10 suggests that even slight deviations from the straight stepping behavior (10% in this case) reduce the current to half of the value as compared to the single-species case at identical cytosolic particle concentrations. Thus, jamming transitions might also be more relevant *in vivo* than previously thought. Therefore, it might be revealing to probe this phenomenon experimentally in multispecies setups and to speculate about its biological implications.

In these ways, our work has various consequences for intracellular transport, and it yields a generic theory for collective motion of differently moving agents. On a theoretical level, our analysis is in line with results of the TASEP for single-species transport. But since the TASEP has relevance beyond the field of transport processes, our results also form a bridge to other intensively studied fields of statistical physics: Our model constitutes a simple system far from thermal equilibrium that can be investigated in great detail with the theory developed in this paper. It exhibits a wide range of phenomena that are insufficiently understood and have rarely been observed in analytically well-accessible models such as driven lattice gases. First, in contrast to many other driven lattice gas models, the average particle distribution exhibits complex pattern formation. While a detailed mathematical study of these patterns is beyond the scope of this work, our construction of the hindrance function and the corresponding reduction to one dimension can form a basis for a more rigorous investigation. Second, our model features a nontrivial jamming transition. While jamming also has severe and intricate implications for the TASEP and similar models, the origin of jams in our model is not only the consequence of mere overcrowding but also of the spatial arrangement of the constituents. This is of interest as jamming transitions arise in many different problems, such as traffic flow, granular media, or glassforming liquids [83]. Nonetheless, it is still a demanding and ongoing task to establish a concise theoretical framework for these phenomena [84,85], although it is an open question whether a general connection exists [86,87]. The challenge involved in finding a mathematical formulation of jamming processes also becomes evident in view of the Biham-Middleton-Levine model [67] for traffic flow: Although the model has been extensively studied for more than 15 years, a rigorous analytic approach to describe its jamming transition is still elusive and considered to be an unsolved mathematical problem [68,88,89]. In this light, our study opens a new perspective on jamming processes as well as pattern formation in terms of simple, analytically accessible models, and it further elucidates the intriguing principles of collective behavior emerging in nonequilibrium systems.

ACKNOWLEDGMENTS

We thank Silke Bergeler, Isabella Graf, Johannes Knebel, Timo Krüger, Louis Reese, and Moritz Striebel for discussions and feedback on this paper. This research was supported by the German Excellence Initiative via the program "NanoSystems Initiative Munich" (NIM), and the Deutsche Forschungsgemeinschaft (DFG) via project B02 within the Collaborative Research Center (SFB 863)

"Forces in Biomolecular Systems." We also gratefully acknowledge financial support by the DFG Research Training Group GRK2062 (Molecular Principles of Synthetic Biology).

APPENDIX A: DERIVATION OF THE MAXIMAL DENSITY $\rho_{\max}$ FOR $\delta = 1/2$, $W = 2$

One of the critical differences of our model in comparison to one-species transport is complete jamming of particles at densities far below full occupation. In this section, we focus on these completely jammed configurations and determine their number of inaccessible lattice sites and thus the maximal density $\rho_{\max}$.

Complete jamming occurs only for vanishing out rates. One might expect that it is possible to focus on the case $\beta = 0$. This results in a much easier stochastic process, which we refer to as the filling process. Our stochastic simulations, however, show that a more careful analysis is required when β vanishes: The average system density exhibits different values for arbitrarily small out rates $\beta \to 0$ than for out rates that strictly equal zero, $\beta = 0$. For example, for $W = 2$ and $\delta = 1/2$, our simulations show that the density converges to a constant value of $\rho_{\max} \approx 0.73$ for small but nonzero values of β (tested for different values of β up to 10^{-10}). Setting $\beta = 0$, the system realizes a different density of $\rho_{\text{filling}} = 0.79$. Our analysis of completely jammed configurations hence has to treat the cases $\beta = 0$ and $\beta \to 0$ separately.

To obtain a relation between the densities corresponding to $\beta = 0$ and $\beta \to 0$, it is of relevance to understand how such a discontinuous behavior of the density can arise. Ultimately, it can be traced back to an instability of subconfigurations that arise in the filling process. A possible configuration is shown in Fig. 11(a). The filling process creates configurations that contain particles that do not block other particles [crossed particles in Fig. 11(a)]. Consequently, it is possible to remove these loose particles from a completely jammed system without allowing further particle motion. In the stationary state, however, each particle that is removed from the system has to be compensated by a new particle, on average. Therefore, loose particles are suppressed in any stationary state that exhibits a nonvanishing, yet arbitrarily small, stationary current. The system undergoes a discontinuous phase transition when the out rate changes from zero to a finite value.

Based on this reasoning, it is possible to derive analytic expressions of the average system density created by the filling process ρ_{filling} and the maximal (dynamic) system density $\rho_{\max}$ corresponding to $\beta \to 0$. For simplicity, we restrict our discussion to $W = 2$ lanes and $\delta = 1/2$ throughout this section. Our analysis includes the following steps: We first focus on the filling process with $\beta = 0$. For this stochastic process, it is possible to obtain an *exact* analytic solution for the probability of finding an arbitrary configuration and therefore for ρ_{filling}. The result further allows us to compute the probability p_{loose} of finding a loose particle in a configuration created by the filling process. When a nonvanishing current is established, the presence of loose particles is suppressed, and the density decreases correspondingly, which will be computed in the last step of our derivation.

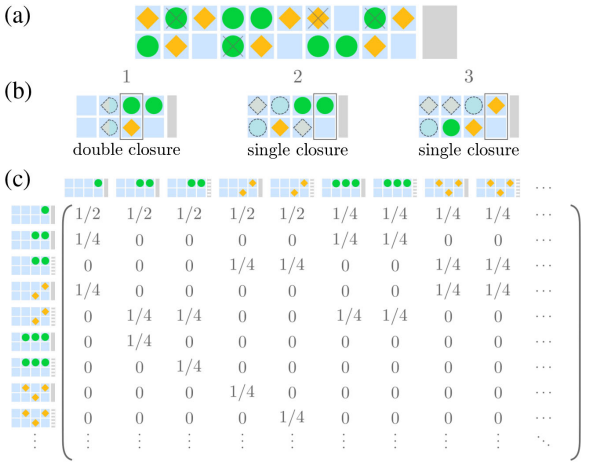

FIG. 11. Illustrations for the filling process, $\beta = 0$, $\alpha \to 0$. (a) During the filling process, loose particles (crossed particles) are created. Loose particles are particles that can be removed from a jammed configuration without allowing further particle motion. Thus, they are suppressed in any stationary state that exhibits an arbitrary nonvanishing current. (b) If a column is fully occupied (box in group 1), the next particle (shaded particles) cannot pass this column; therefore, a truncation of the state space with respect to particles to the right is possible. This is referred to as double closure. If a linear array of at least two particles of the same species is followed by a particle of the other species, either a double closure is created or a single occupied column can be identified (boxes in groups 2 and 3), beyond which none of the following particles (shaded particles) can pass. This also allows one to truncate configurations to the right of this column, and it is referred to as a single closure. (c) Transition matrix of the stochastic process for $\beta = 0$, $\alpha \to 0$. The state space reduces to arrays of particles of the same species that follow a double (solid end) or single closure (shaded end). A single particle can only arise after a double closure, as single closures immediately create arrays of length two. In (a) and (b), a gray area denotes the system boundary.

1. The filling process

The filling process is defined as the stochastic process arising for $\beta = 0$. Typically, in jammed configurations, the system properties are independent of the in rate α, which suggests that we should also consider the limit $\alpha \to 0$. Then, we can assume that particles arrive at the right lattice end independently, which further simplifies our

discussion. Our mathematical formulation should describe the sequence of lattice occupations when particles are added sequentially. Specifically, a (discrete) time step is defined by a new particle getting stuck in the system. A naïve way to denote the state space would be to enumerate the $3^{2\times L}$ possible lattice occupations. However, this leads to a very irregular and high-dimensional state space that precludes an exact solution. Figure 11(b) shows several configurations that are jammed at the lattice end but empty at the front. Light-colored particles denote the possible positions at which the next particle can end up. In all cases, the next particle cannot pass the column that is marked with a box. This means that its final position is independent of the configuration to the right of this box. We can identify such a column where particles cannot pass in two different cases: First, whenever a column is filled completely [box in group 1, Fig. 11(b)], no more changes can be made to the configuration to the right of this column. We refer to this column as double closure. Second, whenever a linear array of particles of the same species is followed by a particle of the other species, a column that cannot be passed can be identified. In this case, either a double closure may be created or a new kind of closure arises. Specifically, if no double closure is created, we can always identify a half-occupied column [boxes in groups 2 and 3, Fig. 11(b)], beyond which no further change is possible. We refer to this column as a single closure. The above reasoning then suggests the following truncation scheme for the state space: Whenever a closure occurs, we can truncate the state space with respect to the occupation to the right of it. This significantly reduces the complexity of the state space. The remaining possible configurations are linear arrays of a single species to the left of either of the two different types of closures. Given this reduced state space, it is possible to write down the resulting (infinite-dimensional) transition matrix that characterizes the underlying stochastic process. The result reads

$$M = \begin{pmatrix}
1/2 & 1/2 & 1/2 & 1/2 & 1/2 & 1/4 & 1/4 & 1/4 & 1/4 & \cdots \\
1/4 & 0 & 0 & 0 & 0 & 1/4 & 1/4 & 0 & 0 & \cdots \\
0 & 0 & 0 & 1/4 & 1/4 & 0 & 0 & 1/4 & 1/4 & \cdots \\
1/4 & 0 & 0 & 1/4 & 1/4 & 0 & 0 & 1/4 & 1/4 & \cdots \\
0 & 1/4 & 1/4 & 0 & 0 & 1/4 & 1/4 & 0 & 0 & \cdots \\
0 & 1/4 & 0 & 0 & 0 & 0 & 0 & 0 & 0 & \cdots \\
0 & 0 & 1/4 & 0 & 0 & 0 & 0 & 0 & 0 & \cdots \\
0 & 0 & 0 & 1/4 & 0 & 0 & 0 & 0 & 0 & \cdots \\
0 & 0 & 0 & 0 & 1/4 & 0 & 0 & 0 & 0 & \cdots \\
\vdots & \vdots & \vdots & \vdots & \vdots & \vdots & \vdots & \vdots & \vdots & \ddots
\end{pmatrix},$$

where the states are enumerated as shown in Fig. 11(c). This matrix encodes the evolution of probabilities for occupations after a closure and the frequencies at which double as well as single closures occur. For an infinite system, the occupational probabilities of the stochastic process will converge to a steady state, which corresponds to the eigenvector of the stochastic matrix M with eigenvalue one. The result reads

$$P_{\text{st.state}} = \begin{pmatrix}
2\sqrt{3}-3 \\
\frac{1}{4}(2-\sqrt{3}) \\
\frac{1}{4}(13\sqrt{3}-22) \\
\frac{1}{4}(2-\sqrt{3}) \\
\frac{1}{4}(13\sqrt{3}-22) \\
(11\sqrt{3}-19)(2-\sqrt{3})^0 - \frac{1}{16}(2-\sqrt{3})\left(\frac{1}{4}\right)^0 \\
\frac{1}{16}(2-\sqrt{3})\left(\frac{1}{4}\right)^0 \\
(11\sqrt{3}-19)(2-\sqrt{3})^0 - \frac{1}{16}(2-\sqrt{3})\left(\frac{1}{4}\right)^0 \\
\frac{1}{16}(2-\sqrt{3})\left(\frac{1}{4}\right)^0 \\
(11\sqrt{3}-19)(2-\sqrt{3})^1 - \frac{1}{16}(2-\sqrt{3})\left(\frac{1}{4}\right)^1 \\
\frac{1}{16}(2-\sqrt{3})\left(\frac{1}{4}\right)^1 \\
(11\sqrt{3}-19)(2-\sqrt{3})^1 - \frac{1}{16}(2-\sqrt{3})\left(\frac{1}{4}\right)^1 \\
\frac{1}{16}(2-\sqrt{3})\left(\frac{1}{4}\right)^1 \\
\vdots
\end{pmatrix}. \tag{A1}$$

With these steady-state probabilities for lattice configurations, we can derive an exact result for the average particle density in an infinite system. We compute the frequencies of blocks of subconfigurations with a closure at the left being added to the system. These frequencies can be determined by the transition rates and the steady-state probabilities. For example, an array of two T particles following a double closure [second configuration in the enumeration scheme of Fig. 11(c)] can be "closed" by an arriving S particle such that a stable block dimension 2×2 occupied by three particles is created. As the probability of an S particle arriving at the respective site is $1/4$, the corresponding frequency for this block to occur is $1/4P_2$. We weigh these frequencies with the block lengths and densities, which yields the system density in the limit $L\to\infty$. Our analytic approach results in a value of $\rho_{\text{filling}} = 0.79$. Notably, we made no approximations in this computation. Consequently, it should coincide with the

system densities for $\beta = 0$ and $\alpha \to 0$. Indeed, simulations with respective parameter values confirm our result.

2. Maximal dynamic density $\rho_{\max}$

As illustrated above, the presence of unstable, loose particles will lead to a different density as soon as β goes from zero to arbitrarily small values. Therefore, computing the number of loose particles that arise in the filling process is key to determine the density decrease as soon as the system becomes dynamic. In the first step to compute the maximal density $\rho_{\max}$, we determine the probability of finding a loose particle. In the second step, we show how to correctly replace the corresponding occupational density and thereby estimate $\rho_{\max}$.

Loose particles can only arise whenever both lanes are occupied at a given position μ, i.e., within a double-occupied column. The probability of double-occupied columns created by the filling process is easily computed from the filling density. For further convenience, we introduce a new random variable $c_\mu \in \{0, 1\}$ that equals 1 if the μth column is fully occupied (irrespective of the particle species, i.e., for $n^X_{1,\mu} = 1 \wedge n^X_{2,\mu} = 1$) and 0 otherwise. Then,

$$P(c_\mu = 1) = 2\left(\rho_{\text{filling}} - \frac{1}{2}\right), \tag{A2}$$

where $P(c_\mu = 1)$ is the probability of finding a fully occupied column. Then, a loose particle occurs in a double-occupied column in two different situations: first, when this column is followed by a column to its left that is occupied by only one particle. This will always result in a loose particle in the double-occupied column. The second situation is if the double-occupied column is followed by another double-occupied column to its left where a particle from each species is present. Then, the two particles of the left column are directed to a single site, which creates a loose particle next to this site. To compute the corresponding probabilities, we use the exact solution of the filling process. In detail, we can determine the probability of a double closure being followed by a fully occupied column. This scenario is identical to the conditional probability of a double-occupied column being followed by another double-occupied column and, using the above solution of the filling process, is given by $p(c_\mu = 1|c_{\mu-1} = 1) \approx 0.64$. In half of these cases, the fully occupied column on the left is populated by particles from different species. This corresponds to the second case described above and therefore creates a loose particle. If the double-occupied column is *not* immediately followed by another double-occupied column [corresponding to $(1 - p(c_\mu = 1|c_{\mu-1} = 1))$], the first case as described above occurs, and again a loose particle is created. Taking all these considerations together leads to

$$\begin{aligned} p_{\text{loose}} &= \frac{1}{2}p(c_\mu = 1; c_{\mu-1} = 1) + (1 - p(c_\mu = 1; c_{\mu-1} = 1)) \\ &\approx 0.39. \end{aligned} \tag{A3}$$

Here, we use the definition of the conditional probability, $p(c_\mu = 1; c_{\mu-1} = 1) = p(c_\mu = 1|c_{\mu-1} = 1) \times p(c_\mu = 1)$.

Knowing the probability of a site being occupied by a loose particle, it seems tempting to subtract the corresponding occupations from the filling density ρ_{filling}. But particle rearrangements in a dynamic system will continuously create new loose particles. Hence, we have to replace sites occupied by a loose particle with sites of a suitable effective density ρ_{eff}.

To this end, consider a hole (i.e., an empty site) that propagates from right to left through the system. In each hopping step, the hole might either hit a column that contains a loose particle with probability p_{loose} or one that contains only stable particles with probability $1 - p_{\text{loose}}$. As only loose particles contribute to a modification of the density, we are only interested in the first case. Let the average time between two consecutive holes arriving at any given position in the steady be denoted by T. A fully occupied column that contains a loose particle will, on average, remain in this state for a time T before a hole arrives. Then, the hole either hits the loose or the stable particle in this column. If the stable particle is removed, the density is not changed, and the column remains at full occupation until the next hole arrives, i.e., for another time T. On the other hand, the column remains at half occupation for a time T if the loose particle is removed. This leads to an effective (time-averaged) density of

$$\rho_{\text{effective}} = \frac{1}{2T} \cdot \left(T + T \cdot \left(\frac{1}{2} \cdot \frac{1}{2} + \frac{1}{2} \cdot 1\right)\right) = \frac{7}{8}. \tag{A4}$$

Hence, the filling density ρ_{filling} and the maximal dynamic system density $\rho_{\max}$ are related via

$$\rho_{\max} \approx \rho_{\text{filling}} - p_{\text{loose}}(1 - \rho_{\text{effective}}). \tag{A5}$$

The result is $\rho_{\max} \approx 0.74$, which is in very good agreement with stochastic simulations that yield $\rho_{\max} \approx 0.73$. This validates our understanding of topological hindrance for jammed configurations.

Because of approximations in the above calculation, our computed value for $\rho_{\max}$ is, opposed to the one for ρ_{filling}, not an exact result. Specifically, we implicitly assume that for nonvanishing $\beta \to 0$, occupations are created in the same way as they are in the filling process $\beta = 0$. The good quality of our result therefore indicates that, as a hole propagates through a jammed system, empty lattice sites are filled by particles in a mostly uncorrelated fashion. Note that the filling density does, in principle, depend on the particle in rate α. If particles are injected with a high

frequency, mutual interactions—while traveling to the jammed end—lead to correlations and sorting effects that ultimately cause varying values for ρ_{filling}. This dependency of the filling density on α is, however, irrelevant for our computation of the maximal (dynamic) density $\rho_{\max}$: Correlations that build up during the particles' motion can also be neglected in the case $\beta \to 0$ as the system is almost completely jammed.

The theoretical arguments of this section addressing a transition from the filling density to the maximal dynamic density are further illustrated with the following consideration. Figure 12 shows the temporal evolution of the average system density with a very small out rate, starting from an empty system. The out rate was chosen such that, on average, the system completely fills with particles before a first particle exits. Indeed, we observe that the density gradually increases until ρ_{filling} is reached. In particular, the density overshoots the maximal dynamic density $\rho_{\max}$. As soon as particles leave the system, loose particles are removed, which causes the average density to decrease and fluctuate around $\rho_{\max}$. These fluctuations are also explained by our above argumentation: As single holes travel through the system, particles are reordered, and loose particles are transiently created, which leads to an (also transient) increase of the system density.

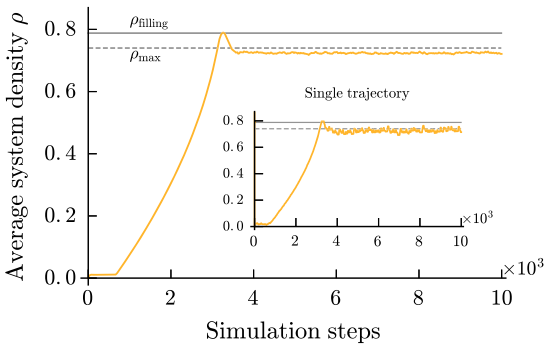

FIG. 12. Temporal evolution of the system density for $\alpha \to 0$, $\beta \to 0$, $\beta \ll \alpha$. As the number of simulation steps increases (x axis), particles enter the system, "pile up" at the end, and create an average density close to $\rho_{\text{filling}} \approx 0.79$ (solid line). As soon as particles leave the system, the presence of loose particles is suppressed, which leads to a drop of the average density until the maximal dynamic density $\rho_{\max} \approx 0.73$ is reached. The dashed line depicts the result of the analytic approach for $\rho_{\max}$ described in this section. Here, the density is obtained from an ensemble and spatial average. A single realization (inset) shows that the average system density (i.e., spatial average) oscillates around $\rho_{\max}$, which can be explained by large reordering events if stable particles are removed after several loose particles are extracted. Simulation parameters include $\alpha = 0.02$, $\beta = 10^{-4}$, $\delta = 1/2$, $W = 2$, $L = 4096$.

APPENDIX B: DERIVATIVES OF THE HINDRANCE FUNCTION

In the following, we calculate the derivatives of the hindrance function for the two extremal cases $\rho \to 0$ and $\rho \to \rho_{\max}$, as used in Sec. V. To do so, we determine the change in current $\mathrm{d}J$ in response to a change in density $\mathrm{d}\rho$ at a given lattice site and equate it with the derivative of the current-density relation, Eq. (12),

$$\frac{d}{d\rho} J(\rho) = 1 - H(\rho) - \rho H'(\rho) - 2\rho. \tag{B1}$$

In the mean-field approximation, a lattice site is occupied with a particle with probability ρ irrespective of the neighboring lattice sites. We find an S particle at any given lattice site with probability $\delta\rho$ and a T particle with probability $(1-\delta)\rho$, respectively. Increasing the density by a value $\mathrm{d}\rho$, we have two contributions to the change of the current: first, a decrease since particles are more likely to be blocked, and, second, an increase because the additional density itself may contribute to the overall current. Both contributions can again be split into two separate cases. We are either dealing with a focused state [see Fig. 3(b), group 1], where two particles are blocked simultaneously, or with the case where only one particle is affected. Two particles from neighboring lanes are focused on the same lattice site with probability $\rho^2\delta(1-\delta)$, resulting in a current reduction of $-\rho^2\delta(1-\delta)\mathrm{d}\rho$. A single particle is blocked with probability $\rho\delta\big(1-\rho(1-\delta)\big) + (1-\delta)\rho(1-\delta\rho)$. Here, $\rho\delta\big(1-\rho(1-\delta)\big)$ is the probability of only one S particle being blocked and $(1-\delta)\rho(1-\delta\rho)$ of only one T particle being blocked. The same contributions can be derived for the increase in current due to the removal of a single particle. Summing this all up, we obtain

$$\begin{aligned}\frac{d}{d\rho} J = &-\rho^2\delta(1-\delta) - \rho\delta\big(1-\rho(1-\delta)\big) \\ &- (1-\delta)\rho(1-\delta\rho) + (1-\delta)\delta\rho(1-\rho) \\ &+ (1-\delta)(1-\delta\rho)(1-\rho) + \delta\big(1-(1-\delta)\rho\big)(1-\rho) \\ = &\,(1-2\rho)\big(1-\delta(1-\delta)\rho\big).\end{aligned} \tag{B2}$$

This expression reduces to the derivative of the TASEP current-density relation for $\delta = 0$ and $\delta = 1$.

The mean-field result is not correct, in general, for our system but becomes exact in the limit $\rho \to 0$. Using Eq. (B1), our result for the derivative of the hindrance function reads

$$1 - H(\rho) - \rho H'(\rho) - 2\rho \stackrel{!}{=} (1-2\rho)\big(1-\delta(1-\delta)\rho\big). \tag{B3}$$

As, by definition, $H(\rho)/\rho \to H'(0)$ for $\rho \to 0$, we obtain

$$H'(0) = \delta(1-\delta). \tag{B4}$$

We proceed in a similar way for the case $\rho \to \rho_{\max}$. However, instead of an uncorrelated system, we face total correlations between particle occupations; a site is only occupied if the one in front is also. Filling the last hole in a jammed configuration will not increase the current, but it will prevent the last possible particle motion. This means that we are left with those parts of Eq. (B2) that have a negative contribution. Evaluating the corresponding equation at the maximal density $\rho_{\max}$, we find

$$\begin{aligned}\frac{d}{d\rho}J &= -\delta\rho_{\max}(1-\rho_{\max}(1-\delta)) \\ &\quad -(1-\delta)\rho_{\max}(1-\delta\rho_{\max}) - \delta(1-\delta)\rho_{\max}^2 \\ &= -\rho_{\max} + \delta(1-\delta)\rho_{\max}^2. \end{aligned}\tag{B5}$$

Again, using Eq. (B1) and the definition of the maximal density $H(\rho_{\max}) = 1-\rho_{\max}$, we obtain

$$H'(\rho_{\max}) = -\delta(1-\delta)\rho_{\max},$$

for the derivative of $H(\rho_{\max})$. Note that, as opposed to the limit $\rho \to 0$, this is not an exact result but should be interpreted as a refined mean-field approximation.

APPENDIX C: DERIVATION OF CURRENT AND DENSITY RESPONSE TO THE CONTROL PARAMETERS IN THE HIGH- AND LOW-DENSITY PHASES

In this section, we derive the dependence of the current and density on the in rate α and out rate β. As for the TASEP, collective behavior in the low-density phase only depends on the in rate α, whereas the high-density phase is determined by the out rate β.

1. Low-density phase

For many driven lattice gases, current conservation is used to relate the system's current and density to in and out rates. For the case of the TASEP, the low-density phase is dictated by an influx $J = \alpha(1-\rho_1)$. Furthermore, there is no boundary layer at the left lattice end in the low-density phase such that the density at the first site equals the bulk density. Thus, because of current conservation, $\rho_1 = \alpha$ for the TASEP. For our model, however, we face a new problem. Simulations suggest that, even in the low-density phase, the occupation of a first lattice site is not equal to the bulk density and is also not identical to the reservoir density α. This is due to nontrivial correlations between occupations at the left lattice end (see Fig. 13), which we compute in the following. Indeed, the density at the first site is always slightly higher than α. Also, when, for example, the in rate of T particles, α_T, is increased, the density of S particles at a first lattice site $\rho_{i,1}^S$ increases and vice versa. The latter observation, in particular, contradicts equating $\rho_{i,1}^S = \alpha_S$. This behavior can be understood in the following way. Consider, for example, a T particle at the first lattice site. This T particle can never prevent an S particle to hop in front of it; the T particle can be blocked by the S particle, but it cannot block the S particle. Therefore, this T particle will, on average, stay longer at the first lattice site as compared to the TASEP, and the corresponding density $\rho_{i,1}$ will be higher than α. The exact flux-balance condition for T particles, Eq. (5), reads

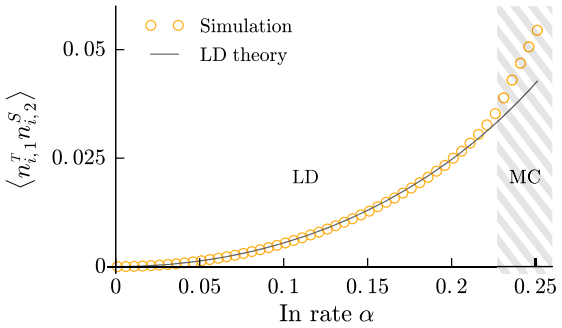

FIG. 13. Second moment $\langle n_{i,1}^T n_{i,2}^S \rangle$ of occupations of different species at the first two lattice sites as predicted by our theory (lines) and stochastic simulations (symbols) for the special case $\delta = 1/2$ and $W = 2$. Deviations between theory and simulation only occur close to the phase transition at $\alpha \approx 0.22$.

$$\alpha_T(1-\langle n_{i,1}^T\rangle - \langle n_{i,1}^S\rangle) = \langle n_{i,1}^T\rangle - \langle n_{i,1}^T n_{i,2}^T\rangle - \langle n_{i,1}^T n_{i,2}^S\rangle. \tag{C1}$$

Again, correlators of the form $\langle n_{i,1}^{X_1} n_{i,2}^{X_2}\rangle$ lead to an unclosed set of equations. To overcome this problem, we approximate second moments. Note that all particles enter the system from the left reservoir in an uncorrelated fashion. The way T particles can block and are blocked by other T particles follows the same scheme as in the TASEP. Therefore, it is reasonable to assume that correlations balance (as for the TASEP). Thus, we factorize $\langle n_{i,1}^T n_{i,2}^T\rangle \approx \langle n_{i,1}^T\rangle\langle n_{i,2}^T\rangle$ for the same species. This is different for $\langle n_{i,1}^T n_{i,2}^S\rangle$, where a TASEP-like balance of the blockage and getting blocked no longer holds true as argued above.

Explicitly writing down the master equation for $\langle n_{i,1}^T n_{i,2}^S\rangle$ in the steady state leads to

$$\begin{aligned}\frac{d}{dt}\langle n_{i,1}^T n_{i,2}^S\rangle = 0 &= \alpha_T\langle(1-n_{i,1}^T - n_{i,1}^S)n_{i,2}^S\rangle \\ &\quad + \langle n_{i,1}^T n_{i-1,1}^S(1-n_{i,2}^T - n_{i,2}^S)\rangle \\ &\quad - \langle n_{i,1}^T n_{i,2}^S(1-n_{i+1,3}^T - n_{i+1,3}^S)\rangle. \end{aligned}\tag{C2}$$

As particles that enter the system are uncorrelated, we can set $\langle n_{i,1}^T n_{j,1}^S\rangle = \rho_{i,1}^T\rho_{j,1}^S$ for $i \neq j$. Furthermore, we are

interested in a solution that is valid in the low-density phase, where we expect α to be small and $\rho_{i,1}$ to be of order (but not necessarily equal to) α, i.e., $\rho_{i,1} \propto \mathcal{O}(\alpha)$. If correlations are weak, we can also assume that $\langle n_{i,\mu} n_{j,\nu} \rangle \propto \mathcal{O}(\alpha^2)$ and $\langle n_{i,\mu} n_{j,\nu} n_{k,\xi} \rangle \propto \mathcal{O}(\alpha^3)$. The transitions from the low-density phase to the maximal-current and high-density phases take place at lower values of α as compared to the TASEP (cf. Fig. 5), which ensures very low values for the density in the low-density phase in our model. Then, upon truncating at third order in α, we arrive at an equation for $\langle n^T_{i,1} n^S_{i,2} \rangle$ that is valid for low densities:

$$\langle n^T_{i,1} n^S_{i,2} \rangle \approx \alpha_T \rho^S_{i,1} + \rho^T_{i,1} \rho^S_{i,1}. \tag{C3}$$

Here, we also assume that $\rho^S_{i,2} \approx \rho^S_{i,1}$ [90]. An analogous equation can be derived for $\langle n^S_{i,1} n^T_{i,2} \rangle$. Inserting the results in Eq. (C1) and its analogue for the influx of S particles, we find

$$\alpha_T (1 - \rho^T_{i,1}) = \rho^T_{i,1} (1 - \rho^T_{i,1} - \rho^S_{i,1}), \tag{C4a}$$

$$\alpha_S (1 - \rho^S_{i,1}) = \rho^S_{i,1} (1 - \rho^T_{i,1} - \rho^S_{i,1}). \tag{C4b}$$

Equations (C4) can be interpreted as a two-species TASEP, where particles from different species cannot block each other when entering the system. This means that, for low densities, the possibility of overtaking particles from the other species when entering the system effectively acts as if no exclusion was present for different species; particles from the same species still exclude each other. Equations (C4) can be solved for $\rho^T_{i,1}$ and $\rho^S_{i,1}$, which fixes the current and bulk density in the system.

For the case of identical in rates, the solution of Eqs. (C4) is of a particularly simple form, and the total current is given by

$$J = \frac{\alpha}{4} (2 - \alpha + \sqrt{4 + (\alpha - 12)\alpha}). \tag{C5}$$

Even though this result is independent of the number of lanes, the actual current in the system can never become higher than the respective maximal current of the bulk, which, in turn, depends on the number of lanes. As soon as the bulk limits transport, the transition to the maximal-current phase is triggered. For higher in rates, the conservation of the maximal current dictates the density at the first lattice sites. A comparison with simulation data for different numbers of lanes is shown in Fig. 14. The low-density theory agrees with the data up to the point of the phase transition. The exact value of the in rate α at which the transition into the MC phase takes place depends on the number of lanes.

In summary, Eq. (C4) correctly describes the behavior of our system in the low-density phase that is found to be independent of the number of lanes W of the system.

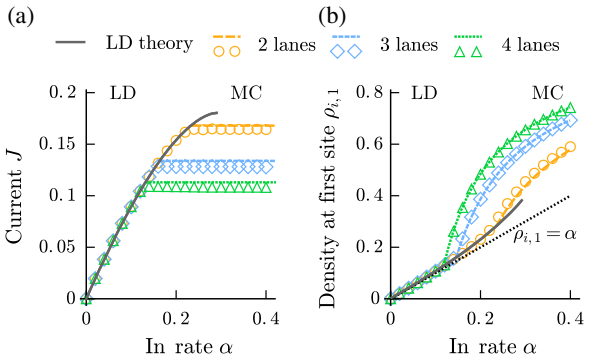

FIG. 14. Comparison between low-density theory (lines) and stochastic simulations (symbols) for the special case $\delta = 1/2$. (a) Current plotted against the in rate α in the LD phase for different numbers of lanes W. For low in rates, the current increases monotonically until it becomes constant at a point that depends on the number of lanes; the respective current corresponds to the maximal current of the bulk. Low-density theory agrees with simulation results for the LD phase. The low-density theory is independent of the number of lanes. (b) Density at the first lattice site $\rho_{i,1}$ plotted against the in rate α for different numbers of lanes. In the LD phase, the density is dictated by the left boundary and agrees with the low-density theory. After the transition to the maximal-current phase, the density is determined by conservation of the maximal current. Again, the corresponding value for the maximal current depends on the respective number of lanes, which leads to a distinct behavior for different numbers of lanes in the MC phase.

Dependencies on the number of lanes are only relevant for phase transitions that can be derived by applying the extremal current principle.

2. High-density phase

In the high-density phase, the system's current is dictated by the right boundary and determined by an outflux of particles $J = \beta \rho_L$. Here, ρ_L denotes the density at the last lattice site for an arbitrary lane i. Because of current conservation, this outflux must equal the bulk current,

$$\beta \rho_L = \rho (1 - H(\rho) - \rho), \tag{C6}$$

where ρ denotes the density in the bulk. As for the low-density phase, we lack knowledge about the value of the density at the dominating boundary, in this case ρ_L. Clearly, the mean-field result $\rho_L = 1 - \beta$ cannot be used. This becomes evident when we consider jammed systems that exhibit a maximal density $\rho_{\max}$ that, in general, does not equal $1 - \beta$. However, we expect the density at the right lattice end to be of the order of the bulk density, $\rho_L \approx \rho$. Using this assumption in Eq. (C6) we obtain a unique solution for the particle current. The result is shown in Fig. 15 and is in agreement with stochastic simulations.

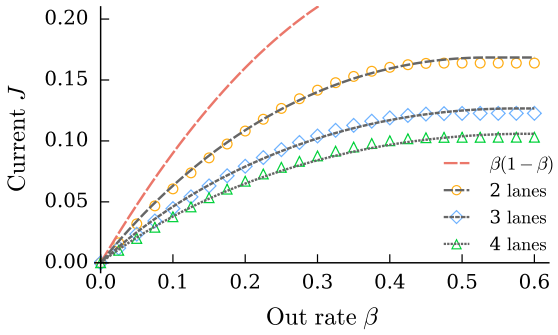

FIG. 15. Average system current as a function of the out rate β in the high-density phase for different numbers of lanes for the special case $\delta = 1/2$. Comparison between stochastic simulations (symbols) and theoretical predictions (lines). The current increases monotonically with increasing out rate. For sufficiently high out rates, the system enters the maximal-current phase, and the current becomes constant. The assumption of $\rho_L = 1 - \beta$ with a corresponding out flux of $J = \beta(1-\beta)$ (uppermost dashed line) fails to describe our model.

APPENDIX D: SUPPLEMENTAL SIMULATIONS

Here, we present additional data from simulations that supplement several statements made in the main text.

1. Rotational symmetry of the density profile

In the main text, we discussed how density profiles have to be identical for every lane because any stationary state has to be unique. However, the time needed to reach this stationary state can be very long since the system may get stuck in metastable configurations that break symmetry. Figure 16 shows that indeed all lanes admit identical density profiles in our simulations. This demonstrates that simulation times are chosen sufficiently long to ensure convergence to the (rotationally invariant) stationary state.

2. Relation between the species fraction of the current and the density

In Sec. IV of the main text, we have shown that, in the mean-field approximation, the current species fraction δ is identical to the density species fraction ρ^S/ρ. However, this result does not hold true in general. To assess the difference between the species fraction of the density and that of the current, we perform stochastic simulations for a wide range of parameter values. As illustrated in Fig. 17, our simulations show that deviations between both quantities are relatively small (below 10%). This justifies using δ as the general species fraction in this paper.

There are, however, important exceptions where this equivalence cannot be employed. If we regard systems with a small aspect ratio L/W and significantly asymmetric species mixtures, the species fractions of current and density strongly differ. Figure 18 shows differences of up to 60% between these quantities in stochastic simulations, with corresponding parameter values. In all of these cases, the naïve assumption $\rho^S \approx \delta\rho$ clearly fails, and the individual densities have to be considered separately.

3. Current-density relation for a system with a large number of lanes

The current density relation for a large number of lanes shows very drastic modifications as compared to the TASEP (see Fig. 19). Most of the possible density values are not realized at all in the stationary state. Furthermore, the maximal current is far below the one known from the TASEP. As for low numbers of lanes, a very small fraction of the second species (2%–5%) is already sufficient to drastically reduce transport efficiency.

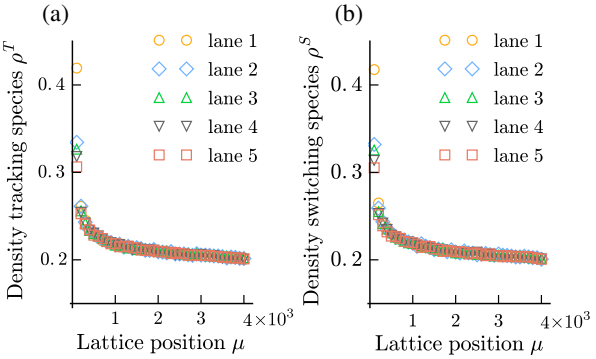

FIG. 16. Comparison of the density profiles of all lanes for a system with $W = 5$ lanes. The density profiles are identical for each lane and for both species. No symmetry breaking takes place. In order to improve visibility, only every 100th lattice site is plotted for every lane, with a different offset for each lane. Other parameters include $L = 4096$, $\delta = 0.5$, $\alpha = 10^{-4}$, $\beta = 10^{-6}$.

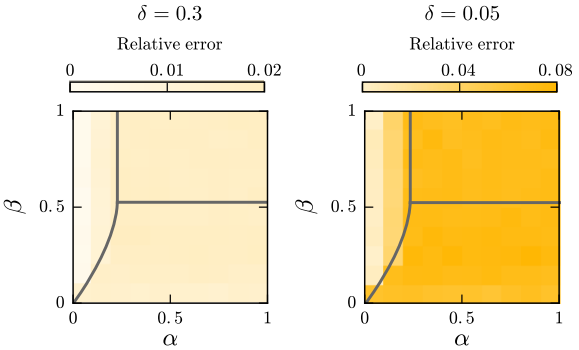

FIG. 17. Relative deviation of the density species fraction from δ for the special case of $W = 2$ lanes and $L = 4096$ sites. Color denotes simulation results for the relative deviation and thus the error that is made when assuming a density species fraction of value δ. Lines indicate the phase boundaries as predicted by our theory.

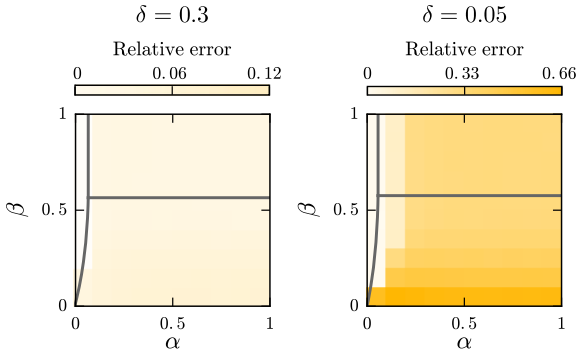

FIG. 18. Relative deviation of the density species fraction from δ for the special case $W = 13$ lanes and $L = 512$ sites. Color denotes simulation results for the relative deviation and thus the error that is made when assuming a density species fraction of value δ. Lines indicate the phase boundaries as predicted by our theory.

4. Robustness of the density patterns with respect to model extensions

One of the most intriguing features of our main model is the formation of regular density patterns. However, while this is clearly an interesting phenomenon to study in the context of nonequilibrium physics, it is an open question whether such patterns may occur in a biological systems. While a rigorous and complete analysis of pattern formation in this context is out of the scope of this work, we would like to provide an outlook on potential changes due to different model extensions. Figure 20 shows how the density patterns change as compared to Fig. 8(a) of the main text if different modifications are included.

Modeling of particles as dimers does not significantly affect the formation of patterns [see Fig. 20(a)]; they again appear robustly and with the same wavelength as before.

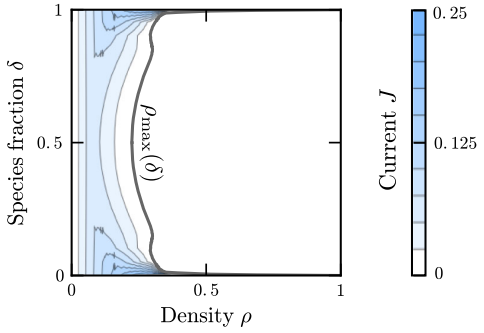

FIG. 19. Current-density relation obtained from stochastic simulations with $W = 13$ lanes and $L = 16\,384$ sites. The emerging current of an arbitrary lane (blue) shows a dependence not only on the average system density but also on the fraction of lane-switching particles, δ. The system jams at a maximal density $\rho_{\max}(\delta)$ (bold gray line); densities between $\rho_{\max}$ and full occupation are not realized in the stationary state.

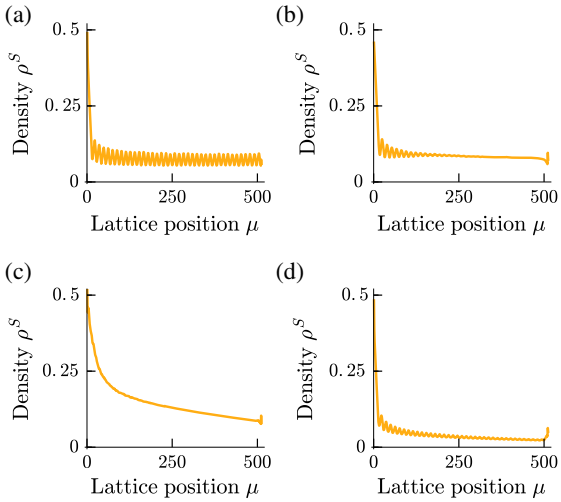

FIG. 20. Effects of model extensions on density patterns. (a) Dimers show the same kind of density patterns as monomers. (b) If lane-switching dimers do not follow a unique trajectory ($\theta = 0.95$), density patterns occur but are subject to spatial decay. (c) As soon as dimers are allowed to attach randomly on the lattice ($\omega_a^S = \omega_a^T = 5 \times 10^{-5}$), the system loses its characteristic length scale and the density profile becomes smooth. (d) Random dimer detachment ($\omega_d^S = \omega_d^T = 10^{-3}$) still allows for the formation of density patterns. While the wavelength stays the same, the amplitude of the oscillations is reduced. Other parameters include $W = 13$, $L = 512$, $\alpha = 0.6$, $\beta = 0.2$, $\delta = 1/2$.

Since no differences between monomers and dimers are observed, we restrict our discussion to the dimeric case for the rest of this section.

Including nonstrict lane hopping leads to a spatial decay of oscillatory patterns [Fig. 20(b)]. On the other hand, random particle attachment smoothens the density profiles globally [Fig. 20(c)]. Finally, random particle detachment (even for comparably high detachment rates) still results in oscillatory patterns [Fig. 20(d)]. This can be explained in the following way: To establish density patterns, particles of different species need to jam periodically because of particles they have encountered before. For the main model, the typical length scale needed for this to happen is the width of the lattice. In the case of nonstrict lane hopping, the period of circulating once around the system is stochastic, which gradually destroys the "phase" of our density oscillations. If we add random particle detachment to the system, length scales are not changed: Some particles may leave the system, which makes jams less likely but does not alter the length scale on which those jams appear. Random particle attachment critically changes this phenomenology: A certain lattice position no longer corresponds to a fixed run length of a specific particle. Therefore, the stationary density profile becomes translationally invariant, which, in turn, has to suppress density patterns when averaged over large time windows.

[1] J. Howard, *Mechanics of Motor Proteins and the Cytoskeleton* (Sinauer Associates, Sunderland, 2001).

[2] J. Nilsson and P. Nissen, *Elongation Factors on the Ribosome*, Curr. Opin. Struct. Biol. **15**, 349 (2005).

[3] G. Woehlke and M. Schliwa, *Walking on Two Heads: The Many Talents of Kinesin*, Nat. Rev. Mol. Cell Biol. **1**, 50 (2000).

[4] R. A. Cross, *The Kinetic Mechanism of Kinesin*, Trends Biochem. Sci. **29**, 301 (2004).

[5] A. Gennerich and R. D. Vale, *Walking the Walk: How Kinesin and Dynein Coordinate Their Steps*, Curr. Opin. Cell Biol. **21**, 59 (2009).

[6] C. Leduc, K. Padberg-Gehle, V. Varga, D. Helbing, S. Diez, and J. Howard, *Molecular Crowding Creates Traffic Jams of Kinesin Motors on Microtubules*, Proc. Natl. Acad. Sci. U.S.A. **109**, 6100 (2012).

[7] C. T. MacDonald, J. H. Gibbs, and A. C. Pipkin, *Kinetics of Biopolymerization on Nucleic Acid Templates*, Biopolymers **6**, 1 (1968).

[8] T. Chou, K. Mallick, and R. K. P. Zia, *Non-equilibrium Statistical Mechanics: From a Paradigmatic Model to Biological Transport*, Rep. Prog. Phys. **74**, 116601 (2011).

[9] M. Mobilia, T. Reichenbach, H. Hinsch, T. Franosch, and E. Frey, *Stochastic Models in Biological Sciences* (Polish Academy of Science, Warsaw, 2008), pp. 101–120.

[10] S. Ray, E. Meyhöfer, R. A. Milligan, and J. Howard, *Kinesin Follows the Microtubule's Protofilament Axis*, J. Cell Biol. **121**, 1083 (1993).

[11] J. Yajima and R. A. Cross, *A Torque Component in the Kinesin-1 Power Stroke*, Nat. Chem. Biol. **1**, 338 (2005).

[12] R. A. Walker, E. D. Salmon, and S. A. Endow, *The Drosophila Claret Segregation Protein is a Minus-End Directed Motor Molecule*, Nature (London) **347**, 780 (1990).

[13] X. Pan, S. Acar, and J. M. Scholey, *Torque Generation by One of the Motor Subunits of Heterotrimeric Kinesin-2*, Biochem. Biophys. Res. Commun. **401**, 53 (2010).

[14] J. Yajima, K. Mizutani, and T. Nishizaka, *A Torque Component Present in Mitotic Kinesin Eg5 Revealed by Three-Dimensional Tracking*, Nat. Struct. Mol. Biol. **15**, 1119 (2008).

[15] R. D. Vale and Y. Y. Toyoshima, *Rotation and Translocation of Microtubules in vitro Induced by Dyneins from Tetrahymena cilia*, Cell **52**, 459 (1988).

[16] T. Nishizaka, T. Yagi, Y. Tanaka, and S. Ishiwata, *Right-Handed Rotation of an Actin Filament in an in vitro Motile System*, Nature (London) **361**, 269 (1993).

[17] M. Brunnbauer, R. Dombi, T. H. Ho, M. Schliwa, M. Rief, and Z. Ökten, *Torque Generation of Kinesin Motors Is Governed by the Stability of the Neck Domain*, Mol. Cell **46**, 147 (2012).

[18] V. Bormuth, B. Nitzsche, F. Ruhnow, A. Mitra, M. Storch, B. Rammner, J. Howard, and S. Diez, *The Highly Processive Kinesin-8, Kip3, Switches Microtubule Protofilaments with a Bias Toward the Left*, Biophys. J. **103**, L4 (2012).

[19] M. Bugiel, E. Böhl, and E. Schäffer, *The Kinesin-8 Kip3 Switches Protofilaments in a Sideward Random Walk Asymmetrically Biased by Force*, Biophys. J. **108**, 2019 (2015).

[20] S. Can, M. A. Dewitt, and A. Yildiz, *Bidirectional Helical Motility of Cytoplasmic Dynein around Microtubules*, eLife **3**, e03205 (2014).

[21] W. L. Stepp, G. Merck, F. Mueller-Planitz, and Z. Ökten, *Kinesin-2 Motors Adapt Their Stepping Behavior for Processive Transport on Axonemes and Microtubules*, EMBO Rep. **18**, 1947 (2017).

[22] A. I. Curatolo, M. R. Evans, Y. Kafri, and J. Tailleur, *Multilane Driven Diffusive Systems*, J. Phys. A **49**, 095601 (2016).

[23] B. Derrida, E. Domany, and D. Mukamel, *An Exact Solution of a One-Dimensional Asymmetric Exclusion Model with Open Boundaries*, J. Stat. Phys. **69**, 667 (1992).

[24] B. Derrida, M. R. Evans, V. Hakim, and V. Pasquier, *Exact Solution of a 1D Asymmetric Exclusion Model Using a Matrix Formulation*, J. Phys. A **26**, 1493 (1993).

[25] G. M. Schütz and E. Domany, *Phase Transitions in an Exactly Soluble One-Dimensional Exclusion Process*, J. Stat. Phys. **72**, 277 (1993).

[26] G. M. Schütz, *Phase Transitions and Critical Phenomena* (Academic Press, London, 2001), Vol. 19.

[27] M. Gorissen, A. Lazarescu, K. Mallick, and C. Vanderzande, *Exact Current Statistics of the Asymmetric Simple Exclusion Process with Open Boundaries*, Phys. Rev. Lett. **109**, 170601 (2012).

[28] S. Katz, J. L. Lebowitz, and H. Spohn, *Phase Transitions in Stationary Nonequilibrium States of Model Lattice Systems*, Phys. Rev. B **28**, 1655 (1983).

[29] T. Chou, *How Fast Do Fluids Squeeze through Microscopic Single-File Pores?*, Phys. Rev. Lett. **80**, 85 (1998).

[30] T. Reichenbach, T. Franosch, and E. Frey, *Exclusion Processes with Internal States*, Phys. Rev. Lett. **97**, 050603 (2006).

[31] T. Reichenbach, E. Frey, and T. Franosch, *Traffic Jams Induced by Rare Switching Events in Two-Lane Transport*, New J. Phys. **9**, 159 (2007).

[32] A. Schadschneider, D. Chowdhury, and K. Nishinari, *Stochastic Transport in Complex Systems* (Elsevier, Amsterdam, 2011).

[33] T. Chou and G. Lakatos, *Clustered Bottlenecks in mRNA Translation and Protein Synthesis*, Phys. Rev. Lett. **93**, 198101 (2004).

[34] Note that in the macroscopic limit, x becomes a continuous variable and the lattice is treated as a continuum.

[35] E. Seneta, *Non-negative Matrices and Markov Chains* (Springer Science & Business Media, Berlin, 2006).

[36] M. J. Lighthill and G. B. Whitham, *On Kinematic Waves. II. A Theory of Traffic Flow on Long Crowded Roads*, Proc. R. Soc. A **229**, 317 (1955).

[37] J. Krug, *Boundary-Induced Phase Transitions in Driven Diffusive Systems*, Phys. Rev. Lett. **67**, 1882 (1991).

[38] V. Popkov and G. M. Schütz, *Steady-State Selection in Driven Diffusive Systems with Open Boundaries*, Europhys. Lett. **48**, 257 (1999).

[39] R. A. Blythe and M. R. Evans, *Nonequilibrium Steady States of Matrix Product Form: A Solver's Guide*, J. Phys. A **40**, R333 (2007).

[40] J. Hager, J. Krug, V. Popkov, and G. Schütz, *Minimal Current Phase and Universal Boundary Layers in Driven Diffusive Systems*, Phys. Rev. E **63**, 056110 (2001).

[41] A. Melbinger, L. Reese, and E. Frey, *Microtubule Length-Regulation by Molecular Motors*, Phys. Rev. Lett. **108**, 258104 (2012).
[42] V. Popkov and G. M. Schütz, *Shocks and Excitation Dynamics in a Driven Diffusive Two-Channel System*, J. Stat. Phys. **112**, 523 (2003).
[43] E. Pronina and A. B. Kolomeisky, *Two-Channel Totally Asymmetric Simple Exclusion Processes*, J. Phys. A **37**, 9907 (2004).
[44] M. R. Evans, Y. Kafri, K. E. P. Sugden, and J. Tailleur, *Phase Diagram of Two-Lane Driven Diffusive Systems*, J. Stat. Mech. (2011) P06009.
[45] J. Brankov, N. Pesheva, and N. Bunzarova, *Totally Asymmetric Exclusion Process on Chains with a Double-Chain Section in the Middle: Computer Simulations and a Simple Theory*, Phys. Rev. E **69**, 066128 (2004).
[46] E. Pronina and A. B. Kolomeisky, *Theoretical Investigation of Totally Asymmetric Exclusion Processes on Lattices with Junctions*, J. Stat. Mech. (2005) P07010.
[47] R. Wang, M. Liu, and R. Jiang, *Theoretical Investigation of Synchronous Totally Asymmetric Exclusion Processes on Lattices with Multiple-Input-Single-Output Junctions*, Phys. Rev. E **77**, 051108 (2008).
[48] M. Liu and R. Wang, *Asymmetric Exclusion Processes on m-Input n-Output Junctions with Parallel Update*, Physica (Amsterdam) **388A**, 4068 (2009).
[49] B. Embley, A. Parmeggiani, and N. Kern, *Understanding Totally Asymmetric Simple-Exclusion-Process Transport on Networks: Generic Analysis via Effective Rates and Explicit Vertices*, Phys. Rev. E **80**, 041128 (2009).
[50] H. J. Hilhorst and C. Appert-Rolland, *A Multi-lane TASEP Model for Crossing Pedestrian Traffic Flows*, J. Stat. Mech. (2012) P06009.
[51] Z. J. Ding, R. Jiang, and B. H. Wang, *Traffic Flow in the Biham-Middleton-Levine Model with Random Update Rule*, Phys. Rev. E **83**, 047101 (2011).
[52] S. Klumpp, T. M. Nieuwenhuizen, and R. Lipowsky, *Self-Organized Density Patterns of Molecular Motors in Arrays of Cytoskeletal Filaments*, Biophys. J. **88**, 3118 (2005).
[53] B. Embley, A. Parmeggiani, and N. Kern, *HEX-TASEP: Dynamics of Pinned Domains for TASEP Transport on a Periodic Lattice of Hexagonal Topology*, J. Phys. Condens. Matter **20**, 295213 (2008).
[54] I. Neri, N. Kern, and A. Parmeggiani, *Totally Asymmetric Simple Exclusion Process on Networks*, Phys. Rev. Lett. **107**, 068702 (2011).
[55] T. Ezaki and K. Nishinari, *A Balance Network for the Asymmetric Simple Exclusion Process*, J. Stat. Mech. (2012) P11002.
[56] I. Neri, N. Kern, and A. Parmeggiani, *Modeling Cytoskeletal Traffic: An Interplay between Passive Diffusion and Active Transport*, Phys. Rev. Lett. **110**, 098102 (2013).
[57] M. R. Evans, D. P. Foster, C. Godrèche, and D. Mukamel, *Asymmetric Exclusion Model with Two Species: Spontaneous Symmetry Breaking*, J. Stat. Phys. **80**, 69 (1995).
[58] G. M. Schütz, *Critical Phenomena and Universal Dynamics in One-Dimensional Driven Diffusive Systems with Two Species of Particles*, J. Phys. A **36**, R339 (2003).
[59] S. Klumpp and R. Lipowsky, *Phase Transitions in Systems with Two Species of Molecular Motors*, Europhys. Lett. **66**, 90 (2004).
[60] R. Juhász, *Weakly Coupled, Antiparallel, Totally Asymmetric Simple Exclusion Processes*, Phys. Rev. E **76**, 021117 (2007).
[61] S. Prolhac, M. R. Evans, and K. Mallick, *The Matrix Product Solution of the Multispecies Partially Asymmetric Exclusion Process*, J. Phys. A **42**, 165004 (2009).
[62] D. Johann, D. Goswami, and K. Kruse, *Segregation of Diffusible and Directionally Moving Particles on a Polar Filament*, Phys. Rev. E **89**, 042713 (2014).
[63] It is possible to get from any arbitrary state to another arbitrary state in a finite number of steps by letting the system run empty and filling it with the respective configuration.
[64] T. M. Liggett, *Continuous Time Markov Processes: An Introduction* (American Mathematical Society, Providence, 2010).
[65] D. T. Gillespie, *Stochastic Simulation of Chemical Kinetics*, Annu. Rev. Phys. Chem. **58**, 35 (2007).
[66] We can renumber the lane indices j at position i as $j \to j - (i \bmod W)$. This leads to a system with dynamical rules as in the original system, where lane-switching particles now track lanes and vice versa.
[67] O. Biham, A. A. Middleton, and D. Levine, *Self-Organization and a Dynamical Transition in Traffic-Flow Models*, Phys. Rev. A **46**, R6124 (1992).
[68] O. Angel and J. B. Martin, *The Jammed Phase of the Biham-Middleton-Levine Traffic Model*, Electron. Commun. Probab. **10**, 167 (2005).
[69] Because of Eq. (10) and the spatially constant current, spatial variations of the hindrance function are directly related to those of the density profile.
[70] In principle, the current itself can be used for an expansion in the density, but since we are specifically interested in the influence of topological hindrance, the hindrance function H is chosen.
[71] In general, we may expect the current-density relation to be smooth, which leads to additional constraints. However, higher-order expansions would not allow one to obtain a closed analytic solution for the expansion coefficients. Since a second-order approximation of the hindrance function is sufficient to find a meaningful result, we do not provide numeric approximations for higher orders.
[72] There is actually an additional phase at an out rate of strictly zero. This phase has no counterpart in the TASEP and is discussed in detail in Appendix A.
[73] E. Reithmann, L. Reese, and E. Frey, *Nonequilibrium Diffusion and Capture Mechanism Ensures Tip Localization of Regulating Proteins on Dynamic Filaments*, Phys. Rev. Lett. **117**, 078102 (2016).
[74] I. R. Graf and E. Frey, *Generic Transport Mechanisms for Molecular Traffic in Cellular Protrusions*, Phys. Rev. Lett. **118**, 128101 (2017).
[75] I. Pinkoviezky and N. S. Gov, *Exclusion and Hierarchy of Time Scales Lead to Spatial Segregation of Molecular Motors in Cellular Protrusions*, Phys. Rev. Lett. **118**, 018102 (2017).

[76] G. Lakatos, J. O'Brien, and T. Chou, *Hydrodynamic Mean Field Solutions of 1D Exclusion Processes with Spatially Varying Hopping Rates*, J. Phys. A **39**, 2253 (2006).

[77] A. Parmeggiani, T. Franosch, and E. Frey, *Phase Coexistence in Driven One-Dimensional Transport*, Phys. Rev. Lett. **90**, 086601 (2003).

[78] A. Parmeggiani, T. Franosch, and E. Frey, *Totally Asymmetric Simple Exclusion Process with Langmuir Kinetics*, Phys. Rev. E **70**, 046101 (2004).

[79] P. Pierobon, E. Frey, and T. Franosch, *Driven Lattice Gas of Dimers Coupled to a Bulk Reservoir*, Phys. Rev. E **74**, 031920 (2006).

[80] For example, the dynamics of the system may be dominated by the bulk instead of just either of the two boundaries.

[81] S. P. Maurer, N. I. Cade, G. Bohner, N. Gustafsson, T. Boutant, and E. Surrey, *EB1 Accelerates Two Conformational Transitions Important for Microtubule Maturation and Dynamics*, Curr. Biol. **24**, 372 (2014).

[82] M. Bugiel, A. Mitra, S. Girardo, S. Diez, and E. Schäffer, *Measuring Microtubule Supertwist and Defects by Three-Dimensional-Force-Clamp Tracking of Single Kinesin-1 Motors*, Nano Lett. **18**, 1290 (2018).

[83] A. J. Liu and S. R. Nagel, *Jamming and Rheology: Constrained Dynamics on Microscopic and Macroscopic Scales* (CRC Press, Boca Raton, 2001).

[84] A. S. de Wijn, D. M. Miedema, B. Nienhuis, and P. Schall, *Criticality in Dynamic Arrest: Correspondence between Glasses and Traffic*, Phys. Rev. Lett. **109**, 228001 (2012).

[85] C. P. Goodrich, A. J. Liu, and S. R. Nagel, *Solids between the Mechanical Extremes of Order and Disorder*, Nat. Phys. **10**, 578 (2014).

[86] A. J. Liu and S. R. Nagel, *The Jamming Transition and the Marginally Jammed Solid*, Annu. Rev. Condens. Matter Phys. **1**, 347 (2010).

[87] A. J. Liu and S. R. Nagel, *Nonlinear Dynamics: Jamming Is Not Just Cool Any More*, Nature (London) **396**, 21 (1998).

[88] P. Winkler, *Mathematical Puzzles: A Connoisseur's Collection* (AK Peters, Natick, 2004).

[89] P. Winkler, *Mathematical Mind-Benders* (CRC Press, Boca Raton, 2007).

[90] Note that the site index μ was kept here mainly to keep track of the correct form of correlations between sites and lanes rather than due to a rapid spatial change of correlations or densities.

2.3 Directional reversal of the collective motion of kinesins

This section deals with a remarkable phenomenon regarding the motion of several kinesins: directional reversal. Triggered by various experimental factors, multiple molecular motors have been shown to reverse their direction of motion. The underlying biomolecular mechanisms, however, have remained obscure. In this project, we used statistical analyses and theoretical modeling to address directional switching of the motion of molecular motors that is caused by a clustering of these molecules. The key result of this work is a novel model for the directional reversal of kinesins. The proposed mechanism relies on the assumption that forces that antagonize the movement of kinesins have an anisotropic impact on the stepping behavior of the molecular motors. Our analysis based on experiments of our collaborators on this project, the group of Prof. Leah Gheber, and theoretical modeling unraveled biomolecular interactions between the molecular motors and showed that the proposed mechanism for a directional switch accurately reproduced experimental observations. Strikingly, our proposed mechanism for directional reversal of the motion of kinesins unifies previous unrelated findings and hypotheses on how the directionality of kinesins can be affected. In fact, our work shows that the different known ways of how the directionality of the motion of molecular motors can be changed may be different aspects of the same mechanism: An anisotropic response of active motion to opposing forces. The work was performed in collaboration with Prof. Leah Gheber's group at the Ben-Gurion University of the Negev. All experimental data were recorded by Prof. Leah Gheber's group and, in particular, by Dr. Himanshu Pandey. This project is currently prepared for publication in a peer-reviewed journal [1].

2.3.1 Background

Thus far, we have already discussed two examples where the distribution of molecular motors along a microtubule has significant effects on the functionality of cellular processes: For regulating proteins that diffuse along the microtubule, we showed that a capture mechanism elucidated in Section 2.1 ensures their efficient localization and thereby contributes substantially to their functionality. For helically moving kinesins, as discussed in Section 2.2, topological effects lead to self-organization

into patterns which decrease transport efficiency. Here, we turn to another class of molecular motors that are crucial for cellular processes: kinesin-5 motors. In most eukaryotic cells, ranging from yeast to humans cells, this class of kinesins is essential to establish and maintain a bipolar mitotic spindle during cell division [142–144]. Kinesin-5 motors are tetrameric molecules with a length of approximately 80 nm, that can simultaneously bind and thus crosslink two microtubules [145, 146]. This process is essential since kinesin-5 motors have been shown to slide apart antiparallel microtubule pairs [147, 148], which is thought to be one of the main biomechanical reasons for the bipolarity of the mitotic spindle.

One intensely studied subclass of kinesin-5 motors are the corresponding members in yeast, of which budding yeast's Cin8 may well be the most prominent one. *In vivo*, Cin8 fulfills an important role in spindle assembly and kinetochore positioning [149–152]. Despite the simplicity of the organism, Cin8 and several other kinesin-5 motors of yeast show characteristics in their motion that are absent in their more evolved homologs present in higher organisms: While the fundamental model for kinesin motion was long thought to be a walking mechanism towards the plus end of microtubules [101, 108–110], Cin8 and other kinesin-5 motors in yeast don't follow this scheme of motility. Indeed, opposed to the motion of most kinesins [142, 153], Cin8 has been shown to move processively towards minus ends of microtubules in single-molecule assays [154]. Even more strikingly, several studies have unraveled another surprising feature of Cin8 and other similar kinesin-like motors: The ability to switch directionality in response to the change of several experimental and biomolecular conditions. Up to now, directional switching has been reported for three kinesin-5 motors in yeast (Cin8 [154, 155] and Kip1 [156] of budding yeast, as well as Cut7 [157, 158] of fission yeast) as well as for the kinesin-14 KlpA [159]. In all cases, the directionality of motion of the molecules can be converted between minus-end-directed and plus-end-directed motion upon varying experimental factors. While this directional switching is by now a well-established phenomenon that has been addressed in a multitude of studies, it still leaves many open questions. So far, its biomolecular origin is unknown and also its potential contribution to cellular processes *in vivo* remains to be understood. One particularly puzzling fact is that directional switching is triggered by varying different apparently unrelated experimental conditions that bear no obvious similarity to each other. To provide an overview of the multiple observations and seemingly contradictory corresponding models for a directional switching, we briefly summarize the different experimental findings.

Directional switching of the motion of kinesins was first observed for Cin8 in motility/gliding assays [154]. In these experiments, a microtubule is propelled over a surface that was coated with kinesins. Depending on the surface density of Cin8, microtubules were observed to be either driven with their plus end leading (low surface densities) or with their minus end leading (high surface densities). Moreover, the study reported a weak dependence on the length of microtubules. In detail, short

microtubules were gliding faster than longer microtubules at low motor densities. Therefore, it was hypothesized that directional switching depends also on the length of the microtubule and not only on the surface density. The authors of this study, therefore, concluded that it might be the number of molecular motors engaged with the microtubule or—in other words—the coupling of motors to a microtubule that triggers Cin8's directional switching. Shortly after the observation of the directional switching of Cin8 in gliding assays, Gerson-Gurwitz et al. [155] reported that directional switching of Cin8 could also be triggered for individual motors and without collective binding to a microtubule: Upon varying the ionic strength of the buffer, single molecules of Cin8 changed directionality from minus-end-directed motion (high ionic strength) to plus-end-directed motion (low ionic strength). However, also changes in the molecular structure affected Cin8's directionality. Similar observations have recently been made for another yeast kinesin-5: fission yeast's Cut7 [158]. Analogous to the gliding assays with Cin8, also gliding assays with Cut7 exhibited a directional switching when the surface density of motors was modified. Additionally, changing the salt concentration of the buffer in the gliding assays affected directionality as well: The movement of gliding microtubules could be converted back and forth between minus-end and plus-end directed motion by varying the ionic strength of the solution in the same experimental setup. Interestingly, directionality could also be changed when adding minus directed non-Cut7 motors (Klp2) to the surface and even by adding a non-motile microtubule linker (dynein microtubule binding domain). This led the authors of this study to conclude that, eventually, it is the density of molecules in general that reverses Cut7's directionality due to steric clashes between neighboring motors. Even further complexity entered the field of kinesin's directional reversal recently with yet another way how the directionality of Cin8 can be affected. In single-molecule measurements, Shapira et al. [160] observed the ability of Cin8 to form aggregates of a few molecules (clusters) while moving on a microtubule. Strikingly, these clusters showed a tendency to move towards the plus end while—on the same microtubule—other individual Cin8 molecules still showed a tendency to move towards the minus end of the microtubule. Similar behavior was also found for the kinesin-14 KlpA [159]. Finally, it should be noted that a recent study also addressed the stall force of Cin8 [161]. While it was not possible to measure forces for a single Cin8 molecule attached to a bead, the study used novel force spectroscopy and correlation analysis methods to identify force pulses on stalled microtubules in a Cin8-based gliding assay. In this way, the authors could show that Cin8 produces forces in the plus- and minus direction with a similar stall force of approximately 1.5 pN.

In summary, the directionality of several kinesin-5's in yeast and a kinesin-14 can be switched by different factors: (a) In gliding assays, by changing the surface density of molecular motors. (b) By changing the ionic strength of the buffer. (c) By clustering of particles. A connection between these observations or even a concise

picture of the directional reversal of kinesins remained, however, elusive. To address this issue, we focused on the clustering behavior of budding yeast's Cin8. Based on a quantitative analysis of the dynamics of Cin8 clusters as observed in the experiments of our collaborators together with theoretical modeling we propose a new model for directional switching. Strikingly, our proposed model unifies previous results and thereby provides a consistent picture of kinesin's directional reversal.

2.3.2 Quantifying the motility of clusters of Cin8 particles

To study the motility of Cin8, our collaborators analyzed data from single-molecule experiments where they tracked Cin8 particles and clusters of particles using total internal reflection fluorescence microscopy. Fig 2.10 (a) shows kymographs (space-time plots) of the motion of Cin8 along different microtubules. In accordance with previous findings [154], single Cin8 particles (faint traces) showed a tendency to move processively towards the minus end of the microtubule. Moreover, these traces were also characterized by notable randomness which may indicate a diffusive component of motion. In addition to the faint traces of particles that moved—on average—towards the minus ends, the kymographs exhibited traces of particles with increased intensity that showed a tendency to move towards the plus ends. These observations agree with previous measurements [160] and indicate that Cin8 forms clusters consisting of multiple particles that exhibit a different motility than single Cin8 particles. To understand Cin8 clustering, we first inferred the number of particles in each individual cluster. This identification was possible due to photobleaching of individual GFP molecules as illustrated in Fig. 2.10 (b). The temporal evolution of the intensity of different trajectories showed discrete bleaching events of single GFPs. In this way, it was possible to identify the average intensity of a single Cin8 particle and, consequently, to infer the expected number of particles per diffraction-limited spot. This approach was further supported by the distribution of the intensities of all signals observed at a given time in the experiment: Fig. 2.10(c) shows the distribution of intensities that were measured in the first frame of a recording of the single-molecule experiment. In accordance with the previous identification of the intensity of an individual Cin8 particle, the distribution showed maxima at multiples of this value. Therefore, the intensity distribution of the experiments strongly suggested that many signals corresponded to aggregates of Cin8 molecules.

In the next step, our collaborators analyzed the motility of individual signals by analyzing the signal traces. In detail, the average velocity of each signal was related to its intensity which, in turn, correlates with the expected number of Cin8 particles that contribute to the respective signal. Fig. 2.11 shows the observed particle intensities and average velocities of different trajectories. While the majority (70%) of minus-end-directed traces corresponded to intensities of monomeric Cin8, the majority (approximately 88%) of plus-end-directed traces was likely to represent clusters of

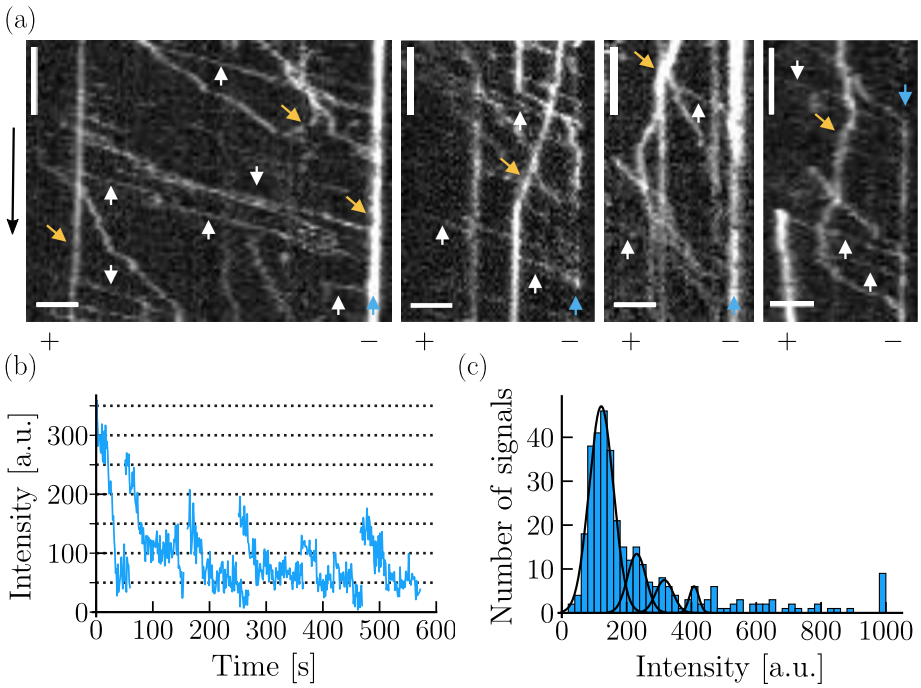

Figure 2.10 Representative kymographs (space-time plots) of motion of Cin8 observed in single-molecule experiments using total internal reflection fluorescence microscopy. **(a)** Single molecules (faint traces) typically exhibited rapid motion towards the minus end (white arrows). Motion towards the plus end (yellow arrows) was observed as well, typically for traces that showed an intense signal (bright traces) which, in turn, suggests that these traces corresponded to clusters of Cin8 molecules. Blue arrows indicate clustering of Cin8 at the minus end of the microtubule. Scale bars correspond to 20 s (vertical scale bars) and 2 µm (horizontal scale bars). Plus and minus signs denote the respective microtubule end. The black arrow denotes the direction of time. **(b)** The temporal evolution of the intensity of several signals (six traces aligned next to each other) showed discrete steps because of photo bleaching. The size of these steps showed an approximate size of 50 arbitrary units (a.u.), which likely corresponded to the bleaching of a single GFP molecule. The two leftmost traces likely show the bleaching of dimeric Cin8 clusters (two tetramers with eight GFP molecules) while the remaining four traces likely represent signals of a single Cin8 tetramer (four GFP molecules). **(c)** Intensity distribution of all signals in the first frame of a time-lapse sequence. The first peak in the distribution of intensities is centered at approximately 100 a.u. which is in accordance with the average intensity of a Cin8 tetramer with four GFP molecules where each GFP contributed approximately 50 a.u.. Other peaks are centered at approximately 200 a.u., 300 a.u., and 400 a.u., which likely corresponded to Cin8 clusters with two, three, or four Cin8 molecules, respectively. Solid lines represent fits of Gaussians to the respective intensity peaks. All experimental data were produced and analyzed by Prof. Leah Gheber's group.

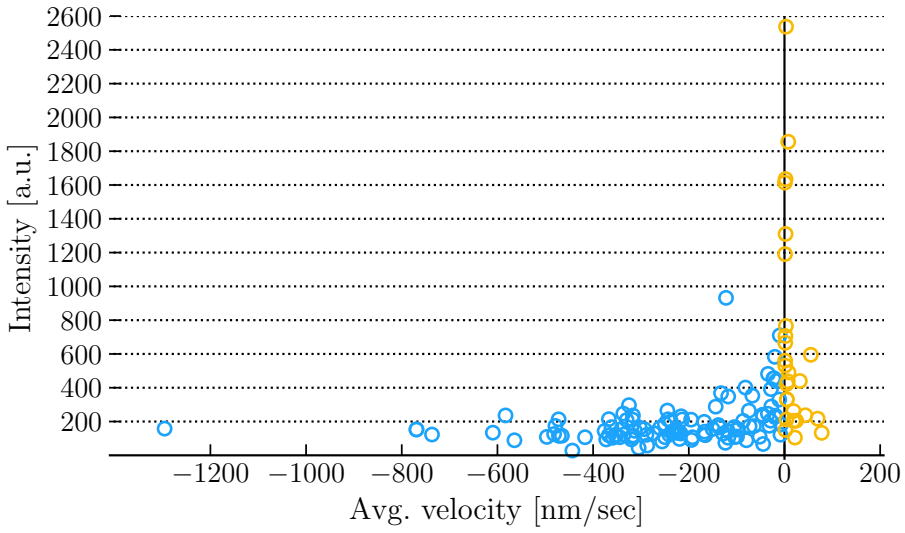

Figure 2.11 Intensity and average velocity of different trajectories of particles and clusters recorded in experiments where the motion of signals was tracked over time. The plot shows a total of $n = 134$ traces of which $n_{\text{minus}} = 107$ were minus-end-directed (blue circles) and $n_{\text{plus}} = 27$ were plus-end directed (orange circles). Approximately 70% of the minus-end-directed traces were monomers. In contrast, the majority (approximately 88%) of plus-end-directed traces corresponded to clusters of more than two tetramers of Cin8. For this estimate, a threshold value of 200 arbitrary units (a.u.) was used to approximately discriminate between single particles and clusters. All experimental data were produced by Prof. Leah Gheber's group.

Cin8. Thus, the experimental data showed that particle clustering correlates with Cin8's directional reversal.

To quantitatively characterize the motility of individual Cin8 particles and particle clusters our collaborators then categorized the different trajectories according to three classes: single particles, dimeric clusters and particle clusters that contained more than two particles. Since clusters with more than two particles were only observed rarely, a further subdivision of clusters with more than two particles was not performed. For each of the classes, our collaborators then performed a displacement analysis of trajectories as shown in Fig. 2.12. Although not all clusters showed reversed motion, there was a clear trend of particle clusters to move towards the plus end whereas single particles had a clear trend to move towards the minus end. Based on the measured tracks and intensities of signals, our collaborators computed the mean squared displacement (MSD) and the mean displacement (MD) for the three categories. In this way, it was possible to obtain the average drift velocity v and the diffusion coefficient D of the particles' motion. Whereas the drift velocity has to arise due to

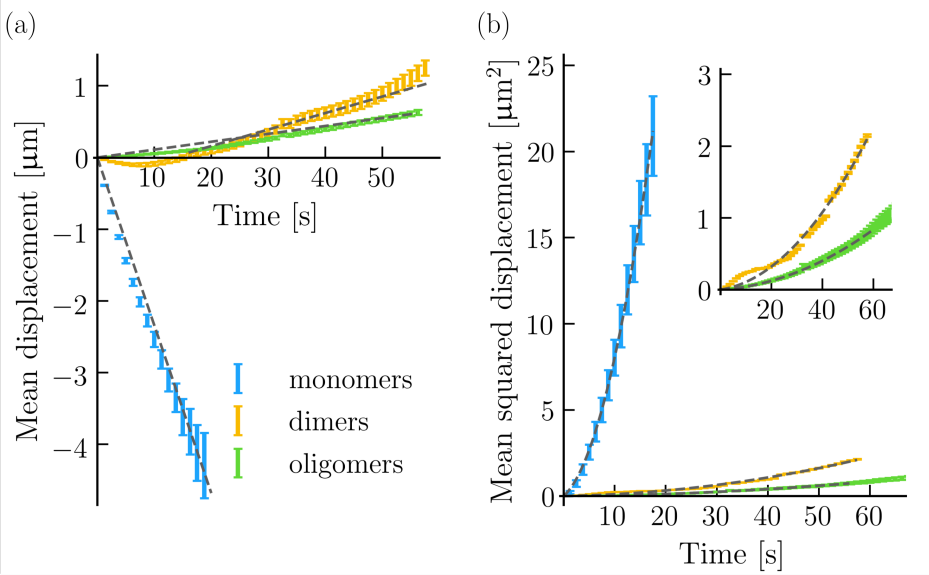

Figure 2.12 Analysis of the mean displacement and the mean squared displacement of single Cin8 particles as well as clusters with two Cin8 particles and clusters with more than two Cin8 particles. **(a)** Mean displacement (MD) for different times as obtained by an ensemble average of trajectories measured in single-molecule experiments that allowed for the tracking of individual Cin8 particles and clusters of Cin8 particles. The data show that single Cin8 particles (monomers, blue) move—on average—fast towards the minus end while clusters of two Cin8 particles (dimers, orange) and more than two Cin8 particles (oligomers, green) moved—on average—slowly towards the plus end. **(b)** Mean squared displacement (MSD) of the same trajectories as in (a) plotted against time. Data show the MSD of individual particles (blue), dimeric clusters of particles (orange), and clusters with more than two particles (green). Dashed lines represent statistical weighted linear (for MD: $\langle x(t)\rangle = v_{\mathrm{MD}} \cdot t$) or quadratic fits (for MSD: $\langle x(t)^2\rangle = v_{\mathrm{MSD}}^2 \cdot t^2 + 2D_{\mathrm{MSD}} \cdot t$) to the experimental data. The inset in (b) shows the magnified MSD of clusters with two Cin8 molecules and clusters with more than two Cin8 molecules for a better illustration. The bars show the standard error of the mean. Note that the displacement of dimeric clusters shows a different evolution over approximately the first 16 s. This is likely the impact of individual particles that are mistakenly categorized as dimeric clusters (average dwell time of monomers corresponds to 16 s). Experiments were performed at 1 mM ATP. All experimental data were produced by Prof. Leah Gheber's group.

active forces, it is important to note that the diffusion coefficient in this analysis doesn't necessarily reflect passive diffusive motion but may also originate from bidirectional active motion. The results of the displacement analysis are summarized in Fig. 2.12 and Table 2.1. This statistical analysis of ensembles of trajectories quantitatively confirmed the picture already suggested by the kymographs and the statistical analysis of individual trajectories as shown in Fig. 2.11: While single particles moved—on average—towards the minus end, particle clusters moved—on average—towards the

1 mM ATP	v_{MD} [nm/s]	v_{MSD} [nm/s]	D_{MSD} [10^3 nm^2/s]
Single Cin8 particles	-234 ± 7.7	229 ± 66	102 ± 11
Dimeric Cin8 cluster	23 ± 0.7	31 ±6	5.1 ± 0.4
Oligomeric Cin8 clusters	11 ± 0.2	14 ± 2	1.1 ± 0.1

Table 2.1 Summary of the drift velocities and diffusion coefficients for the three categories of cluster sizes obtained from the displacement analysis. Values were obtained by fitting the linear function $\langle x(t)\rangle = v_{MD} \cdot t$ to the temporal evolution of the MD and the quadratic function $\langle x(t)^2\rangle = v_{MSD}^2 \cdot t^2 + 2D_{MSD} \cdot t$ to the temporal evolution of the MSD, where $x(t)$ denotes the position of the respective particles at time t on the microtubule and angle brackets refer to an ensemble average over different traces. Oligomeric clusters denote clusters with more than two Cin8 particles. All experimental data were produced and analyzed by Prof. Leah Gheber's group.

plus end. The analysis further revealed three important characteristics of the motility of Cin8: First, clusters with two Cin8 molecules moved approximately ten-fold slower than individual Cin8 molecules. Second, single Cin8 molecules showed a large diffusive component of approximately 0.1 µm/s. Third, the diffusion coefficient of clusters of Cin8 molecules was two orders of magnitude smaller than that of individual Cin8 motors. A valuable quantity that is often used to characterize kinesin motion is the randomness of motion r or—equivalently—the Fano factor [162]. It is defined as

$$r = \lim_{t\to\infty} \frac{\langle (x(t) - \langle x(t)\rangle)^2)\rangle}{a\langle x(t)\rangle}. \tag{2.2}$$

The randomness characterizes stochasticity during the translocation of a molecule. For example, for unidirectional but stochastic motion with a single stochastic transition in each step of translocation we find $r = 1$ [162]. For Cin8, the displacement analysis revealed a significant randomness of motion with a value of approximately $r = 100$. This value is much higher than that expected for unidirectionally stepping kinesins: For kinesin-1, experiments yielded a typical value between $r = 0.3$ and $r = 1$ [162–164]. While it is hard to unravel the exact reason for this discrepancy, it nevertheless shows that the motion of Cin8 adopts a statistical signature that is very different to that of unidirectionally moving kinesins. Reasons for this behavior might be Cin8's bidirectional motion that is either caused by active motion in both directions, passive diffusion, or both.

To assess the role of active motion for the formation of clusters and for the motility of clusters, our collaborators further varied the ATP concentration and performed experiments with ADP. Results are summarized in Table 2.2. The key observation was that clusters also formed at low ATP and ADP concentrations, which indicates that active motion is not a critical prerequisite for the formation of clusters. Moreover,

7.5 μM ATP	v_{MD} [nm/s]	v_{MSD} [nm/s]	D_{MSD} [10^3nm^2/s]
Single Cin8 particles	-70 ± 3	54 ± 21	31 ± 2
Dimeric Cin8 cluster	-33 ± 0.9	35 ±9	15 ± 1
Oligomeric Cin8 clusters	-34 ±1.1	34 ± 7	4.7± 1
ADP	v_{MD} [nm/s]	v_{MSD} [nm/s]	D_{MSD} [10^3nm^2/s]
Single Cin8 particles	-	-	10 ± 0.1
Dimeric Cin8 cluster	-	-	7 ± 0.3
Oligomeric Cin8 clusters	-	-	n.a.

Table 2.2 Summary of the drift velocities and diffusion coefficients for the three categories of cluster sizes obtained from the displacement analysis of experiments at low ATP concentrations and in the presence of ADP. Values were obtained by fitting the linear function $\langle x(t)\rangle = v_{MD} \cdot t$ to the temporal evolution of the MD and the quadratic function $\langle x(t)^2\rangle = v_{MSD}^2 \cdot t^2 + 2D_{MSD} \cdot t$ to the temporal evolution of the MSD, where $x(t)$ denotes the position of the respective particles at time t on the microtubule and angle brackets refer to an ensemble average over different traces. For the experiments with ADP no directed motion was observed. Higher oligomers were not analyzed due to the small number of signals in that category. All experimental data were produced and analyzed by Prof. Leah Gheber's group.

decreasing ATP concentrations lowered the drift velocities as well as the diffusion coefficients of individual Cin8 molecules and clusters. While an ATP-dependent decrease of the diffusion coefficient may indicate the contribution of bidirectional stepping to the overall motility of Cin8, a clear statement is not possible since also the dwell times of Cin8 particles and clusters differed when changing the ATP concentration or when using ADP. These different dwell times might indicate different affinities of Cin8 for the microtubule when changing the ATP concentration. As different affinities can, however, lead to a different drag that a motor experiences in its motion along the microtubule, the observed decrease of the diffusion coefficient might also stem from different affinities.

2.3.3 Cin8 motors are subject to weak attractive interactions that reduce the diffusivity of clusters

The detailed quantification of Cin8's motile behavior as an individual molecule and in clusters left several open questions: Foremost, why did clusters move—on average—in the opposite direction than individual Cin8 molecules? Second, why was the diffusive component of the motion of clusters of Cin8 particles two orders of magnitude lower than that of individual particles? We will begin our quantitative analysis by focusing on the latter question.

To address the significantly lowered diffusion coefficient of particle clusters, we first analyzed the statistics of the motion of single Cin8 molecules. The two quantities identified in the mean squared displacement analysis were the average drift velocity and the diffusive component of particle motion. While the average particle drift has to arise due to active forces, the origin of a diffusive component is more intricate. It is important to note that the diffusion coefficient that is identified by the mean squared displacement analysis doesn't necessarily reflect passive, thermal forces but, very generally, reflects the variance and therefore randomness of motion. To interpret the drift and diffusion coefficients, we related these values to stochastic translocation events of single Cin8 particles or clusters along the microtubule. It is reasonable to assume that particles are subject to a periodic binding potential where the periodicity is given by the size of a tubulin dimer. Then, the translocation of particles corresponds to stochastic hopping events over a distance of $a = 8.4\,\mathrm{nm}$, which is the approximate size of a tubulin dimer [165]. The variance, and thus diffusivity, of a displacement due to such a discrete, stochastic motion is affected by two factors: First, by the temporal stochasticity of the hopping events and, second, by the number of stochastic reactions that are required to effectively translocate a particle (or cluster). Intuitively, it should be clear that, for example, steps in opposing directions increase the effective diffusivity. This is because, in such a scenario, more stochastic substeps are required to displace a particle than are required for the same net displacement based on unidirectional motion. In other words, the same overall displacement is more random for bidirectional than for unidirectional motion. Importantly, the drift and diffusion coefficients determined by the displacement analysis detailed in Section 2.3.2 allowed us to specifically compute the stochastic rates m^{single} and p^{single} at which a single Cin8 particle transitions to a binding site in the plus-end and in the minus-end direction, respectively. In detail, the diffusion coefficient and average drift velocity of the particle are related to these rates via

$$v^{\mathrm{single}} = a\,(p^{\mathrm{single}} - m^{\mathrm{single}}) \tag{2.3a}$$

$$D^{\mathrm{single}} = \frac{1}{2}\,a^2\,(p^{\mathrm{single}} + m^{\mathrm{single}}). \tag{2.3b}$$

Inserting the values of the mean displacement and diffusion coefficient of single particles as listed in Table 2.1 results in the following transition rates: $m^{\mathrm{single}} = 1460\,\mathrm{s}^{-1}$ and $p^{\mathrm{single}} = 1432\,\mathrm{s}^{-1}$. Hence, the statistics of motion of single Cin8 particles shows clear statistical traces of bidirectional motility. Indeed, most of Cin8's motion does not lead to a net displacement along the filament but cancels on average. The reason for this behavior may either be passive diffusive motion, active stepping in both directions, or a combination of these processes. To determine which of these possibilities is most likely it is helpful to consider the maximal stepping rate of kinesins: At saturating ATP concentrations, kinesin-1 exhibits a maximal velocity of approximately $v_{\mathrm{max}} \approx$

0.9 µm/s [164, 166]. Since kinesin-1 hydrolyzes one ATP molecule per step [167, 168], the maximal ATP turnover rate therefore equals approximately 110 ATP molecules per second. As ATP associates with the motor domain of kinesins—an amino acid sequence of the protein that is highly conserved among different species [52]—it is plausible to assume a similar rate of ATP turnover for Cin8. We can thus use the maximal rate of ATP turnover of kinesin-1 to estimate the maximal plausible contribution of ATP-driven bidirectional stepping to the diffusion coefficient of an individual Cin8 particle. In detail, if we consider the case where each ATP hydrolysis is coupled to a 8.4 nm step in either direction with equal probability, the turnover frequency of kinesin-1 would only lead to a diffusion coefficient of approximately 0.004 $\mu m^2/s$. This value is two orders of magnitude smaller than the corresponding value determined experimentally for Cin8. On the other hand, 0.1 $\mu m^2/s$ is a very typical value for the diffusion coefficient of proteins that diffuse passively along the microtubule [72–74] (see also Section 2.1). Therefore, the most likely explanation of the large diffusion coefficient of the motion of individual Cin8 particles is passive diffusion. That being said, it should also be stressed that a dominating component due to passive forces doesn't imply that (bidirectional) active stepping doesn't contribute to the diffusion coefficient of individual particles, but only that the corresponding contribution is small. In summary, the displacement analysis suggests that the largest component of Cin8's motion is likely due to passive diffusive motion. On top of this passive motion, active stepping in either one or both directions adds, but contributes probably only to a small degree to the randomness of motion.

Having addressed the large diffusive component in the motion of single particles, we now turn towards the statistics of the motion of clusters. One plausible candidate to cause the large discrepancy between the diffusion coefficient of clusters and that of individual molecules are weak attractive forces between the motors. Such forces may not only cause the clustering itself but also affect their motion. In order to gain a quantitative understanding of the impact of attractive forces on the motion of particle clusters we considered a first model for the collective dynamics of Cin8 along microtubules as the first step of our analysis. Our previous analyses for individual Cin8 particles suggest that Cin8's dominating mode of motion is passive diffusion. This finding motivated us to address the reduced diffusivity of clusters in an equilibrium model that disregards active motion of particles and, consequently, also Cin8's directional reversal for the moment.[12] The equilibrium model was defined as follows: Motion of Cin8 was described as discrete hopping events of particles on a lattice that represents the microtubule.[13] As before, the lattice spacing a is given by the size of a tubulin dimer, $a = 8.4$ nm [165]. On the lattice, particles excluded each other to account for steric interactions. In the equilibrium model, motion was not

12 In Section 2.3.4, we complement this equilibrium model by active motion.

13 For simplicity and because of Cin8's comparably large size of 80 nm we did not discriminate between motion along different protofilaments.

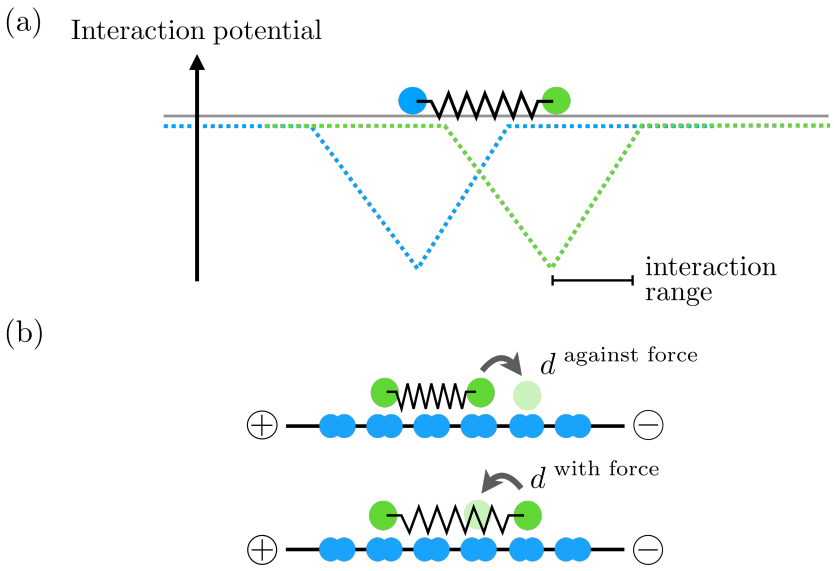

Figure 2.13 Illustration of the equilibrium model for the collective motion of Cin8 particles. Particles moved on a one dimensional lattice that represents the microtubule and interact via exclusion and weak attractive forces (schematically illustrated by a spring). **(a)** The interaction of particles was modeled as a constant force or—equivalently—a linearly decreasing interaction potential for distances smaller than a specific interaction range. **(b)** For interacting particles, the attractive force affected the rates to move to neighboring lattice sites. The rate $d^{\text{against force}}$ to move against the force that arises from an interaction with another particle is related to the reverse rate $d^{\text{with force}}$ (motion in the direction of the force) by a Boltzmann factor: $d^{\text{against force}}/d^{\text{with force}} = \exp(-\beta\Delta E) =: \delta$, where ΔE is the difference of energy associated with moving the particles further apart over a distance $a = 8.4$ nm [165]. Moreover, $\beta = 1/\mathrm{k}T$ with T being the temperature and k the Boltzmann constant. In the model, we only implemented nearest-neighbor interactions. Note that forces are illustrated schematically by springs although we assumed constant forces for interacting particles.

biased but thought to originate from passive diffusive motion. Thus, hopping to the neighboring lattice site on the right (towards the minus end) and to the neighboring lattice site on the left (towards the plus end) for non-interacting particles occurred at equal rates d_0, given that the respective target site was vacant. In addition, we implemented Langmuir kinetics: Particles appeared on vacant lattice sites at a rate k_{on}, which represented the binding of particles from a surrounding solution with a spatially and temporally constant Cin8 concentration. Particles disappeared from an occupied lattice site at a rate k_{off}. Interactions of particles were modeled as follows: In addition to exclusion, we assumed that particles are subject to an interaction potential as illustrated in Fig. 2.13 that further constrains their motion. Specifically, for distances below a given interaction range the interaction energy between particles was assumed to increase linearly. Phrased differently, we assumed that a constant

attractive force $F^{\text{interaction}}$ acts on pairs of particles with a distance equal or less than the interaction range. Consequently, detailed balance constrained particle motion as well as particle detachment for interacting particles. Let $d^{\text{against force}}$ denote the rate for motion against the force from an interacting particle $d^{\text{with force}}$ the rate of the opposite process. Then, these rates have to fulfill

$$d^{\text{against force}}/d^{\text{with force}} = \exp(-\beta\Delta E) = \exp(-\beta\Delta F^{\text{interaction}} a), \tag{2.4}$$

where ΔE denotes the difference of energy related to the movement, and, as before, $F^{\text{interaction}}$ the force between interacting particles. Further, $\beta = \mathrm{k}T$ with k being the Boltzmann constant and T the temperature. As a further simplification, we restricted interactions to the nearest neighbors which implies that a particle can interact at most with two other particles. This simplification will be justified *a posteriori* since only very small interaction ranges produced stable clusters in simulations. As the Boltzmann factor merely relates the ratio of the two rates, we have the freedom of choosing how to split the contribution between motion against the direction of the force and motion with the direction of the force. Here, we chose to give the full weight to motion against the direction of force while motion in the direction of the force was not accelerated. To be consistent with motion outside the potential, the resulting rates read

$$d^{\text{against force}} = d_0 \exp(-\beta F^{\text{interaction}} a) \tag{2.5a}$$

$$d^{\text{with force}} = d_0. \tag{2.5b}$$

For thermodynamic consistency, we further have to relate particle detachment to the interaction energy between particles

$$k_{\text{off}}^{\text{potential}} = k_{\text{off}} \exp\Big(-\beta \sum_{\mathrm{i} \in \mathrm{nn}} \Delta E(d_i)\Big). \tag{2.6}$$

Here, the sum $\sum_{\mathrm{i} \in \mathrm{nn}}$ only runs over nearest neighbors and $\Delta E(d_i)$ is the interaction energy related to two particles at distance d_i. Thus, we also consistently neglected interactions with particles other than the nearest one to the left and to the right, respectively, for particle detachment.

Given these stochastic rules for particle dynamics, we then turned to simulations of the model based on the Gillespie algorithm [169]. Parameter values other than the interaction range and the attractive force between particles could be directly inferred from experimental data (see Appendix D for details). Our simulations showed that the proposed model leads indeed to the formation of clusters, see also Fig. 2.28. In order to infer the interaction range, we investigated which values of the corresponding parameter lead to a stable—yet not dominating—formation of clusters:

In Appendix A we detail that the formation of stable clusters at Cin8 concentrations corresponding to the *in vitro* experiments constrains the interaction range to a value of $d_{\mathrm{ir}} = 3a \approx 25\,\mathrm{nm}$. For smaller interaction ranges, clusters hardly formed whereas larger interaction ranges caused the formation of clusters with many particles that were inconsistent with experimental observations. Hence, we used an interaction range of three lattice sites.

Before we moved to a quantitative analysis of the formation of clusters and the diffusion coefficient of clusters in our model, we first had to specify the defining properties of a particle cluster. In an experimental setup, a particle cluster is an accumulation of particles with mutual distances below the resolution limit of approximately 400 nm. To translate this behavior to the simulations, we associated two particles to the same cluster if their distance was smaller or equal than 400 nm, which corresponds to approximately 48 lattice sites. It is important to note that this distance differs from the interaction range. In this way, a particle cluster refers to non-interacting particles whenever the distance between them is larger than the interaction range but smaller than the resolution limit, see also Appendices B and C.

Fig. 2.14 shows simulation results for the diffusion coefficient of clusters of two particles for different values of attractive forces between particles. The diffusion coefficient decreases rapidly upon increasing the strength of attractive interactions. Thus, an attractive interaction between particles can indeed explain the reduction of the diffusion coefficient of dimeric clusters by orders of magnitude as compared to the diffusion coefficient of an individual Cin8 molecule. Intuitively, this can be understood by considering that two interacting particles induce a drag to each other. As each individual particle is associated to a binding site on the microtubule an interaction with a neighboring particle will mitigate its motility and therefore the overall motility of the particle cluster. These results from stochastic simulations are further supported by a mathematical analysis of the dynamics of clusters. In Appendix B, we show how the motility of a cluster composed of two particles is mathematically related to the motility of its individual constituents. Analytic results of the corresponding mathematical approach are also presented in Fig. 2.14 and agree very well with stochastic simulations. Importantly, the theoretical analysis based on model simulations and the mathematical approach allowed us to quantitatively determine the strength of attractive forces between Cin8 particles: To explain the measured diffusion coefficient of clusters with two Cin8 particles, an attractive force of approximately 1.4 pN is necessary. Strikingly, this value is very close to the measured stall force of Cin8 in the plus-end and minus-end direction, $F^{\mathrm{stall}} = 1.5\,\mathrm{pN}$.

The presence of weak attractive forces does not only impact the motion of particle clusters but also increases the dwell time of particles within a cluster as compared to non-interacting particles. Therefore, longer dwell times of clusters as compared to individual, non-interacting particles should be a clear indicator of attractive forces. Indeed, an increased dwell time of clusters was confirmed by the experimental data

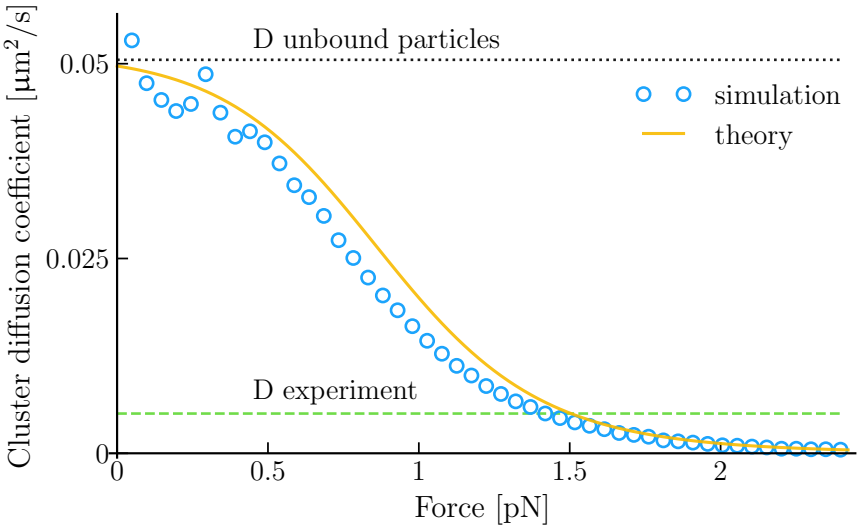

Figure 2.14 Diffusion coefficient of clusters with two particles for varying attractive forces $F^{\text{interaction}}$ between particles. The diffusion coefficient of a cluster with two particles obtained from stochastic simulations (circles) and our analytic approach (solid line, see Appendix B for details) decreased rapidly for increasing attractive interactions between the two particles. A comparison of our theoretical approach with the experimentally determined diffusion coefficient of dimeric clusters (dashed line) allowed us to estimate the attractive interactions between two Cin8 particles. This approach yields a force of approximately $F^{\text{interaction}} \approx 1.4\,\text{pN}$ between Cin8 particles. As a check for consistency, we also show the value for the diffusion coefficient of two non-interacting particles (dotted line): $D^{\text{dimeric cluster}}_{\text{unbound}} = D^{\text{single}}/2$, where D^{single} denotes the diffusion coefficient of a non-interacting particle. For weak attractive forces between particles, the diffusion coefficient of clusters approaches the theoretical value for the diffusion coefficient of two unbound particles. Parameter values: $d_0 = 1432\,\text{s}^{-1}$, $d^{\text{against force}} = \delta \cdot d_0$, $k_{\text{on}} = 2 \times 10^{-5}\,\text{s}^{-1}$, $k_{\text{off}} = 0.0625\,\text{s}^{-1}$. Here, $\delta = \exp(-\beta F^{\text{interaction}} a)$ denotes the Boltzmann factor, $\beta = 1/\text{k}T$, and $a = 8.4\,\text{nm}$ is the lattice spacing [165]. A temperature corresponding to $\beta^{-1} = 4.11\,\text{pN nm}$ was used. Simulated lattice size was $L = 5000$.

of our collaborators: While individual particles showed an average dwell time of 16 seconds, clusters consisting of two Cin8 particles—on average—showed a dwell time of 62 seconds.[14]

Taken together, our theoretical analysis complemented by single-molecule experiments strongly suggests the presence of weak attractive forces between Cin8 particles. Moreover, mathematical analysis and simulations related the diffusion coefficient of two-particle clusters to the strength of these interactions. Based on our displacement

14 Values correspond to measurements at 1 mM ATP.

analysis, this revealed forces of approximately 1.4 pN within a distance of approximately 25 nm between particles. The presence of attractive forces between Cin8 particles was further supported by increased dwell times of particle clusters as compared to single particles.

2.3.4 An anisotropic response of Cin8 to drag reverses the motion of clusters

The central component of any model for directional reversal has to be active motion. Thus, we complemented our equilibrium model of the previous section with directed motion to study potential origins of a directional switching. In detail, motion was assumed to be the sum of a rate $d(F)$ (Eqs. 2.5) due to passive diffusion that contributes equally to both directions and an active component $a_{\pm}(F)$ for plus-end and minus-end-directed motion, respectively. In general, also the latter component shows a dependency on an external force F. The overall rate for motion towards the minus end then reads $m(F) := d(F) + a_{-}(F)$. Likewise, the total rate for motion towards the plus end is given by $p(F) := d(F) + a_{+}(F)$.

The implicit underlying assumption of this superposition of rates is a rapid switching without memory between three internal states: A diffusive state, a plus end directed, and a minus end directed state. To motivate this choice, consider the following: The origin of Cin8's diffusive behavior is still elusive on a biomolecular level. One plausible interpretation of its motility is, however, that Cin8 switches between a purely diffusive state where it is associated comparably loosely to the microtubule and a more tightly associated state where it moves actively. Switching between a strongly and weakly associated state is typical for kinesins [170] and, for example for MCAK, a nucleotide dependent change of its diffusive motion has been observed [87]. To account for bidirectionality of the active motion, also this state of motility should be composed of two substates, which are plus-end or minus-end directed, respectively. Then, upon averaging over time, a stationary distribution of these three internal states emerges which we can associate with the probabilities P_{+}^{active}, P_{-}^{active} and P^{passive}. These probabilities have to be multiplied with the respective velocities of the motion of particles that is associated with the respective internal state to obtain the effective rates implemented in our model. Thus, if relaxation to a steady state distribution of the internal states occurs on timescales that are short as compared to those of the experiments, our assumption for the superposition of bidirectional active and passive motion follows.

Motivated by these considerations, we formulated our non-equilibrium model for the collective motion of Cin8 based on two key assumptions. The first central modeling component is that active motion occurs in both directions. Similar to passive motion, also active motion is, in general, affected by external forces. Thus, to consistently address interacting particles in our model, we specified the response of

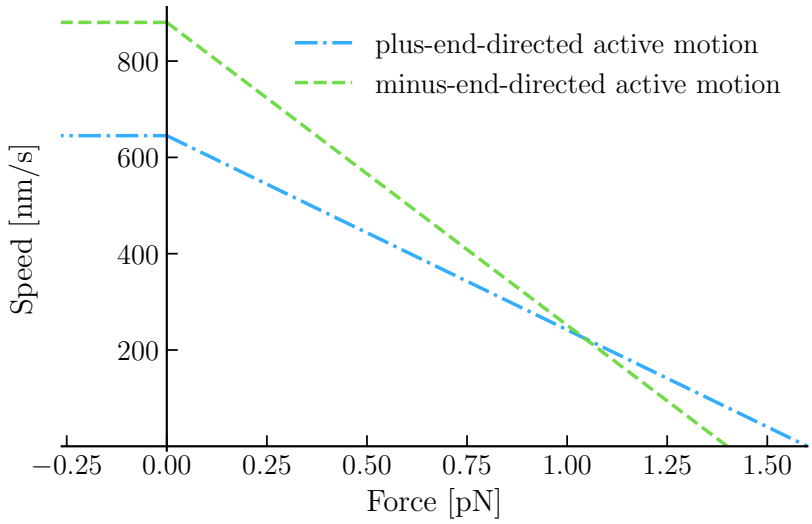

Figure 2.15 Illustration of the anisotropic response of active motion in the plus-end and minus-end direction, respectively, to opposing forces. We assumed that active motion occurs in both directions on the microtubule. The responses of active motion in the plus-end and minus-end direction to an external force were anisotropic: Minus-end directed motion was assumed to be faster at vanishing external forces but showed a smaller stall force ($F_-^{\text{stall}} = 1.4\,\text{pN}$) than plus-end-directed active motion ($F_+^{\text{stall}} = 1.6\,\text{pN}$). Note that here we refer to forces that oppose the direction of motion which implies that the forces show differing directions for both curves. We assumed that active motion is not accelerated by a force in the direction of motion (here negative signs). The force-velocity curves were inspired by those measured for kinesin-1 [107, 163, 171–174].

active motion $a_\pm(F)$ to an external force. In this respect, the second key assumption was that active motion depends anisotropically on external forces: While minus-end-directed motion was assumed to be faster than plus-end-directed motion at vanishing opposing forces, we assumed that plus-end-directed motion dominates when moving against large opposing forces. Note that for many kinesins it has been shown that active motion ceases when moving against forces larger than a certain threshold value, the so-called stall force [107, 163, 171–174]. Thus, our assumption can be rephrased by saying that minus-end-directed motion dominates for particles that move freely (no opposing force) but that the stall force of plus-end-directed motion is larger than that of minus-end-directed motion. These basic assumptions for the response of the rates $a_\pm(F)$ to an external force are illustrated in Fig. 2.15. We chose stall forces corresponding to the values $F_+^{\text{stall}} = 1.6\,\text{pN}$ and $F_-^{\text{stall}} = 1.4\,\text{pN}$. This choice agrees approximately with recent measurements that suggested a stall force of approximately $F_+^{\text{stall}} \approx F_-^{\text{stall}} \approx 1.5\,\text{pN}$ for plus-end and minus-end-directed motion

of Cin8, respectively [161].[15] Note that attractive interactions between particles with a strength of $F^{\text{interaction}} = 1.4\,\text{pN}$ as quantified in previous section stall active motion in the minus-end direction as assumed in the model: $a_-(F^{\text{interaction}}) = 0$. Since a diffusive component, however, remains present at such forces, particles move also bidirectionally when moving against the force of particle interactions. For simplicity, we assumed a linear decrease of the velocity of directed motion for forces against the direction of motion. Moreover, we assumed that forces in the direction of motion don't accelerate the active motion of particles. This functional dependency was inspired by the measured response of kinesin-1's stepping rate to opposing and supporting forces [107, 163, 171–174] which can be well approximated by such a relation. In essence, our basic assumptions are equivalent to an anisotropic response of active motion in plus-end and minus-end direction to varying drag. If a Cin8 particle experiences an opposing force (drag) above a certain threshold value, its drift velocity effectively reverses since active motion in the plus-end direction exhibits a larger stall force. Attention should, however, be paid to the fact that we address forces that antagonize the motion of particles such that the respective direction of a force in Fig. 2.15 is different for the plus-end and minus-end-directed active motion. Taking everything together, our model then exhibited three distinct rates for motion in each of the directions:

- $p_0 = d_0 + a_+(0)$ for unconstrained motion towards the plus end.
- $p^{\text{against force}}(F^{\text{interaction}}) = d_0 \cdot \delta(F^{\text{interaction}}) + a_+(F^{\text{interaction}})$ for motion towards the plus end when moving against a force due to particle interactions. Here, $\delta(F^{\text{interaction}}) := \exp(-\beta F^{\text{interaction}} a)$ denotes the Boltzmann factor, see also Eqs. 2.5.
- $p^{\text{with force}} = p_0$ for motion towards the plus end when moving in the direction of a force due to particle interactions.
- $m_0 = d_0 + a_-(0)$ for unconstrained motion towards the minus end.
- $m^{\text{against force}}(F^{\text{interaction}}) = d_0 \cdot \delta(F^{\text{interaction}}) + a_-(F^{\text{interaction}})$ for motion towards the minus end when moving against a force due to particle interactions.
- $m^{\text{with force}} = m_0$ for motion towards the minus end when moving in the direction of a force due to particle interactions.

Note that, due to our choice of splitting the Boltzmann weight (see Eqs. 2.5), and since we assumed that active motion is not accelerated by forces in the direction of motion,

15 It should be noted that the corresponding measurements of the stall force were conducted in a motility assay where a multitude of motors is engaged with a single microtubule. Therefore, the stall forces were not measured directly for individual particles but could only be inferred indirectly which likely complicates a very precise measurement of the corresponding values.

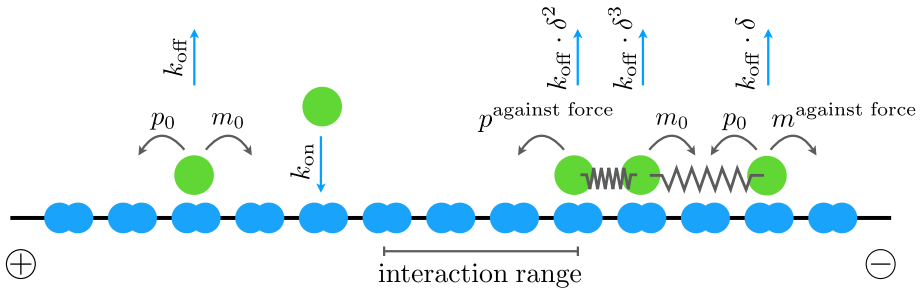

Figure 2.16 Illustration of the model for the collective dynamics of Cin8. Particles in the Cin8 model moved stochastically on a discrete lattice with a lattice spacing $a = 8.4$ nm and excluded each other. Non-interacting particles moved towards the plus and minus end at rates p_0 and m_0, respectively, and detached at rate k_{off}. Particles attached to vacant lattice sites at rate k_{on}. Particles interacted within a range of $d_{\text{ir}} = 3a$ of each particle. The rates for motion against the force of a particle interaction read $p^{\text{against force}}(F^{\text{interaction}}) = d_0 \cdot \delta(F^{\text{interaction}}) + a_+(F^{\text{interaction}})$ and $m^{\text{against force}}(F^{\text{interaction}}) = d_0 \cdot \delta(F^{\text{interaction}}) + a_-(F^{\text{interaction}})$, where $a_\pm$ are illustrated in Fig. 2.15. Here, $\delta(F^{\text{interaction}}) = \exp(-\beta F^{\text{interaction}} a)$ denotes the Boltzmann factor and $F^{\text{interaction}}$ is the force between two interacting particles. Due to our specific choice of dynamics, motion in the direction of the force of a particle interaction was not affected, $m^{\text{with force}} = m_0$ and $p^{\text{with force}} = p_0$. For simplicity, we only accounted for nearest neighbor interactions. Particles interacting with other particles in each direction behaved like a non-interacting particle since forces cancel. Detachment was weighted by the same Boltzmann factor δ that affected diffusive motion. Specifically, the detachment rate was multiplied by δ^n where $n = \max[\{0, (n_{\text{ir}} - d_{\text{right neighbor}})\}] + \max[\{0, (n_{\text{ir}} - d_{\text{left neighbor}})\}]$. Here, $n_{\text{ir}} = 3$ denotes the interaction range in units of lattice sites and $d_{\text{right neighbor}}$ and $d_{\text{left neighbor}}$ denote the distances to the left and right neighboring particle in units of lattice sites, respectively.

also the total rates to move in the direction of a force equal those of non-interacting particles, $m^{\text{with force}} = m_0$ and $p^{\text{with force}} = p_0$. Further note that we have included $a_-(F^{\text{interaction}})$ in the description above for sake of completeness, although for most purposes of this section we assume $a_-(F^{\text{interaction}}) = 0$ as detailed above. Besides this behavior for active motion, the model is identical to the previously formulated equilibrium model detailed in Section 2.3.3. An illustration of the model is shown in Fig. 2.16.

Although the velocity-force relation and, in particular, the differing stall forces are merely assumptions, there are various experimental findings supporting this arguing. First, a recent experimental study showed the capability of Cin8 to produce forces in both directions [161], thus justifying active stepping in both directions. Moreover, the corresponding stall forces were estimated to be roughly 1.5 pN in both directions which approximately agrees with the value of attractive forces between particles found in our analysis detailed above. This experimental observation, however, constrained

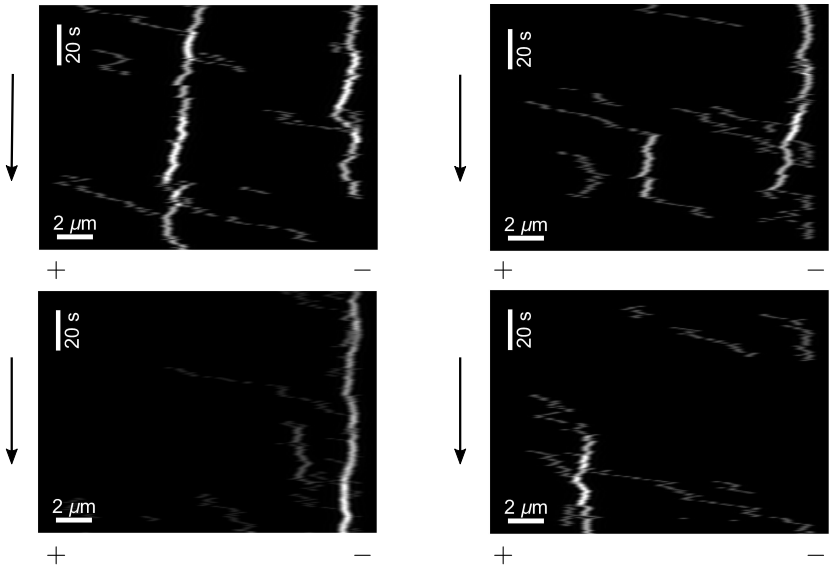

Figure 2.17 Space-time plots (kymographs) obtained from stochastic simulations of the Cin8 model that accounts for active motion. Simulation data were convoluted with a point-spread function with appropriate dimensions to generate images comparable to those generated by the microscopy setup, see also Appendix C for details. In this way, particles below the resolution limit of approximately 400 nm are not resolved anymore in the kymograph but show an increased intensity (brightness) at the respective position. While single particles (faint traces) exhibited a tendency to move to the minus end (right), clusters (bright traces) showed a tendency to move towards the plus end (left). Plus and minus signs denote the respective microtubule end. The black arrow denotes the direction of time. Simulation parameters are listed in Table 2.5. The system length was set to $L = 2000$.

the values for the stall forces in our model as detailed above. Second, the capability of kinesins to step backwards was reported previously also for kinesin-1 for high backward loads [107, 175, 176]. While the relation of Cin8's directional reversal to backward stepping of kinesin-1 is unclear, these experiments nonetheless show that the assumption of a stepping mechanism that comprises forward and backward steps is plausible for kinesin motion in principle.

Fig. 2.17 shows kymographs (space-time plots) obtained from simulations of the full Cin8 model that accounts for weak interactions together with the active stepping behavior detailed above. Note that the raw simulation data were convoluted with an appropriate point-spread function. This procedure served two purposes: First, in the raw data, single particles were hardly visible due to their small spatial extension in relation to the overall system sizes which were of the order of several thousand lattice sites. Second, convolution with a point spread function emulated the image formation in an experimental microscopy setup, where the signals of the point emitters are convoluted by the point-spread function of the microscope. For further details

on the convolution method see also Appendix C. Strikingly, our assumption of an anisotropic response of Cin8 to drag is sufficient to explain the directional switch due to motor clustering: Indeed, similar to the experimental observations, clusters of particles formed that—on average—moved towards the plus-end. We therefore concluded that the reversed motion of particle clusters can be reproduced by our model which indicates Cin8's ability to move actively in both directions with an anisotropic response to an opposing force.

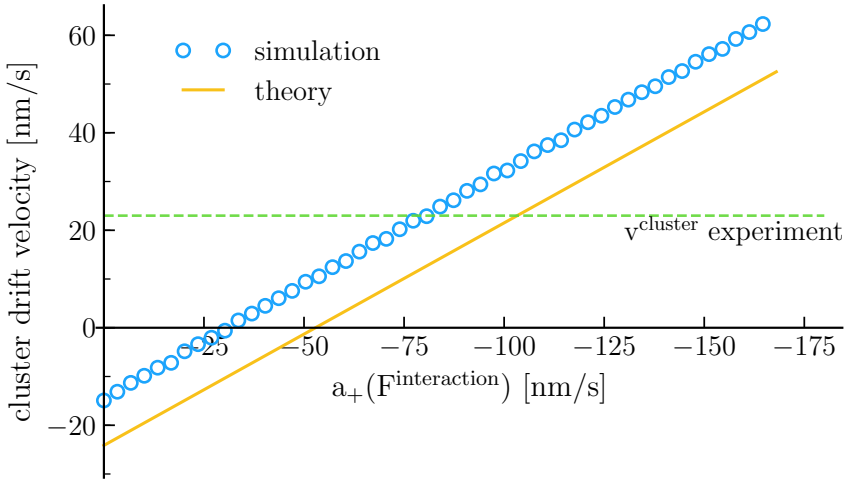

Figure 2.18 Effective drift velocity of a dimeric cluster for a varying rate $a_+(F^{\text{interaction}})$. Simulation results (circles) and mathematical analysis (solid line) show a linear relation between the rate $a_+(F^{\text{interaction}})$ of an individual particle and the drift velocity $v^{\text{dimeric cluster}}$ of a dimeric particle cluster. A comparison of the simulation results with the drift velocity of a dimeric particle cluster determined in experiments (dashed line) suggested $a_+(F^{\text{interaction}}) \approx -81\,\text{nm/s}$ for an individual particle within a cluster. Here, a negative sign indicates minus-end-directed motion. Note that we assumed that the force between interacting particles stalls active motion in the minus-end direction, $a_-(F^{\text{interaction}}) = 0$. Particle dynamics were chosen to fulfill the linear relationship and stall forces ($F_+^{\text{stall}} = 1.6\,\text{pN}$, $F_-^{\text{stall}} = 1.4\,\text{pN}$) specified in Fig. 2.15 as well as the measured drift velocity of approximately $v^{\text{single}} = -234\,\text{nm/s}$ (Table 2.1) of a non-interacting particle: $d_0 = 1432\,\text{s}^{-1}$, $d^{\text{against force}} = 78.8\,\text{s}^{-1}$, $a_+(0) = 1.6$ ($a_+(F^{\text{interaction}})/0.2$), $a_-(0) = a_+(0) + 28\,\text{s}^{-1}$, $k_{\text{on}} = 2 \times 10^{-5}\,\text{s}^{-1}$, $k_{\text{off}} = 0.0625\,\text{s}^{-1}$. Simulated lattice size was $L = 5000$.

To quantify the stepping rates of individual Cin8 particles within a cluster we resorted again to the displacement analysis introduced in Section 2.3.2. Based on our knowledge of the approximate strength of interactions between particles we systematically varied the rate of active stepping of an individual particle within a cluster in the simulations. Resulting drift velocities of a particle cluster with two

Parameter	Value
Interaction range	25 nm
Interaction strength	5.8 kT
Force between interacting particles (cluster force)	1.4 pN
Speed of active motion towards plus end against cluster force	81 nm/s
Speed of active motion towards minus end against cluster force	0 nm/s
Diffusion coefficient for motion against cluster force	5.6×10^3 nm^2/s

Table 2.3 Summary of the model parameters in terms of physical quantities. Here, a temperature corresponding to kT = 4.11 pN nm was used implicitly assumed.

	v_{MD} [nm/s]	v_{MSD} [nm/s]	D_{MSD} [10^3nm^2/s]
Single Cin8 particles	- 229	227	109
Dimeric Cin8 clusters	23.0	22.0	5.30
Trimeric Cin8 clusters	17.8	16.5	2.38
Tetrameric Cin8 clusters	11.5	9.58	1.79
Pentameric Cin8 clusters	9.86	8.25	1.32

Table 2.4 Summary of the effective drift velocities and diffusion coefficients of single particles and clusters of the fully quantified model for the collective motion of Cin8. Values were obtained by fitting the linear function $\langle x(t)\rangle = v_{MD} \cdot t$ to the temporal evolution of the MD and the quadratic function $\langle x(t)^2\rangle = v_{MSD}^2 \cdot t^2 + 2D_{MSD} \cdot t$ to the temporal evolution of the MSD, where $x(t)$ denotes the position of the respective particles at time t on the microtubule and angle brackets refer to an ensemble average over different traces. In simulations we referred to a cluster when the distance between particles was smaller or equal than 48 lattice sites. An attachment rate of $k_{on} = 2 \times 10^{-5}$ s^{-1} was used. Other model parameters are listed in Table 2.5. A lattice size of $L = 5000$ was used.

Cin8 molecules as obtained by stochastic simulations and our mathematical analysis are shown in Fig. 2.18. To match the average velocity of dimeric clusters as measured in the experiment, a drift velocity of 81 nm/s towards the plus-end was required for an individual particle in the cluster. As a result, this analysis determined all model parameters and thereby quantified Cin8's motile properties and the interaction between particles. The resulting values are summarized in Table 2.3. Moreover, the drift velocities and diffusion coefficients of single particles and clusters obtained with this set of parameters are listed in Table 2.4 which accurately reproduce those identified experimentally (see Table 2.1).

How can we understand that clusters move in the opposite direction as compared to single particles? While this may seem intuitive at first glance, this phenomenon is subtle in its details. Consider two particles at adjacent lattice sites as illustrated in Fig. 2.19 (1). Since an attractive force is present between both particles, their diffusive

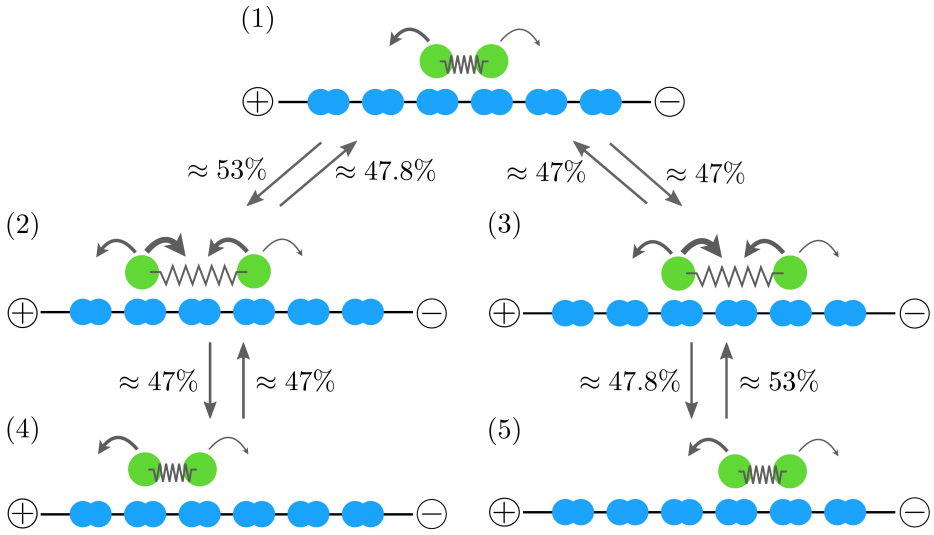

Figure 2.19 Illustration that an anisotropic dependency of active motion on drag implies a reversed motion of clusters with two particles. Due to the asymmetric response of active motion to an external force, particles move against an opposing force with a preference towards the plus end. Therefore, a cluster in a completely compressed state (1) stretches with a slightly higher probability towards the plus-end direction [transition (1)→(2) with probability (53%)] than it does towards the minus-end direction [transition (1)→(3) with probability 47%]. In a cluster configuration where the particles are separated at least by one lattice site but are still interacting with each other [states (2) and (3)] the most likely reaction is a compression of the cluster (approximately 95%) which occurs preferentially towards the minus end since no force opposes motion. Absence of an opposing force, however, also implies a larger diffusive component in the corresponding transition rate as compared to the rate of stretching a cluster. Thus, the probabilities to compress a cluster towards the minus and to the plus end, respectively, differ only insignificantly (47.8% vs. 47%). As a result, a caterpillar-like motion of a cluster towards the plus end [transition (1)→(2)→(4)] shows a higher transition probability than the collective motion of a cluster towards the minus end [transition (1)→(3)→(5)]. Since the force between particles is assumed to be constant for distances smaller than the interaction range, analogous arguments can be made when starting from a state that is already stretched. Moreover, also for clusters that contain more than two particles a similar argument for the particles at the boundaries can be applied, which also implies preferred plus-end directed motion in these cases.

component and their rate to move actively is changed as compared to a single particle outside of a cluster. For attractive forces that are large enough to reverse motion, hopping of the left particle towards the plus end is the most likely reaction. Hence, the cluster preferentially stretches by the motion of the left particle towards the plus end [transition (1)→(2)]. In this stretched state, the most likely reaction to occur is

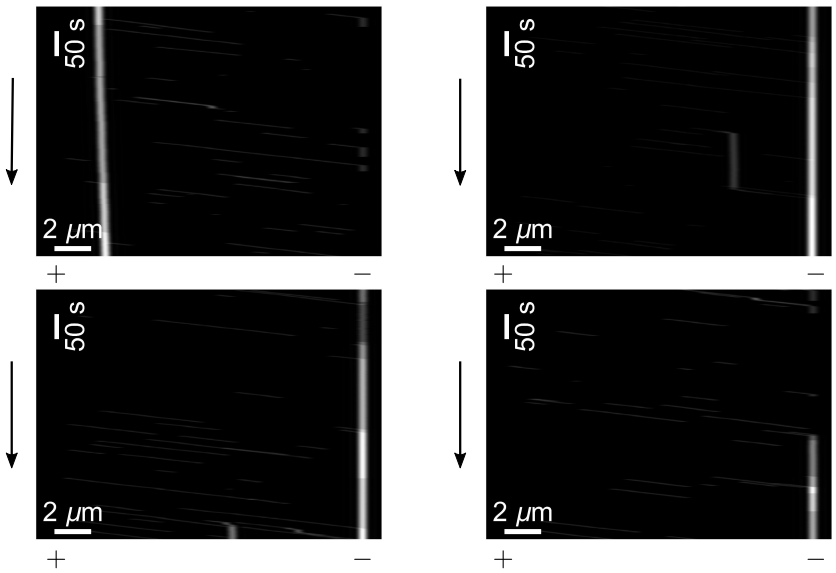

Figure 2.20 Representative kymographs of simulations with a negligible diffusive component of the motion of Cin8. When the diffusive component in the motion of particles was lowered in the model, clusters either showed no net displacement or show a slight tendency to move towards the minus end. Thus, switching the directionality of the motion of clusters depends on a diffusive component in the motion of particles. Plus and minus signs denote the respective lattice end. Black arrows denote the direction of time. Parameter values were $m_0 = 29.8\,s^{-1}$, $p_0 = 1.8\,s^{-1}$, $m^{\text{against force}} = 0.1\,s^{-1}$, $p^{\text{against force}} = 9.7\,s^{-1}$, $k_{on} = 4 \times 10^{-5}\,s^{-1}$, $k_{off} = 0.0625\,s^{-1}$, $L = 2000$.

a transition back into a compressed state [transition (2)→(1) and (2)→(4)]. Since motion towards another particle is not subject to an opposing force, the preferred directionality is minus-end directed. The absence of an opposing force, however, also implies that diffusive motion is suppressed less strongly than in the presence of an opposing force. Consequently, the corresponding transition probabilities towards the minus-end and plus-end, respectively, differ only insignificantly [transition (2)→(4) with probability 47%; transition (2)→(1) with probability 47.8%]. Therefore, the large diffusive component of Cin8's motion enables a cluster of particles to generate overall plus-directed motion. The result is a caterpillar-like motion of a particle cluster towards the plus-end. To further support this reasoning we also performed simulations of a modified model where particles showed a negligible diffusive component in their motion. Indeed, simulation results as depicted in Fig. 2.20 support that a directional switching of the motion of clusters is absent in this modified model. Therefore, the ability of clusters of particles to move towards the plus end is a consequence of (a) an anisotropic response of the active (bidirectional) motion of particles to opposing forces and (b) a large diffusive component in the motion of particles.

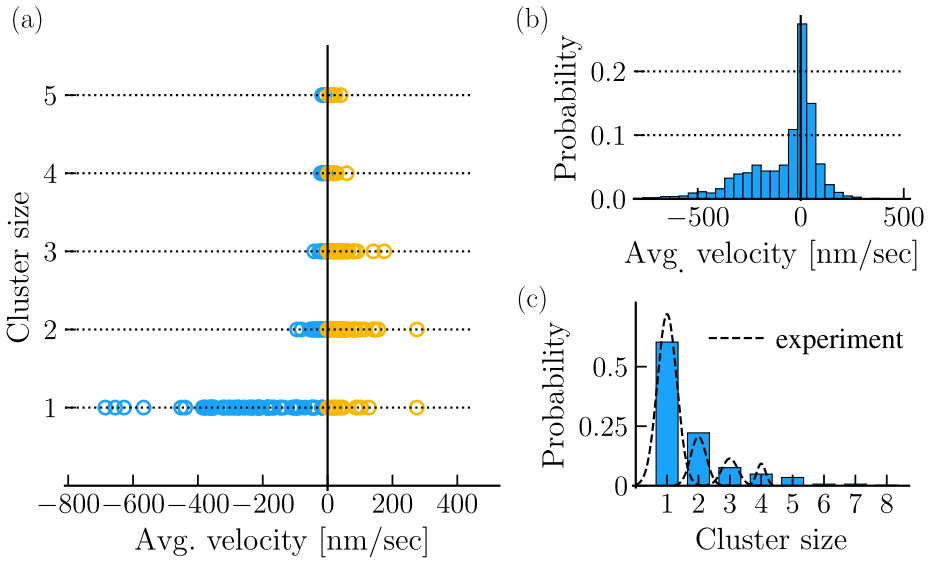

Figure 2.21 Distribution of the velocities and numbers of particles of trajectories of single Cin8 particles and clusters in simulations. (a) The plot shows simulation data for the average velocity of different trajectories of individual particles and clusters plotted against the respective number of particles in the cluster (cluster size). While single particles moved—on average—towards the minus end (negative sign, blue circle) with a very broad distribution of velocities, particle clusters showed less random behavior and moved—on average—towards the plus end (positive sign, orange circles). Panels **(b)** and **(c)** show the distribution of velocities (irrespective of the number of particles of the respective trajectory) and the distribution of the number of particles of a cluster (cluster size) obtained from stochastic simulations. The probability distribution of the number of particles in a cluster agrees excellently with the experimental data (dashed Gaussians). Other parameter values as listed in Table 2.5. A lattice size of $L = 2750$ was used. For better comparability with the experimental data the number of evaluated trajectories was reduced in (a) by reducing the simulated time (1000 s in (a); 5000 s in (b) and (c)).

2.3.5 The model for the collective dynamics of Cin8 accurately reproduces the distributions of cluster sizes and velocities

The probability to observe a cluster of a given size is, in general, expected to be mostly determined by the interaction strength which we have estimated by the diffusion coefficient of Cin8 clusters containing two particles. Thus, only if the strength of the interaction energy was quantified to a good degree by our analysis, the model will reproduce a distribution of the number of particles in a cluster that agrees with the experiment. Moreover, the parameters were chosen to fix the velocities and diffusion coefficients of single particles and clusters with two particles. Therefore, the distributions of velocities for clusters that contained more than two particles were not

fitted by this procedure but correspond to an emerging property of the model. Because of this reasoning, we turned towards the distribution of the numbers of particles in a cluster (referred to as cluster size) and velocities of different trajectories as a further means to quantitatively assess the agreement of our Cin8 model with the experimental data. A resulting comparison is shown in Fig. 2.21. Both, the distribution of the average velocities and the number of particles in a cluster of different trajectories obtained from simulations [Fig. 2.21(a)], as well as the distribution of the numbers of particles in a cluster [2.21(a)] show the excellent accordance of our model with the experimental data as depicted in Figs. 2.11 and 2.10(c), respectively. This finding supports that interactions and motility of Cin8 are estimated to a very good degree by our theoretical approach.

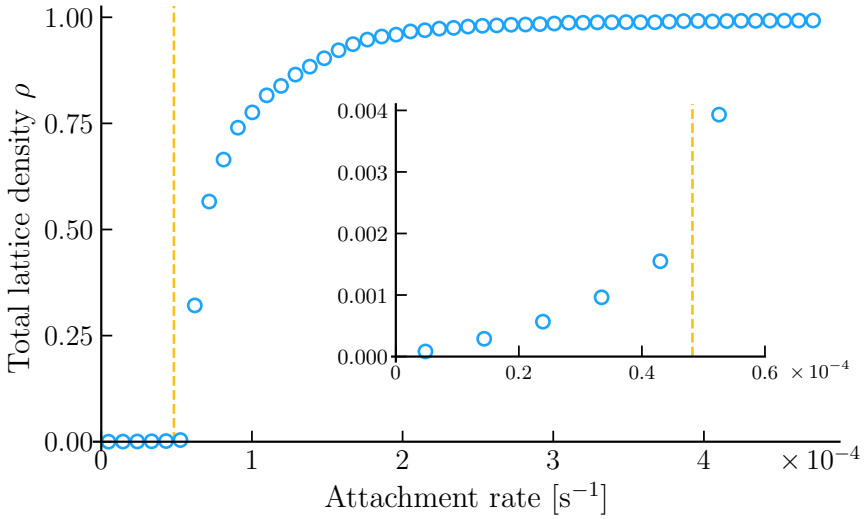

Figure 2.22 Average occupation of the lattice obtained from simulations with varying particle attachment rates. When the attachment rate of particles was increased—which corresponds to increasing particle concentrations in the experiment—the average occupation of the lattice by particles ρ showed an abrupt change at $k_{on} \approx 5 \times 10^{-5}$ s. For larger attachment rates, clusters tended to grow steadily until almost the complete lattice was occupied. Interestingly, cluster growth in simulations was observed to become significant for attachment rates very close to those measured in the experimental setup ($k_{on}^{Experiment} \approx 4.8 \times 10^{-5}$ s, dashed line) at concentrations of c = 1–2 pM. The inset shows the same data for very small densities and attachment rates. Note that the figure may not display the steady state values of the density as the simulations converged only very slowly to the stationary state for high concentrations. Simulated time was $t = 8 \times 10^5$ s. Parameter values as listed in table 2.5. A lattice size of $L = 2750$ was used.

One very apparent feature that we observed in simulations was a rapid onset in the formation of clusters when increasing the Cin8 concentration. Above a certain concentration, we observed a constant growth of clusters accompanied by a rapidly growing particle density along the microtubule. Fig. 2.22 shows the particle density averaged over the whole lattice for varying Cin8 concentrations as obtained by our stochastic simulations. These simulations showed a sharp transition from a sparsely occupied lattice to a highly occupied lattice when increasing the particle concentration (equivalent to increasing the attachment rate). The reason for this behavior is that the increasing probability of particles to collide facilitates the formation of clusters. Since additional interaction energy is required to detach a particle from a cluster as compared to a non-interacting particle, clusters show an increased dwell time as compared to single particles. Thus, a stable yet not dominating formation of clusters constrains the Cin8 concentration to a range where the attachment rate of particles is (a) high enough to allow for the formation of clusters but (b) low enough such that a cluster—on average—breaks before colliding with another particle or cluster. Strikingly, as shown in Fig. 2.22, the attachment rate that correspond to the onset of the formation of stable clusters as predicted by our simulations ($k_{\mathrm{on}}^{\mathrm{simulation}} \approx 5 \times 10^{-5}$ s) coincides excellently with the attachment rate measured in the experiment ($k_{\mathrm{on}}^{\mathrm{experiment}} \approx 4.8 \times 10^{-5}$ s), where the onset of clustering was found empirically.

To gain insights in the formation of clusters on time scales of *in vitro* experiments, we performed additional simulations where the average cluster size at a given attachment rate was determined by an ensemble average of 250 simulations with (shorter) simulated time windows of 2300 seconds that are of the order of magnitude as the experiments .[16] The result is presented in Fig. 2.23. The simulated time window of 2300 seconds was not sufficient to create a sharp transition in the formation of clusters as the one displayed in Fig. 2.22. Instead, the simulations showed a gradual increase of the average number of particles composing a cluster when increasing the attachment rate. However, these simulations allowed us to identify the range of attachment rates where the formation of small and stable clusters is expected. Experimentally, evaluation of microscopy images becomes difficult when predominantly large clusters are present. Then, the overall illumination signal is too strong to distinguish between individual signals. We therefore defined the range of attachment rates that is expected to lead to reasonable experimental results as that where the average number of particles in a cluster is between 1.5 and 3. In the corresponding range of attachment rates, clusters are expected to form but won't dominate the lattice. The corresponding range is shaded in green color in Fig. 2.23. The attachment rate determined in the experiments is located precisely in this regime, which further demonstrates the very

16 In the corresponding simulations, the first 500 seconds were not evaluated to allow particles to bind to the microtubule; The number of particles of clusters was recorded over 1800 seconds following an initial time window of 500 seconds.

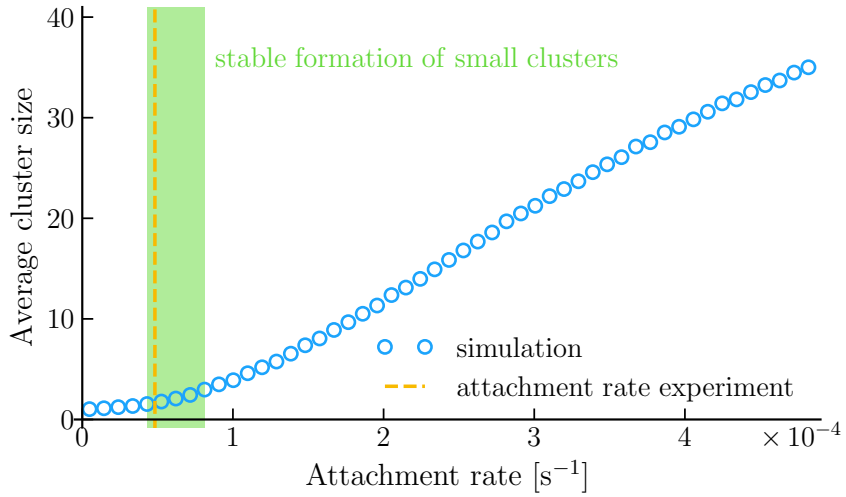

Figure 2.23 Average number of particles of a cluster (cluster size) on short time scales recorded in simulations with different attachment rates. The figure shows ensemble averages (circles) for the number of particles of a cluster recorded over 1800 seconds following an initial delay-time window of 500 seconds to initialize particle binding to the lattice. An ensemble size of 250 simulations was used for each data point. The green shaded area corresponds to the region of attachment rates that led to an average of 1.5 to 3 particles per cluster in the simulations. This range approximately corresponds to the region where we expect small clusters to be measurable in experiments. The attachment rate determined in experiments (dashed line) is located accurately in this region. Note that also single particles were included in the above evaluation. Parameter values as listed in Table 2.5. A lattice size of $L = 2750$ was used.

good agreement of our stochastic simulations and the experiment with respect to the formation and stability of clusters.

Motivated by these observations our collaborators performed additional *in vitro* measurements at different Cin8 concentrations. Indeed, high Cin8 concentrations led to a strong formation of clusters also in the experiments. Representative kymographs for varying Cin8 concentrations obtained from experiments and simulations are compared in Fig. 2.24. Supplementing this qualitative comparison, we further addressed the distribution of the number of particles of a cluster at varying concentrations quantitatively. The result is presented in Fig. 2.25, which again shows a great agreement of our model with experimental measurements.

Taken together, our model not only captures the motility of individual Cin8 molecules and clusters but also accurately reproduces the clustering behavior observed in experiments.

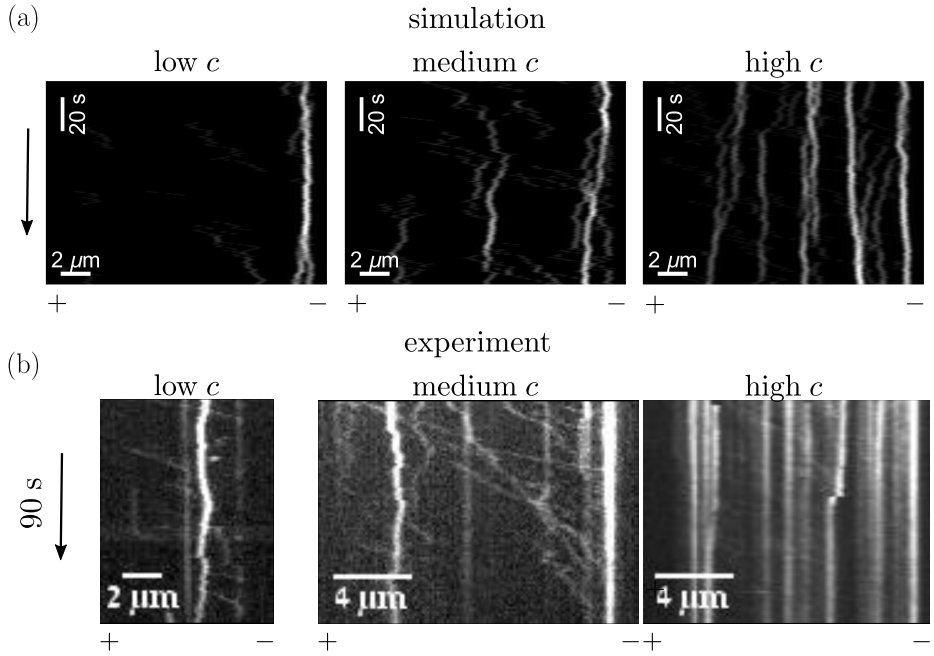

Figure 2.24 Representative kymographs from simulations and experiments at different Cin8 concentrations. Kymographs obtained from simulations (top row) and experiments (bottom row) were recorded at three different concentrations. Simulations and experiments consistently suggest strong clustering of Cin8 when increasing the concentration. Attachment rates in (a) were $k_{\text{on}} = \{5 \times 10^{-5}, 6.67 \times 10^{-5}, 1.25 \times 10^{-4}\}\,\text{s}^{-1}$ from the left to the right. Lattice size in simulations was $L = 2000$. Other parameters as listed in Table 2.5. In (b), concentrations were $c = \{0.75\text{–}1.5, 1\text{–}2, 1.875\text{–}3.75\}$ pM from the left to the right. The total time window for each kymograph in (b) is 90 seconds. The black arrows indicate the direction of time. Plus and minus signs denote the respective lattice end. All experimental data were produced by Prof. Leah Gheber's group.

2.3.6 An anisotropic response of Cin8 to drag consistently explains previous experimental results

Thus far, we have shown how a simple mechanistic model for Cin8's motion and interaction can consistently and quantitatively describe the clustering of Cin8 and, importantly, the directional reversal of particle clusters. The central idea was that Cin8's motility is based on (a) active motion in the plus-end *and* minus-end direction that superimposes with a substantial diffusive component, and (b), that the active motion in both directions shows an anisotropic response to external forces that oppose this motion. In experiments, Cin8's motion can not only be reversed by a clustering of particles but also by varying the surface densities of Cin8 in gliding assays or by varying salt concentrations. Hence, it is important to relate our considerations to

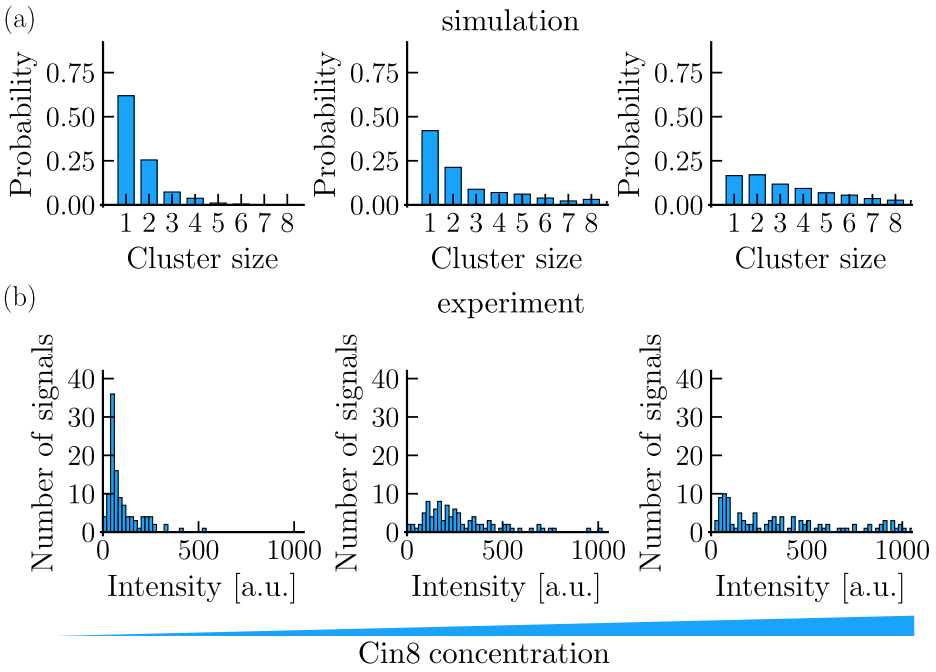

Figure 2.25 Comparison of the distribution of the number of particles in a cluster (cluster size) determined in experiments and simulations at different concentrations of Cin8. Both, simulations (a) and experiments (b) consistently show that for increasing Cin8 concentrations (left to right) very large clusters of Cin8 form and dominate the lattice/microtubule for high concentrations. Simulation results agree with the experimental data. Since the concentration of particles could not be determined with a high accuracy in the experiments, we fixed the attachment rate at medium concentrations to approximately reproduce the distribution of intensities observed in experiments. The other attachment rates for the simulations were then computed such that the relative change is equivalent to the variation of the Cin8 concentration of the experiments in (b). Attachment rates in (a) were $k_{\text{on}} = \{5 \times 10^{-5}, 6.67 \times 10^{-5}, 1.25 \times 10^{-4}\}\ \text{s}^{-1}$ from the left to the right. Lattice size in simulations was $L = 2000$. Other parameters as listed in Table 2.5. In (b) concentrations were $c = \{0.75\text{–}1.5, 1\text{–}2, 1.875\text{–}3.75\}$ pM from the left to the right. All experimental data were produced by Prof. Leah Gheber's group.

these results as well. In the following, we address the implications of our model for directional reversal for those two experiments.

2.3.6.1 Directional switching induced by changing ionic strengths

Several previous experimental studies showed the ability of yeast kinesin-5 motors to switch directionality when the salt concentration of the buffer is changed. This effect was reported for single-molecule studies with Cin8 [155, 177, 178] as well as for gliding assays with Cut7 [158]. Varying the salt concentration of the buffer causes a change in

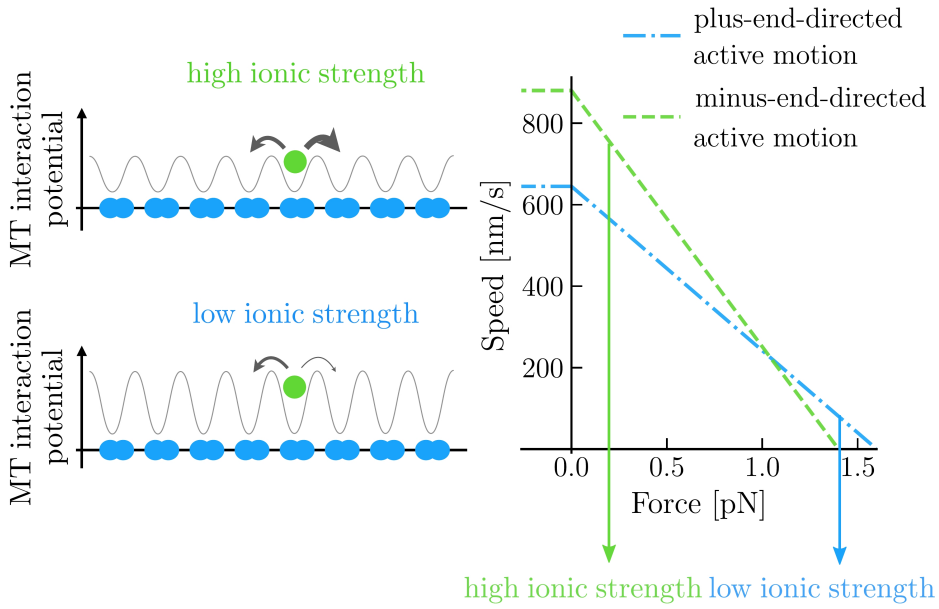

Figure 2.26 Accordance of our proposed model with a directional switch induced by changing salt concentrations. A buffer with a high ionic strength (left panel, upper illustration) shields electrostatic interactions more strongly as compared to a buffer with low ionic strengths (left panel, lower illustration) and thus leads to weaker interactions with the microtubule. Therefore, a moving Cin8 particle will experience a higher resisting force (drag) when moving along a microtubule at high ionic strength than at low ionic strength (two arrows, right panel). In our model, this implies reversal of motion if the drag is large enough.

the strength of electrostatic interactions. Specifically, higher salt concentrations shield electrostatic interactions and thus lead to weaker interactions very generally. For Cin8 this means that a particle is attached more weakly to the microtubule for high salt concentrations than it is for low salt concentrations. Thus, the energy barriers between different binding sites will be lowered as well, see Fig. 2.26 for an illustration. As a consequence, this decrease of interactions for high ionic strengths is expected to reduce the force that opposes a Cin8 particle (here referred to as drag for simplicity) when moving along the microtubule. It is therefore reasonable to assume that active stepping is subject to stronger opposing forces for low salt concentrations than it is for high salt concentrations. Our basic modeling hypotheses then predict for a switch of directionality in the motion of Cin8 for changing ionic strengths whenever the forces that oppose Cin8's movement along a microtubule become large enough.

In order to support this hypothesis, our collaborators performed additional experiments at different salt concentrations. While this is still ongoing work, preliminary results indeed support that lowered salt concentrations simultaneously affect the drag and the directionality of Cin8's motion: In experiments with a buffer of low ionic

strength a diffusion coefficient of $D^{\text{single}} = 20 \times 10^3$ nm$^2/s$ was measured, which is significantly lower (approximately five-fold) than the one at high ionic strengths, see Table 2.1. Moreover, while single particles at high ionic strengths showed pronounced and robust motion towards the minus end, single particles at low ionic strengths showed a decreased preference to move towards minus-ends. Specifically, the drift velocity towards the minus ends was substantially decreased and several particles were plus-end directed or undirected (zero net drift)—two effects that were not observed for buffers with high ionic strengths. The decrease of the diffusion coefficient measured in these experiments allowed us to roughly estimate the increase of the forces that oppose the motion of Cin8 along a microtubule. Following the Arrhenius law [179, 180] the decrease of the diffusion coefficient when changing the ionic strenght is associated to an increase of energy barriers by $\Delta E = 1.6\,\text{kT}$ that has to be overcome by Cin8 particles as they move along the microtubule lattice. Assuming a symmetric and periodic binding potential with a period of 8.4 nm [165] leads to maxima of the binding energy that are located at a distance of 4.2 nm from the minima. This assumption results in additional drag forces of roughly 1.6 pN at lowered ionic strengths, where we have assumed a temperature corresponding to 4.11 pN nm. Our estimate is approximately consistent with our previous assumptions that suggested a directional reversal for forces of this magnitude, see Fig. 2.26. Based on this arguing, we therefore conclude that our proposed model for the directional reversal of Cin8 also explains previous observations concerning the motility of Cin8 at varying salt concentrations.

2.3.6.2 Directional switching in gliding assays

Directional switching of Cin8's motion was uncovered in gliding assays with varying surface densities of Cin8 [154], and other kinesins have been reported to show this behavior as well [156, 158, 159]. In the corresponding experiments, the directionality of microtubules driven over a surface coated with molecular motors switched when varying the density of molecular motors bound to the surface. How do these observations relate to our proposed model for directional reversal? Directional switching in gliding assays would be in agreement with our model when changing the surface density of molecular motors corresponds to a change in the opposing force that an individual kinesin experiences when pushing the gliding microtubule. This scenario is plausible whenever the molecular motors act in an unsynchronized fashion. Then, a large number of motors that are engaged with a microtubule increases the overall binding strength of the surface and the microtubule. This increased rigidity may result in an increased resistance for individual molecular motors that try to move the microtubule. Recent experimental studies indeed suggested such a behavior for Cin8: The impact of forces of an individual Cin8 molecule on a stalled microtubule in a gliding assay was observed to decrease with an increasing density of molecular motors on the surface [161]. Therefore, an individual motor may require larger forces

to translocate the microtubule at high surface densities than at low surface densities. Ultimately, these forces may become large enough such that, according to our model, minus-end-directed motion effectively stalls while plus-end-directed motion can still cause a movement of the microtubule. In this respect, also the findings by Britto et al. [158] for Cut7, which showed that the addition of non-kinesin-5 motors in gliding assays can induce a directional switch of gliding microtubules, is captured by our model: As it is irrelevant if opposing forces arise due to the increased number of kinesin-5 motors engaged with the microtubule or due to the binding of other proteins, our model suggests a directional switch in both cases. Importantly, also results from a recent theoretical study suggest that our basic assumptions are in agreement with directional switching in gliding assays: Based on computer simulations of a gliding assay, Saito and Kaneko [181] observed a directional switch in the motion of gliding microtubules when the drift velocity of Cin8 particles depended asymmetrically on the intramolecular strain of a Cin8 molecule. The latter requirement is, however, equivalent to our basic modeling assumptions. Thus, our suggested mechanism for the directional reversal of kinesins may also explain directional switching observed in gliding assays and could therefore unify our view on Cin8's directional reversal. In fact, our model shows that all previously observed ways to change the directionality of motion of Cin8 may be different aspects of the same mechanism: An anisotropic response of active motion to drag.

2.3.7 Conclusion and outlook

In this section we have addressed the directional reversal of the yeast kinesin-5 Cin8 by statistical analyses and stochastic modeling. The central result is a new model for the directional switching of Cin8 that significantly advances our view on this phenomenon by bringing together multiple—seemingly unrelated—observations.

Our model sheds light on the biomolecular origins of directional switching due to the formation of clusters of particles:

- As shown by our analysis, the formation and motility of Cin8 clusters is explained by attractive forces between motors. Strikingly, our theoretical considerations allowed us to compute the strength and range of these forces: 1.4 pN between motors for distances smaller than 25 nm.
- Directional reversal in our model is the result of an anisotropic response of motion to opposing forces; While motion at small or no opposing forces is assumed to occur predominantly towards the minus end, the relative contribution of motion towards the plus end is assumed to increase as particles have to move against large opposing forces.
- Based of the anisotropic response of active motion to drag, clusters of Cin8 particles can generate drift due to their significant diffusive component of

motion: As an opposing force suppresses diffusion exponentially, the motion against opposing forces exhibits a higher relative drift than motion which is not hindered by an opposing force. Therefore, the movement of particles against forces arising from particle interactions is effectively more directed than that of non-interacting particles. This behavior ultimately enables a cluster to move towards the plus end in a caterpillar-like fashion.

- In this way, our model accurately reproduced the statistics of motion of single Cin8 particles and clusters of particles determined in experiments.

- Furthermore, our fully quantitative model accurately reproduced also the clustering behavior at different Cin8 concentrations: The probability of observing a cluster of a given size in the simulations agreed precisely with that observed in the experiments. Moreover, inspired by our stochastic simulations, we quantitatively verified a sharp transition of the probability to observe large clusters of Cin8 molecules when the Cin8 concentration in the experiments was increased.

In this way, our model provides a consistent picture of the clustering behavior of Cin8 and the reversed directionality of the motion of clusters with respect to individual particles. Importantly, these insights significantly change our view on previous findings with respect to Cin8's directional switch being triggered by factors other than clustering. Specifically, our model is consistent with a directional switch that is induced by lowering the ionic strength of the buffer. Also, our proposed mechanism is likely to be consistent with a directional switch due to a change of the surface density of molecular motors in a gliding assay:

- Our model of Cin8's directional switch agrees with the finding that directionality is affected by the ionic strength of the buffer: Due to enhanced electrostatic interactions, lowering the ionic strength increases the force that opposes the motion of a motor along a microtubule. This increased resistance, in turn, leads to a reversal of the directionality in the motion of Cin8 according to the hypothesized anisotropic response of particle motion to opposing forces. Indeed, preliminary results of experiments at low ionic strengths strongly support this view: Minus-end-directed motion was mitigated and the movement of several individual particles was reversed as compared to experiments at high ionic strengths. Simultaneously, the diffusivity of individual particles was approximately five-fold decreased, which suggests additional drag forces of roughly 1.6 pN.

- In a gliding assay, increasing the number of molecular motors that are simultaneously bound to a microtubule may also increase opposing forces that a single motor experiences when pushing the microtubule. This is because the overall stiffness of the microtubule-to-surface binding increases when more motors are

bound, consequently making it harder for an individual motor to translocate the microtubule. If these opposing forces are large enough, our proposed mechanism for Cin8's directional reversal predicts a switch of the gliding direction of microtubules when increasing the surface density of molecular motors in gliding assays. Importantly, also a recent theoretical study reported a directional switch in simulations of a gliding assay in the case of an asymmetric dependency of the motor velocity on intramolecular strain [181].

In view of the above considerations, our model unites various previous experimental findings related to directional reversal; A mechanism for directional switching based on (a) bidirectional active motion of Cin8 and (b) an anisotropic response of this active motion to drag connects previous models and consistently explains experimental findings.

As an outlook for future work, it should also be noted that further analyses are still required to resolve the phenomenon of directional reversal fully. As a first step, it is planned to transfer our quantified model to simulations of a gliding assay. While Saito et al. [181] already reported the possibility of a directional switch in simulations of gliding assays with assumptions very similar to our modeling hypotheses, it will be illuminative to specifically simulate particles with the parameters identified by the analysis presented in this section. These simulations will then answer whether (a) the molecular parameters identified by our study are consistent with a directional switch of Cin8-based gliding assays and (b) provide a quantitative means to analyze experimental data of gliding assays such as those conducted to estimate Cin8's stall force [161]. On the experimental side, the most important step is a direct measurement of the potential bidirectional active motion of Cin8 and of the potential asymmetric response of Cin8's active motion to opposing forces. It should be noted that this is likely a difficult task as previous experiments with optical traps and beads coated with Cin8 molecules failed due to reasons that are currently unclear: Opposed to measurements with other kinesins, Cin8 was not able to displace Cin8-coated beads from the center of an optical trap; Only multi-motor gliding assays could be used to infer forces exerted by individual Cin8 molecules on a microtubule indirectly [161]. It was hypothesized that it is because of inherent features related to the directional switching mechanism of Cin8 that standard experiments based on optical traps may be unsuitable to measure the force production by single Cin8 molecules. In this respect, simulations of gliding assays might indeed provide a valuable contribution by relating forces exerted on a microtubule in a gliding assay to that produced by an individual motor.

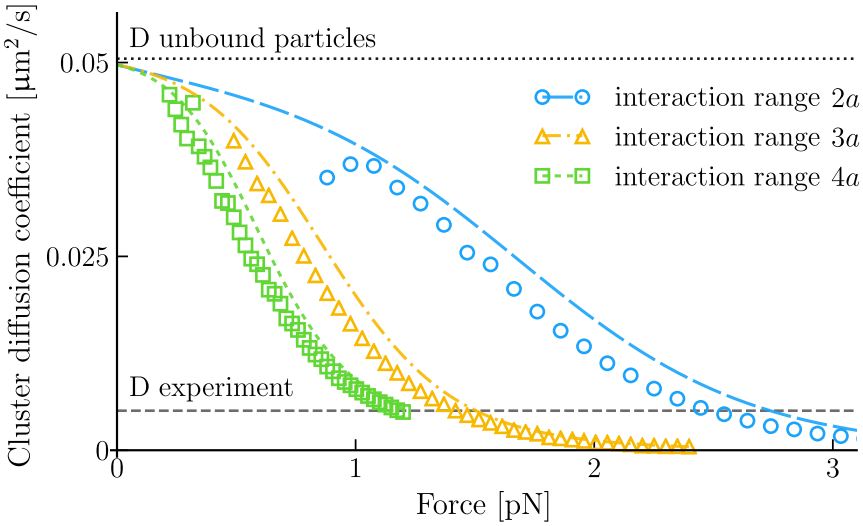

Figure 2.27 Diffusion coefficient of clusters with two particles for different attractive forces $F^{\text{interaction}}$ between particles and different interaction ranges. The plot shows the diffusion coefficient of dimeric particle clusters obtained from simulations (symbols) and our theoretical analysis (dashed colored lines, see also Section B) of the equilibrium model presented in Section 2.3.3. The analysis allowed us to determine the strength of attractive forces that lead to a diffusion coefficient compatible with that measured in the experiments (dashed gray line). Parameter values other than those denoted in the figure are $p_0 = m_0 = 1432\,\text{s}^{-1}$, $p^{\text{against force}} = m^{\text{against force}} = \delta \cdot p_0$ with $\delta = \exp(-\beta F^{\text{interaction}} a)$ being the Boltzmann factor and $\beta = 1/\text{k}T$. Here, $a = 8.4\,\text{nm}$ denotes the lattice spacing and a temperature corresponding to $\beta^{-1} = 4.11\,\text{pN nm}$ was used. Attachment and detachment rates were $k_{\text{on}} = 2 \times 10^{-5}\,\text{s}^{-1}$, $k_{\text{off}} = 0.0625\,\text{s}^{-1}$, respectively. A lattice size of $L = 5000$ was used.

Appendix

A Determination of the interaction range

In order to choose an appropriate interaction range d_{ir} in the model, we performed simulations using an interaction range of either two, three, or four lattice sites. The motility of clusters is expected to be influenced not only by the force between particles but also by the range of interactions. Therefore, in analogy to the procedure described in Section 2.3.3, we first systematically increased the attractive force between particles of the equilibrium model presented in Section 2.3.3 for each of the three different interaction ranges. We then measured the diffusion coefficient of dimeric particle clusters observed in the corresponding simulations. This approach allowed us to determine the respective values of attractive forces between particles that reproduce

the diffusion coefficient measured in the experiments for each of the three interaction ranges. An overview of the simulation results is shown in Fig. 2.27.

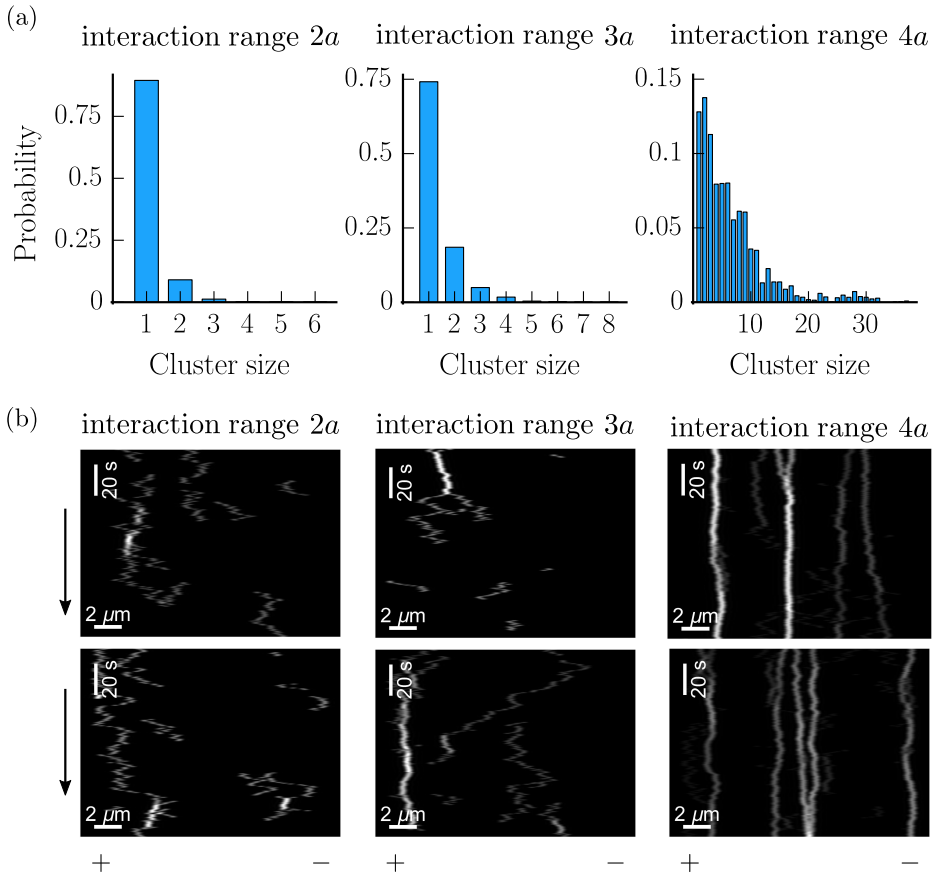

Figure 2.28 Analysis of the number of particles in a cluster (cluster size) for different interaction ranges. (a) Distribution of the number of particles in a cluster obtained from simulations of the equilibrium model (see also Section 2.3.3) for $d_{\mathrm{ir}} = \{2a, 3a, 4a\}$. Only for interaction ranges of $d_{\mathrm{ir}} = 3a$ the formation of clusters was significant yet not dominating; For $d_{\mathrm{ir}} = 2a$ clusters hardly formed and for $d_{\mathrm{ir}} = 4a$ the formation of large clusters dominated the system. **(b)** Illustrative kymographs obtained from simulations with $d_{\mathrm{ir}} = \{2a, 3a, 4a\}$ supporting that the formation of stable but small clusters is only likely for $d_{\mathrm{ir}} = 3a$. Other parameters in (a) and (b) were $p_0 = m_0 = 1432\,\mathrm{s}^{-1}$, $p^{\text{against force}} = m^{\text{against force}} = \{9.6, 79, 130\}\ \mathrm{s}^{-1}$ for $d_{\mathrm{ir}} = \{2a, 3a, 4a\}$, respectively, $k_{\mathrm{on}} = 4.8 \times 10^{-5}\,\mathrm{s}^{-1}$, $k_{\mathrm{off}} = 0.0625\,\mathrm{s}^{-1}$. The corresponding Boltzmann weight for particle detachment consistent with the reduced hopping rate against the force of interactions reads $\delta = \{6.7 \times 10^{-3}, 5.5 \times 10^{-2}, 9 \times 10^{-2}\}$. Lattice size was set to $L = 2000$ in (a) and (b). Plus and minus signs denote the respective lattice end. Black arrows indicate the direction of time.

In the next step, we used this quantification of the forces of interactions between particles and performed simulations at particle attachment rates that corresponded to

those measured in the experiments. Representative kymographs for $d_{\mathrm{ir}} = \{2a, 3a, 4a\}$ are shown in Fig. 2.28(b). While an interaction range of $d_{\mathrm{ir}} = 2a$ hardly led to the formation of clusters, an interaction range of $d_{\mathrm{ir}} = 4a$ already led to systems that were dominated by large clusters. This qualitative observation was further supported by the distribution of the number of particles in a cluster measured in simulations for the different interaction ranges as shown in Fig. 2.28. Unlike the behavior for interaction ranges of size $d_{\mathrm{ir}} = \{2a, 4a\}$, an interaction range of $d_{\mathrm{ir}} = 3a$ produced clusters that exhibited sizes and lifetimes compatible with experiments. Indeed, the simulated distribution of the number of particles in a cluster is in great agreement with those observed in experiments as shown in Fig. 2.10(c). Taken together, this stability analysis of clusters suggests that—at attachment rates measured in the experiment—only an interaction range of $d_{\mathrm{ir}} = 3a$ is in agreement with experimental data while interaction ranges of $d_{\mathrm{ir}} = \{2a, 4a\}$ produce unstable systems where clusters either hardly form or dominate the system.

B Theoretical relation between the motility of single particles in a cluster and the motility of the cluster

In this section, we aim for an analytic expression for the motility of a cluster with two particles in terms of the motility parameters of its individual particles. Two particles are considered to belong to the same cluster whenever their distance to each other is below or equal to a specific threshold value. Based on the experimental setup, we estimated this distance by $d_{\mathrm{max}} \approx 400\,\mathrm{nm} \approx 48\,a$, where a is the lattice spacing and thus the size of a tubulin dimer $a = 8.4\,\mathrm{nm}$ [165]. For the case of a cluster composed of two particles, we can uniquely describe the configuration by the distance $d = i\,a$ between the two particles, with $i \in \{1, 2, \ldots, n_{\mathrm{max}}\}$ and $n_{\mathrm{max}} = 48$ being the maximal distance of the particles in numbers of lattice sites. The corresponding probabilities to find such a state will be denoted by P_i. To describe the motility of the cluster, we consider transitions between these differently stretched states in the comoving frame of reference. A cluster with given inter-particle distance i may *stretch* at rate s or *compress* at rate c by moving either one of its two composing particles further away or closer to the other particle, respectively. In general, these rates differ depending on whether the particles interact with each other or not. For a complete mathematical description we further have to equip the transitions between differently stretched states with appropriate boundary conditions that define how clusters are destroyed and created. For a maximally stretched cluster with an inter-particle distance of $d_{\mathrm{max}} = n_{\mathrm{max}}a$, a further stretching event will cause a breaking of the cluster. To ensure probability conservation, we mapped these breaking events of a cluster to the creation of a new cluster. The distribution of initial distances between two particles when a cluster is created is elusive. Therefore, we assumed, for simplicity, that new clusters are created with a uniformly distributed distance between the two particles.

Moreover, we neglected the breaking of a cluster due to a detachment of one of the particles because of the small transition rate of this process. The corresponding master equations then read

$$\frac{\mathrm{d}}{\mathrm{d}t}P_i = -P_i(c^{\mathrm{ir}} + s^{\mathrm{ir}}) + P_{i+1}c^{\mathrm{ir}} + P_{i-1}s^{\mathrm{ir}} + n_{\max}^{-1}P_{n_{\max}}s \quad \text{for} \quad i \in \{2, \ldots, n_{\mathrm{ir}} - 1\}, \tag{2.7a}$$

$$\frac{\mathrm{d}}{\mathrm{d}t}P_i = -P_i(c + s) + P_{i+1}c + P_{i-1}s + n_{\max}^{-1}P_{n_{\max}}s \quad \text{for} \quad i \in \{n_{\mathrm{ir}} + 1, \ldots, n_{\max} - 1\}. \tag{2.7b}$$

Here, $s^{\mathrm{ir}} = m^{\text{against force}} + p^{\text{against force}}$ is the rate of stretching the cluster when its particles are interacting, $c^{\mathrm{ir}} = m^{\text{with force}} + p^{\text{with force}} = p + m$ denotes the corresponding rate for compressing the cluster, and $s = c = m + p$ is the rate of stretching or compressing the cluster when its particles are not interacting. Furthermore, $d_{\mathrm{ir}} = n_{\mathrm{ir}} \cdot a$ denotes the interaction range within which the particles are subject to a weak attractive force. These equations are supplemented with the following boundary conditions:

$$\frac{\mathrm{d}}{\mathrm{d}t}P_1 = -P_1 s^{\mathrm{ir}} + P_2 c^{\mathrm{ir}} + n_{\max}^{-1}P_{n_{\max}}s, \tag{2.8a}$$

$$\frac{\mathrm{d}}{\mathrm{d}t}P_{n_{\mathrm{ir}}} = -P_{n_{\mathrm{ir}}}(c^{\mathrm{ir}} + s) + P_{n_{\mathrm{ir}}+1}c + P_{n_{\mathrm{ir}}-1}s^{\mathrm{ir}} + n_{\max}^{-1}P_{n_{\max}}s, \tag{2.8b}$$

$$\frac{\mathrm{d}}{\mathrm{d}t}P_{n_{\max}} = -P_{n_{\max}}(c + s) + P_{n_{\max}-1}s + n_{\max}^{-1}P_{n_{\max}}s. \tag{2.8c}$$

We solved Eqs. 2.7 and 2.8 in the stationary state. The general solution of the linear and non-homogeneous recurrence relation reads

$$P_i = \frac{P_{n_{\max}}s^{\mathrm{ir}}}{n_{\max}(s^{\mathrm{ir}} - c^{\mathrm{ir}})}i + C_1\left(\frac{s^{\mathrm{ir}}}{c^{\mathrm{ir}}}\right)^i + C_2 \quad \text{for} \quad i \in \{1, \ldots, n_{\mathrm{ir}}\}, \tag{2.9}$$

$$P_i = -\frac{P_{n_{\max}}}{2n_{\max}}i^2 + C_3 i + C_4 \quad \text{for} \quad i \in \{n_{\mathrm{ir}} + 1, \ldots, n_{\max}\}, \tag{2.10}$$

where C_i are constants and where we have used $c = s$. It should be noted that the term proportional to $(s^{\mathrm{ir}}/c^{\mathrm{ir}})^i$ reflects the Boltzmann distribution and would be the correct distribution of distances if we would consider a cluster that can't be destroyed when it is fully stretched. Since we, however, explicitly implemented the breaking of maximally stretched clusters with a subsequent uniform repositioning (terms proportional $n_{\max}^{-1}P_{n_{\max}}s$) the distance distribution is driven out of equilibrium which adds further terms to the solution. To determine the constants, we solved the three boundary conditions Eqs. 2.8 as well as a normalization condition, $\sum_{i=1}^{n_{\max}} P_i = 1$. While solving the corresponding equations is straightforward, the closed-form

expression of the solution is lengthy. Therefore, we here only provide the steady-state probability distribution of cluster configurations for the specific case of parameters given in Table 2.5:

$$P_i = -2.1 \cdot 10^{-6} + 15.9 \cdot (0.0549)^i - 1.3 \cdot 10^{-7} i \quad \text{for} \quad i \in \{1, \ldots, n_{\mathrm{ir}}\} \tag{2.11a}$$

$$P_i = 2.64 \cdot 10^{-3} + 1.12 \cdot 10^{-6} i - 1.12 \cdot 10^{-6} i^2 \quad \text{for} \quad i \in \{n_{\mathrm{ir}} + 1, \ldots, n_{\max}\}. \tag{2.11b}$$

Fig. 2.29 shows the excellent accordance of this solution with simulation results for the distribution of the distances between the particles in the cluster.

To derive the statistics for the motion of the whole cluster we then focused on transitions between the different states. Specifically, the center of mass of the cluster moves a distance $a/2$ whenever either one of the two particles moves to a neighboring lattice site. To account for the modified dynamics of interacting particles, we have to distinguish between distances between the particles that are smaller and larger than the interaction range. We then arrive at

$$\begin{aligned} m^{\text{cluster}} = {} & P_1 m^{\text{against force}} + \sum_{i=2}^{n_{\mathrm{ir}}-1} P_i (m^{\text{against force}} + m^{\text{with force}}) \\ & + P_{n_{\mathrm{ir}}} (m^{\text{with force}} + m) + \sum_{i=n_{\mathrm{ir}}+1}^{n_{\max}-1} 2 P_i m + P_{n_{\max}} m \end{aligned} \tag{2.12a}$$

$$\begin{aligned} p^{\text{cluster}} = {} & P_1 p^{\text{against force}} + \sum_{i=2}^{n_{\mathrm{ir}}-1} P_i (p^{\text{against force}} + p^{\text{with force}}) \\ & + P_{n_{\mathrm{ir}}} (p^{\text{with force}} + p) + \sum_{i=n_{\mathrm{ir}}+1}^{n_{\max}-1} P_i 2p + P_{n_{\max}} p. \end{aligned} \tag{2.12b}$$

The summation above takes into account that particles in a fully compressed cluster can only move in one direction due to exclusion. Moreover, breaking and recreation of a cluster is not considered as motility event, which explains the different coefficients of terms proportional to $P_{n_{\max}}$. The drift and diffusion coefficient of the cluster is then given by equations analogous to Eqs. 2.3 with $\tilde{a} = a/2 = 4.2$ nm.

C Convolution method for the generation of kymographs

In order to generate images from simulations that are comparable to images of the microscopy setup, we convoluted all particle positions with a point spread function:

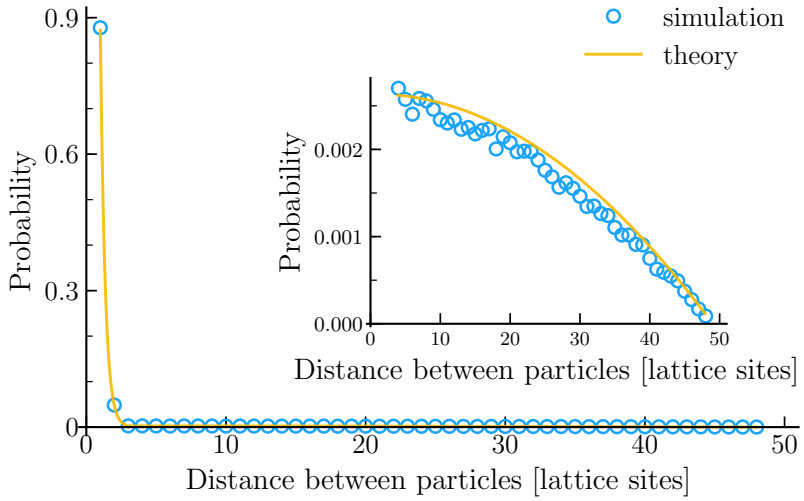

Figure 2.29 Probability distribution for the inter-particle distance in a cluster with two particles. The distribution of different distances d between two particles in a dimeric cluster obtained by our mathematical approach (solid line) agrees excellently with the distribution obtained by simulations (circles). Strongly compressed (small d) dimeric clusters with very small inter-particle distances are significantly more likely than strongly stretched states (large d). This explains the lowered motility (drift and diffusion coefficients) of particle clusters as compared to individual particles since the attractive interactions between particles and steric hindrance mitigate the motility of the cluster for small distances between the particles. The inset shows the magnified distribution of distances between particles in a dimeric cluster outside of the interaction range, $d = \{4, \ldots, n_{\max}\}a$. For distances close to the maximal distance $n_{\max}$ the probability decreases since any further elongation of a maximally stretched, dimeric cluster results in its breaking. The latter effect drives the distribution of distances out of equilibrium such that the result differs from a Gibbs-Boltzmann distribution. Attachment rate was $k_{\text{on}} = 2 \times 10^{-5}\,\text{s}^{-1}$ and the simulated lattice size was $L = 5000$. Other parameters as in Table 2.5.

$I(r) = I_0 \cdot (2J_1(2\pi r/\beta)/(2\pi r/\beta))^2$ with r the radial distance to the origin, I_0 the maximal intensity, J_1 the Bessel function of the first kind of order one, and $\beta = 0.78$. The optical resolution of the experimental setup was estimated by 400 nm. Fig. 2.30 shows a corresponding point spread function that was also used to generate kymographs from the simulated data.

D Model parameters

We inferred the model parameters by using the fitted values of v_{MD} and D_{MSD} as stated in Table. 2.1 and by using Eq. 2.3. The detachment rate was inferred from

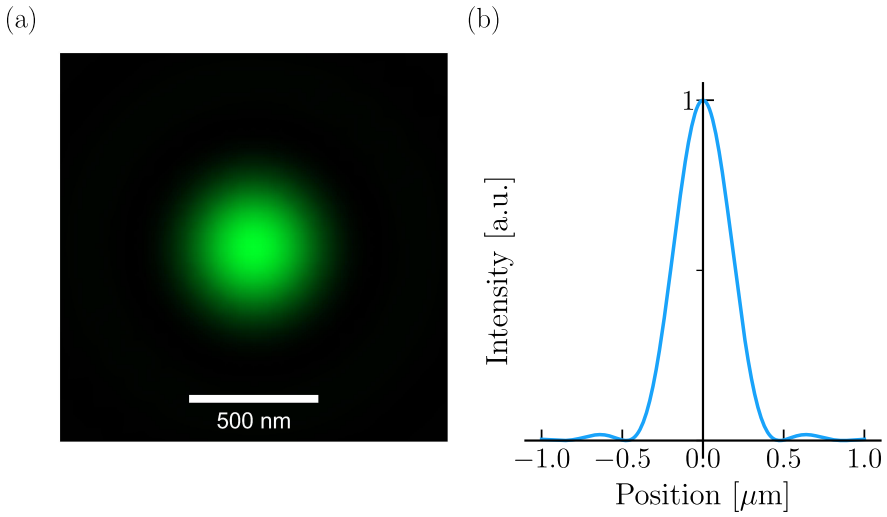

Figure 2.30 Illustration of the point spread function used to generate images from simulated kymographs. We used a point spread function corresponding to an estimated optical resolution of 400 nm. The function which was used to generate the kymographs is shown as two-dimensional plot in **(a)**; the corresponding one-dimensional profile is shown in **(b)**.

the average dwell time of individual Cin8 particles measured in the experiment, $\tau = (16 \pm 2)$ s. The attachment rate of Cin8 particles was also measured at 1–2 pM: $k_{\text{on}} = 5.74 \pm 0.68 \cdot 10^{-3}$ molecules $\mu\text{m}^{-1}\text{s}^{-1}$, which was converted to the attachment rate per lattice site of size $a = 8.4$ nm. A list of the ensuing model parameters used for the Cin8 model is provided in Table 2.5.

Parameter	Value [s^{-1}]
Minus-end-directed motion; non-interacting particles p_0	1.54×10^3
Plus-end-directed motion; non-interacting particles m_0	1.51×10^3
Minus-end-directed motion against the force of interactions $p^{\text{against force}}$	7.88×10^1
Plus-end-directed motion against the force of interactions $m^{\text{against force}}$	8.84×10^1
Attachment k_{on}	4.82×10^{-5}
Detachment non-interacting particle k_{off}	6.25×10^{-2}
Boltzmann weight for detachment rate δ	5.5×10^{-2}

Table 2.5 Summary of the parameters for the Cin8 model. Here, the Boltzmann weight for detachment refers to the additional weight multiplied with the detachment rate of interacting particles. Specifically, the detachment rate is multiplied by δ^n where $n = \max[\{0, (n_{\text{ir}} - d_{\text{right neighbor}})\}] + \max[\{0, (n_{\text{ir}} - d_{\text{left neighbor}})\}]$. Here, $n_{\text{ir}} = 3$ denotes the interaction range in units of lattice sites and $d_{\text{right neighbor}}$ and $d_{\text{left neighbor}}$ denote the distances to the left and right neighboring particle in units of lattice sites, respectively.

3 Cell-wide organization of proteins

3.1 The formation of dynamic vortex patterns by active curved polymers

This section addresses the analysis of a model for the self-organization of active, curved polymers into dynamic vortex patterns. The model was motivated by recent experimental findings [2] on the protein FtsZ which plays a vital role in bacterial cell division by forming the protein ring that initiates the constriction of the cell. In detail, these *in vitro* studies showed the ability of curved FtsZ polymers to translocate on a membrane because of treadmilling and to thereby self-organize into ring-like patterns. In the research project described in the following, we used methods from the field of active matter to address the collective dynamics of FtsZ polymers. The central result of our work was that active motion along circular and chiral tracks is sufficient to organize the collective motion of polymers into dynamic vortex patterns, even in the absence of attractive forces between the polymers. Results related to this project were published in the manuscript *"Active Curved Polymers Form Vortex Patterns on Membranes"* [63] in the journal *Physical Review Letters*. To this work, I contributed as second author. The following section provides an introduction and the scientific background related to this publication. The corresponding publication is reprinted in section 3.1.3 of this thesis.

3.1.1 Background

3.1.1.1 Bacterial cell division and the Z ring

As in eukaryotic cells, also bacterial cells vitally depend on the ability of biomolecules to organize into large, functional structures. Again, cell division is a good example where this remarkable capability becomes evident: In many bacteria, a self-organizing system of reactive proteins interacts to correctly identify the cell's middle [182–187]. There, the tubulin homologue FtsZ assembles into an annular structure, the so-called Z ring. This protein ring marks the future division site and initiates cell division [188–

192]. More precisely, in the presence of GTP, FtsZ polymerizes into polar filaments that show a—probably nucleotide-dependent—intrinsic curvature [193–198]. These filaments form the central building block of the Z ring, which is thought of as a disordered conglomerate of many overlapping FtsZ filaments [199–201]. Once the Z ring has successfully assembled, it recruits a multitude of different proteins involved in the synthesis of the cell wall and, ultimately, initiates cytokinesis by a mechanism that is still unknown [190, 202, 203]. Surprisingly, unlike the eukaryotic counter piece—the actomyosin ring—motor proteins are most likely not involved in the Z ring's contraction [204]. Nevertheless, while it is beyond doubt that the Z ring and FtsZ in general play a vital role in bacterial cell division, the mechanisms behind the formation of the Z ring and its constriction are mostly unknown.

This question has been fueled by recent findings that, in fact, the Z ring is a very dynamic structure [2, 34, 202, 203, 205]. FtsZ filaments are likely to incorporate new monomers at one end of the polar filament while monomers preferentially leave the polymer at the opposing end. This mechanism ultimately transforms FtsZ's (de)polymerase activity into a nonequilibrium process. In recent *in vitro* studies with reconstituted FtsZ on a supported lipid bilayer, FtsZ filaments have been shown to—based on this mechanism—undergo treadmilling motion that allows a single FtsZ filament to effectively translocate in a directed fashion [2, 34]. Due to the intrinsic curvature of the filaments and because of biomolecular details of their anchoring to the lipid bilayer, FtsZ filaments move along chiral and circular tracks over the surface. Moreover, these studies addressed not only the behavior of individual particles but also the collective properties of many filaments moving on the membrane. It was found that the dynamic FtsZ filaments self-organize into different patterns on the lipid bilayer, of which the most remarkable ones were probably dynamic polymer rings composed of moving FtsZ filaments. Strikingly, the average diameter of these rings coincided with the typical diameter of bacterial cells. While the explicit contributions of treadmilling and the GTPase activity of FtsZ to the formation of the Z ring and its constriction are still not fully understood, it has been shown that FtsZ filaments are also dynamic within the Z ring *in vivo* and, in particular, that this motion plays a crucial role in cell division [202, 203]. It is therefore important to understand how active motion contributes to the organization of FtsZ into patterns and, foremost, ring-like structures.

From a more abstract perspective, the findings that actively moving particles self-organize into patterns are reminiscent of active matter systems [206, 207]. Those systems deal with the collective motion of self-propelled agents that are subject to local alignment rules. One characteristic feature of active matter systems is the emergence of patterns above a certain density of agents/particles in the system. Strikingly, self-organization of cytoskeletal filaments into patterns has already been observed experimentally: In gliding assays where cytoskeletal filaments were propelled over a surface coated with molecular motors, the collective dynamics of these filaments

self-organized into patterns (such as polar waves or nematic lanes) as soon as the surface density of the filaments exceeded a certain critical value [30, 31, 33]. We therefore wanted to know: Do the ring-like patterns that have been observed for the collective dynamics of FtsZ polymers correspond to an emergent phenomenon of an active matter system or, phrased differently, do the patterns emerge because of specific interactions of FtsZ or because of generic principles related to the active motion of FtsZ polymers? Before summarizing the key results of our study and presenting the publication itself, we will briefly review some central findings in the field of active matter and, in particular, the emergence of order in systems of self-propelled particles.

3.1.1.2 Self organization in active matter systems

Active matter is defined as systems of entities which transduce energy into directed motion [206, 207]. Over the last years, this field of physics has been intensively studied. Similar to driven lattice gases, that exhibit boundary driven phase transitions and that are discussed in Chapter 2, also active matter systems are far from thermal equilibrium and feature a rich phenomenology that outreaches that of equilibrium physics in several respects. What is prohibited by the Mermin-Wagner theorem [208] in equilibrium systems is indeed realized in active matter systems: A phase transition to a symmetry-broken, long-range ordered state in two dimensions despite only short-range interactions. One prominent subclass of active matter are systems of self-propelled agents that interact with each other only locally via mechanical repulsion. A typical feature of such system of self-propelled particles is—loosely speaking—a transition towards more organized collective motion above a certain density of particles and below a certain level of noise [206, 207, 209]. The characteristics of the ordered states, in general, depend on the interaction of the actively moving particles. For example, the collective motion of particles that are subject to isotropic interactions (such as repulsive collisions of spherical particles) has been shown to phase separate into regions with gas-like disorder and solid-like order—a phenomenon known as motility-induced phase separation [210]. If, on the other hand, particles exhibit an intrinsic orientation and interact by local alignment, a transition to a state with macroscopic polar or nematic order emerges [30, 206]. In the following, we provide a rough overview of the emergence of such organized, collective motion in systems of self-propelled agents in theory and experiment.

The theoretical foundation of systems of self-propelled particles dates back to the work of Vicsek et al. [211]. In detail, the work described a system of particles that show an intrinsic orientation and that move actively with a constant speed v in the direction of their intrinsic orientation. In each time step, particles align with neighbors in a small vicinity of each particle but are also subject to noise. The key observation by Vicsek et al. was that—above a certain threshold density and below a certain level of noise—the system establishes macroscopic polar order.

Refined numerical simulations later suggested that the change from a disordered to an ordered state stems indeed from a first-order phase transition [212, 213]. Building on the idea to describe such agent-based systems by a continuum theory, Toner and Tu constructed a hydrodynamic, phenomenological theory that is based on general symmetry arguments [214, 215]. With this theory, it was possible to formally describe the transition towards the ordered state and reveal, for example, the two-dimensional long-range order of this state. By now, also a formal connection between a microscopic Vicsek-type model and a hydrodynamic field theory has successfully been established by Bertin et al. [216, 217]. The corresponding approach is based on the Boltzmann equation that was additionally equipped with an advective term. Particle collisions are thus included in a coarse-grained fashion and can be related to the system's large-scale behavior. The resulting equations of this *kinetic Boltzmann* approach were indeed very similar to the equations derived on phenomenological grounds by Toner and Tu. In particular, the coefficients in the equations of the kinetic Boltzmann approach are directly related to the microscopic variables and could thereby, in principle, get extracted from experiments

In parallel to these theoretical studies, much effort has also been devoted to experimental realizations and studies of active matter systems and, in particular, the emergence of collective coherent motion. Clustering of particles with characteristics very similar to a phase separation has been observed in systems with self-propelled colloidal particles [218–220]. Similarly, such colloidal systems as well as systems with vibrated discs have been shown to undergo a transition towards ordered collective motion for high particle densities [221, 222]. Interestingly, transitions to flocking or self-organized coherent collective motion has also been reported for systems with living entities such as bacteria [223–226], insects [227], or even birds and other higher organisms [209]. Another very prominent model system in this field are motility assays of cytoskeletal filaments that indeed bare many similarities to the experiments with FtsZ polymers by Loose et al.[2] and Ramirez-Diaz et al. [34]. There, actin or microtubule filaments are driven by molecular motors over a two-dimensional surface [30, 31]. Collisions between the filaments lead to a local alignment of their orientation [33] and thereby promote the formation of order. Similarly to the theoretical models and other active matter systems, ordered motion emerges on a macroscopic scale when the density of cytoskeletal filaments exceeds a specific critical value [30, 31]. Depending on the experimental details, collective order in the experiments with gliding assays is realized, for instance, in the form of polar waves [30, 31], vortex patterns [32], or nematic lanes [33]. Notably, also the phase coexistence of nematic lanes and polar waves has recently been shown [33]. While all of these studies show that flocking and a transition to ordered macro-states are a widespread experimental phenomenon, it should, however, be stressed that a rigorous connection to the theoretical approaches is still debated [206, 210].

Building on the intuition that already local repulsive interactions together with active motion can order the collective motion of particles and thereby lead to the formation of patterns, we addressed the impact of these two ingredients for systems of curved polymers that move on chiral, circular paths. Indeed, our study showed that even without further interactions actively moving curved polymers self-organize into vortex patterns reminiscent of those observed experimentally. Below, we list the key findings of our corresponding study.

3.1.2 Key findings

This section summarizes results from the publication *"Active Curved Polymers Form Vortex Patterns on Membranes"* to which I contributed as a second author. The manuscript was published in the journal *Physical Review Letters* [63] and is reprinted in Section 3.1.3 of this thesis. Detailed author contributions are listed in the "Abstracts of the projects and contribution" section at the beginning of this thesis.

To study the collective behavior of self-propelled curved filaments on a two-dimensional surface, we employed two distinct theoretical approaches: Brownian dynamics simulations and a kinetic Boltzmann approach. In this way, we comprehensively addressed the corresponding active matter problem by complementing approaches on a single-particle level and a field-theoretical level. The Brownian dynamics simulation explicitly accounted for the dynamics and collisions of polymers on the level of individual particles. The kinetic Boltzmann approach, on the other hand, relied on approximations for the microscopic behavior (collision rules) but provided a coarse-grained field-theoretical approach that was well suited for studying phase transitions more formally. Strikingly, both approaches predicted transitions into differently ordered phases and coincided on a phenomenological level. Thereby, our work established a detailed picture of the emerging properties of our system and proved the robust formation of patterns in systems of actively moving curved filaments.

Remarkably, for intermediate densities and noise levels, the system exhibited a phase of stable, dynamic polymer rings. This shows that active motion in addition to steric interactions alone is already sufficient to self-organize active curved filaments into dynamic vortices similar to the dynamic FtsZ rings observed by Loose and Mitchison; Additional interactions other than hard-core repulsion are not required. By now, such a formation of vortex patterns that is controlled by the surface density of polymers has been confirmed for FtsZ in a recent *in vitro* study that systematically varied the density of FtsZ polymers on a supported membrane [34]. Our study therefore highlighted the impact of active motion on ordering processes that might ultimately be relevant for the formation of the Z ring *in vivo*.

Our kinetic Boltzmann approach further revealed that the onset of pattern formation is governed by a complex Ginzburg-Landau equation with convective spatial

coupling as well as a density-current coupling. This equation represents an interesting mathematical problem on its own right: It constitutes a highly non-trivial extension of the standard complex Ginzburg-Landau equation and is formally distinct to the real Ginzburg-Landau equations that were previously found to describe the formation of patterns in systems of self-propelled particles with preferentially straight paths. While a detailed analysis of this extended Ginzburg-Landau equation still remains an open problem, preliminary numerical analysis suggested the presence of turbulent dynamics, which is absent in analogous theories of the kinetic Boltzmann equation with straight moving particles.

3.1.3 Publication

Active Curved Polymers Form Vortex Patterns on Membranes

by

J. Denk* [,1] , L. Huber* [,1] , E. Reithmann,[1] L. Reese,[1] and E. Frey[1]
*equal contribution,
[1]Arnold Sommerfeld Center for Theoretical Physics and Center for NanoScience,
Department of Physics, Ludwig-Maximilians-Universität München,
Theresienstraße 37, 80333 München, Germany

reprinted on pages 138–143

from

***Phys. Rev. Lett.* 116 (17), 178301 (2016).**
DOI: 10.1103/PhysRevLett.116.178301

Also available on arXiv: 1602.08976.

Supplemental Material reproduced on pages 144–149.

Active Curved Polymers Form Vortex Patterns on Membranes

Jonas Denk, Lorenz Huber, Emanuel Reithmann, and Erwin Frey*
Arnold Sommerfeld Center for Theoretical Physics (ASC) and Center for NanoScience (CeNS), Department of Physics, Ludwig-Maximilians-Universität München, Theresienstrasse 37, D-80333 München, Germany
(Received 16 June 2015; revised manuscript received 9 December 2015; published 25 April 2016)

Recent *in vitro* experiments with FtsZ polymers show self-organization into different dynamic patterns, including structures reminiscent of the bacterial Z ring. We model FtsZ polymers as active particles moving along chiral, circular paths by Brownian dynamics simulations and a Boltzmann approach. Our two conceptually different methods point to a generic phase behavior. At intermediate particle densities, we find self-organization into vortex structures including closed rings. Moreover, we show that the dynamics at the onset of pattern formation is described by a generalized complex Ginzburg-Landau equation.

DOI: 10.1103/PhysRevLett.116.178301

Intracellular structuring is often facilitated by the active dynamics of cytoskeletal constituents. The origin of these driven dynamics and their impact on pattern formation has been extensively studied using artificial motility assays of cytoskeletal filaments [1–4]. Another intriguing example of self-organization due to driven filaments was reported recently by Loose and Mitchison [5]. *In vitro*, the bacterial protein FtsZ forms membrane-bound, intrinsically curved polymers. These seem to exhibit treadmilling dynamics (consuming guanosine triphosphate) and, as a result, move clockwise on the membrane. Depending on the protein density, polymers cluster into dynamic structures such as rotating rings or jammed bundles, despite the absence of attractive interactions [6]. These ring structures are of particular interest, since, *in vivo*, FtsZ builds the contractile Z ring which drives cell division in a yet unknown way [7–9]. But also in the *in vitro* experiments, the pattern-forming mechanism remains unclear even on a qualitative level.

Motivated by these experimental findings, we have studied pattern formation in a class of active systems, where particles move on circular tracks and interact only via steric repulsion. To assess the dynamics of this class, we consider two conceptually different models: First, we emulate active particles as elastic polymers with fixed intrinsic curvature that move with a constant tangential velocity [Fig. 1(a)] and perform Brownian dynamics simulations. Second, we employ a kinetic Boltzmann approach, where pointlike particles move on circular paths and undergo diffusion and binary collisions (with polar symmetry) according to a simplified collision rule [Fig. 1(b)]. As a result, we identify different phases of collective behavior as a function of density and noise level. With both approaches, we find flocking into vortex patterns in the regime of intermediate density and noise strength. Our simulations for extended particles predict the formation of closed ring structures reminiscent of those found in Ref. [5], even in the absence of any attractive interactions. In the mesoscopic limit, our analysis yields that, close to the onset of vortex formation, the dynamics at the onset of ordering is characterized by a novel generalization of the complex Ginzburg-Landau equation.

In our Brownian dynamics simulations, we consider a system of M curved polymers of the same chirality embedded in a two-dimensional membrane of area A with periodic boundary conditions. Each polymer is described as an inextensible wormlike chain [10,11] of length L, persistence length ℓ_p, and intrinsic curvature κ_0. For a given polymer conformation $\mathbf{r}(s)$, parameterized in terms of arc length s, the overall bending energy is given by $E_{\mathrm{bend}} = \frac{1}{2}\ell_p k_B T \int_0^L ds[\kappa(s) - \kappa_0]^2$, where $\kappa(s) = |\partial_s^2 \mathbf{r}(s)|$ denotes the local curvature. Excluded volume interaction is implemented by a repulsive truncated Lennard-Jones potential. To assure motion of the filament contour on a circular track (apart from noise), polymers are propelled with a tangential velocity $\mathbf{v}_0(s) = v_0 \partial_s \mathbf{r}(s)$. This accounts for the effective motion of treadmilling in a simplified way [12].

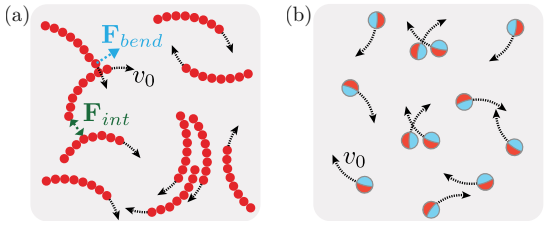

FIG. 1. Systems of active particles, which are driven on chiral, circular tracks with speed v_0: (a) *Microscopic view*: Extended, elastic polymers with intrinsic curvature, where noise and steric interaction trigger bending of filaments. (b) *Mesoscopic view*: Pointlike particles that undergo diffusion as well as binary collisions.

Note that, for this choice, the area explored by a circling polymer is minimal. In the free draining limit, the dynamics of the polymer system is then determined by a set of coupled Langevin equations for the contours $\mathbf{r}^{(m)}(t,s)$ of each polymer $m = 1, 2, \ldots, M$: $\zeta(\partial_t \mathbf{r}^{(m)} - \mathbf{v}_0^{(m)}) = -\delta E[\{\mathbf{r}^{(n)}\}]/\delta \mathbf{r}^{(m)} + \boldsymbol{\eta}^{(m)}$, balancing viscous friction with elastic and repulsive forces generated by the total energy E and Langevin noise $\boldsymbol{\eta}$ with zero mean and $\langle \boldsymbol{\eta}(t,s) \cdot \boldsymbol{\eta}(t',s') \rangle = 4k_B T \zeta \delta(t-t')\delta(s-s')$. To numerically solve the polymer dynamics, we employ a bead-spring representation of the polymers [12,17,18]. For most simulations, we adapted length scales close to those observed in Refs. [5,8]: $\kappa_0^{-1} = 0.5\,\mu$m, $L = 0.9\ \mu$m, and $\ell_p = 10\ \mu$m. The relevant dimensionless parameters that characterize the system are the reduced noise σ and density ρ. Here, $\sigma := k_B T \ell_p/(\zeta v_0 L^2)$ relates thermal forces at length scale ℓ_p with friction forces, and $\rho := (R_0/b)^2$ denotes the squared ratio of the radius of curvature $R_0 = \kappa_0^{-1}$ to the mean polymer distance $b = \sqrt{A/M}$.

For dilute systems $\rho \ll 1$, our simulations show that each polymer is propelled on a circular path and collisions between polymers are infrequent; see Fig. 2(a) and Movie 1 in Supplemental Material [12]. The positions of the polymers' centers of curvature (CC) $\mathbf{r}_{\mathrm{CC}}^{(m)}$ are uncorrelated as in a gas, and we refer to this state as a *disordered state*. On increasing ρ, we observe that a significant fraction of filaments begin to collide and collect into localized vortex structures (*vortex state*). These ringlike structures are highly dynamic. They assemble and persist for several rotations, during which their centers of mass remain relatively static; see Fig. 2(b) and Movie 2 [12]. Despite our simplified kinetic assumption, the overall phenomenology resembles the FtsZ patterns observed by Loose and Mitchison [5], including vortex assembly, disassembly, and localization. In the dense regime $\rho \gtrsim 1$, where each polymer is likely to collide, these vortices are unstable. Instead, the polymers cluster and form jammed "trains" that travel through the system in an irregular fashion; see Fig. 2(c) and Movie 3 [12].

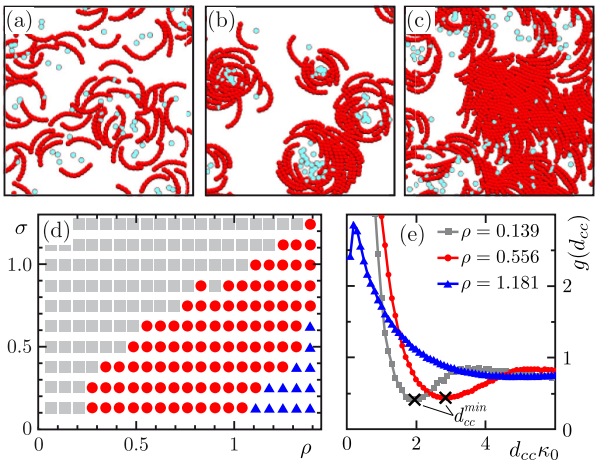

FIG. 2. System snapshots are provided to depict (a) disorder ($\rho = 0.556$, $\sigma = 0.987$), (b) vortices ($\rho = 0.556$, $\sigma = 0.247$), and (c) trains ($\rho = 1.389$, $\sigma = 0.247$). Curvature centers $\mathbf{r}_{\mathrm{CC}}^{(m)}$ are depicted by light blue dots. (d) Phase portrait for varying density ρ and noise σ: disorder states (gray rectangles), vortex states (red circles), and train states (blue triangles). (e) Pair correlation function $g(d_{\mathrm{CC}})$ for the three different states with $\sigma = 0.247$ and ρ indicated in the graph.

In order to quantitatively distinguish between the various observed patterns and organize them into a "phase diagram," we consider the pair correlation function $g(d_{\mathrm{CC}})$ [19,20] of distances $d_{\mathrm{CC}} = |\mathbf{r}_{\mathrm{CC}}^{(m)} - \mathbf{r}_{\mathrm{CC}}^{(n)}|$ between the centers of curvature [Fig. 2(d)]. We regard a system as disordered if $g(d_{\mathrm{CC}})$ exhibits a minimum at a distance $d_{\mathrm{CC}}^{\mathrm{min}}$ equal to the diameter of a free circular path, $d_{\mathrm{CC}}^{\mathrm{min}} \approx 2R_0$. This is distinct from vortex states, where $d_{\mathrm{CC}}^{\mathrm{min}}$, defining an effective vortex diameter, is larger than $2R_0$. Finally, for train states, $g(d_{\mathrm{CC}})$ does not exhibit a local minimum, indicating the absence of an isolated vortex structure; for more details, see Supplemental Material [12]. The ensuing phase diagram is shown in Fig. 2(d). As in other active systems [21–28], pattern formation is favored by increasing density and decreasing noise strength. Jammed states prevail only when the density is high and the noise level low. Note also that the structure of the phase diagram depends on the ratio of filament length L to radius of curvature R_0. Polymers with an arc angle close to $\kappa_0 L = 2\pi$ (closed circles) retain a single-circle structure and do not form any collective structures upon increasing ρ (Movie 4 [12]). Conversely, reducing $\kappa_0 L$ suppresses the formation of closed ring structures, due to inefficient alignment of short polymers. Instead, these polymers cluster into flocks which move on approximately circular paths (Movie 5 [12]). Hence, we conclude that the range of arc angles of FtsZ polymers, $\kappa_0 L \approx 0.6\pi$, observed *in vitro* [5], facilitates the formation of closed polymer rings particularly well [Fig. 2(b)]. In summary, closed polymer rings require explicit curvature and filament lengths larger than a certain threshold value. For other interactions than local, steric repulsion ring structures may also emerge [1,3,29]; straight, rotating rods may form vortex arrays but not closed rings [30].

We complement the Brownian dynamics simulations of active particles that are propelled on circular tracks by considering the mesoscopic limit of a vanishing particle extension. To this end, we have employed a kinetic Boltzmann approach [24,31–36] to determine the collective behavior and the corresponding phase transitions in this limit, irrespective of the microscopic details of the constituent particles. In detail, we simplified the active system to one consisting of spherical particles (of diameter d) moving clockwise with constant speed v_0 on circular orbits of radius R_0. This accounts for both self-propulsion and

spontaneous curvature but neglects the finite extension of the polymers as compared to our Brownian dynamics simulations.

We further assume that a particle's orientation is altered by "self-diffusion" as well as by local binary collisions. In self-diffusion, a particle's instantaneous orientation θ changes at rate λ into $\theta+\eta$, where we assume η to be Gaussian distributed with standard deviation σ. As in other particle-based active systems [32,34,37], binary collisions are modeled by a polar alignment rule where the orientations of the collision partners align along their average angle plus a Gaussian-distributed fluctuation; for simplicity, we take the same width σ as for self-diffusion.

The kinetic Boltzmann equation [24,31–36] for the one-particle distribution function $f(\mathbf{r},\theta,t)$ then reads

$$\partial_t f + v_0[\mathbf{e}_\theta\cdot\partial_{\mathbf{r}} + \kappa_0\partial_\theta]f = \mathcal{I}_d[f] + \mathcal{I}_c[f,f]. \quad (1)$$

It describes the dynamics of the density of particles in phase-space element $d\mathbf{r}d\theta$ which is being convected due to particle self-propulsion and which undergoes rotational diffusion and binary particle collisions, as given by the collision integrals $\mathcal{I}_d[f]$ and $\mathcal{I}_c[f,f]$, respectively; for explicit expressions, please see Supplemental Material [12]. Note here the critical difference from field theories for straight-moving particles [32,38–40]; there is an additional angular derivative in the convection term, which reflects the fact that the particles are moving on circular orbits. In the following, we rescale the time, space, and density such that $v_0=\lambda=d=1$. Then, the only remaining free parameters are the noise amplitude σ, κ_0, and the mean particle density $\bar\rho = A^{-1}\int_A d\mathbf{r}\int_{-\pi}^{\pi} d\theta f(\mathbf{r},\theta,t)$ measured in units of $\lambda/(dv_0)$, i.e., the number of particles found within the area traversed by a particle between successive self-diffusion events.

To identify possible solutions of the Boltzmann equation and analyze their stability, we performed a spectral analysis. Upon expanding the one-particle distribution function in terms of Fourier modes of the angular variable, $f_k(\mathbf{r},t) = \int_{-\pi}^{\pi} d\theta e^{i\theta k} f(\mathbf{r},\theta,t)$, one obtains

$$\partial_t f_k + \frac{v_0}{2}[\partial_x(f_{k+1}+f_{k-1}) - i\partial_y(f_{k+1}-f_{k-1})] - ikv_0\kappa_0 f_k$$
$$= -\lambda(1-e^{-(k\sigma)^2/2})f_k + \sum_{n=-\infty}^{\infty}\mathcal{I}_{n,k}f_n f_{k-n}, \quad (2)$$

where explicit expressions for the collision kernels $\mathcal{I}_{n,k}(\sigma)$ are given in Supplemental Material [12]. For $k=0$, Eq. (2) yields the continuity equation $\partial_t\rho = -\nabla\cdot\mathbf{j}$ for the local density $\rho(\mathbf{r},t) \coloneqq f_0(\mathbf{r},t)$ with the particle current given by $\mathbf{j}(\mathbf{r},t) = v_0(\mathrm{Re}f_1, \mathrm{Im}f_1)^T$. In general, Eq. (2) constitutes an infinite hierarchy of equations coupling lower- with higher-order Fourier modes.

A linear stability analysis of Eq. (2) enables further progress. Since $\mathcal{I}_{n,0}=0$ for all n, a state with spatially homogeneous density $\bar\rho = f_0$ and all higher Fourier modes vanishing is a stationary solution to Eq. (2) (disordered state). To linear order, the dynamics of small perturbations δf_k with respect to this uniform state is given by $\partial_t\delta f_k = \mu_k(\bar\rho,\sigma)\delta f_k$, where $\mu_k(\bar\rho,\sigma) = (\mathcal{I}_{0,k}+\mathcal{I}_{k,k})\bar\rho - \lambda(1-e^{-(k\sigma)^2/2})$. For a polar collision rule, as considered here, only μ_1 can become positive, defining a critical density $\rho_c(\sigma)$ at $\mu_1(\rho_c,\sigma) \coloneqq 0$ [Fig. 3(a)]. Above the threshold ($\bar\rho>\rho_c$), the spatially homogeneous state is unstable, the particle current grows exponentially, and collective motion may emerge.

In close proximity to the critical density $\rho_c(\sigma)$, a weakly nonlinear analysis yields further insights into the dynamics of the system and the ensuing steady states. Here we follow Ref. [31] and assume small currents $f_1 \ll 1$ at the onset. Then, balancing of the terms in the continuity equation, the equation for f_1, and terms involving f_1 in the equation for f_2 implies the scaling $\rho-\bar\rho\sim f_1$, $f_2\sim f_1^2$ as well as weak spatial and temporal variations $\partial_{x/y}\sim f_1$, $\partial_t\sim f_1$. To include the lowest-order damping term in f_1, we retain terms up to cubic order in f_1. This yields the following hydrodynamic equation for the complex particle current $v_0 f_1(\mathbf{r},t) = j_x(\mathbf{r},t) + ij_y(\mathbf{r},t)$:

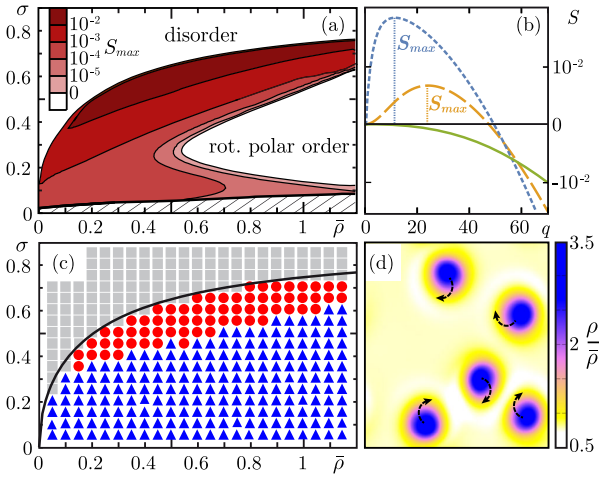

FIG. 3. (a) Stability of homogeneous solutions of Eq. (2) as a function of σ and $\bar\rho$ in units of $\lambda/(dv_0)$. White and red areas denote regions where finite wavelength perturbations of the homogeneous solutions are stable and unstable, respectively. The color code denotes the value of the maximal growth rate $S_{\max}$. (b) Dispersion relation of $S(q)$ (q in units of $2\pi/\sqrt{A}$) for $\bar\rho=0.8$ and $\sigma=0.7$ (short-dashed line), $\sigma=0.6$ (long-dashed line), and $\sigma=0.4$ (solid line). Vertical lines indicate $S_{\max}$. (c) Phase diagram for density $\bar\rho$ and σ displaying phases of homogeneous disorder (gray rectangles), swirls (red circles), and homogeneous order (blue triangles). The solid line marks the analytic solution of $\rho_c(\sigma)$. An overlay of (a) and (c) can be found in Supplemental Material [12]. (d) Snapshot of swirl patterns ($\bar\rho=0.8$, $\sigma=0.7$). All swirls are moving clockwise on circular paths.

$$\partial_t f_1(\mathbf{r},t) = [\alpha(\rho-\rho_c) + iv_0\kappa_0]f_1 - \xi|f_1|^2 f_1 - \frac{v_0}{2}\nabla\rho - \beta f_1^*\nabla f_1 - \gamma f_1\nabla^* f_1 + \nu\nabla^*\nabla f_1, \quad (3)$$

where $\nabla := \partial_x + i\partial_y$. While this equation shows similar functional dependencies on local density and current as found in systems without [41] and with straight propulsion [32], the coefficients α, ξ, ν, γ, and β are now *complex valued* (for explicit expressions, please see Supplemental Material [12]). This can be traced back to the angular convection term in Eq. (1) or, equivalently, to the corresponding phase-shift term in Eq. (2). As a consequence, the field theory of active systems with particles moving on circular orbits with defined chirality is generically given by a complex Ginzburg-Landau (GL) equation with convective spatial coupling as well as density-current coupling. This constitutes a highly interesting generalization of the standard (diffusive) complex GL equations [42,43] and is qualitatively different from real GL-type equations that were previously applied in the context of self-propelled particles [31]. Above the threshold, $\bar{\rho} > \rho_c(\sigma)$, the active chiral hydrodynamics described by the generalized GL equation (3) exhibits a uniform oscillatory solution with $f_1 = F_1 e^{i\Omega_0 t}$, i.e., a state in which particles move on a circular (chiral) path with an angular velocity $\Omega_0 = v_0\kappa_0 - \alpha(\bar{\rho}-\rho_c)\mathrm{Im}[\xi]/\mathrm{Re}[\xi]$; the amplitude $F_1 = \{\alpha(\bar{\rho}-\rho_c)/\mathrm{Re}[\xi]\}^{1/2}$ gives the particle density. However, a linear stability analysis of Eq. (3) shows that for densities slightly larger than ρ_c this oscillatory solution is linearly unstable against finite wavelength perturbations in the current and density fields. Preliminary numerical solutions of the generalized GL equation [Eq. (3)] take the form of rotating spots of high density that appear to show turbulent dynamics [12,44]. This is qualitatively distinct from the high-density bands found for straight-moving particles [23,45] and the vortex field of a fluid coupled to torque dipoles [46,47].

Far above the threshold, closure relations such as those discussed above [31] may become invalid and with them the ensuing hydrodynamic equations. Therefore, we proceed with the full spectral analysis of the Boltzmann equation [Eq. (2)] as detailed in Supplemental Material [12]. First, we numerically calculate the spatially homogeneous solutions for all angular Fourier modes f_k below some cutoff wave vector $k_{\max}$. For given values of $\bar{\rho}$ and σ and a desired accuracy ε of this mode truncation scheme, the cutoff is chosen such that $|f_{k_{\max}+1}| < \varepsilon$. We find that for $\bar{\rho} < \rho_c(\sigma)$ a spatially homogeneous state where all modes but f_0 vanish is the only stable state. In contrast, above the threshold [$\bar{\rho} > \rho_c(\sigma)$], there is a second solution for which $|f_1| > 0$. It corresponds to a polar ordered state whose orientation is changing periodically in time with frequency $v_0\kappa_0$. For moderate $\bar{\rho}-\rho_c$, the amplitude quantitatively agrees with the result from the generalized GL equation; see Supplemental Material [12]. In a second step, we consider wavelike perturbations, $\delta f_k(\mathbf{q})$ with wave vector $\mathbf{q}$, of the spatially homogeneous oscillatory solution in a corotating frame. The largest real part of all eigenvalues of the corresponding linearized system for δf_k then yields the linear growth rate $S(q)$ [Fig. 3(b)]. In accordance with the linear stability analysis of Eq. (3), we find that for densities slightly larger than ρ_c a spatially homogeneous solution is unstable against finite wavelength perturbations. The dispersion relation $S(q)$ exhibits a band of unstable modes, with the maximal growth rate $S_{\max}$ decreasing as one moves away from the threshold ρ_c [Figs. 3(a) and 3(b)]. Actually, there is lobelike regime in parameter space where $S(q) < 0$ [Fig. 3(a)], and hence a homogeneously polar ordered state with rotating direction is stable. We emphasize here that our stability portrait [Fig. 3(a)] is independent of κ_0 and hence equally valid for systems of straight-moving particles. For our two approaches [Figs. 2(d) and 3(a)], the onset to order is governed by a similar trend [12], common for active systems [28,48]: Disorder prevails for low density or high noise, and order is promoted for high density or low noise.

To determine the spatiotemporal dynamics in the regime where neither a spatially homogeneous state nor a homogeneously polar ordered state are stable, we resort to a modified version of the SNAKE algorithm [34] to numerically solve Eq. (1). It accurately reproduces the threshold value $\rho_c(\sigma)$ at which the spatially homogeneous state becomes unstable [Fig. 3(c)]. Above the threshold ($\bar{\rho} > \rho_c$), we find that local density fluctuations quickly grow and evolve into stable swirls, i.e., disklike flocks of high density and polar order moving on circular paths; see Fig. 3(d) and Movie 6 in Supplemental Material [12]. The radius of such a path is approximately given by R_0. These swirl patterns closely resemble the swirling flocks observed in the Brownian dynamics simulations for short polymer arc angles (Movie 5 [12]), as well as our preliminary numerical solutions of the generalized GL equation [Eq. (3)] [12,44]. Moreover, in accordance with the spectral analysis, we find a second threshold density, above which the system settles into a homogeneously polar ordered state with a periodically changing orientation (Movie 7 [12]). The amplitude and frequency of the polar order agree with the numerical results of the spectral analysis to high accuracy [12], while the numerically determined phase boundaries differ. The SNAKE algorithm produces stable swirl patterns only in a parameter regime where our linear stability analysis yields significant growth rates. This is mainly due to spurious noise caused by the discretization of the angular variable, which tends to suppress inhomogeneities in the regime of small growth rates. Furthermore, the finite system size constricts the band of possible modes and allows only for patterns of sufficiently short length scales.

For active systems of circling particles that interact via steric repulsion, our microscopic and mesoscopic treatments strongly suggest that a phase of collective vortex structures is a generic feature. Within this class, our work

shows that extended polymers which as a whole follow circular tracks can form closed rings. Concerning our motivation of circling FtsZ, further research is needed to elucidate the dynamics of treadmilling; yet our minimal kinetic assumption suggests that varying the particle density alone suffices to regulate the patterns as observed by Loose and Mitchison [5]. Compared to systems of straight-moving particles, we find qualitatively new phenomena [12,44]. For those systems, it was already reported that (globally achiral) vortices can occur due to collisions of particles of asymmetric shape [49] or due to memory in orientation [3,50]. Some of our findings, like the polymer length dependence of patterns and the possible emergence of active turbulence [51,52], pose interesting questions for future work. Our analysis yields a mapping of the emergent dynamics onto a generalized Ginzburg-Landau equation, providing a connection between active matter and nonlinear oscillators [44].

We thank F. Thüroff, L. Reese, and J. Knebel for helpful discussions. This research was supported by the German Excellence Initiative via the program "NanoSystems Initiative Munich" (NIM) and the graduate school "Quantitative Biosciences Munich" (QBM), and the Deutsche Forschungsgemeinschaft (DFG) via project B02 within the Collaborative Research Center (SFB 863) "Forces in Biomolecular Systems."

J. D. and L. H. contributed equally to this work.

*frey@lmu.de

[1] V. Schaller, C. A. Weber, B. Hammerich, E. Frey, and A. R. Bausch, Proc. Natl. Acad. Sci. U.S.A. **108**, 19183 (2011).
[2] V. Schaller, C. A. Weber, C. Semmrich, E. Frey, and A. R. Bausch, Nature (London) **467**, 73 (2010).
[3] Y. Sumino, K. H. Nagai, Y. Shitaka, D. Tanaka, K. Yoshikawa, H. Chaté, and K. Oiwa, Nature (London) **483**, 448 (2012).
[4] R. Suzuki, C. A. Weber, E. Frey, and A. R. Bausch, Nat. Phys. **11**, 839 (2015).
[5] M. Loose and T. J. Mitchison, Nat. Cell Biol. **16**, 38 (2013).
[6] E. L. Meier and E. D. Goley, Curr. Opin. Cell Biol. **26**, 19 (2014).
[7] M. Ingerson-Mahar and Z. Gitai, FEMS Microbiol. Rev. **36**, 256 (2012).
[8] H. P. Erickson, D. E. Anderson, and M. Osawa, Microbiol. Mol. Biol. Rev. **74**, 504 (2010).
[9] P. Szwedziak, Q. Wang, T. A. M. Bharat, M. Tsim, and J. Löwe, eLife **3**, e04601 (2014).
[10] O. Kratky and G. Porod, Recl. Trav. Chim. Pays-Bas **68**, 1106 (1949).
[11] N. Saitô, K. Takahashi, and Y. Yunoki, J. Phys. Soc. Jpn. **22**, 219 (1967).
[12] See Supplemental Material at http://link.aps.org/supplemental/10.1103/PhysRevLett.116.178301 for a detailed description of the numerical methods and analytical derivations, which contains Refs. [13–16].
[13] P. Kloeden and E. Platen, *Numerical Solution of Stochastic Differential Equations* (Springer, Berlin, 1992).
[14] R. E. Goldstein and S. A. Langer, Phys. Rev. Lett. **75**, 1094 (1995).
[15] M. Hinczewski, X. Schlagberger, M. Rubinstein, O. Krichevsky, and R. R. Netz, Macromolecules **42**, 860 (2009).
[16] C. Bennemann, J. Baschnagel, W. Paul, and K. Binder, Comput. Theor. Polym. Sci. **9**, 217 (1999).
[17] G. Chirico and J. Langowski, Biopolymers **34**, 415 (1994).
[18] H. Wada and R. R. Netz, Europhys. Lett. **77**, 68001 (2007).
[19] J. K. G. Dhont, *An Introduction to Dynamics of Colloids* (Elsevier, Amsterdam, 1996).
[20] X. Lu and Y. Hu, *Molecular Thermodynamics of Complex Systems* (Springer, Heidelberg, 2008).
[21] T. Vicsek, A. Czirók, E. Ben-Jacob, I. Cohen, and O. Shochet, Phys. Rev. Lett. **75**, 1226 (1995).
[22] I. H. Riedel, K. Kruse, and J. Howard, Science **309**, 300 (2005).
[23] H. Chaté, F. Ginelli, G. Grégoire, and F. Raynaud, Phys. Rev. E **77**, 046113 (2008).
[24] E. Bertin, M. Droz, and G. Grégoire, Phys. Rev. E **74**, 022101 (2006).
[25] T. Ihle, Phys. Rev. E **83**, 030901 (2011).
[26] F. Ginelli, F. Peruani, M. Bär, and H. Chaté, Phys. Rev. Lett. **104**, 184502 (2010).
[27] F. Peruani, J. Starruß, V. Jakovljevic, L. Søgaard-Andersen, A. Deutsch, and M. Bär, Phys. Rev. Lett. **108**, 098102 (2012).
[28] M. C. Marchetti, J. F. Joanny, S. Ramaswamy, T. B. Liverpool, J. Prost, M. Rao, and R. A. Simha, Rev. Mod. Phys. **85**, 1143 (2013).
[29] Y. Yang, F. Qiu, and G. Gompper, Phys. Rev. E **89**, 012720 (2014).
[30] A. Kaiser and H. Löwen, Phys. Rev. E **87**, 032712 (2013).
[31] A. Peshkov, E. Bertin, F. Ginelli, and H. Chaté, Eur. Phys. J. Spec. Top. **223**, 1315 (2014).
[32] E. Bertin, M. Droz, and G. Grégoire, J. Phys. A **42**, 445001 (2009).
[33] A. Peshkov, I. S. Aranson, E. Bertin, H. Chaté, and F. Ginelli, Phys. Rev. Lett. **109**, 268701 (2012).
[34] F. Thüroff, C. A. Weber, and E. Frey, Phys. Rev. X **4**, 041030 (2014).
[35] C. A. Weber, F. Thüroff, and E. Frey, New J. Phys. **15**, 045014 (2013).
[36] F. Thüroff, C. A. Weber, and E. Frey, Phys. Rev. Lett. **111**, 190601 (2013).
[37] A. Peshkov, S. Ngo, E. Bertin, H. Chaté, and F. Ginelli, Phys. Rev. Lett. **109**, 098101 (2012).
[38] J. Toner and Y. Tu, Phys. Rev. Lett. **75**, 4326 (1995).
[39] A. Baskaran and M. C. Marchetti, Phys. Rev. E **77**, 011920 (2008).
[40] S. Mishra, A. Baskaran, and M. C. Marchetti, Phys. Rev. E **81**, 061916 (2010).
[41] I. S. Aranson and L. S. Tsimring, Phys. Rev. E **71**, 050901 (R) (2005).
[42] I. S. Aranson and L. Kramer, Rev. Mod. Phys. **74**, 99 (2002).
[43] V. García-Morales and K. Krischer, Contemp. Phys. **53**, 79 (2012).

[44] L. Huber, J. Denk, E. Reithmann, E. Frey (to be published).
[45] H. Chaté, F. Ginelli, G. Grégoire, F. Peruani, and F. Raynaud, Eur. Phys. J. B **64**, 451 (2008).
[46] S. Fürthauer, M. Strempel, S. W. Grill, and F. Jülicher, Eur. Phys. J. E **35**, 89 (2012).
[47] S. Fürthauer, M. Strempel, S. W. Grill, and F. Jülicher, Phys. Rev. Lett. **110**, 048103 (2013).
[48] S. Ramaswamy, Annu. Rev. Condens. Matter Phys. **1**, 323 (2010).
[49] H. H. Wensink, V. Kantsler, R. E. Goldstein, and J. Dunkel, Phys. Rev. E **89**, 010302 (2014).
[50] K. H. Nagai, Y. Sumino, R. Montagne, I. S. Aranson, and H. Chaté, Phys. Rev. Lett. **114**, 168001 (2015).
[51] J. Dunkel, S. Heidenreich, K. Drescher, H. H. Wensink, M. Bär, and R. E. Goldstein, Phys. Rev. Lett. **110**, 228102 (2013).
[52] V. Bratanov, F. Jenko, and E. Frey, Proc. Natl. Acad. Sci. U.S.A. **112**, 15048 (2015).

Supplemental Material: Active Curved Polymers form Vortex Patterns on Membranes

Jonas Denk, Lorenz Huber, Emanuel Reithmann, and Erwin Frey*
Arnold Sommerfeld Center for Theoretical Physics (ASC) and Center for NanoScience (CeNS), Department of Physics, Ludwig-Maximilians-Universität München, Theresienstrasse 37, 80333 München, Germany

COMMENT ON TREADMILLING

In their experiments [1], Loose and Mitchison observe that FtsZ polymers undergo depolymerization and polymerization processes leading to an effective translation in the direction of the polymers' backbones. However, the underlying molecular details are unclear, as they involve many qualitatively and quantitatively unknown reactions and a yet unstudied interplay of different auxiliary proteins (*e.g.* FtsA, ZipA). Here, we neglect these details and focus on the collective effects of many FtsZ polymers retaining only their effective movement along circular tracks. To realize this kind of motion we assume an intrinsic particle velocity.

NUMERICAL IMPLEMENTATION OF BROWNIAN DYNAMICS

In the following, we discuss the details of the implementation of the Brownian dynamics simulations. We use a bead-spring model [2, 3] that comprises the following discretization scheme: a polymer of length L is subdivided into N beads at positions $\mathbf{r}_i = (x_i, y_i)^T$ $(i = 1, 2, ..., N)$, with $N-1$ bonds of length a; the (normalized) bond vectors are given by $\partial_s \mathbf{r} \approx \frac{\mathbf{r}_{i+1}-\mathbf{r}_i}{a} =: \hat{\mathbf{t}}_i$; the bending angle between two adjacent bonds is given by $\theta_i = \arccos(\hat{\mathbf{t}}_{i+1} \cdot \hat{\mathbf{t}}_i)$. The corresponding bending energy reads

$$E_{bend} = \frac{\ell_p}{2a} k_B T \sum_{i=1}^{N-2} (\theta_i - \theta_0)^2. \tag{S1}$$

where $\theta_0 \approx a\kappa_0$ is the spontaneous bending angle. In the bead-spring model, neighboring beads are connected by stiff harmonic springs. The corresponding stretching energy is given by

$$E_{stretch} = \frac{k}{2} \sum_{i=1}^{N-1} (|\mathbf{r}_{i+1} - \mathbf{r}_i| - a)^2. \tag{S2}$$

In the simulations, the spring constant k is chosen larger than all other force constants to account for the fact that biopolymers are nearly inextensible; as a consequence, stretching modes relax fast compared to other dynamic processes. At the same time, k cannot be chosen arbitrarily large as this would strongly limit the maximal simulation time T_{max} (see below for values).

In the two-dimensional system of M polymers, we assume steric repulsion between adjacent polymer segments $\mathbf{r}_i^{(m)}$ $(m = 1, 2, ..., M)$. As an interaction potential we use a truncated Lennard-Jones potential [4–6]

$$(E_{int})_{ij}^{(mn)} = \epsilon \left[\left(\frac{a}{r_{ij}^{(mn)}} \right)^{12} - \left(\frac{a}{r_{ij}^{(mn)}} \right)^{6} \right] \Theta(a - r_{ij}^{(mn)}), \tag{S3}$$

with $r_{ij}^{(mn)} = |\mathbf{r}_i^{(m)} - \mathbf{r}_j^{(n)}|$, ϵ the potential strength, and $\Theta(r)$ the Heaviside step function. At distances smaller than the bond length a, the potential is strongly repulsive.

In the Langevin description, the equation of motion is given by a force balance between elastic, active, thermal and dissipative terms. For the i-th bead of a polymer, the equation of motion reads

$$\begin{aligned} \zeta \partial_t \mathbf{r}_i &= -\frac{\delta E}{\delta \mathbf{r}_i} + \mathbf{F}_i^{prop} + \boldsymbol{\eta}_i \\ &= \mathbf{F}_i^{bend} + \mathbf{F}_i^{stretch} + \mathbf{F}_i^{int} + \mathbf{F}_i^{prop} + \boldsymbol{\eta}_i \end{aligned} \tag{S4}$$

where $E = E_{bend} + E_{stretch} + E_{int}$, $\mathbf{F}_{prop}$ is the propulsive force and the amplitude of the thermal forces is given by $\langle \boldsymbol{\eta}_i(t) \cdot \boldsymbol{\eta}_j(t') \rangle = 4 k_B T \zeta \delta_{ij} \delta(t - t')$. The bending, stretching and interaction forces $\mathbf{F}_i^{bend}, \mathbf{F}_i^{stretch}, \mathbf{F}_i^{int}$ are obtained by variation of the corresponding energetic terms with respect to the position vector $\mathbf{r}_i$ [2, 3]. We employ the following implementation of the tangential propulsive force $\mathbf{F}^{prop} = \zeta v_0 \partial_s \mathbf{r}$:

$$\mathbf{F}_i^{prop} = \zeta v_0 \begin{cases} \hat{\mathbf{t}}_1 & i = 1 \\ (\hat{\mathbf{t}}_{i-1} + \hat{\mathbf{t}}_i)/2 & 1 < i < N \\ \hat{\mathbf{t}}_{N-1} & i = N \end{cases} \tag{S5}$$

For the integration of Eq. (S4) we use an Euler-Maruyama iteration scheme [7] with sufficiently small time steps $\Delta = 0.0001\tau$ with the unit time $\tau = \zeta a^2/(k_B T)$. In our simulations, we used the following set of parameters: $L = 9a, \ell_p = 100a, k = 500 k_B T/a^2, \epsilon = 1 k_B T, \theta_0 = 0.2, \zeta = 1$ and a periodic system of area $A = 60a \times 60a$ (such that it can contain many consecutive polymer lengths). In the main text, the unit of length is set to $a = 100\,nm$, such that $L = 0.9\,\mu m, \ell_p = 10\,\mu m$ are roughly similar to FtsZ filaments. The noise strength $\sigma = k_B T \ell_p/(\zeta v_0 L^2)$ was varied as follows: we changed the temperature scale in the interval $k_B T \in [0, 1]$ for $v_0 = 5$, and for $k_B T = 1$ varied v_0 in the range $v_0 \in [1, 5]$. The maximal simulation times T_{max} for all simulations in the main text were chosen such that the single polymer rotation time $\tau_R = 2\pi/(\kappa_0 v_0)$ is much smaller. We

took $T_{max} > 400\tau_R$ and $T_{max} > 700\tau$ for our data to provide a sufficiently large sampling interval for both convective and diffusive motion. To consolidate the results, data were recorded for 10 independent simulation for each given set of parameters.

ANALYSIS OF THE PAIR CORRELATION FUNCTION

To analyze the patterns observed in the Brownian dynamics simulations, we consider the pair correlation function $g(d_{cc})$ [8, 9] of center distances $d_{cc} = |\mathbf{r}_{cc}^{(m)} - \mathbf{r}_{cc}^{(n)}|$. The positions $\mathbf{r}_{cc}^{(m)}$ are the curvature centers of each polymer, generated by averaging over the local curvature and all local reference positions on a contour (see Fig. S1(a)). In contrast to the positions $\mathbf{r}^{(m)}$, the curvature centers do not oscillate due to self-propulsion and hence represent a more stable measure of particle position.

Figure S1(b) displays the contour of $g(d_{cc})$ for parameters $k_BT = 0.5$ and $v_0 = 5$ (i. e. $\sigma = 0.247$). For sufficiently small ρ, the density exhibits a local minimum at d_{cc}^{min}, the diameter of a vortex. This implies that there is a preferred vortex size and structure connected to the distance d_{cc}^{min}. These minima were determined after applying a Gaussian filter to suppress random fluctuation artifacts and then used to distinguish the observed patterns according to the 'phase' criteria introduced in the main text: *disordered states* for $d_{cc}^{min} \approx 2R_0$, *vortex states* for $d_{cc}^{min} > 2R_0$ and *train states* without d_{cc}^{min}.

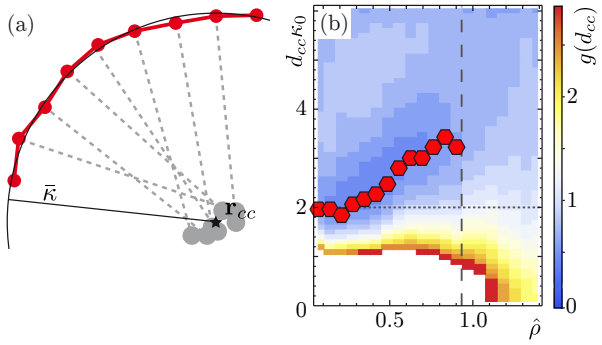

FIG. S1. **(a)** Illustration of the curvature center $\mathbf{r}_{cc}$ as determined by averaging over local centers with a mean contour curvature $\bar{\kappa}$ (polymer in red). **(b)** Heat map of the pair correlation function for $\sigma = 0.247$ in terms of distances d_{cc} and densities ρ. Red polygons denote the positions of d_{cc}^{min}. The short dashed line depicts the free polymer radius and the long dashed line marks the regime where d_{cc}^{min} vanishes.

DERIVATION OF THE HYDRODYNAMIC EQUATIONS

To assess the dynamics at larger scales, we employed a kinetic Boltzmann approach. The corresponding generalized Boltzmann equation for $f(\theta, \mathbf{r}, t)$ is given by Eq. (1). The self-diffusion and collision integrals $\mathcal{I}_d$ and $\mathcal{I}_c$, respectively, are given by

$$\mathcal{I}_d[f] = \lambda \langle \int_{-\pi}^{\pi} \mathrm{d}\phi f(\phi) \left[\delta(\theta - \phi - \eta) - \delta(\theta - \phi)\right] \rangle_\eta \,, \tag{S6}$$

$$\mathcal{I}_c[f; f] = \langle \int_{-\pi}^{\pi} \mathrm{d}\phi_1 \int_{-\pi}^{\pi} \mathrm{d}\phi_2 \mathcal{S}(|\phi_1 - \phi_2|) f(\phi_1) f(\phi_2) \times \left[\delta(\theta - \frac{1}{2}(\phi_1 + \phi_2) - \eta) - \delta(\theta - \phi_1)\right] \rangle_\eta \,, \tag{S7}$$

where $\mathcal{S}(\psi) = 4dv_0 |\sin(\frac{\psi}{2})|$ is the scattering cross section for spherical particles of diameter d and velocity v_0 in two dimensions as detailed in Ref. [10]. The collision integral represents ferromagnetic alignment of two particles with orientation ϕ_1 and ϕ_2 along their average angle $\theta = \frac{1}{2}(\phi_1 + \phi_2)$. The brackets denote an average over a Gaussian-distributed noise variable η. To obtain a dimensionless form we used the rescaling

$$\begin{aligned} t &\to t \cdot \lambda^{-1} \,, \\ \mathbf{x} &\to \mathbf{x} \cdot v_0 \lambda^{-1} \,, \\ f &\to f \cdot \rho_0 \,, \\ \kappa_0 &\to \kappa_0 \cdot v_0 \lambda^{-1} \,, \end{aligned}$$

with $\rho_0 = \lambda/(dv_0)$. Measuring time, space and density in units of λ^{-1}, $v_0\lambda^{-1}$, and ρ_0, respectively, allows to set $d = \lambda = v_0 = 1$. Then, the only remaining free parameters are the noise amplitude σ, κ_0, and the mean particle density $\bar{\rho} = A^{-1} \int_A \mathrm{d}\mathbf{r} \int_{-\pi}^{\pi} \mathrm{d}\theta\, f(\mathbf{r}, \theta, t)$. To proceed, we performed a Fourier transformation of the angular variable: $f_k(\mathbf{r}, t) = \int_{-\pi}^{\pi} \mathrm{d}\theta\, \mathrm{e}^{\mathrm{i}\theta k} f(\mathbf{r}, \theta, t)$. This leads to the Boltzmann equation in Fourier space, Eq. (2), where the Fourier transforms $\mathcal{I}_{n,k}$ are given by

$$\mathcal{I}_{n,k} = \int_{-\pi}^{\pi} \frac{\mathrm{d}\Phi}{2\pi} \mathcal{S}(|\Phi|) \left[\hat{P}_k \cos(\Phi(n - k/2)) - \cos(\Phi n)\right] \,. \tag{S8}$$

$\hat{P}_k = \mathrm{e}^{-(k\sigma)^2/2}$ is the Fourier transform (characteristic function) of the Gaussian noise with standard deviation σ. Note that $\mathcal{I}_{n,0} = 0$ for all n. For $k = 0$, Eq. (2) hence yields the continuity equation $\partial_t \rho = -\frac{1}{2}(\nabla f_1^* + \nabla^* f_1) = -\nabla \cdot \mathbf{j}$ for the local density $\rho(\mathbf{r}, t) := f_0(\mathbf{r}, t)$ with the particle current given by $\mathbf{j}(\mathbf{r}, t) = v_0(\mathrm{Re} f_1, \mathrm{Im} f_1)^T$. In order to get a closed equation for the particle current at onset, we assume small currents $f_1 \ll 1$ and use the

truncation scheme: $\rho - \bar{\rho} \sim f_1$, $\partial_{x/y} \sim f_1$, $\partial_t \sim f_1$, $f_2 \sim f_1^2$ with vanishing higher modes as presented for polar particles with ferromagnetic interaction in Ref. [11]. In analogy to Ref. [10], we retained only terms up to cubic order in f_1 in the Boltzmann equation, Eq. (2), for $k = 1$. The equation for f_1 then couples to the nematic order field f_2 via a term $\sim f_1^* f_2$ of order f_1^3, where the star denotes complex conjugate. Writing down contributions from Eq. (2) for $k = 2$ of quadratic order in f_1 yields an expression for f_2 as a function of f_1. The expression for f_2 can then be substituted into Eq. (2) for $k = 1$ to obtain a closed equation for f_1. Together with the continuity equation, the hydrodynamic equations for the density and the particle current read

$$\partial_t \rho = -\frac{1}{2}(\nabla f_1^* + \nabla^* f_1)\,, \tag{S9a}$$

$$\begin{aligned}\partial_t f_1 =& [\alpha(\rho-\rho_c) + \mathrm{i}v_0\kappa_0]\, f_1 - \xi|f_1|^2 f_1 + \nu\nabla^*\nabla f_1 \\ &- \gamma f_1 \nabla^* f_1 - \beta f_1^* \nabla f_1 - \frac{v_0}{2}\nabla\rho\,,\end{aligned} \tag{S9b}$$

where $\nabla := \partial_x + \mathrm{i}\partial_y$. The coefficients are given by

$$\begin{aligned}\alpha &:= (\mathcal{I}_{0,1} + \mathcal{I}_{1,1}),\\ \rho_c &= \frac{\lambda(1-\hat{P}_1)}{\mathcal{I}_{0,1}+\mathcal{I}_{1,1}}\,,\\ \nu &:= -\frac{1}{4}\frac{1}{\lambda(\hat{P}_2-1) + 2\mathrm{i}v_0\kappa_0 + (\mathcal{I}_{0,2}+\mathcal{I}_{2,2})\rho}\,,\\ \xi &:= -4(\mathcal{I}_{-1,1}+\mathcal{I}_{2,1})\nu\mathcal{I}_{1,2}\,,\\ \beta &:= 2(\mathcal{I}_{-1,1}+\mathcal{I}_{2,1})\nu\,,\\ \gamma &:= 4\nu\mathcal{I}_{1,2}\,.\end{aligned} \tag{S10}$$

We note that the employed truncation scheme implies fast relaxation of the nematic order field f_2 such that $\partial_t f_2$ is assumed to be negligible on time scales of the dynamics of f_1. f_2 is then slaved to f_1 via $f_2 = -2\nu\nabla f_1 + \gamma f_1^2$.

Linear stability analysis

For $\rho < \rho_c$ Eqs. (S9) are solved by the homogeneous isotropic state: $\rho = \bar{\rho} = const.$, $f_1 = 0$. For $\rho > \rho_c$ there is a second solution given by the homogeneous oscillatory state: $\rho = \bar{\rho}$, $f_1 = F_1 \mathrm{e}^{\mathrm{i}\Omega_0 t}$ with $F_1 = (\alpha(\bar{\rho}-\rho_c)/\mathrm{Re}[\xi])^{1/2}$ and $\Omega_0 = v_0\kappa_0 - \alpha(\bar{\rho}-\rho_c)\mathrm{Im}[\xi]/\mathrm{Re}[\xi]$.

Homogeneous isotropic state

To study the stability of the homogeneous isotropic state we substitute $\rho = \bar{\rho} + \delta\rho$ and $f_1 = \delta f_1$ with the wave-like perturbations of the form

$$\begin{aligned}\delta\rho(\mathbf{r},t) &\sim \delta\rho_{\mathbf{q}}\, \mathrm{e}^{\mathrm{i}\mathbf{q}\cdot\mathbf{r}}\,,\\ \delta f_1(\mathbf{r},t) &\sim \delta f_{1,\mathbf{q}}\, \mathrm{e}^{\mathrm{i}\mathbf{q}\cdot\mathbf{r}}\,,\end{aligned} \tag{S11}$$

where $\delta\rho_{\mathbf{q}}$ and $\delta f_{1,\mathbf{q}}$ are in general complex amplitudes that are assumed to be small. Periodic boundary conditions in our numeric solution impose $|\mathbf{q}| = n\frac{2\pi}{L}$, $n\epsilon\mathbb{Z}$, where $L = \sqrt{A}$ and A is the area of the (quadratic) system. The linearized set of equations of motion for the perturbations $\delta\rho_{\mathbf{q}}(t)$, $\delta f_{1,\mathbf{q}}(t)$ and $\delta f_{1,\mathbf{q}}^*(t)$ has the characteristic polynomial

$$\begin{aligned}&- q^2\alpha(\bar{\rho}-\rho_c) + q^4\Re[\nu]\\ &+ \left(2(\alpha(\bar{\rho}-\rho_c) - \Re[\nu]q^2)^2 + 2(v_0\kappa_0 - \Im[\nu]q^2)^2 + q^2\right) S\\ &+ 4\left(-\alpha(\bar{\rho}-\rho_c) + \Re[\nu]q^2\right) S^2 + 2S^3\,.\end{aligned} \tag{S12}$$

where S is the eigenvalue of the linearized set of equations for $\delta\rho_{\mathbf{q}}(t)$, $\delta f_{1,\mathbf{q}}(t)$ and $\delta f_{1,\mathbf{q}}^*(t)$. We note that $\Re[\nu]$ is positive for all densities. For $\bar{\rho} < \rho_c$, all coefficients in (S12), including the S-independent terms are positive, such that (S12) only yields S with negative real part. Thus, for $\bar{\rho} < \rho_c$ the homogeneous isotropic state is linearly stable against inhomogeneous wave-like perturbations. For $\bar{\rho} - \rho_c > 0$, the real part of S becomes positive where the fastest growing mode is always at $q = 0$.

Homogeneous oscillatory state

To study the stability of the homogeneous oscillatory solution we substitute small perturbations in the basis of the homogeneous oscillating solution:

$$\begin{aligned}\rho =& \bar{\rho} + \delta\rho_{(0)}\\ &+ \sqrt{\frac{\alpha(\bar{\rho}-\rho_c)}{\Re[\xi]}}\,\delta\rho_{(1)}\mathrm{e}^{\mathrm{i}\Omega_0 t} + \sqrt{\frac{\alpha(\bar{\rho}-\rho_c)}{\Re[\xi]}}\,\delta\rho_{(1)}^*\mathrm{e}^{-\mathrm{i}\Omega_0 t},\\ f_1 =& F_1\mathrm{e}^{\mathrm{i}\Omega_0 t} + \delta f_{(0)}\\ &+ \sqrt{\frac{\alpha(\bar{\rho}-\rho_c)}{\Re[\xi]}}\,\delta f_{(1)}\mathrm{e}^{\mathrm{i}\Omega_0 t} + \sqrt{\frac{\alpha(\bar{\rho}-\rho_c)}{\Re[\xi]}}\,\delta f_{(2)}\mathrm{e}^{-\mathrm{i}\Omega_0 t},\end{aligned} \tag{S13}$$

where the amplitudes $\delta\rho_{(0)}$, $\delta\rho_{(1)}$, $\delta f_{(0)}$, $\delta f_{(1)}$ and $\delta f_{(2)}$ are again of the form (S11). Truncating at the lowest order of $(\bar{\rho}-\rho_c)$, which is $\sqrt{\alpha(\bar{\rho}-\rho_c)}$, yields a closed set of linear equations for the amplitudes. The eigenvalue with the largest real part of this linear system determines the growth rate $S(q)$ of wave-like perturbations. We find that the dispersion relation yields positive $S(q)$ for finite q (see Fig S2).

NUMERICAL LINEAR STABILITY ANALYSIS IN THE FULL PHASE SPACE

In the derivation and the stability analysis of Eqs. (S9) we rely on the assumption of small particle currents which might be justified at onset. However, this assumptions is in general questionable and not well justified for

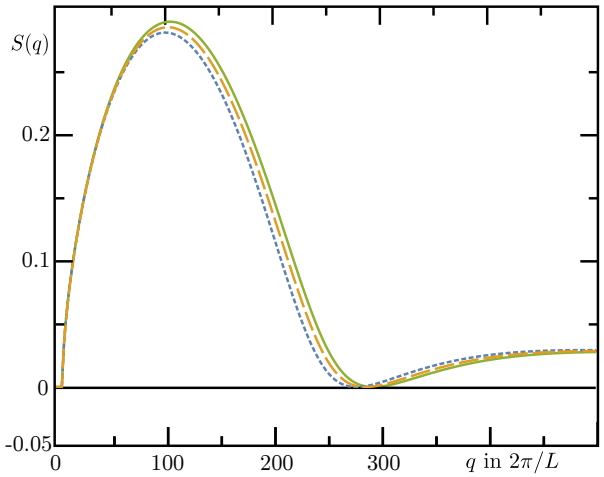

FIG. S2. Dispersion relations for $\sigma = 0.6$, 0.4 and 0.1 (short-dashed, long-dashed and solid lines, respectively) at $\bar{\rho} = 0.8$.

densities much larger than ρ_c. To obtain a stability map for the full phase space (Fig. 3), we first calculated the homogeneous solution of Eq. (2) retaining only modes up to $k_{\max}$. Given some values of $\bar{\rho}$ and σ and a desired accuracy ϵ of this mode truncation scheme the cutoff is chosen such that $|f_{k_{max+1}}| < \epsilon$. As a next step, we linearized Eq. (2) with respect to this solution and calculated the maximal growth rate $S(\mathbf{q})$ of wave-like perturbations with wave vector $\mathbf{q}$. If $S(\mathbf{q}) > 0$ for some $|\mathbf{q}|$, the homogeneous solution is unstable whereas if $S(\mathbf{q}) < 0$ for all $|\mathbf{q}|$, the corresponding homogeneous solution is stable.

Note that the homogeneous version of Eq. (2) (neglecting all gradient terms) is invariant under a phase shift $f_k \to f_k e^{ikv_0\kappa_0 t}$. Choosing the orientation of the polar order at $t = 0$ to be aligned along the x-axis, Eq. (2) is solved by $f_k = |f_k|e^{ikv_0\kappa_0 t}$ with the time and space independent amplitude $|f_k|$. $|f_k|$ is then determined by the stationary homogeneous version of Eq. (2):

$$0 = \lambda(\hat{P}_k - 1)|f_k| + \sum_{n=-\infty}^{\infty} \mathcal{I}_{n,k}\,|f_n||f_{k-n}|\,. \quad \text{(S14)}$$

This equation is identical to the stationary homogeneous Boltzmann equation for straight moving particles; i.e. where $\kappa_0 = 0$. Hence, the solutions for the amplitudes $|f_k|$ are identical to the solutions for the Fourier modes in systems of straight moving particles [10]. To proceed, we truncate the infinite sum in Eq. (S14) at $k_{\max}$ and calculate the solution of all $|f_k|$ with $|k| \leq k_{\max}$. Fig. S3 depicts the solution for the amplitude $|f_1|$ as compared to the solution of the generalized Ginzburg-Landau equation as well as the SNAKE algorithm. The explicit solution for $|f_1|$ and higher modes justifies the scaling scheme used to derive Eqs. (S9) in the vicinity of ρ_c [Fig. S3, inset]. For decreasing noise σ or increasing density $\bar{\rho}$ an increasing number of Fourier modes starts to grow [Fig. S3, inset]. In our numerical calculations we typically included $30 - 50$ Fourier modes. The dashed region in Fig. 3(a) indicates the regime where we cannot find a nontrivial solution to Eq. (S14) by neglecting Fourier modes above the chosen $k_{\max} = 50$ and where we would have to choose a larger $k_{\max}$.

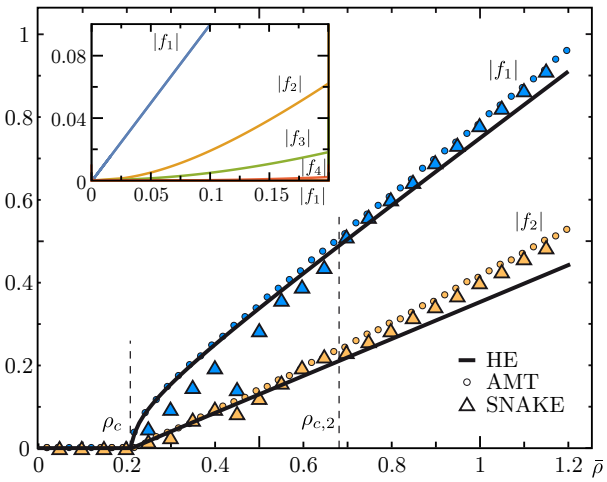

FIG. S3. Homogeneous solution for f_1 and f_2 for $\sigma = 0.5$ obtained from the hydrodynamic equations Eqs. (S9) (HE), the adapted mode truncation scheme (AMT), and the SNAKE algorithm. Note that within ρ_c and $\rho_{c,2}$ (dashed vertical lines), the SNAKE algorithm yields swirl states and hence the corresponding mode values do not represent homogeneous states. The inset depicts the solutions for the first modes obtained from the AMT and shows nonlinear scaling of higher modes with respect to $|f_1|$.

With the substitution $f_k = (|f_k| + \delta f_k)e^{ikv_0\kappa_0 t}$ the linear system for δf_k then reads

$$\partial_t \delta f_k = -\tfrac{v_0}{2}(\nabla \delta f_{k-1} + \nabla^* \delta f_{k+1}) + \lambda(\hat{P}_k - 1)\delta f_k + \sum_{n=-\infty}^{\infty} (\mathcal{I}_{n,k} + \mathcal{I}_{k-n,k})|f_{k-n}|\delta f_n\,. \quad \text{(S15)}$$

Here, we performed a coordinate transformation to a frame rotating with angular frequency κ_0 such that $\nabla \to e^{ikv_0\kappa_0}\nabla$. Assuming wave-like perturbations as in Eq. (S11), we solved Eq. (S15) for the maximal eigenvalue and get the growth rate as a function of the wavenumber in the rotating frame (see Fig. 3(b)). The maximum taken over all wavenumbers $|\mathbf{q}| > 0$ then defines the maximal growth rate S_{max} of wave-like perturbations. In agreement to previous results [10], we found that the growth rate is maximal for $\mathbf{q}$ parallel to the particle current. The contour plot of S_{max} as a function of $\bar{\rho}$ and σ yields the phase diagram Fig. 3(a). Note again, that our stability analysis and the resulting phase diagram Fig. 3(a) is independent of curvature and also valid for the well-studied system of propelled particles without

curvature [10, 12, 13]. Hence, Fig. 3(a) shows that the Boltzmann approach is capable of reproducing phases of all states observed in [12, 14] including a transition from travelling wave patterns to global homogeneous order.

NUMERICAL SOLUTION OF THE BOLTZMANN EQUATION WITH SNAKE

In order to study the resulting steady states in the regime where our linear stability analysis predicts inhomogeneities, we numerically solved the generalized Boltzmann equation, Eq. (1). To this end we employed the SNAKE algorithm as introduced in Ref. [15]. As tesselations we used a quadratic periodic regular lattice with equally sized angular slices. Circling propulsion was included by rotating the angular distribution of each lattice site with a frequency $v_0\kappa_0$ in addition to the straight convection steps. The system was initialized with a disordered state with small random density fluctuations around the mean density $\bar{\rho} = A^{-1}\int_A \rho(\mathbf{r}, t)$. Changing κ_0 did not change the observed patterns qualitatively. In the limiting case of very small κ, we observed traveling wave patterns as reported in Refs. [12, 14, 15]. For Fig. 3(c), Movie 6, and Movie 7 we used a lattice of of 200×200 grid points with lattice field size 2 and angular disretization of 24 angular slices; hence, $A = 400 \times 400 = 160000$. In the swirl phase the swirl size grows for growing $\bar{\rho} - \rho_c$ whereas the radius of a swirl's motion stays at approximately κ_0^{-1}. Fig. S4 shows the parameter values of $\bar{\rho}$ and σ where the SNAKE algorithm exhibits steady swirl patterns together with the phase diagram obtained from the adapted mode truncation scheme.

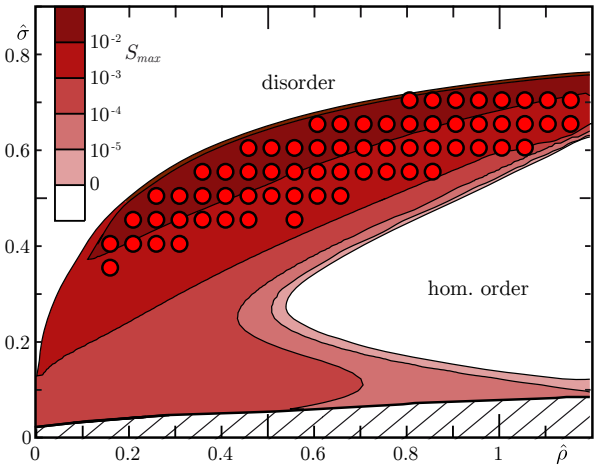

FIG. S4. Overlay of the parameter values where the SNAKE algorithm exhibits steady swirl patterns (red dots) together with the phase diagram obtained from the adapted mode truncation scheme (with $k_{\max} = 50$). In the shaded region, neglected Fourier modes become important.

REMARK ON THE SHAPE OF THE PHASE CURVES

When comparing the transition to order in the phase diagrams 2 and S4 it should be noted that our particle-based and continuum approaches are distinct in the following features: polymer fluctuations vs. effective diffusion, multi-particle collisions vs. binary alignment, extended polymers vs. point particles. The functional form of $\rho_c(\sigma)$ (S10) depends on the choice of diffusion and collision noise (e.g. equally Gaussian distributed). In contrast, the form of the transition line in our Brownian dynamics simulations depends on the choice of the phenomenological criteria (*disordered states* for $d_{cc}^{min} \approx 2R_0$, *vortex states* for $d_{cc}^{min} > 2R_0$ and *train states* without d_{cc}^{min}). These differences result in different shapes of the phase boundaries. In addition, the observed patterns in the vortex phase are distinct. While for our particle-based model we find closed, rotating rings, dense, rotating swirls are observed in the continuum model (Fig. 2(b) and Fig. 3(d)). These differences are interesting and should be considered as part of the results we obtained. For example, these differences will guide future model building for specific models, e.g. the dynamics of FtsZ, as they emphasise what molecular details need to be accounted for. For the discussion of this work, however, our emphasis was on the topology of the phase diagram (similar trend of the onset to order) and the fact that in both models one finds a vortex phase.

MOVIE DESCRIPTIONS

Movie1.mp4: Brownian dynamics simulation of a system with $M = 10$ polymers with $v_0 = 5, k_BT = 1$ and hence $\rho = 0.069$, $\sigma = 0.247$.

Movie2.mp4: Brownian dynamics simulation of a system with $M = 80$ polymers with $v_0 = 5, k_BT = 1$ and hence $\rho = 0.556$, $\sigma = 0.247$.

Movie3.mp4: Brownian dynamics simulation of a system with $M = 200$ polymers with $v_0 = 5, k_BT = 1$ and hence $\rho = 1.389$, $\sigma = 0.247$.

Movie4.mp4: Brownian dynamics simulation with parameters as in Movie 3, except for a changed curvature angle $\theta_0 = 0.333$, resulting in an polymer arc angle $L\kappa_0 = 3$.

Movie5.mp4: Brownian dynamics simulation with parameters as in Movie 3, except for a changed contour length $L = 6$, resulting in an polymer arc angle $L\kappa_0 = 1.2$.

Movie6.mp4: SNAKE solution for $\bar{\rho} = 0.2$ and $\sigma = 0.45$ with $\kappa_0 = 0.1$. The colour code denotes the local density $\rho/\bar{\rho}$. The orientation and length of the arrows indicates the orientation and amplitude of the local particle current.

Movie7.mp4: SNAKE solution for $\bar{\rho} = 0.75$ and $\sigma = 0.2$ with $\kappa_0 = 0.1$. The colour code denotes the local density $\rho/\bar{\rho}$. The orientation and length of the arrows indicates the orientation and amplitude of the local particle current.

Hydroswirl.mp4: Preliminary results of the explicit integration [16] of the hydrodynamic Eqs. (S9). The video shows the time evolution of the density field $\rho(\mathbf{r}, t)$, for parameters close above threshold $\bar{\rho} > \rho_c$. The system size is $A = 80 \times 80 = 640$, $\bar{\rho} = 0.5$, $\sigma = 0.6$, and $R_0 = 5$.

* frey@lmu.de

[1] M. Loose and T. J. Mitchison, Nat. Cell Biol. **16**, 38 (2013).

[2] G. Chirico and J. Langowski, Biopolymers **34**, 415 (1994).

[3] H. Wada and R. R. Netz, Europhys. Lett. **77**, 68001 (2007).

[4] R. E. Goldstein and S. A. Langer, Phys. Rev. Lett. **75**, 1094 (1995).

[5] M. Hinczewski, X. Schlagberger, M. Rubinstein, O. Krichevsky, and R. R. Netz, Macromol. **42**, 860 (2009).

[6] C. Bennemann, J. Baschnagel, W. Paul, and K. Binder, Comput. Theor. Polym. Sci. **9**, 217 (1999).

[7] P. Kloeden and E. Platen, *Numerical Solution of Stochastic Differential Equations* (Springer, Berlin, 1992).

[8] J. K. G. Dhont, *An Introduction to Dynamics of Colloids* (Elsevier, Amsterdam, 1996).

[9] X. Lu and Y. Hu, *Molecular Thermodynamics of Complex Systems* (Springer, Heidelberg, 2008).

[10] E. Bertin, M. Droz, and G. Grégoire, J. Phys. A-Math. Theor. **42**, 445001 (2009).

[11] A. Peshkov, E. Bertin, F. Ginelli, and H. Chaté, Eur. Phys. J.-Spec. Top. **223**, 1315 (2014).

[12] H. Chaté, F. Ginelli, G. Grégoire, F. Peruani, and F. Raynaud, Eur. Phys. J. B **64**, 451 (2008).

[13] T. Ihle, Phys. Rev. E **83**, 030901 (2011).

[14] H. Chaté, F. Ginelli, and F. Raynaud, Phys. Rev. E **77**, 046113 (2008).

[15] F. Thüroff, C. A. Weber, and E. Frey, Phys. Rev. X **4**, 041030 (2014).

[16] In preparation.

3.2 Cell-wide organization of pigment organelles

The last section of this thesis is devoted to a cell-wide view on intracellular organization: An *in silico* reconstitution of the distribution of pigment organelles in so-called melanophore cells. Melanophores are specific skin cells in fish and amphibians that allow these animals to rapidly adapt their skin color. This adaptation is achieved by either aggregating dark pigment organelles in the center of melanophores (resulting in a bright color of the cell) or by dispersing the pigment organelles evenly in the melanophore (resulting in a dark color of the cell). Redistributing the pigment organelles in such a way requires the active transport of these organelles on the microtubules and actin filaments of the cells. Because of the excellent experimental accessibility of the motion of its pigment organelles *in vivo*, melanophores have by now become a paradigm for studying intracellular transport and intracellular organization in general. While it is a long-standing hypothesis that a switch between an aggregated and a dispersed state of a melanophore relies on the transfer of these organelles from microtubules to actin filaments and vice versa, the underlying biomolecular principles that govern the redistribution of pigment organelles are elusive. In this research project we collaborated closely with the group of Dr. Zeynep Ökten at the TU Munich to address the regulation of the distribution of pigment organelles by experiments and theoretical approaches. In detail, we used computational modeling to relate the experimental results of our collaborators to the cell-wide distribution of pigment organelles *in silico*. The combination of experiments and theoretical approaches allowed us to identify a key factor for the redistribution of pigment organelles within a cell: the probability at which the organelles are transferred from an actin filament to a microtubule at an intersection of two filaments. Our simulations unraveled that a change of only this probability is sufficient to reconstitute a switch between a dispersed state and an aggregated state of a melanophore. Moreover, we used our theoretical model to reveal potential evolutionary pathways that might have governed the regulatory mechanisms of intracellular organization of amphibians. All experimental results in this section were obtained by the group of Dr. Zeynep Ökten and, in particular, by Dr. Angela Oberhofer and Peter Spieler. This project is currently prepared for publication in a peer-reviewed journal [3].

3.2.1 Background

One recurring topic of this thesis is that the formation and maintenance of structure in living systems demands a permanent turnover of energy. As we have already seen at various examples, molecular motors are a critical component in this respect as they play a vital role in intracellular organization. In this section, we discuss a model system that provides a very broad view on the formation and maintenance of structure in cells: The active transport of organelles within a cell. In general, the positioning of many of the cell's components requires active transport by molecular motors on the cytoskeleton. This holds true for organelles such as lysosomes [47], mitochondria [48], the Golgi apparatus [49] and the endoplasmic reticulum [50, 51]. Here we focus on the organization of pigment organelles, the so-called melanosomes, within a cell [53–57]. Melanosomes are comparably large (diameter of approximately 500 nm) organelles that are responsible for the synthesis and storage of melanin. They are found in skin cells of mammals and lower vertebrates [59]. As melanosomes absorb light and thus have a dark appearance, they determine the skin color of these organisms and are critical, for example, in the protection against UV radiation [228]. The dynamics and organization of melanosomes in cells has by now become a paradigm in the study of intracellular transport since the motion of melanosomes can, even *in vivo*, easily be detected because of their large size and dark color [58]. Importantly, melanosomes move on both components of the cytoskeleton, actin filaments and microtubules. This inter-cytoskeletal motion can be established because molecular motors associated to both types of filaments are simultaneously bound to the surface of melanosomes (see also Fig. 3.2): Kinesin (plus-end directed motor on microtubules), dynein (minus-end directed motor on microtubules), and myosin (actin-associated motor that moves to the barbed ends) allow melanosomes to move on the actin and microtubule network [56].

A fascinating example of a change in the intracellular organization of melanosomes can be found in early and lower vertebrates: Fish and amphibians possess highly specialized skin cells, so-called melanophores, that allow the corresponding animals to adapt their skin color in response to environmental changes [58]. This change of skin color is achieved by a cell-wide reorganization of the melanosomes in the melanophores. The melanophores switch between a so-called aggregated state, where the melanosomes accumulate in the center of the cell, and a so-called dispersed state, where the melanosomes are distributed throughout the cell [58]. As a result, melanophores in an aggregated state appear bright whereas melanophores in a dispersed state appear dark, see also Fig. 3.1 for an illustration. *In vivo*, this transition is determined by the activity of the protein kinase A (PKA) [58, 229–231]. How a variation of the PKA level in cells relates to biomolecular changes that could govern a redistribution of pigment organelles is, however, unknown. By now, it is well established that this dynamic redistribution of melanosomes depends on the presence of actin filaments as

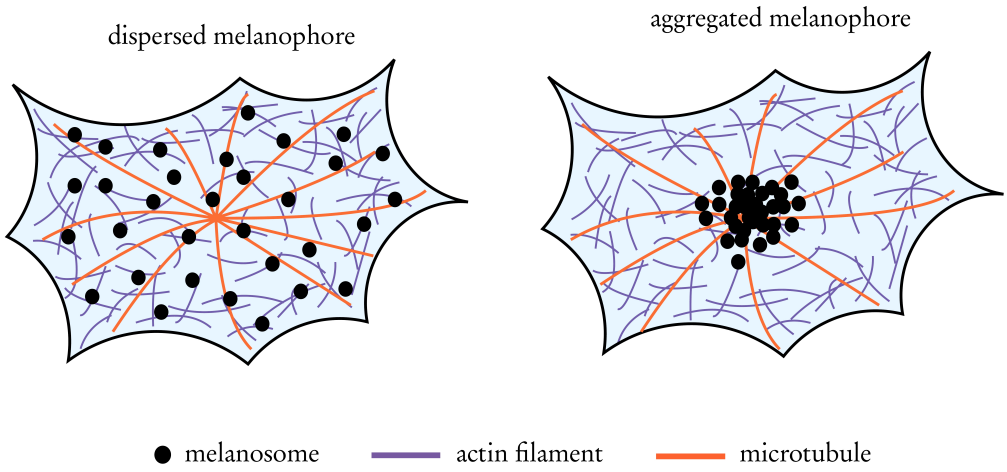

Figure 3.1 Illustration of the dispersion and aggregation of melanosomes in melanophores. Fish and amphibians possess highly-specialized skin cells (melanophores) that allow these animals to rapidly change the color of their skin. This is achieved by a redistribution of dark, pigment filled organelles (melanosomes) in the cell. In the dispersed state of a melanophore (left), the melanosomes distribute throughout the cell, which causes a dark color. In the aggregated state of melanophores (right), the melanosomes accumulate in the center of the cell which leads to a bright color.

well as microtubules: Aggregation of melanosomes requires an intact microtubule network in fish as well as in amphibians [54, 57, 232]. Likewise, removal of the actin network of melanophores in the dispersed state leads either to the motion of melanosomes towards the periphery of the cell in fish or to the motion of melanosomes to the center of the cell in amphibians [53, 54, 57]. These and other findings therefore show that a crosstalk between both cyoskeletal networks—actin filaments and microtubules—is essential for the function of melanophores [84, 233–235]. While the central role of a transfer of melanosomes between the cytoskeletal networks is without question, the principles that determine their organization in a cell are unknown on the biomolecular level.

In this respect, progress was recently made by Oberhofer et al. [236]: The corresponding research project focused on the impact of PKA—the signaling factor that drives the switch between aggregation and dispersion of melanosomes in amphibians and fish—on myosin-based transport complexes of mouse cells. These transport complexes move melanosomes on actin filaments in the respective cells and consist of the myosin motors itself and further molecules that link the motors to a melanosome *in vivo* (see also Fig. 3.2(b) for an illustration). The study showed that the transport complexes are indeed phosphorylated by PKA. Surprisingly, the functional consequence

of this phosphorylation was neither a change of the velocities at which the complexes moved along actin filaments nor their affinity to actin filaments. Instead, the probability of the myosin-based transport complexes to switch between microtubule and actin filaments at intersections of filaments was changed by a phosphorylation. In this way, the regulatory impact of PKA could be traced back to being a mediator of the crosstalk of melanosome motion on the actin and on the microtubule networks. Let us note that an exchange between microtubules and actin filaments can be mediated already by myosin alone (i.e. in the absence of the microtubule-based molecular motors dynein and kinesin): It has been shown previously that—while being an actin-associated motor protein—myosin can also bind to and move on microtubules [84]. Bound there, myosin performs unbiased diffusive motion in contrast to the directed motion it undergoes on actin filaments.

Although the findings by Oberhofer et al. revealed a first potential biomolecular origin of the regulation of an exchange of organelles between actin filaments and microtubules, the *in vivo* relevance remained elusive for two reasons: (a) The studied myosin-based transport complexes corresponded to those of mammalian cells (mouse), where the regulatory role of PKA is, however, unclear. (b) It is unknown how the behavior of an organelle at a single crossing relates to a cell-wide organization of organelles.

Here, we present novel findings related to the organization of melanosomes in fish and amphibian cells. The findings resulted from a close collaboration with the group of Dr. Zeynep Ökten at the TU Munich, which sought to overcome both of the above mentioned limitations. Our study addressed the aspects of a cell-wide organization of melanosomes on two levels: Firstly, results from our experimental collaborators succeeded in unraveling biomolecular principles of the cyoskeletal crosstalk of melanosomes in amphibians and fish *in vitro*. Secondly, we used computational modeling to relate these *in vitro* findings to the cell-wide collective dynamics of melanosomes. In this way, we showed that the *in vitro* findings are indeed related to the functional behavior of melanophores, as they generated a switch between an aggregated and a dispersed state of melanophores in simulated cells. We further used our model to illuminate general principles in the regulation of the melanosome distribution in melanophores. Thereby, we retraced a potential evolutionary pathway that might have governed the regulatory mechanism employed in amphibians.

3.2.2 Myosin-based transport complexes mediate a cytoskeletal crosstalk *in vitro*

The experimental studies of our collaborators focused again on the *in vitro* dynamics of the reconstituted myosin-based transport complex that moves melanosomes on actin filaments. As already briefly mentioned above, this transport complex consists of the myosin motor itself as well as additional proteins that mediate binding to pigment

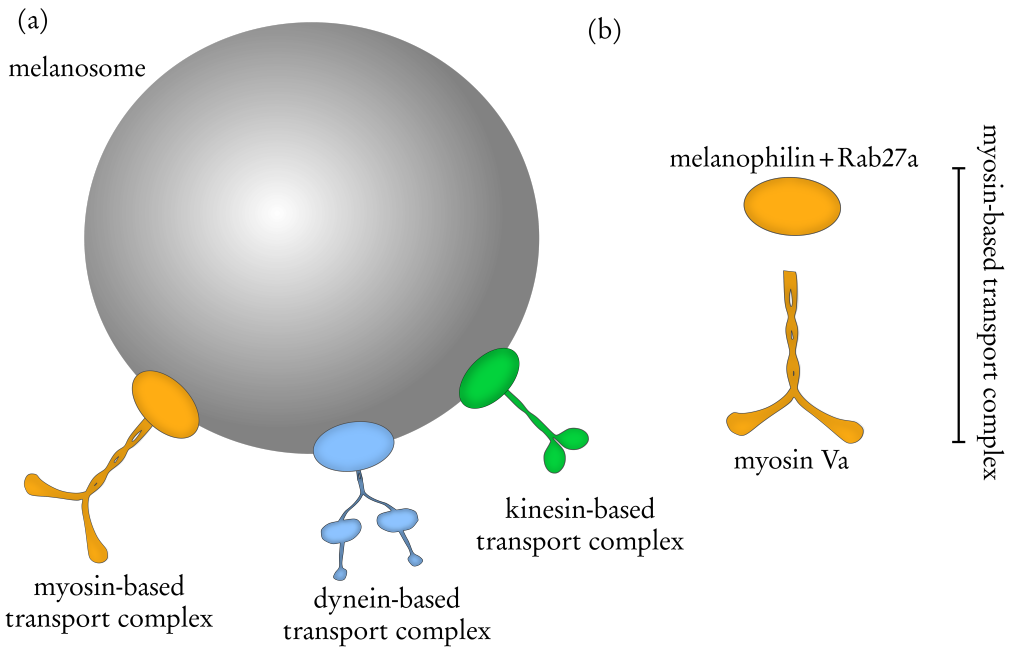

Figure 3.2 Illustration of a melanosome and the related complexes that transport the melanosome along cytoskeletal filaments. (a) Several kinesin, dynein, and myosin transport complexes are typically bound simultaneously to the membrane of a melanosome. To attach to melanosomes, the molecular motors require additional proteins (ellipses) that mediate the binding. **(b)** The transport complex studied in the *in vitro* experiments of our collaborators consisted of myosin Va motors, melanophilin, and Rab27a. The latter two proteins are required to bind the myosin motors to the membrane of the melanosome. Note that the ratio of sizes of the molecular motors and the melanosome is not chosen realistically but for illustrative purposes; Real melanosomes are more than an order of magnitude larger than molecular motors. Moreover, we only illustrated three melanosome-bound molecular motors although *in vivo* it is likely that a much larger number is bound to the melanosomes.

organelles *in vivo* (see also Fig. 3.2). Opposed to the previous experimental study detailed above, our collaborators now investigated myosin-based transport complexes from model organisms where it is known that PKA causes a cell-wide redistribution of melanosomes. Specifically, the myosin-based transport complexes from zebrafish and Xenopus frog were reconstituted. The motion of these transport complexes was then studied *in vitro* on an immobilized network of actin filaments and microtubules by using total internal reflection fluorescence microscopy (TIRF). An image obtained from such an experiment is shown in Fig. 3.3 for illustrative purposes. It should be noted that only myosin-based transport complexes could be reconstituted. *In vivo*, however, also dynein and kinesin are simultaneously bound to a pigment organelle. Therefore, this study dissects the regulatory impact of myosin motors on the collective

dynamics of organelles while in cells also dynein and kinesin might contribute to regulation.

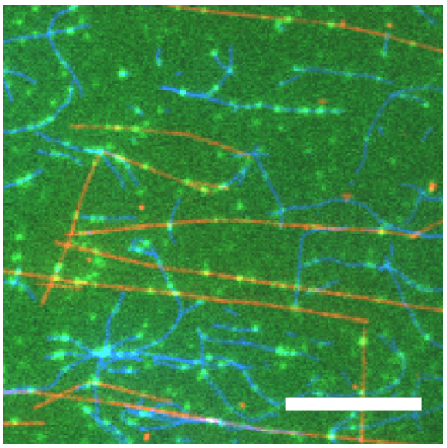

Figure 3.3 Image of the reconstituted cytoskeletal network and transport complexes obtained by total internal reflection fluorescence microscopy (TIRF). Fluorescently labeled actin filaments (blue) and microtubules (red) were immobilized on a surface. On this reconstituted cytoskeletal network, the motion of myosin-based transport complexes (green) was observed and quantified. Scale bar is 10 µm. The image was recorded by the group of Dr. Zeynep Ökten.

Using this experimental setup, our collaborators quantified the motion of complexes that either passed a microtubule-actin crossing or switched to the other filament in dependence on the phosphorylation state; Complexes that fell off the filament at an intersection were not taken into account. Interestingly, the myosin transport complex from zebrafish was not regulated by phosphorylation while the switching behavior of the transport complex from Xenopus showed a phosphorylation-dependent change. Specifically, the probability to switch from actin onto microtubules was regulated, while the probability to switch from microtubules onto actin filaments was unaffected by phosphorylation. The results of these experiments are summarized in Fig. 3.4. Similar to previous findings for the mammalian transport complex, neither the velocities of the transport complexes nor their affinity to actin filaments (as quantified by the run length) showed a significant change due to phosphorylation. An overview of these results is provided in Table 3.1.

Collectively, this *in vitro* analysis of the myosin-based transport complex on actin filaments and microtubules provides a first mechanistic insight in a cytoskeletal crosstalk.

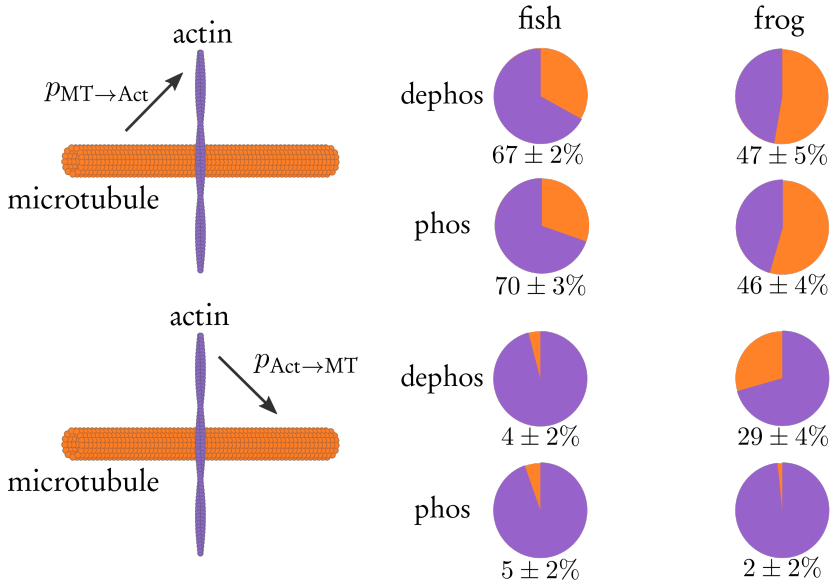

Figure 3.4 Phosphorylation regulates the transfer of myosin-based transport complexes from actin filaments to microtubules in Xenopus frog. While the myosin-based transport complex of zebrafish did not show a response to phosphorylation, the transport complex of Xenopus showed a significant change in the probability to switch from actin filaments to microtubules. Surprisingly, the probability for the transverse process—to switch from microtubules to actin filaments—was not affected by phosphorylation. All results related to experimental data were produced by the group of Zeynep Ökten.

3.2.3 Modeling the cell-wide organization of melanosomes

To simulate the cell-wide organization of pigment organelles in melanophores we developed a stochastic model that allowed us to relate the switching behavior of transport complexes at individual crossings to the global distribution of melanosomes in a cell. Specifically, we wanted to impose the changing probabilities to switch between filaments as measured for a myosin-based transport complex experimentally to the motion of a whole melanosome. This means that also biased, bidirectional motion on microtubules was simulated, as it results when kinesin and dynein are bound to a melanosome in addition to the myosin motors [234]. In other words, we wanted to know how the changes of the switching probabilities measured for myosin complexes impact the collective motion of whole melanosomes *in vivo*. The following section details the implementation of the model for melanosome organization and is split into two parts: (a) A description of the implementation of the virtual melanophore and the related cytoskeletal architecture. (b) A description of the dynamics of virtual melanosomes within our virtual cells. The choice of parameters of the model is provided in Appendix A.

Xenopus frog	Phos	Dephos
Velocity	241 ± 115 nm/s	239 ± 121 nm/s
Run length	900 ± 100 nm	1000 ± 200 nm

Table 3.1 Overview of the motile parameters of the myosin-based transport complex of Xenopus frogs on actin filaments. Neither the velocity of single transport complexes nor their run length (average distance travelled on an actin filament before detachment) showed a significant change between a dephosphorylated and a phosphorylated state. All results related to experimental data were produced by the group of Zeynep Ökten.

3.2.3.1 Construction of the virtual melanophore

Our virtual cells were composed of three discretized and interconnected domains that correspond to the *cytoplasm*, the *microtubule network* and the *actin network* that are discussed in the following.

To create a virtual cell, the cytoplasmic layer was created in the first step. A specific (two-dimensional) cell geometry was defined which was then translated into a two-dimensional lattice of the corresponding (discretized) shape. In most simulations we used a circular shape of the cell.

In the next step, we constructed the cytoskeletal architecture of the cell. We added two species of filaments to our virtual cell that correspond to actin and microtubule filaments, respectively. Each filament was implemented as a one dimensional lattice that we placed randomly in the virtual cell. The filaments showed an intrinsic orientation. By attributing a direction to each filament, we could associate any of the filament ends with either the plus (barbed) or minus (pointed) ends of microtubules and actin filaments, respectively. Attributing a directionality to each filament, in turn, determined the direction of motion of melanosomes on the filaments.

Actin filaments were successively placed in the cell in the following manner: Initially, we drew the orientation of the filament from a uniform distribution in the range $[0,2\pi)$. This ensured an isotropic orientation of the actin filaments. Thereafter, we randomly selected the length of the filament from an exponential distribution with a mean length of 1.5 µm. Lastly, we selected a random position for the center of mass of this filament in the cell. For most simulations, we chose a homogeneous distribution for the center of masses of the filaments. In case a filament would have been positioned completely or partially outside of the virtual cell, we drew a new center of mass from the same distribution as before until a valid position was found. Note that this specific choice to place actin filaments was adapted to experimental findings for melanophores of Xenopus frogs. There, actin filaments have been shown to be distributed approximately homogeneously within the cell, with an isotropic orientation, and a length distribution that approximately equals our choice [58, 237].

Microtubules were implemented as radially arranged filaments that emerged from the center (minus end located close to center) of the cell towards the periphery (plus end located close to the periphery). The angle of orientation was again chosen from a uniform distribution in the range $[0,2\pi)$ to ensure isotropy of the network. The starting point of microtubules was slightly shifted away from the center towards small radii such that microtubules did not intersect. Similarly, also the plus ends of microtubules were cut slightly below the maximum radius. While the algorithm also allowed us to implement an arbitrary distribution of lengths for the microtubules in principle, we implemented microtubules that radiate to the cell periphery in most cases. The main reason for this assumption was that a detailed information on the distribution of the lengths of microtubules of Xenopus melanophores is lacking. Our specific implementation therefore corresponds to a conservative choice for the purposes of our modeling that are detailed in the next section. In essence, we wanted to probe if motion on the actin network can outperform motion on microtubules. Thus, by choosing the largest possible length for the microtubules we ensured that their impact is not underestimated in the virtual melanophore.

In summary, our virtual melanophores consisted of three different discrete "domains": (1) The cytoplasm, which was a two-dimensional lattice in the shape of the given cell geometry. (2) The actin network, which was an ensemble of short, one-dimensional lattices with an exponential length distribution and a homogeneous as well as isotropic arrangement. (3) The microtubule network, which was an ensemble of isotropic and radially arranged, one-dimensional lattices of (typically) equal length. To study the impact of a crosstalk between the cytoskeletal elements we connected the different filaments with each other as well as with the cytoplasmic domain.

Crossings of filaments from the same filament species were only relevant for the actin network as microtubules do not intersect because of our choice for their radial arrangement. Upon placing a new filament in our virtual cell, we checked for crossings with each of the existing filaments. In case the new filament intersected one or several other filaments, we identified which lattice sites are affected on the corresponding filament. In this way, we ultimately obtained lists of crossings for intersections of two actin filaments and for intersections of an actin filament with a microtubule. Note that due to our discrete implementation, a single lattice site could be associated with several crossings. In addition to these intra- and interconnections within and between the filament layers, we also connected filaments to the cytoplasmic layer. To do so, we projected each of the lattice sites of the filaments onto the cytoplasmic lattice and connected the lattice site on the filament with that in the cytoplasm. Note that the same cytoplasmic lattice site could, in general, be associated with multiple lattice sites of filaments.

After the construction of our virtual melanophore, we randomly placed the virtual melanosomes on the lattice sites. The stochastic dynamics of the melanosomes are described in the following.

3.2.3.2 Dynamics of virtual melanosomes

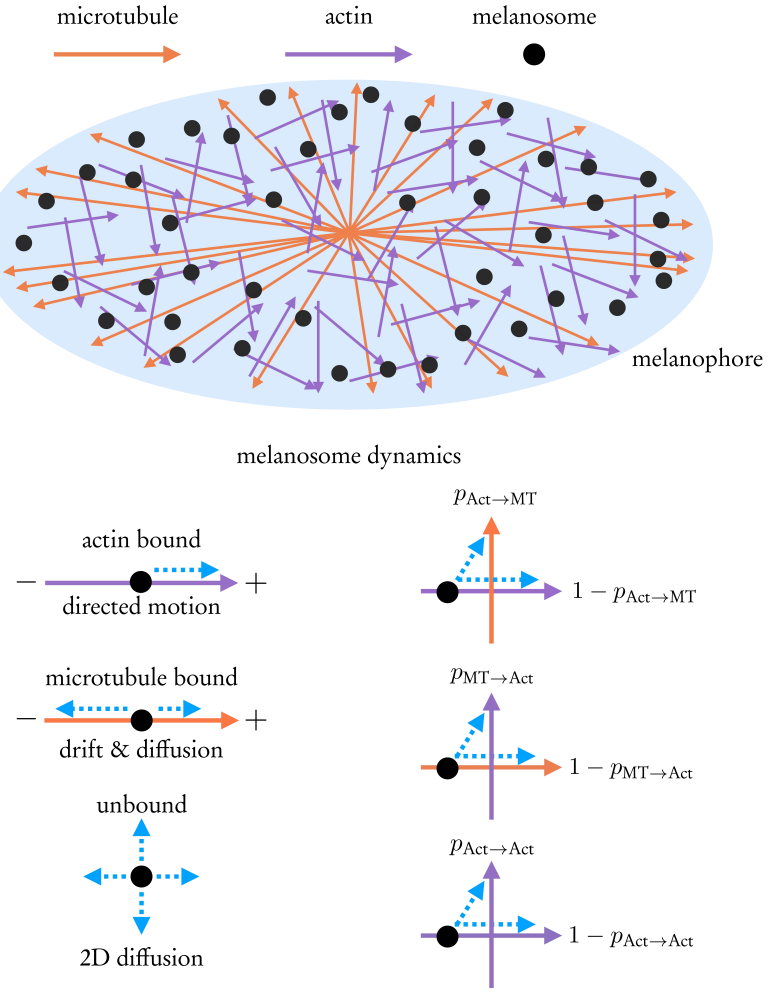

Figure 3.5 Illustration of the computational model for collective melanosome motion. Melanophores were modeled as two-dimensional circles that contain one-dimensional actin and microtubule filaments with an intrinsic orientation (upper panel). The distribution of actin filaments was homogeneous and isotropic. Microtubules were arranged radially and extended from the center of the cell to the periphery. The dynamics of melanosomes was either (i) directed towards barbed ends when bound to actin, (ii) bidirectional but with a dominating minus-end directed component (see also Section 3.2.4 for a comment on this choice) when bound to microtubules (iii) diffusive in two dimensions when unbound. On intersections of filaments melanosomes could either continue on the same filament or switch onto another filament with respective probabilities $p_{\mathrm{Act}\to\mathrm{MT}}$, $p_{\mathrm{MT}\to\mathrm{Act}}$, and $p_{\mathrm{Act}\to\mathrm{Act}}$.

Particles (i.e. virtual melanosomes) obeyed the following dynamic rules: In general, motion was modeled as stochastic transitions between lattice sites. For each of the domains, particle dynamics was different. When bound to actin filaments, particles moved unidirectionally at rate r^+_{actin} to neighboring lattice sites in the direction of the barbed end. When bound to microtubules, virtual melanosomes moved bidirectionally to neighboring lattice sites in both directions on the microtubule. This implementation mimicked a transport mediated by dynein *and* kinesin motors. Note that such a bidirectional motion was also observed *in vivo* [234]. The corresponding transition rates are denoted with r^+_{MT} for motion towards the plus end and r^-_{MT} for motion towards the minus end, respectively. Particles in the cytoplasmic layer moved with isotropic rates $r_{\text{Cytoplasm}}$ to neighboring lattice sites in all four directions, which corresponds to discretized two-dimensional diffusive motion.

Particles interacted by steric exclusion whenever they were bound to filaments. Specifically, this means that motion was only possible when the respective target lattice site was vacant. In the cytoplasmic layer, particles didn't interact and multiple occupations of a single lattice site were allowed.

At intersections of two filaments, particles could switch from one filament to the other. The respective rates are denoted with $r_{\text{Act}\to\text{MT}}$ for the transitions from actin to microtubule filaments, $r_{\text{MT}\to\text{Act}}$ for the transitions from microtubules to actin filaments, and $r_{\text{Act}\to\text{Act}}$ for the transitions from one actin filament to another. In experiments, the effective probabilities to switch from one filament to another were determined. To transfer these effective probabilities to our model, we disallowed a particle to switch back to the original filament before the particle has moved at least one lattice site further. Thus, the respective probabilities to switch onto another filament (switching probabilities) are related to the rates by $p_{\text{Act}\to\text{MT}} = r_{\text{Act}\to\text{MT}}/(r_{\text{Act}\to\text{MT}} + r^+_{\text{actin}})$ for the switching probability from actin to microtubule filaments, $p_{\text{MT}\to\text{Act}} = r_{\text{MT}\to\text{Act}}/(r_{\text{MT}\to\text{Act}} + r^+_{\text{MT}} + r^-_{\text{MT}})$ for switching events from microtubules to actin filaments, and $p_{\text{Act}\to\text{Act}} = r_{\text{Act}\to\text{Act}}/(r_{\text{Act}\to\text{Act}} + r^+_{\text{actin}})$ for switching from one actin filament to another. Switching onto another filament was only possible when the respective target site was vacant.

The interaction of filaments with the cytoplasm was as follows: Particles from a specific lattice site in the cytoplasmic domain could attach at rate $r_{\text{Cytoplasm}\to\text{MT}} = r_{\text{Cytoplasm}\to\text{Act}}$ to associated lattice sites on microtubules and actin filaments, respectively. Such an attachment process was only allowed when the respective lattice site on the filament was vacant. We assumed that melanosomes bind equally likely to microtubules and actin filaments. This approximation is reasonable whenever the binding process is limited by the time scales imposed by three dimensional diffusion but not by the time scales of the reaction itself. The detachment of particles that are bound to actin filaments and microtubules occurred at rates $r_{\text{Act}\to\text{Cytoplasm}}$ and $r_{\text{MT}\to\text{Cytoplasm}}$, respectively. As we implemented non-interacting particles in the cytoplasm, this process occurred irrespective of whether the associated lattice site in the

cytoplasm was occupied or vacant. At the plus (barbed) ends of actin filaments and microtubules we implemented increased detachment rates $r^{\text{end}}_{\text{Act}\rightarrow\text{Cytoplasm}} = r^{+}_{\text{Act}}$ and $r^{\text{end}}_{\text{MT}\rightarrow\text{Cytoplasm}} = r^{+}_{\text{MT}}$, respectively. In this way, melanosomes were assumed to "walk off" filament ends.

An illustration of the model that summarizes the implementation of the virtual melanophore and the particle dynamics is shown in Fig. 3.5.

3.2.4 Measured biomolecular changes provoke a switch between aggregation and dispersion *in silico*

The *in vitro* measurements of our collaborators showed that the key target in the regulation of myosin-based transport complexes of Xenopus frogs is the probability at which they switch from actin to microtubule filaments. Other biomolecular characteristics, such as the velocity of motors or their affinity, did not show a significant response to a PKA-dependent phosphorylation in the experiments. We therefore wanted to understand how these measurements for Xenopus translate to the cell-wide organization of melanosomes and, ultimately, how they relate to the functionality of melanophores.

To this end, we transferred the results of our collaborators to the *in silico* setup detailed in the previous section. *In vivo*, the transition from an aggregated to a dispersed state might be accompanied by a change in the dynamics of microtubule-based molecular motors (i.e. dynein and kinesin) [238]. However, in this research project we specifically wanted to study the impact of the experimental results independently of other potential regulatory factors. Thus, to differentiate the impact of a change in the switching probabilities from that of a potential change in the dynamics of melanosomes on microtubules, we kept the dynamics of virtual melanosomes on microtubules constant throughout our simulations. Specifically, we implemented a predominantly centripetal motion of the melanosomes on the microtubule network, which favors aggregation of melanosomes in the cell center. Implementing centripetal rather than centrifugal motion of melanosomes on microtubules had the following reason: Maintaining a dispersed state in melanophores of Xenopus frogs relies on the actin network. It has been shown that a depolymerization of the actin cytoskeleton of a melanophore in the (late) dispersed state causes a centripetal motion of melanosomes which results in the clustering of the pigment organelles in the center of the cell [54]. This finding shows that the preferred direction of motion of melanosomes on microtubules is minus-end directed, even in melanophores in a dispersed state. Thus, the maintenance of the dispersed state requires an intact actin-based transport system. Our choice of dynamics of melanosomes on microtubules therefore correspond to addressing the questions: Can the motion of melanosomes on actin filaments outperform the centripetal motion of melanosomes on microtubules? Can a change in the

probability of melanosomes to switch from actin filaments to microtubules already by itself induce a switch from an aggregated to a dispersed state of a melanophore?

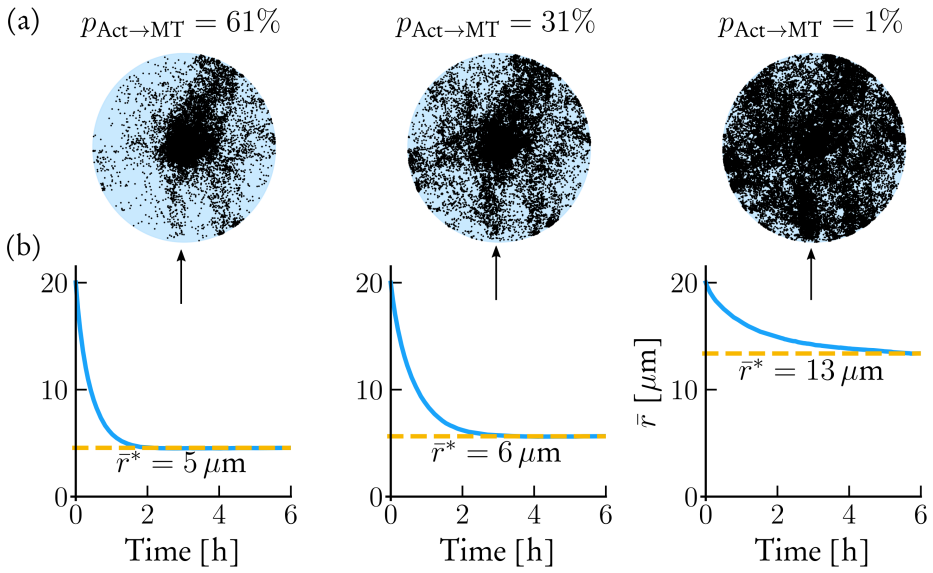

Figure 3.6 Decreasing the probability $p_{\text{Act}\to\text{MT}}$ to switch from actin filaments to microtubules provokes the dispersion of melanosomes *in silico*. **(a)** Illustration of a virtual cell at the three different values $p_{\text{Act}\to\text{MT}} = \{61\%, 31\%, 1\%\}$ for $p_{\text{MT}\to\text{Act}} = 46\%$ (corresponding to the value measured for transport complexes of Xenopus frogs in the experiments, see also Fig. 3.4). Low values of $p_{\text{Act}\to\text{MT}}$ caused a much broader distribution of the simulated melanosomes in the cell which leads to a brighter appearance as for melanophores *in vivo*. **(b)** The average distance of pigment organelles to the center of the cell $\bar{r}(t)$ determined in our simulations converged to a stationary value $\bar{r}^*$ (dashed orange line) that depended on the probabilities $p_{\text{MT}\to\text{Act}}$ and $p_{\text{Act}\to\text{MT}}$. The stationary average distance of the organelles to the center $\bar{r}^*$ increased rapidly for decreasing values of $p_{\text{Act}\to\text{MT}}$ which shows that a change in this value provokes dispersion of our virtual melanophores. Probabilities of melanosomes to switch from actin filaments to microtubules corresponded to that of panel (a), $p_{\text{Act}\to\text{MT}} = \{61\%, 31\%, 1\%\}$. The simulations were performed at $p_{\text{MT}\to\text{Act}} = 46\%$. Snapshots in (a) correspond to the last time frame of the simulation corresponding to the data shown in (b). The radius of the cell was set to 30 µm. Other parameter values as given in Table 3.2

Using this approach, our simulations yielded the following insights. For high switching probabilities $p_{\text{Act}\to\text{MT}}$ melanosomes were transferred to the microtubule network which consequently caused aggregation in our simulations, as expected. Strikingly, however, even completely without a change of the dynamics on microtubules—that is without downregulating dynein activity—decreasing the switching probability from actin filaments to microtubules provoked the dispersion of the virtual melanosomes. When the respective probability was lowered, pigment organelles were transferred onto the actin network which, in fact, outperformed the centripetal

motion on microtubules. As a result, the melanosomes distributed broadly in the virtual cell. Corresponding results from simulations are presented in Fig. 3.6 (a) that shows the same virtual cell for three different values of $p_{\mathrm{Act}\to\mathrm{MT}} = \{61\%, 31\%, 1\%\}$ at $p_{\mathrm{MT}\to\mathrm{Act}} = 46\%$. Note that in experiments $p_{\mathrm{Act}\to\mathrm{MT}}$ for myosin-based transport complexes from Xenopus frogs changed from 2% to 29% due to phosphorylation at an approximately constant value of $p_{\mathrm{MT}\to\mathrm{Act}} \approx 46\%$ (see also Fig. 3.4). The observation that dispersion can be provoked by decreasing $p_{\mathrm{Act}\to\mathrm{MT}}$ is particularly remarkable when considering that motion on the actin network was frequently interrupted by cytosolic excursions after falling off the network at filament ends. Cytosolic melanosomes, however, attached equally likely to nearby actin and microtubule filaments such that long and uninterrupted paths of melanosomes on the actin network were unlikely.

In order to introduce a quantitative measure of the degree of dispersion, we determined the average distance of virtual melanosomes to the center of the cell at a specific time t:

$$\bar{r}(t) = \frac{1}{N}\sum_{i=1}^{N} r_i(t), \tag{3.1}$$

where $r_i(t)$ is the distance of the i-th pigment to the center of the cell at time t and N is the total number of pigment organelles. As our virtual melanophores evolved in time, the average distance of organelles to the center converged to a stationary value $\bar{r}^*$. This value depended on the switching probabilities $p_{\mathrm{Act}\to\mathrm{MT}}$ and $p_{\mathrm{MT}\to\mathrm{Act}}$ as illustrated in Fig. 3.6 (b). Importantly, $\bar{r}^*$ was significantly larger for small values of $p_{\mathrm{Act}\to\mathrm{MT}}$ than for large values of $p_{\mathrm{Act}\to\mathrm{MT}}$ which shows that a regulation of the distribution of melanosomes is possible by solely changing the corresponding probability.

In the next step we tested whether changes in the distribution of melanosomes occur reversibly. We therefore alternated between low and high values of $p_{\mathrm{Act}\to\mathrm{MT}}$ in the simulations on time scales that allowed for a relaxation of the melanosome dynamics between the switches. On timescales of approximately an hour, the cell-wide distribution of pigment organelles could indeed be converted back and forth between an aggregated and a dispersed state, as shown in Fig. 3.7. Interestingly, these timescales also approximately correspond to those measured *in vivo* [58, 59]. Taken together, these data show that a switch between a dispersed and an aggregated state of a melanophore *in silico* occurs when simulating the different phosphorylation-dependent switching probabilities measured *in vitro*.

To gain further understanding of the relevance of the *in vitro* measurements, we wanted to understand whether a redistribution of melanosomes in our simulations occurs efficiently and robustly in the range of values determined experimentally for $p_{\mathrm{MT}\to\mathrm{Act}}$ and $p_{\mathrm{Act}\to\mathrm{MT}}$. We thus changed the probability $p_{\mathrm{Act}\to\mathrm{MT}}$ in a range of 1-99% for three different values of $p_{\mathrm{MT}\to\mathrm{Act}} \approx \{30\%, 40\%, 50\%\}$ and determined the

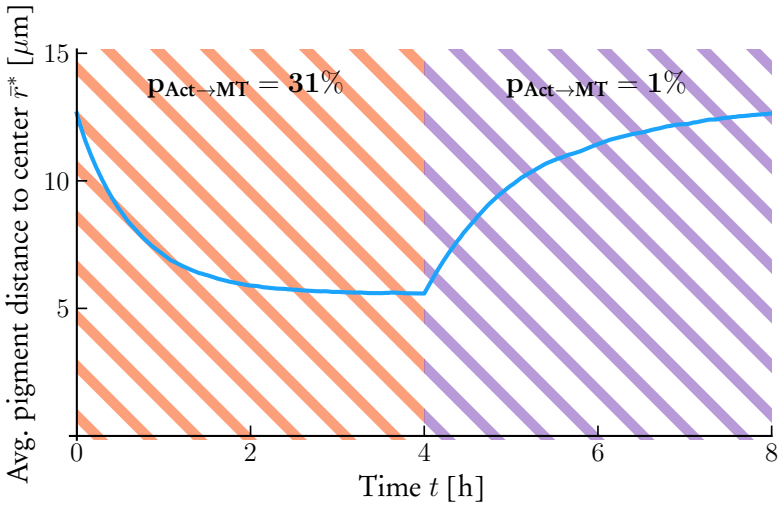

Figure 3.7 ***In silico*** **reconstitution of a switch between dispersion and aggregation of melanosomes.** The figure shows the temporal evolution of the average distance of melanosomes to the cell center in a simulation where we implemented a switch in $p_{\mathrm{Act}\to\mathrm{MT}}$ from a high ($p_{\mathrm{Act}\to\mathrm{MT}} = 31\%$, orange shading) to a low ($p_{\mathrm{Act}\to\mathrm{MT}} = 1\%$, purple shading) probability at time t = 4 h. A redistribution of melanosomes between an aggregated and a dispersed state occurred reversibly and on timescales of approximately one hour that correspond to those *in vivo* [58, 59]. The simulation was performed at $p_{\mathrm{MT}\to\mathrm{Act}} = 46\%$, which approximately corresponds to the value measured for the myosin-based transport complexes of Xenopus frogs measured *in vitro*. We used parameter values as given in Table 3.2.

corresponding value of the average distance of pigment organelles to the center of the cell in the stationary state $\bar{r}^*$.[1] Note that the variation in $p_{\mathrm{MT}\to\mathrm{Act}}$ investigated here corresponds to a variation around the value measured *in vitro*, see Fig. 3.4. As $\bar{r}^*$ showed a dependency on the specific cytoskeletal network that was randomly realized in our simulations, we performed simulations in 15 virtual cells and computed the ensemble average. The result is depicted in Fig. 3.8 and shows that a redistribution of melanosomes occurs robustly and efficiently in the range of probabilities $p_{\mathrm{MT}\to\mathrm{Act}}$ and $p_{\mathrm{Act}\to\mathrm{Mt}}$ that correspond to those measured *in vitro*: The degree of dispersion as quantified by $\bar{r}^*$ was particularly sensitive for variations of $p_{\mathrm{Act}\to\mathrm{MT}}$ in the range from 1-40%. This range, in particular, includes the phosphorylation-dependent change of switching probabilities observed experimentally of $p_{\mathrm{Act}\to\mathrm{MT}}$ from 2% to 29% when phosphorylating the transport complexes, see Fig. 3.4. Moreover, variations in $p_{\mathrm{MT}\to\mathrm{Act}}$ close to a value of 46% (i.e. close to the *in vitro* value) didn't affect $\bar{r}^*$ to

1 We did not simulate probabilities of 0% and 100% as we had the impression that this might correspond to unrealistic scenarios.

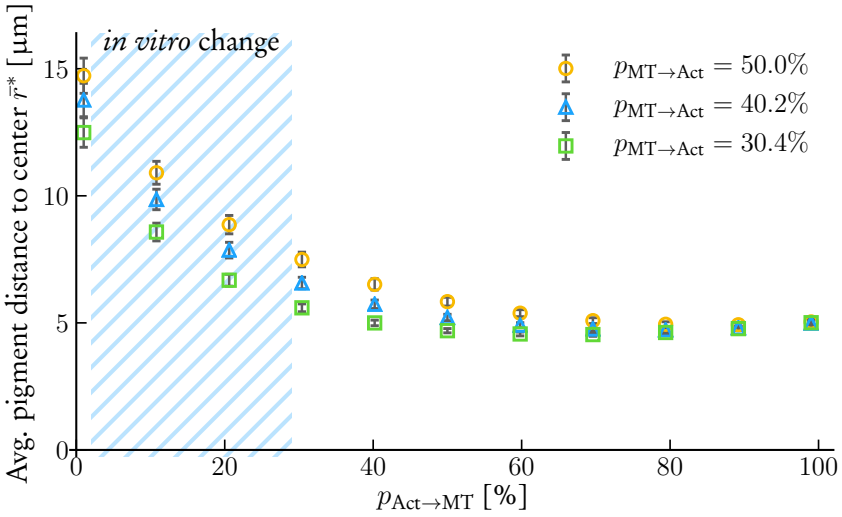

Figure 3.8 ***In vitro*** **measurements correspond to an effective and efficient means to change the cell-wide organization of melanosomes.** In simulations, we changed $p_{\mathrm{Act}\to\mathrm{MT}}$ in a range of 1-99% for three different fixed values of $p_{\mathrm{MT}\to\mathrm{Act}} = \{30.4\%, 40.2\%, 50\%\}$ and determined the corresponding values of $\bar{r}^*$. The average distance of organelles to the center $\bar{r}^*$ was only responsive to a variation in $p_{\mathrm{Act}\to\mathrm{MT}}$ in the region from approximately 0-40%. This coincides excellently with the change from $p_{\mathrm{Act}\to\mathrm{MT}} = 2\%$ to $p_{\mathrm{Act}\to\mathrm{MT}} = 29\%$ (blue shaded area) that was measured *in vitro* when phosphorylating the transport complexes of Xenopus, see also Fig. 3.4. Moreover, changes in $p_{\mathrm{MT}\to\mathrm{Act}}$ close to the value of $p_{\mathrm{MT}\to\mathrm{Act}} = 46\%$ (corresponding to that measured *in vitro* for Xenopus) had little impact on the distribution of melanosomes in the cell. Each data point corresponds to an average over 15 cells. Error bars show the standard error of the mean. We used parameter values as given in Table 3.2.

a large degree. We therefore concluded that the *in vitro* measurements relate to an efficient and robust means to regulate the cell-wide distribution of melanosomes.

In summary, our *in silico* analysis highlights the relevance of the *in vitro* experiments of our collaborators: The measured change of the switching probability $p_{\mathrm{Act}\to\mathrm{MT}}$ is likely to contribute to the collective dynamics of pigment organelles not only in a secondary role, but as a key player in the cell-wide organization of melanosomes. In fact, while an additional regulation of kinesin and dynein might support a rapid transition from an aggregated to a dispersed state, our simulations show that it is *per se* not required and that it can be compensated by regulating the cytoskeletal crosstalk.

3.2.5 The cell-wide distribution of melanosomes is regulated more effectively by changing the switching from actin to microtubules than vice versa

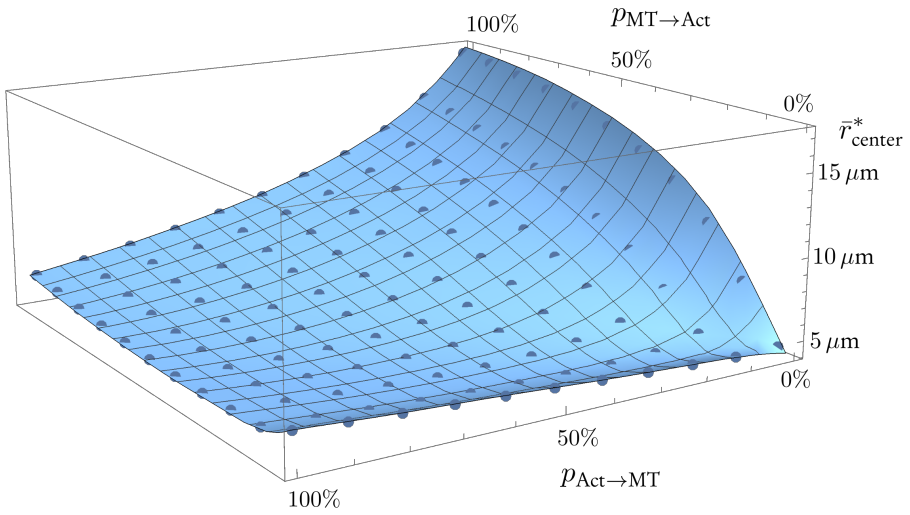

Figure 3.9 Manifold of regulation of the cell-wide melanosome distribution due to variations in the switching probabilities. We measured the stationary value of the average distance of melanosomes to the center of the cell $\bar{r}^*$ in virtual melanophores for varying probabilities $p_{\mathrm{MT}\to\mathrm{Act}}$ and $p_{\mathrm{Act}\to\mathrm{MT}}$ for 11 equidistant values in the range from 1-99%. Each of the data points (blue points) obtained in simulations corresponds to an ensemble average over 15 virtual melanophores to suppress the randomness that arises from different realizations of the (random) cytoskeletal networks. A two-dimensional spline was fitted to the data to interpolate values in the complete $p_{\mathrm{Act}\to\mathrm{MT}}$-$p_{\mathrm{MT}\to\mathrm{Act}}$ plane. In light of the resulting manifold, we can address the problem of a regulation of the degree of dispersion very generally by focusing on changes in $\bar{r}^*$ due to variations in $p_{\mathrm{MT}\to\mathrm{Act}}$ and $p_{\mathrm{Act}\to\mathrm{MT}}$, respectively. We used parameter values as given in Table 3.2.

In vitro, a PKA-dependent phosphorylation of the myosin-based transport complexes of Xenopus frogs only resulted in a significant change of the probability $p_{\mathrm{Act}\to\mathrm{MT}}$ to turn from an actin to a microtubule filament; The transverse process—switching from microtubules to actin filaments characterized by $p_{\mathrm{MT}\to\mathrm{Act}}$—did not show a PKA-dependent response. We therefore sought for functional origins of this behavior. Studying this problem by *in vitro* experiments is—with current experimental methods—not feasible, as it is not possible to vary both switching probabilities, $p_{\mathrm{Act}\to\mathrm{MT}}$ and $p_{\mathrm{MT}\to\mathrm{Act}}$, over a broad range. Opposed to that, such a scenario is very well accessible *in silico*, which consequently allowed us to compare the consequences

of changes in both probabilities. To this end, we systematically varied $p_{\mathrm{Act}\to\mathrm{MT}}$ and $p_{\mathrm{MT}\to\mathrm{Act}}$ in ten equidistant steps from 1-99%. For each combination of switching probabilities the virtual melanosomes converged to a stationary average distance to the cell center $\bar{r}^*$ which, in turn, quantified the degree of dispersion. Again, we simulated 15 different virtual cells and took the ensemble average. We then fitted a two-dimensional spline to the data to interpolate values for the stationary pigment distances $\bar{r}^*$ in the complete $p_{\mathrm{MT}\to\mathrm{Act}}$ vs. $p_{\mathrm{Act}\to\mathrm{MT}}$ plane. The result of this analysis is presented in Fig. 3.9. In view of the manifold determined by $\bar{r}^*(p_{\mathrm{MT}\to\mathrm{Act}}, p_{\mathrm{Act}\to\mathrm{MT}})$, the question of regulating the distribution of melanosomes within a cell could be rephrased as follows: How can $\bar{r}^*$ be changed effectively and efficiently by variations of the switching probabilities $p_{\mathrm{MT}\to\mathrm{Act}}$ and $p_{\mathrm{Act}\to\mathrm{MT}}$? A redistribution of particles is only efficient when a small change in the switching probabilities leads to a significant change in $\bar{r}^*$, in other words if $\bar{r}^*$ responds sensitively. Thus, a reasonable value for the efficiency of our regulatory problem is the magnitude of the gradient of the manifold $\bar{r}^*(p_{\mathrm{MT}\to\mathrm{Act}}, p_{\mathrm{Act}\to\mathrm{MT}})$. While, in principle, a simultaneous variation of both probabilities $p_{\mathrm{MT}\to\mathrm{Act}}$ and $p_{\mathrm{Act}\to\mathrm{MT}}$ may contribute to the regulation of the organization of melanosomes, we focused on changing either of the rates. This had the following reason: The *in vitro* results of our collaborators for transport complexes of Xenopus frogs suggested that primarily the probability of $p_{\mathrm{Act}\to\mathrm{MT}}$ is changed by the signaling factor that triggers dispersion (PKA). Opposed to that, $p_{\mathrm{MT}\to\mathrm{Act}}$ did not show a response to the signaling factor. Thus, we wanted to dissect the efficiency of a regulation of the melanosome distribution by changing either $p_{\mathrm{Act}\to\mathrm{MT}}$ or $p_{\mathrm{MT}\to\mathrm{Act}}$. To this end, we compared the absolute values of the partial derivatives of the stationary average distance of melanosomes to the center with respect to both switching probabilities, $|\partial_{p_{\mathrm{MT}\to\mathrm{Act}}}\bar{r}^*(p_{\mathrm{MT}\to\mathrm{Act}}, p_{\mathrm{Act}\to\mathrm{MT}})|$ and $|\partial_{p_{\mathrm{Act}\to\mathrm{MT}}}\bar{r}^*(p_{\mathrm{MT}\to\mathrm{Act}}, p_{\mathrm{Act}\to\mathrm{MT}})|$. The results are shown in Fig. 3.10. Importantly, $\bar{r}^*$ showed a high sensitivity for variations in $p_{\mathrm{Act}\to\mathrm{MT}}$ (dark orange area in Fig. 3.10) over a much broader range than for variations in $p_{\mathrm{MT}\to\mathrm{Act}}$. Intuitively, this can be understood in the following way: In order to outperform the centripetal motion on microtubules, a melanosome must compensate any inward displacement by a larger, isotropic displacement on the actin network. Thus, dispersing the melanosomes in the cell requires sufficiently long passages of actin-based motility. Consequently, large values of $p_{\mathrm{Act}\to\mathrm{MT}}$ impede any regulatory impact of varying $p_{\mathrm{MT}\to\mathrm{Act}}$, which limits this way of regulation. Our theoretical considerations further supported the relevance of the *in vitro* results of our collaborators: The change of the probabilities to switch between microtubules and actin filaments identified *in vitro* (black arrow in Fig. 3.10; for values see also Fig 3.4) is located in a particularly sensitive region of the $p_{\mathrm{MT}\to\mathrm{Act}}$-$p_{\mathrm{Act}\to\mathrm{MT}}$ plane. Furthermore, the switching probabilities measured for the transport complexes of zebrafish (green point in Fig. 3.10; for values see also Fig 3.4) are located in a region where only a variation of $p_{\mathrm{Act}\to\mathrm{MT}}$ would lead to a change in the distribution of melanosomes in a cell. Our regulatory manifold hence suggests a clear pathway for the evolution of

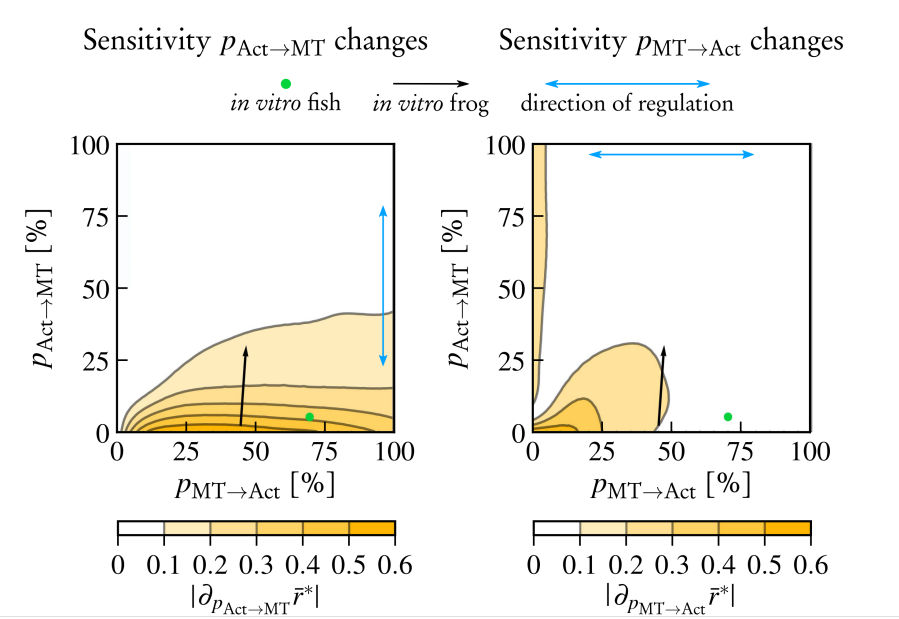

Figure 3.10 Regulatory sensitivity of the degree of dispersion $\bar{r}^*$ for changes in the probabilities to switch from actin to microtubule filaments and vice versa. The figure shows the absolute value of the partial derivatives $|\partial_{p_{\mathrm{Act}\to\mathrm{MT}}}\bar{r}^*(p_{\mathrm{MT}\to\mathrm{Act}}, p_{\mathrm{Act}\to\mathrm{MT}})|$ (left) and $|\partial_{p_{\mathrm{MT}\to\mathrm{Act}}}\bar{r}^*(p_{\mathrm{MT}\to\mathrm{Act}}, p_{\mathrm{Act}\to\mathrm{MT}})|$ (right), respectively, of the regulatory manifold as depicted in Fig. 3.9. These quantities determine the sensitivity of $\bar{r}^*$ (which measures the degree of dispersion) when changing the probabilities $p_{\mathrm{MT}\to\mathrm{Act}}$ and $p_{\mathrm{Act}\to\mathrm{MT}}$. Regulation of the melanosome distribution via $p_{\mathrm{Act}\to\mathrm{MT}}$ showed a much larger region that is sensitive (dark orange area) as compared to a regulation via $p_{\mathrm{MT}\to\mathrm{Act}}$. The phosphorylation-dependent change of the switching probabilities measured *in vitro* for transport complexes of Xenopus frogs (black arrow) is located in a region with a particularly high regulatory sensitivity. The myosin-based transport complex of the earlier organism (i.e. zebrafish) showed *in-vitro* switching probabilities $p_{\mathrm{MT}\to\mathrm{Act}}$ and $p_{\mathrm{Act}\to\mathrm{MT}}$ (green point) that are located in a region that would only be sensitive for changes in $p_{\mathrm{Act}\to\mathrm{MT}}$. Blue arrows indicate the direction of regulation in the respective plots. Parameter values as given in Table 3.2.

a regulatory mechanism when starting from the value corresponding to the earlier organism (i.e. zebrafish): regulating the probability $p_{\mathrm{Act}\to\mathrm{MT}}$. While it should be noted that, of course, our analysis identifies just one of several potential regulatory pathways, it is nonetheless remarkable that the pathway suggested by our regulatory manifold is in excellent accordance with the evolutionary changes traced back by the *in vitro* analysis of our collaborators (Fig 3.4).

Taking everything together, our theoretical analyses detailed above revealed the following functional characteristics related to a regulation of the melanosome distribution in a cell: (a) The distribution of melanosomes is affected by variations of $p_{\mathrm{MT}\to\mathrm{Act}}$ only in a very limited fashion. Opposed to that, a regulation by changes of

$p_{\mathrm{Act}\to\mathrm{MT}}$ is possible in a robust manner. (b) The myosin-based transport complexes used in the *in vitro* experiments of our collaborators operated in a range of switching probabilities where the cell-wide organization of melanosomes responds particularly well to variations of $p_{\mathrm{MT}\to\mathrm{Act}}$. (c) Our general analysis of the regulatory efficiency strongly suggests the evolution towards a regulation of $p_{\mathrm{Act}\to\mathrm{MT}}$ when starting at switching probabilities that correspond to zebrafish (i.e. an earlier organism than the Xenopus frog). It is noteworthy that a previous study already suggested that the regulation of the probability to switch from actin filaments to microtubules fulfills an important role for the organization of melanosomes in fish melanophores [235]. The *in vitro* measurements of our collaborators (Fig. 3.4) showed that this regulation can't be mediated by myosin in fish cells and is thus probably mediated by kinesin and/or dynein. Our theoretical findings explain why a regulation of exactly this probability is beneficial and show that myosin has adopted the ability of carrying out this central role in Xenopus frogs.

While our analysis detailed above provides a reasonable measure for small variations of the switching probabilities, it doesn't quantify the maximal potential change in $\bar{r}^*$ when the switching probabilities are changed over a broad range. In other words, we have so far quantified the sensitivity of regulation but are lacking a measure for the maximal potential impact of a specific scheme of regulation. To overcome this limitation, we analyzed the maximal difference of $\bar{r}^*$ along the curves defined by $p_{\mathrm{MT}\to\mathrm{Act}} \in [0.01, 0.99]; p_{\mathrm{Act}\to\mathrm{MT}} = \text{const.}$ and vice versa. Together with this measure for the *effectiveness* (i.e. the maximal potential impact) of a regulation upon variations in $p_{\mathrm{Act}\to\mathrm{MT}}$ and $p_{\mathrm{MT}\to\mathrm{Act}}$, respectively, we also determined the *maximal sensitivity* for the respective changes, measured in terms of the maximal value of the partial derivative in the respective direction: $s^{\max}_{\mathrm{Act}\to\mathrm{MT}}(p_{\mathrm{MT}\to\mathrm{Act}}) = \max_{p_{\mathrm{Act}\to\mathrm{MT}}\in[0.01,0.99]}[\partial p_{\mathrm{Act}\to\mathrm{MT}}\bar{r}^*(p_{\mathrm{MT}\to\mathrm{Act}}, p_{\mathrm{Act}\to\mathrm{MT}})]$ and $s^{\max}_{\mathrm{MT}\to\mathrm{Act}}(p_{\mathrm{Act}\to\mathrm{MT}}) = \max_{p_{\mathrm{MT}\to\mathrm{Act}}\in[0.01,0.99]}[\partial p_{\mathrm{MT}\to\mathrm{Act}}\bar{r}^*(p_{\mathrm{MT}\to\mathrm{Act}}, p_{\mathrm{Act}\to\mathrm{MT}})]$. The result of this approach is presented in Fig. 3.11. This analysis unfolded further principles of the regulation of cell-wide melanosome organization: While a regulation of the distribution of melanosomes is, in principle, effective by changing $p_{\mathrm{MT}\to\mathrm{Act}}$ in the range $p_{\mathrm{Act}\to\mathrm{MT}} \lessapprox 30\%$, the melanosome distribution is not particularly sensitive against such changes (small values for the maximal sensitivity) basically over the whole range of values for $p_{\mathrm{Act}\to\mathrm{MT}}$. Conversely, a regulation by changing $p_{\mathrm{Act}\to\mathrm{MT}}$ is effective (large values for the effectiveness) in a range of $p_{\mathrm{MT}\to\mathrm{Act}} \gtrapprox 30\%$ and sensitive (large values for the maximal sensitivity) in the range $p_{\mathrm{MT}\to\mathrm{Act}} \gtrapprox 10\%$. Remarkably, a fixed probability of $p_{\mathrm{MT}\to\mathrm{Act}} \approx 46\%$ (dashed line in Fig. 3.11) as measured *in vitro* is located closely to a global, simultaneous optimum of the effectiveness and sensitivity of regulation via changes in $p_{\mathrm{Act}\to\mathrm{MT}}$.

In summary, our analysis of the maximal regulatory effectiveness and sensitivity further supports the notion that only a regulation of the melanosome distribution via changes in $p_{\mathrm{Act}\to\mathrm{MT}}$ works robustly while a regulation via variations in $p_{\mathrm{MT}\to\mathrm{Act}}$

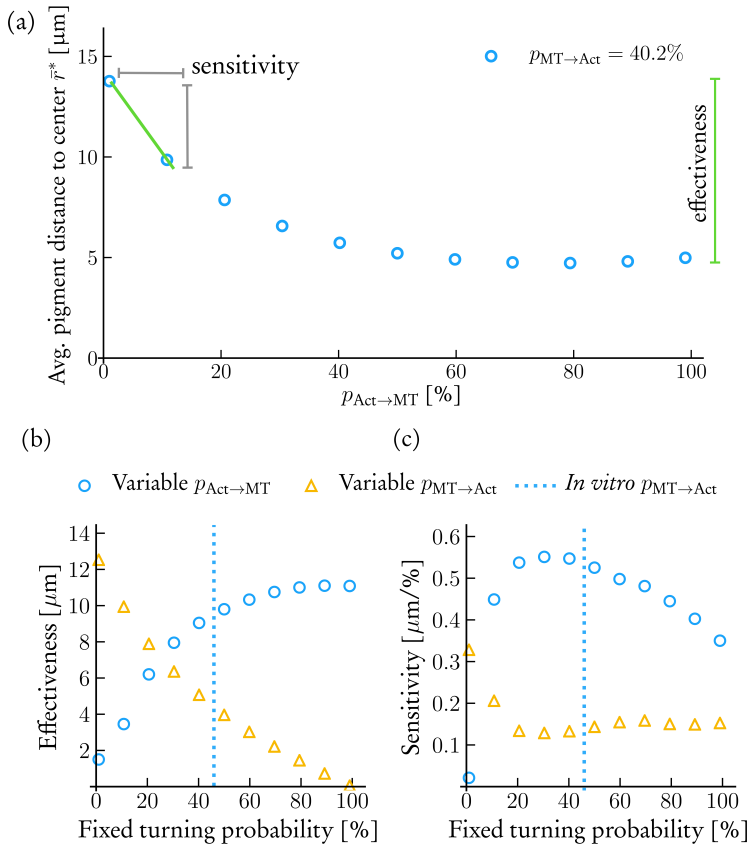

Figure 3.11 The intracellular distribution of melanosomes is regulated effectively and sensitively by changes in $p_{\mathrm{Act}\to\mathrm{MT}}$. (a) Illustration of our definition of the effectiveness and sensitivity at the example of varying $p_{\mathrm{Act}\to\mathrm{MT}}$. Each fixed value of $p_{\mathrm{MT}\to\mathrm{Act}}$ (here 40.2%) is related to a curve $\bar{r}^*(p_{\mathrm{Act}\to\mathrm{MT}})$ (blue points). For each such curve, we defined the effectiveness as the maximal range of $\bar{r}^*$ and the maximal sensitivity as the maximal (absolute) value of the slope. Hence, we can associate an effectiveness and a sensitivity for every (fixed) value of $p_{\mathrm{MT}\to\mathrm{Act}}$. Analogous to this example for varying $p_{\mathrm{Act}\to\mathrm{MT}}$ and fixed $p_{\mathrm{MT}\to\mathrm{Act}}$, we also computed the effectiveness and sensitivity for varying $p_{\mathrm{MT}\to\mathrm{Act}}$ and fixed $p_{\mathrm{Act}\to\mathrm{MT}}$. **(b)** Resulting effectiveness and sensitivity for a regulation by changes in $p_{\mathrm{Act}\to\mathrm{MT}}$ [blue circles in panels (b) and (c)] and by changes in $p_{\mathrm{MT}\to\mathrm{Act}}$ [orange triangles in panels (b) and (c)]. A regulation by changes in $p_{\mathrm{MT}\to\mathrm{Act}}$ was only effective at low fixed values of $p_{\mathrm{Act}\to\mathrm{MT}}$ and not particularly sensitive in the complete range of $p_{\mathrm{Act}\to\mathrm{MT}}$. The regulation of the distribution of melanosomes by changes in $p_{\mathrm{Act}\to\mathrm{MT}}$, on the other hand, was effective and sensitive for $p_{\mathrm{MT}\to\mathrm{Act}} \gtrapprox 30\%$. The value of $p_{\mathrm{MT}\to\mathrm{Act}} = 46\%$ (dashed green line) as measured *in vitro* is close to a global, simultaneous optimum of the effectiveness and sensitivity. Parameter values as given in Table 3.2.

is very limited. Moreover, our analysis strongly suggests that myosin-based transport complexes in Xenopus frogs are optimized in a way to establish an effective yet sensitive regulation of the cell-wide melanosome distribution.

3.2.6 Conclusion and outlook

In this section we have studied the cell-wide distribution of pigment organelles. In early and lower vertebrates, a redistribution of these organelles in skin cells allows these animals to adapt their skin color to the environment: When the pigment organelles switch from an aggregated state, in which the organelles are accumulated in the center of the cell, to a dispersed state, in which the organelles are distributed throughout the cell, the cells change from a bright to a dark appearance. While it is a well-known fact that this redistribution depends on the motion of the organelles on both cytoskeletal components, actin filaments and microtubules, the underlying biomolecular changes as well as general principles that govern a redistribution of melanosomes remained unknown.

Here we traced a global redistribution of melanosomes back to a change in the transition probability at which organelles switch from an actin to a microtubule filament. Our collaborators on this project, the group of Dr. Zeynep Ökten, unraveled that myosin-based transport complexes that move the organelles on actin in Xenopus frogs developed a switch in this probability that can be triggered by a phosphorylation. Opposing this finding for transport complexes of Xenopus frogs, the corresponding complexes from zebrafish—an organism that evolved earlier—did not show such a response. Here, we used computational modeling to relate the experimental findings for individual proteins to a cell-wide organization and, ultimately, to their functionality. In doing so, we elucidated the following principles of the cell-wide organization of pigment organelles:

- We showed that the measured change of the probability of an individual myosin-based transport complexe to switch from an actin filament to a microtubule indeed reconstitutes a transition between an aggregated and a dispersed state *in silico*. While additional regulation of other factors might facilitate such a transition *in vivo*, our simulations showed that they are *per se* not required to reorganize the organelles *in silico*. Thus, the findings of our collaborators indeed relate to the functionality of melanophores.

- We probed the efficiency and robustness of the *in vitro* measurements in our computational model by measuring the degree if dispersion when varying the switching probability over a broad range. This analysis revealed that the cell-wide organization of pigment organelles was particularly sensitive against changes in the probability to switch from actin filaments to microtubules in the range measured in the experiment. Conversely, a modulation of the opposite

probability (i.e. for switching from a microtubule to an actin filament) around the values measured *in vitro* did not provoke significant changes in the distribution of the virtual melanosomes. Hence, the results from the experiments translate to an efficient yet robust way to regulate the cell-wide organization of organelles.

- With regard to the biomolecular changes observed experimentally for the transport complexes from fish and amphibians, our results suggest a potential evolutionary pathway: Starting from the *in vitro* measurements related to zebrafish, only changes in the probability $p_{\mathrm{Act}\to\mathrm{MT}}$ showed a significant impact on the distribution of organelles. Opposed to that, a change in the transverse probability, $p_{\mathrm{MT}\to\mathrm{Act}}$, did not lead to a relevant redistribution of organelles in a virtual cell. Thus, our theoretical analysis provides a rationale for the evolution of biomolecular properties of the myosin-based transport complex of zebrafish and Xenopus frogs as determined in the experiments.

In summary, our study elucidates principles that determine the cell-wide organization of melanosomes over a broad range: While our collaborators uncovered first biomolecular changes related to the signaling factors that drive a redistribution of melanosomes *in vivo*, we related these molecular properties to the cell-wide collective dynamics of organelles. Nevertheless, the remaining open questions with regard to the regulation of the melanosome distribution in cells should be mentioned as well. Foremost, our study treated the problem from the view of single myosin motors while *in vivo* also dynein and kinesin motors might contribute to a redistribution of melanosomes. The aim of this study was to investigate the contribution of myosin-based transport complexes on a cell-wide organization of melanosomes independently from other factors that might additionally influence the melanosome distribution. For future work, it might, however, be revealing to also study the potential regulatory impact of kinesin and dynein. Additionally, not only other types of motors are bound to melanosomes *in vivo* but also several motors from each of the species are present. Hence, it will be interesting to relate properties of individual motor proteins to the "tug of war" between multiple motors that are simultaneously attached to the melanosomes. Finally, it should also be noted that the reorganization of melanosomes in mammalian cells has a different functional purpose than that in the cells of fish and amphibians: Mammalian cells have lost the capability of dynamically rearranging organelles between an aggregated and a dispersed state. Instead, they have developed mechanisms to transport the organelles to the periphery of a cell where the melanosomes are handed over to the surrounding skin tissue for protection against UV radiation [59]. With regard to this different functionality, it will certainly be revealing to study evolutionary changes that might have governed these different characteristics of the cell-wide organization of pigment organelles in mammalian cells as compared to fish and amphibians.

Appendix

A Parameter selection

In the following, we describe how we inferred the parameters used in our model for the collective dynamics of melanosomes in a melanophore. To begin with, we summarize the parameters with respect to the cytoskeletal architecture.

In melanophores, it is assumed that the orientation of actin filaments is mostly isotropic [237]. Therefore, we selected the orientation of actin filaments in our virtual melanosomes from a uniform distribution in the range $[0,2\pi)$. The length in our model is chosen from an exponential distribution with a mean length of 1.5 µm, which is roughly consistent with experimental data [237]. The average distance between crossings of actin filaments was measured *in vivo* and yielded values between 160 nm and 330 nm [237]. We determined this value in our simulations and chose a number of actin filaments that leads to an average distance of approximately 170 nm. The corresponding density of actin filaments is approximately 9 µm of filament per μm^2 area of the cell. This value is also consistent with the values determined in other experiments [239–241].

For the arrangement of microtubules we could find neither a measurement of the distribution of their ends in Xenopus melanophores nor a measurement of the number of microtubules per cell. We estimated the number of microtubules roughly by 200, which is in accordance with estimates of the number of microtubules in different cells [242].

For the diffusion constant of our virtual melanosomes, we used the following approach: The measured diffusion coefficient of melanosomes *in vivo* is approximately 1.3×10^{-3} $\mu m^2/s$ [243]. *In vivo* measurements of the diffusion constant are, however, likely obstructed by other factors such as molecular crowding. Since we were interested in the corresponding value of an unobstructed motion in the cytoplasm as it occurs on very small length scales, we also computed the theoretical value based on the Stokes-Einstein relation. Assuming an effective cytoplasmic viscosity of 5×10^{-2} Pa s [244] yields a value of approximately 1.7×10^{-2} $\mu m^2/s$ for a melanosome with an approximate diameter of 500 nm [237]. For the simulations we chose a value of 4.5×10^{-3} $\mu m^2/s$, which is located between the measured and the theoretical value.

For the speed of melanosomes on actin filaments we used the results of *in vitro* measurements for single myosin motors performed by our collaborators which yielded values of approximately 240 nm/s, see also Table 3.1. In addition to these measurements for individual myosin-based transport complexes, our collaborators determined also the translocation speed when the transport complexes where additionally bound to melanosomes. As the transport-complex-melanosome construct moved at a speed of 190 nm/s, we concluded that melanosomes move at similar velocities on actin filaments as individual transport complexes and used the latter value (240 nm/s) in our simulations.

For the speed of melanosomes on microtubules we referred to previous *in vivo* measurements [233]. These measurements quantified the bidirectional motion of melanosomes on microtubules and yielded values of approximately 400 nm/s for plus-end as well as minus-end directed transport of melanosomes on microtubules. During aggregation, the average run length of uninterrupted minus-end directed motion was approximately 640 nm while that of uninterrupted plus-end directed motion was approximately 480 nm. This indicates an increased probability of melanosomes to move towards the minus end as compared to move to the plus end. Since we treat bidirectional motion in an effective fashion in our model, the resulting rates to move towards the plus end and minus end can be understood as the respective velocities multiplied by the probability for being in a plus-end or minus-end directed state, respectively. Based on the previous finding, we chose an effective speed of 240 nm/s for the motion of the virtual melanosomes towards the plus end of a microtubule and an effective speed of 390 nm/s for motion towards the minus end of a microtubule. Thus, melanosomes in our model showed a slightly increased minus-end directed component in their motion on microtubules than the melanosomes measured in the *in vivo* experiments [233], which corresponds to a conservative choice of modeling.

For the detachment rates of melanosomes, we assumed that corresponding values are lowered significantly by the fact that multiple motors transport a single melanosome. This assumption is supported by experimental [103] and theoretical [127] findings. We estimated that melanosomes show a 100-fold increased dwell time as compared to single myosin motors on microtubules and actin filaments. Based on the *in vitro* measurements of our experimental collaborators for the run lengths of myosin-based transport complexes (see Table 3.1) and dwell times on microtubules (approximately 3.9 s), we assumed dwell times of $\tau_{\mathrm{MT}} \approx 390\,\mathrm{s}$ of melanosomes on microtubules and $\tau_{\mathrm{Act}} \approx 417\,\mathrm{s}$ on actin filaments. At the plus (barbed) ends of microtubules (actin filaments), we chose values for the detachment rates that equal the speed of translocation on the respective filament type. In this way, the melanosomes simply "walked off" the plus and barbed ends of filaments, respectively.

Measuring the attachment rate of molecular motors that are in close proximity to a cytoskeletal filament is experimentally very challenging. As we could not find a corresponding measurement for the attachment rates of myosin motors to either microtubules or actin filaments, we resorted to previous measurements of the attachment rate for kinesins to microtubules [245]. We estimated that this value would, however, be similar to the attachment rate of mysoin motors to actin filaments or microtubules as the binding process is likely limited by the time scales related to a diffusion in the cytoplasm but not by the time scales related to the binding reaction itself. The above mentioned study measured a value of $5\,\mathrm{s}^{-1}$ for the attachment rate of kinesins to a microtubule in their close proximity which we used for the binding rate of our particles to actin filaments as well as to microtubules.

Our cells had a radius of 30 µm. For discretization, we used a lattice size of $a = 30$ nm, which was inspired by the fact that this corresponds to the step size of myosin motors [246] that we wanted to resolve in the simulations. We used this discretization to relate all of the values detailed above to the respective rates in terms of the lattice spacing. In case of translocation speeds, this transformation is trivial. The diffusion coefficient D of melanosomes in the cytoplasm is related to the "hopping rate" $r_{\text{Cytoplasm}}$ of melanosomes in the cytoplasm by $D = r_{\text{Cytoplasm}} a^2$.

The switching probability of melanosomes from one actin filament to another one at an intersection was indirectly inferred in previous experiments [237]. During dispersion, the corresponding switching probability was estimated to be very low or effectively zero. Thus, we set the value for $p_{\text{Act}\to\text{Act}}$ to 3% in our simulations.

The number of virtual melanosomes in the cell was roughly estimated on a visual basis to be compatible with *in vivo* images of melanophores and to reproduce visible color changes when redistributing. A random number of melanosomes was selected according to a mean density of 33 melanosomes per µm^2 of cell area.

A list of the ensuing parameters employed in our simulations is given in Table 3.2.

Parameter	Value
Radius of the cell	30 µm
Number of actin filaments	17000
Average length of an actin filament	1.5 µm
Number of microtubules	200
Length of a microtubule	30 µm
Melanosome density	33 µm^{-2}
Motion in the cytoplasm $r_{\text{Cytoplasm}}$	5 s^{-1}
Motion on actin filaments r^{+}_{actin}	8 s^{-1}
Plus-end directed motion on microtubules r^{+}_{MT}	8 s^{-1}
Minus-end directed motion on microtubules r^{-}_{MT}	13 s^{-1}
Detachment rate from actin filaments $r_{\text{Act}\to\text{Cytoplasm}}$	0.0024 s^{-1}
Detachment rate from actin ends $r^{\text{end}}_{\text{Act}\to\text{Cytoplasm}}$	8 s^{-1}
Detachment rate from microtubules $r_{\text{MT}\to\text{Cytoplasm}}$	0.0026 s^{-1}
Detachment rate from microtubule ends $r^{\text{end}}_{\text{MT}\to\text{Cytoplasm}}$	8 s^{-1}
Attachment rate to actin filaments $r_{\text{Cytoplasm}\to\text{Act}}$	5s^{-1}
Attachment rate to microtubules $r_{\text{Cytoplasm}\to\text{MT}}$	5s^{-1}
Switching probability actin-actin $p_{\text{Act}\to\text{Act}}$	3%

Table 3.2 Summary of the parameters for our model for the cell-wide organization of melanosomes.

4 Postface

This thesis covers several examples where nonequilibrium processes lead to organization and formation of structure on the probably smallest scale of life: within an individual cell. In Chapter 2, we have seen how proteins organize along individual cytoskeletal filaments: (1) Breaking detailed balance at a single position localizes proteins at their target binding site. (2) Two species of actively moving molecular motors self-organize into patterns along a microtubule, which critically changes their collective dynamics. (3) Specific molecular motors of yeast cells form aggregates, which triggers a reversal of their direction of motion. In Chapter 3, we have discussed examples of protein organization on a cell-wide level: (1) Active motion groups curved polymers into dynamic vortex patterns—a mechanism that might contribute to bacterial cell division. (2) The interplay of active motion of pigment organelles on the different cytoskeletal networks stimulates a cell-wide redistribution of these organelles and thereby allows certain animals to change the color of their skin.

Because the examples where nonequilibrium processes create order are ubiquitous, it seems tempting to raise this observation to a general principle. However, each of our examples differed with respect to the approaches we employed as well as with respect to the specific characteristics of structure formation. In the end, comprehensive theoretical frameworks that describe nonequilibrium systems—and thus living matter—are mostly lacking. While the question of "What is life?" [247] has intrigued scientists for decades, it seems that we are still far away from an answer. Meanwhile, we can resort to studying nonequilibrium systems individually and tailor different approaches for different collective phenomena. In this regard, studying living systems may well be just as diverse, complex—yet fascinating—as life itself.

Bibliography

[1] H. Panday, E. Reithmann, A. Goldstein, J. Al-Bassam, M. Popov, E. Frey and L. Gheber. In preparation. 2019. (Cit. on pp. xv, 5, 87).

[2] M. Loose and T. J. Mitchison. The bacterial cell division proteins FtsA and FtsZ self-organize into dynamic cytoskeletal patterns. *Nature Cell Biology* **16**(1), 38–46, 2013. (Cit. on pp. xvi, xvii, 2, 5, 131, 132, 134).

[3] A. Oberhofer, E. Reithmann, P. Spieler, W. L. Stepp, D. Zimmermann, B. Schmid, E. Frey and Ö. Zeynep. In preparation. 2019. (Cit. on pp. xix, 6, 151).

[4] I. Kant. *Kritik der Urteilskraft*. Philipp Reclam jun., Stuttgart, 1986. (Cit. on p. 1).

[5] E. Karsenti. Self-organization in cell biology: a brief history. *Nature Reviews Molecular Cell Biology* **9**(3), 255–262, 2008. (Cit. on pp. 1, 2).

[6] S. Camazine, J. L. Deneubourg, N. R. Franks, J. Sneyd, E. Bonabeau and G. Theraula. Self-organization in biological systems. Princeton University Press, Princeton, 2003. (Cit. on p. 1).

[7] I. Couzin. Collective minds. *Nature* **445**(7129), 715–715, 2007. (Cit. on p. 1).

[8] E. F. Rossomando and S. Alexander. *Morphogenesis: An Analysis of the Development of Biological Form*. Marcel Dekker, New York, 1992. (Cit. on p. 1).

[9] T. J. Mitchison. Self-organization of polymer-motor systems in the cytoskeleton. *Philosophical transactions of the Royal Society of London. Series B, Biological sciences* **336**(1276), 99–106, 1992. (Cit. on p. 1).

[10] T. Misteli. The concept of self-organization in cellular architecture. *The Journal of Cell Biology* **155**(2), 181–185, 2001. (Cit. on p. 1).

[11] T. Vignaud, L. Blanchoin and M. Théry. Directed cytoskeleton self-organization. *Trends in Cell Biology* **22**(12), 671–682, 2012. (Cit. on pp. 1, 2).

[12] I. Prigogine. *Non-equilibrium statistical mechanics*. Dover Publications, Mineola, New York, 2017. (Cit. on p. 1).

[13] B. Derrida. Non-equilibrium steady states: fluctuations and large deviations of the density and of the current. *Journal of Statistical Mechanics: Theory and Experiment* **2007**(07), P07023–P07023, 2007. (Cit. on p. 1).

[14] T. Chou, K. Mallick and R. K. P. Zia. Non-equilibrium statistical mechanics: from a paradigmatic model to biological transport. *Reports on Progress in Physics* **74**(11), 116601, 2011. (Cit. on pp. 1, 52–55).

[15] S. L. Rogers and V. I. Gelfand. Membrane trafficking, organelle transport, and the cytoskeleton. *Current Opinion in Cell Biology* **12**(1), 57–62, 2000. (Cit. on pp. 1, 3).

[16] R. Subramanian and T. M. Kapoor. Building Complexity: Insights into Self-Organized Assembly of Microtubule-Based Architectures. *Developmental Cell* **23**(5), 874–885, 2012. (Cit. on p. 1).

[17] B. Alberts, A. Johnson, J. Lewis, M. Raff, K. Roberts and P. Walter. *Molecular Biology of the Cell*. 4th edition. Garland Science, New York, 2002. (Cit. on pp. 1, 2, 51, 52).

[18] M. Kirschner and T. Mitchison. Beyond self-assembly: from microtubules to morphogenesis. *Cell* **45**(3), 329–342, 1986. (Cit. on p. 2).

[19] A. A. Hyman and E. Karsenti. Morphogenetic Properties of Microtubules and Mitotic Spindle Assembly. *Cell* **84**(3), 401–410, 1996. (Cit. on p. 2).

[20] D. A. Fletcher and R. D. Mullins. Cell mechanics and the cytoskeleton. *Nature* **463**(7280), 485–492, 2010. (Cit. on pp. 2, 51).

[21] L. Blanchoin, R. Boujemaa-Paterski, C. Sykes and J. Plastino. Actin Dynamics, Architecture, and Mechanics in Cell Motility. *Physiological Reviews* **94**(1), 235–263, 2014. (Cit. on p. 2).

[22] G. Letort, H. Ennomani, L. Gressin, M. Théry and L. Blanchoin. Dynamic reorganization of the actin cytoskeleton. *F1000Research* **4**, 940, 2015. (Cit. on pp. 2, 51).

[23] M. E. Porter and W. S. Sale. The 9 + 2 Axoneme Anchors Multiple Inner Arm Dyneins and a Network of Kinases and Phosphatases That Control Motility. *The Journal of Cell Biology* **151**(5), F37–F42, 2000. (Cit. on p. 2).

[24] P. Satir and M. A. Sleigh. The physiology of cilia and mucociliary interactions. *Annual review of physiology* **52**(1), 137–155, 1990. (Cit. on p. 2).

[25] F. Verde. Taxol-induced microtubule asters in mitotic extracts of Xenopus eggs: requirement for phosphorylated factors and cytoplasmic dynein. *The Journal of Cell Biology* **112**(6), 1177–1187, 1991. (Cit. on p. 2).

[26] F. J. Nédélec, T. Surrey, A. C. Maggs and S. Leibler. Self-organization of microtubules and motors. *Nature* **389**(6648), 305–308, 1997. (Cit. on p. 2).

[27] T. Surrey, F. Nedelec, S. Leibler and E. Karsenti. Physical properties determining self-organization of motors and microtubules. *Science* **292**(5519), 1167–1171, 2001. (Cit. on p. 2).

[28] J. Roostalu, J. Rickman, C. Thomas, F. Nédélec and T. Surrey. Determinants of Polar versus Nematic Organization in Networks of Dynamic Microtubules and Mitotic Motors. *Cell* **175**(3), 796–808.e14, 2018. (Cit. on p. 2).

[29] F. Backouche, L. Haviv, D. Groswasser and A. Bernheim-Groswasser. Active gels: dynamics of patterning and self-organization. *Physical Biology* **3**(4), 264–273, 2006. (Cit. on p. 2).

[30] V. Schaller, C. Weber, C. Semmrich, E. Frey and A. R. Bausch. Polar patterns of driven filaments. *Nature* **467**(7311), 73–77, 2010. (Cit. on pp. 2, 133, 134).

[31] T. Butt, T. Mufti, A. Humayun, P. B. Rosenthal, S. Khan, S. Khan and J. E. Molloy. Myosin Motors Drive Long Range Alignment of Actin Filaments. *Journal of Biological Chemistry* **285**(7), 4964–4974, 2010. (Cit. on pp. 2, 133, 134).

[32] Y. Sumino, K. H. Nagai, Y. Shitaka, D. Tanaka, K. Yoshikawa, H. Chaté and K. Oiwa. Large-scale vortex lattice emerging from collectively moving microtubules. *Nature* **483**(7390), 448–452, 2012. (Cit. on pp. 2, 134).

[33] L. Huber, R. Suzuki, T. Krüger, E. Frey and A. R. Bausch. Emergence of coexisting ordered states in active matter systems. *Science* **361**(6399), 255–258, 2018. (Cit. on pp. 2, 133, 134).

[34] D. A. Ramirez-Diaz, D. A. Garcia-Soriano, A. Raso, J. Mücksch, M. Feingold, G. Rivas and P. Schwille. Treadmilling analysis reveals new insights into dynamic FtsZ ring architecture. *PLOS Biology* **16**(5), e2004845, 2018. (Cit. on pp. 2, 132, 134, 135).

[35] T. Mitchison and M. Kirschner. Dynamic instability of microtubule growth. *Nature* **312**(5991), 237–242, 1984. (Cit. on p. 2).

[36] A. Desai and T. J. Mitchison. Microtubule polymerization dynamics. *Annual Review of Cell and Developmental Biology* **13**(1), 83–117, 1997. (Cit. on pp. 2, 8, 18).

[37] M. F. Carlier. Actin polymerization and ATP hydrolysis. *Advances in biophysics* **26**, 51–73, 1990. (Cit. on p. 2).

[38] S. Petry. Mechanisms of Mitotic Spindle Assembly. *Annual review of biochemistry* **85**(1), 659–683, 2016. (Cit. on p. 2).

[39] D. Oriola, D. J. Needleman and J. Brugués. The Physics of the Metaphase Spindle. *Annual Review of Biophysics* **47**(1), 655–673, 2018. (Cit. on p. 2).

[40] M. A. Jordan and L. Wilson. Microtubules as a target for anticancer drugs. *Nature Reviews Cancer* **4**(4), 253–265, 2004. (Cit. on pp. 2, 3).

[41] M. A. Jordan and L. Wilson. Microtubules and actin filaments: dynamic targets for cancer chemotherapy. *Current Opinion in Cell Biology* **10**(1), 123–130, 1998. (Cit. on p. 3).

[42] J. Howard. *Mechanics of Motor Proteins and the Cytoskeleton*. Sinauer Associates, Sunderland, MA, 2001. (Cit. on pp. 3, 51).

[43] R. D. Vale. The Molecular Motor Toolbox for Intracellular Transport. *Cell* **112**(4), 467–480, 2003. (Cit. on pp. 3, 51).

[44] J. R. Sellers. Myosins: a diverse superfamily. *Biochimica et biophysica acta* **1496**(1), 3–22, 2000. (Cit. on p. 3).

[45] N. Hirokawa, Y. Noda, Y. Tanaka and S. Niwa. Kinesin superfamily motor proteins and intracellular transport. *Nature Reviews Molecular Cell Biology* **10**(10), 682–696, 2009. (Cit. on pp. 3, 51, 57).

[46] R. D. Vale and R. A. Milligan. The Way Things Move: Looking Under the Hood of Molecular Motor Proteins. *Science* **288**(5463), 88–95, 2000. (Cit. on pp. 3, 51).

[47] P. J. Hollenbeck and J. A. Swanson. Radial extension of macrophage tubular lysosomes supported by kinesin. *Nature* **346**(6287), 864–866, 1990. (Cit. on pp. 3, 152).

[48] R. L. Morris and P. J. Hollenbeck. Axonal transport of mitochondria along microtubules and F-actin in living vertebrate neurons. *The Journal of Cell Biology* **131**(5), 1315–1326, 1995. (Cit. on pp. 3, 152).

[49] I. Corthesy-Theulaz, A. Pauloin and S. R. Pfeffer. Cytoplasmic dynein participates in the centrosomal localization of the Golgi complex. *The Journal of Cell Biology* **118**(6), 1333–1345, 1992. (Cit. on pp. 3, 152).

[50] M. Terasaki, J. Song, J. R. Wong, M. J. Weiss and L. B. Chen. Localization of endoplasmic reticulum in living and glutaraldehyde-fixed cells with fluorescent dyes. *Cell* **38**(1), 101–108, 1984. (Cit. on pp. 3, 152).

[51] J. S. Tabb, B. J. Molyneaux, D. L. Cohen, S. A. Kuznetsov and G. M. Langford. Transport of ER vesicles on actin filaments in neurons by myosin V. *Journal of Cell Science* **111 (Pt 21)**, 3221–3234, 1998. (Cit. on pp. 3, 152).

[52] N. Hirokawa. Kinesin and Dynein Superfamily Proteins and the Mechanism of Organelle Transport. *Science* **279**(5350), 519–526, 1998. (Cit. on pp. 3, 52, 97).

[53] V. I. Rodionov, A. J. Hope, T. M. Svitkina and G. G. Borisy. Functional coordination of microtubule-based and actin-based motility in melanophores. *Current Biology* **8**(3), 165–169, 1998. (Cit. on pp. 3, 152, 153).

[54] S. L. Rogers and V. I. Gelfand. Myosin cooperates with microtubule motors during organelle transport in melanophores. *Current Biology* **8**(3), 161–164, 1998. (Cit. on pp. 3, 152, 153, 162).

[55] X. Wu, B. Bowers, Q. Wei, B. Kocher and J. A. Hammer. Myosin V associates with melanosomes in mouse melanocytes: evidence that myosin V is an organelle motor. *Journal of Cell Science* **110 (Pt 7)**, 847–859, 1997. (Cit. on pp. 3, 152).

[56] S. S. Brown. Cooperation between microtubule- and actin-based motor proteins. *Annual Review of Cell and Developmental Biology* **15**(1), 63–80, 1999. (Cit. on pp. 3, 152).

[57] J. F. Kelleher and M. A. Titus. Intracellular motility: How can we all work together? *Current Biology* **8**(11), R394–R397, 1998. (Cit. on pp. 3, 152, 153).

[58] A. A. Nascimento, J. T. Roland and V. I. Gelfand. Pigment cells: a model for the study of organelle transport. *Annual Review of Cell and Developmental Biology* **19**(1), 469–491, 2003. (Cit. on pp. 3, 152, 158, 164, 165).

[59] C. Wasmeier, A. N. Hume, G. Bolasco and M. C. Seabra. Melanosomes at a glance. *Journal of Cell Science* **121**(Pt 24), 3995–3999, 2008. (Cit. on pp. 3, 152, 164, 165, 173).

[60] E. Reithmann, L. Reese and E. Frey. Quantifying protein diffusion and capture on filaments. *Biophysical Journal* **108**(4), 787–790, 2015. (Cit. on pp. 4, 7, 13, 17).

[61] E. Reithmann, L. Reese and E. Frey. Nonequilibrium Diffusion and Capture Mechanism Ensures Tip Localization of Regulating Proteins on Dynamic Filaments. *Physical Review Letters* **117**(7), 078102, 2016. (Cit. on pp. 4, 7, 13, 15, 17).

[62] P. Wilke, E. Reithmann and E. Frey. Two-Species Active Transport along Cylindrical Biofilaments is Limited by Emergent Topological Hindrance. *Physical Review X* **8**(3), 031063, 2018. (Cit. on pp. 4, 51, 58).

[63] J. Denk, L. Huber, E. Reithmann and E. Frey. Active Curved Polymers Form Vortex Patterns on Membranes. *Physical Review Letters* **116**(17), 178301–6, 2016. (Cit. on pp. 5, 131, 135).

[64] E. Mandelkow and E.-M. Mandelkow. Microtubules and microtubule-associated proteins. *Current Opinion in Cell Biology* **7**(1), 72–81, 1995. (Cit. on p. 8).

[65] N. Hirokawa. Microtubule organization and dynamics dependent on microtubule-associated proteins. *Current Opinion in Cell Biology* **6**(1), 74–81, 1994. (Cit. on p. 8).

[66] J. Howard and A. A. Hyman. Microtubule polymerases and depolymerases. *Current Opinion in Cell Biology* **19**(1), 31–35, 2007. (Cit. on p. 8).

[67] A. Akhmanova and M. O. Steinmetz. Control of microtubule organization and dynamics: two ends in the limelight. *Nature Reviews Molecular Cell Biology* **16**(12), 711–726, 2015. (Cit. on p. 8).

[68] A. Akhmanova and M. O. Steinmetz. Tracking the ends: a dynamic protein network controls the fate of microtubule tips. *Nature Reviews Molecular Cell Biology* **9**(4), 309–322, 2008. (Cit. on pp. 8, 10, 11).

[69] K. Jiang and A. Akhmanova. Microtubule tip-interacting proteins: a view from both ends. *Current Opinion in Cell Biology* **23**(1), 94–101, 2011. (Cit. on p. 8).

[70] R. D. Mullins and S. D. Hansen. In vitro studies of actin filament and network dynamics. *Current Opinion in Cell Biology* **25**(1), 6–13, 2013. (Cit. on p. 8).

[71] S. D. Hansen and R. D. Mullins. VASP is a processive actin polymerase that requires monomeric actin for barbed end association. *The Journal of Cell Biology* **191**(3), 571–584, 2010. (Cit. on pp. 8, 9).

[72] J. Helenius, G. Brouhard, Y. Kalaidzidis, S. Diez and J. Howard. The depolymerizing kinesin MCAK uses lattice diffusion to rapidly target microtubule ends. *Nature* **441**(7089), 115–119, 2006. (Cit. on pp. 8, 9, 11, 17, 97).

[73] G. J. Brouhard, J. H. Stear, T. L. Noetzel, J. Al-Bassam, K. Kinoshita, S. C. Harrison, J. Howard and A. A. Hyman. XMAP215 Is a Processive Microtubule Polymerase. *Cell* **132**(1), 79–88, 2008. (Cit. on pp. 8, 9, 11, 97).

[74] J. R. Cooper and L. Wordeman. The diffusive interaction of microtubule binding proteins. *Current Opinion in Cell Biology* **21**(1), 68–73, 2009. (Cit. on pp. 8, 10, 97).

[75] A. Melbinger, L. Reese and E. Frey. Microtubule Length Regulation by Molecular Motors. *Physical Review Letters* **108**(25), 258103–5, 2012. (Cit. on p. 9).

[76] L. Reese, A. Melbinger and E. Frey. Molecular mechanisms for microtubule length regulation by kinesin-8 and XMAP215 proteins. *Interface Focus* **4**(6), 20140031–20140031, 2014. (Cit. on p. 9).

[77] L. Reese, A. Melbinger and E. Frey. Crowding of molecular motors determines microtubule depolymerization. *Biophysical Journal* **101**(9), 2190–2200, 2011. (Cit. on p. 9).

[78] J. R. Cooper, M. Wagenbach, C. L. Asbury and L. Wordeman. Catalysis of the microtubule on-rate is the major parameter regulating the depolymerase activity of MCAK. *Nature Structural & Molecular Biology* **17**(1), 77–82, 2010. (Cit. on p. 9).

[79] A. F. Powers, A. D. Franck, D. R. Gestaut, J. Cooper, B. Gracyzk, R. R. Wei, L. Wordeman, T. N. Davis and C. L. Asbury. The Ndc80 Kinetochore Complex Forms Load-Bearing Attachments to Dynamic Microtubule Tips via Biased Diffusion. *Cell* **136**(5), 865–875, 2009. (Cit. on p. 9).

[80] D. R. Gestaut, B. Graczyk, J. Cooper, P. O. Widlund, A. Zelter, L. Wordeman, C. L. Asbury and T. N. Davis. Phosphoregulation and depolymerization-driven movement of the Dam1 complex do not require ring formation. *Nature Cell Biology* **10**(4), 407–414, 2008. (Cit. on p. 9).

[81] S. Konzack, E. Thies, A. Marx, E.-M. Mandelkow and E. Mandelkow. Swimming against the tide: mobility of the microtubule-associated protein tau in neurons. *The Journal of Neuroscience* **27**(37), 9916–9927, 2007. (Cit. on p. 9).

[82] M. Noujaim, S. Bechstedt, M. Wieczorek and G. J. Brouhard. Microtubules Accelerate the Kinase Activity of Aurora-B by a Reduction in Dimensionality. *PLoS ONE* **9**(2), e86786–9, 2014. (Cit. on p. 9).

[83] R. Dixit, B. Barnett, J. E. Lazarus, M. Tokito, Y. E. Goldman and E. L. F. Holzbaur. Microtubule plus-end tracking by CLIP-170 requires EB1. *Proceedings of the National Academy of Sciences of the United States of America* **106**(2), 492–497, 2009. (Cit. on p. 9).

[84] M. Y. Ali, E. B. Krementsova, G. G. Kennedy, R. Mahaffy, T. D. Pollard, K. M. Trybus and D. M. Warshaw. Myosin Va maneuvers through actin intersections and diffuses along microtubules. *Proceedings of the National Academy of Sciences* **104**(11), 4332–4336, 2007. (Cit. on pp. 9, 153, 154).

[85] K. Kinoshita, B. Habermann and A. A. Hyman. XMAP215: a key component of the dynamic microtubule cytoskeleton. *Trends in Cell Biology* **12**(6), 267–273, 2002. (Cit. on pp. 11, 18, 51).

[86] S. P. Maurer, N. I. Cade, G. Bohner, N. Gustafsson, E. Boutant and T. Surrey. EB1 Accelerates Two Conformational Transitions Important for Microtubule Maturation and Dynamics. *Current Biology* **24**(4), 372–384, 2014. (Cit. on p. 11).

[87] C. T. Friel and J. Howard. The kinesin-13 MCAK has an unconventional ATPase cycle adapted for microtubule depolymerization. *The EMBO Journal* **30**(19), 3928–3939, 2011. (Cit. on pp. 11, 52, 102).

[88] T. Chou and G. Lakatos. Clustered Bottlenecks in mRNA Translation and Protein Synthesis. *Physical Review Letters* **93**(19), 897–4, 2004. (Cit. on p. 15).

[89] G. Lakatos, T. Chou and A. Kolomeisky. Steady-state properties of a totally asymmetric exclusion process with periodic structure. *Physical Review E* **71**(1), 011103–11, 2005. (Cit. on p. 15).

[90] G. Adam and M. Delbrück. Reduction of dimensionality in biological diffusion processes. *Structural Chemistry and Molecular Biology*. San Francisco, 1968, pp. 198–215. (Cit. on p. 16).

[91] L. Mirny, M. Slutsky, Z. Wunderlich, A. Tafvizi, J. Leith and A. Kosmrlj. How a protein searches for its site on DNA: the mechanism of facilitated diffusion. *Journal of Physics A: Mathematical and Theoretical* **42**(43), 434013–24, 2009. (Cit. on p. 16).

[92] A. B. Kolomeisky. Physics of protein-DNA interactions: mechanisms of facilitated target search. *Physical Chemistry Chemical Physics : PCCP* **13**(6), 2088–2095, 2011. (Cit. on p. 16).

[93] O. Bénichou, C. Loverdo, M. Moreau and R. Voituriez. Intermittent search strategies. *Reviews of Modern Physics* **83**(1), 81–129, 2011. (Cit. on p. 16).

[94] M. Sheinman, O. Bénichou, Y. Kafri and R. Voituriez. Classes of fast and specific search mechanisms for proteins on DNA. *Reports on Progress in Physics* **75**(2), 026601–34, 2012. (Cit. on p. 16).

[95] G. A. Klein, K. Kruse, G. Cuniberti and F. Jülicher. Filament Depolymerization by Motor Molecules. *Physical Review Letters* **94**(10), 316–4, 2005. (Cit. on p. 17).

[96] M. Schmitt and H. Stark. Modelling bacterial flagellar growth. *EPL (Europhysics Letters)* **96**(2), 28001, 2011. (Cit. on p. 17).

[97] M. v. Smoluchowski. Versuch einer mathematischen Theorie der Koagulationskinetik kolloider Lösungen. *Zeitschrift für Physikalische Chemie* **92U**(1). (Cit. on p. 18).

[98] T. Maney, A. W. Hunter, M. Wagenbach and L. Wordeman. Mitotic centromere-associated kinesin is important for anaphase chromosome segregation. *The Journal of Cell Biology* **142**(3), 787–801, 1998. (Cit. on p. 18).

[99] K. Kinoshita, I. Arnal, A. Desai, D. N. Drechsel and A. A. Hyman. Reconstitution of physiological microtubule dynamics using purified components. *Science* **294**(5545), 1340–1343, 2001. (Cit. on p. 18).

[100] J. Howard and A. A. Hyman. Dynamics and mechanics of the microtubule plus end. *Nature* **422**(6933), 753–758, 2003. (Cit. on p. 51).

[101] G. Woehlke and M. Schliwa. Walking on two heads: the many talents of kinesin. *Nature Reviews Molecular Cell Biology* **1**(1), 50–58, 2000. (Cit. on pp. 52, 88).

[102] J. Howard, A. J. Hudspeth and R. D. Vale. Movement of microtubules by single kinesin molecules. *Nature* **342**(6246), 154–158, 1989. (Cit. on p. 52).

[103] S. M. Block, L. S. B. Goldstein and B. J. Schnapp. Bead movement by single kinesin molecules studied with optical tweezers. *Nature* **348**(6299), 348–352, 1990. (Cit. on pp. 52, 57, 175).

[104] N. Hirokawa, Y. Noda and Y. Okada. Kinesin and dynein superfamily proteins in organelle transport and cell division. *Current Opinion in Cell Biology* **10**(1), 60–73, 1998. (Cit. on p. 52).

[105] L. S. B. Goldstein and A. V. Philp. The Road Less Traveled: Emerging Principles of Kinesin Motor Utilization. *Annual Review of Cell and Developmental Biology* **15**(1), 141–183, 1999. (Cit. on p. 52).

[106] R. D. Vale, T. S. Reese and M. P. Sheetz. Identification of a novel force-generating protein, kinesin, involved in microtubule-based motility. *Cell* **42**(1), 39–50, 1985. (Cit. on p. 52).

[107] N. J. Carter and R. A. Cross. Mechanics of the kinesin step. *Nature* **435**(7040), 308–312, 2005. (Cit. on pp. 52, 103, 104, 106).

[108] A. Gennerich and R. D. Vale. Walking the walk: how kinesin and dynein coordinate their steps. *Current Opinion in Cell Biology* **21**(1), 59–67, 2009. (Cit. on pp. 52, 88).

[109] A. Yildiz, M. Tomishige, R. D. Vale and P. R. Selvin. Kinesin walks hand-over-hand. *Science* **303**(5658), 676–678, 2004. (Cit. on pp. 52, 88).

[110] R. A. Cross. The kinetic mechanism of kinesin. *Trends in Biochemical Sciences* **29**(6), 301–309, 2004. (Cit. on pp. 52, 88).

[111] S. Ray. Kinesin follows the microtubule's protofilament axis. *The Journal of Cell Biology* **121**(5), 1083–1093, 1993. (Cit. on pp. 52, 57).

[112] C. T. MacDonald, J. H. Gibbs and A. C. Pipkin. Kinetics of biopolymerization on nucleic acid templates. *Biopolymers* **6**(1), 1–25, 1968. (Cit. on p. 52).

[113] C. T. MacDonald and J. H. Gibbs. Concerning the kinetics of polypeptide synthesis on polyribosomes. *Biopolymers* **7**(5), 707–725, 1969. (Cit. on p. 52).

[114] F. Spitzer. Interaction of Markov processes. *Advances in Mathematics* **5**(2), 246–290, 1970. (Cit. on p. 52).

[115] M. Mobilia, T. Reichenbach, H. Hinsch, T. Franosch and E. Frey. Generic principles of active transport. *Banach Center Publications* **80**(80), 101–120, 2008. (Cit. on p. 52).

[116] B. Derrida, M. R. Evans, V. Hakim and V. Pasquier. Exact solution of a 1D asymmetric exclusion model using a matrix formulation. *Journal of Physics A: Mathematical and General* **26**(7), 1493–1517, 1993. (Cit. on p. 54).

[117] J. Krug. Boundary-induced phase transitions in driven diffusive systems. *Physical Review Letters* **67**(14), 1882–1885, 1991. (Cit. on p. 54).

[118] B. Derrida, E. Domany and D. Mukamel. An exact solution of a one-dimensional asymmetric exclusion model with open boundaries. *Journal of Statistical Physics* **69**(3-4), 667–687, 1992. (Cit. on p. 54).

[119] G. Schütz and E. Domany. Phase transitions in an exactly soluble one-dimensional exclusion process. *Journal of Statistical Physics* **72**(1-2), 277–296, 1993. (Cit. on p. 54).

[120] A. Parmeggiani, T. Franosch and E. Frey. Phase Coexistence in Driven One-Dimensional Transport. *Physical Review Letters* **90**(8), 1–4, 2003. (Cit. on p. 56).

[121] A. Parmeggiani, T. Franosch and E. Frey. Totally asymmetric simple exclusion process with Langmuir kinetics. *Physical Review E* **70**(4), 1469–20, 2004. (Cit. on p. 56).

[122] R. Juhász and L. Santen. Dynamics of an exclusion process with creation and annihilation. *Journal of Physics A: Mathematical and General* **37**(13), 3933–3944, 2004. (Cit. on p. 56).

[123] E. D. Andjel, M. D. Bramson and T. M. Liggett. Shocks in the asymmetric exclusion process. *Probability Theory and Related Fields* **78**(2), 231–247, 1988. (Cit. on p. 56).

[124] C. Leduc, K. Padberg-Gehle, V. Varga, D. Helbing, S. Diez and J. Howard. Molecular crowding creates traffic jams of kinesin motors on microtubules. *Proceedings of the National Academy of Sciences* **109**(16), 6100–6105, 2012. (Cit. on p. 56).

[125] I. A. Telley, P. Bieling and T. Surrey. Obstacles on the Microtubule Reduce the Processivity of Kinesin-1 in a Minimal In Vitro System and in Cell Extract. *Biophysical Journal* **96**(8), 3341–3353, 2009. (Cit. on p. 57).

[126] M. Rank and E. Frey. Crowding and Pausing Strongly Affect Dynamics of Kinesin-1 Motors along Microtubules. *Biophysical Journal* **115**(6), 1068–1081, 2018. (Cit. on p. 57).

[127] S. Klumpp and R. Lipowsky. Cooperative cargo transport by several molecular motors. *Proceedings of the National Academy of Sciences* **102**(48), 17284–17289, 2005. (Cit. on pp. 57, 175).

[128] V. Varga, J. Helenius, K. Tanaka, A. A. Hyman, T. U. Tanaka and J. Howard. Yeast kinesin-8 depolymerizes microtubules in a length-dependent manner. *Nature Cell Biology* **8**(9), 957–962, 2006. (Cit. on p. 57).

[129] K. H. Downing and E. Nogales. Tubulin and microtubule structure. *Current Opinion in Cell Biology* **10**(1), 16–22, 1998. (Cit. on p. 57).

[130] R. A. Walker, E. D. Salmon and S. A. Endow. The Drosophila claret segregation protein is a minus-end directed motor molecule. *Nature* **347**(6295), 780–782, 1990. (Cit. on p. 57).

[131] J. Yajima and R. A. Cross. A torque component in the kinesin-1 power stroke. *Nature Chemical Biology* **1**(6), 338–341, 2005. (Cit. on pp. 57, 58).

[132] X. Pan, S. Acar and J. M. Scholey. Torque generation by one of the motor subunits of heterotrimeric kinesin-2. *Biochemical and Biophysical Research Communications* **401**(1), 53–57, 2010. (Cit. on pp. 57, 58).

[133] J. Yajima, K. Mizutani and T. Nishizaka. A torque component present in mitotic kinesin Eg5 revealed by three-dimensional tracking. *Nature Structural & Molecular Biology* **15**(10), 1119–1121, 2008. (Cit. on pp. 57, 58).

[134] R. D. Vale and Y. Y. Toyoshima. Rotation and translocation of microtubules in vitro induced by dyneins from Tetrahymena cilia. *Cell* **52**(3), 459–469, 1988. (Cit. on pp. 57, 58).

[135] T. Nishizaka, T. Yagi, Y. Tanaka and S. Ishiwata. Right-handed rotation of an actin filament in an in vitro motile system. *Nature* **361**(6409), 269–271, 1993. (Cit. on pp. 57, 58).

[136] V. Bormuth, B. Nitzsche, F. Ruhnow, A. Mitra, M. Storch, B. Rammner, J. Howard and S. Diez. The Highly Processive Kinesin-8, Kip3, Switches Microtubule Protofilaments with a Bias toward the Left. *Biophysical Journal* **103**(1), L4–L6, 2012. (Cit. on p. 58).

[137] M. Brunnbauer, R. Dombi, T.-H. Ho, M. Schliwa, M. Rief and Z. Ökten. Torque Generation of Kinesin Motors Is Governed by the Stability of the Neck Domain. *Molecular Cell* **46**(2), 147–158, 2012. (Cit. on p. 58).

[138] A. Mitra, F. Ruhnow, S. Girardo and S. Diez. Directionally biased sidestepping of Kip3/kinesin-8 is regulated by ATP waiting time and motor–microtubule interaction strength. *Proceedings of the National Academy of Sciences* **115**(34), E7950–E7959, 2018. (Cit. on p. 58).

[139] S. Can, M. A. Dewitt and A. Yildiz. Bidirectional helical motility of cytoplasmic dynein around microtubules. *eLife* **3**, 2014. (Cit. on p. 58).

[140] W. L. Stepp, G. Merck, F. M. Planitz and Z. Ökten. Kinesin-2 motors adapt their stepping behavior for processive transport on axonemes and microtubules. *EMBO reports* **18**(11), 1947–1956, 2017. (Cit. on p. 58).

[141] A. I. Curatolo, M. R. Evans, Y. Kafri and J. Tailleur. Multilane driven diffusive systems. *Journal of Physics A: Mathematical and Theoretical* **49**(9), 095601, 2016. (Cit. on p. 58).

[142] R. A. Cross and A. McAinsh. Prime movers: the mechanochemistry of mitotic kinesins. *Nature Reviews Molecular Cell Biology* **15**(4), 257–271, 2014. (Cit. on p. 88).

[143] W. S. Saunders and M. A. Hoyt. Kinesin-related proteins required for structural integrity of the mitotic spindle. *Cell* **70**(3), 451–458, 1992. (Cit. on p. 88).

[144] T. U. Mayer, T. M. Kapoor, S. J. Haggarty, R. W. King, S. L. Schreiber and T. J. Mitchison. Small Molecule Inhibitor of Mitotic Spindle Bipolarity Identified in a Phenotype-Based Screen. *Science* **286**(5441), 971–974, 1999. (Cit. on p. 88).

[145] A. S. Kashlna, R. J. Baskin, D. G. Cole, K. P. Wedaman, W. M. Saxton and J. M. Scholey. A bipolar kinesin. *Nature* **379**(6562), 270–272, 1996. (Cit. on p. 88).

[146] E. R. Hildebrandt, L. Gheber, T. Kingsbury and M. A. Hoyt. Homotetrameric Form of Cin8p, a Saccharomyces cerevisiaeKinesin-5 Motor, Is Essential for Its in VivoFunction. *Journal of Biological Chemistry* **281**(36), 26004–26013, 2006. (Cit. on p. 88).

[147] L. C. Kapitein, E. J. G. Peterman, B. H. Kwok, J. H. Kim, T. M. Kapoor and C. F. Schmidt. The bipolar mitotic kinesin Eg5 moves on both microtubules that it crosslinks. *Nature* **435**(7038), 114–118, 2005. (Cit. on p. 88).

[148] I. Brust-Mascher and J. M. Scholey. Mitotic motors and chromosome segregation: the mechanism of anaphase B: Figure 1. *Biochemical Society Transactions* **39**(5), 1149–1153, 2011. (Cit. on p. 88).

[149] D. M. Roof, P. B. Meluh and M. D. Rose. Kinesin-related proteins required for assembly of the mitotic spindle. *The Journal of Cell Biology* **118**(1), 95–108, 1992. (Cit. on p. 88).

[150] M. A. Hoyt, L. He, K. K. Loo and W. S. Saunders. Two Saccharomyces cerevisiae kinesin-related gene products required for mitotic spindle assembly. *The Journal of Cell Biology* **118**(1), 109–120, 1992. (Cit. on p. 88).

[151] M. K. Chee and S. B. Haase. B-cyclin/CDKs regulate mitotic spindle assembly by phosphorylating kinesins-5 in budding yeast. *PLoS genetics* **6**(5), e1000935, 2010. (Cit. on p. 88).

[152] J. D. Tytell and P. K. Sorger. Analysis of kinesin motor function at budding yeast kinetochores. *The Journal of Cell Biology* **172**(6), 861–874, 2006. (Cit. on p. 88).

[153] H. Miki, Y. Okada and N. Hirokawa. Analysis of the kinesin superfamily: insights into structure and function. *Trends in Cell Biology* **15**(9), 467–476, 2005. (Cit. on p. 88).

[154] J. Roostalu, C. Hentrich, P. Bieling, I. A. Telley, E. Schiebel and T. Surrey. Directional Switching of the Kinesin Cin8 Through Motor Coupling. *Science* **332**(6025), 94–99, 2011. (Cit. on pp. 88, 90, 118).

[155] A. Gerson-Gurwitz, C. Thiede, N. Movshovich, V. Fridman, M. Podolskaya, T. Danieli, S. L. a. mper, D. R. Klopfenstein, C. F. Schmidt and L. Gheber. Directionality of individual kinesin-5 Cin8 motors is modulated by loop 8, ionic strength and microtubule geometry. *The EMBO Journal* **30**(24), 4942–4954, 2011. (Cit. on pp. 88, 89, 116).

[156] V. Fridman, A. Gerson-Gurwitz, O. Shapira, N. Movshovich, S. Lakamper, C. F. Schmidt and L. Gheber. Kinesin-5 Kip1 is a bi-directional motor that stabilizes microtubules and tracks their plus-ends in vivo. *Journal of Cell Science* **126**(18), 4147–4159, 2013. (Cit. on pp. 88, 118).

[157] M. Edamatsu. Bidirectional motility of the fission yeast kinesin-5, Cut7. *Biochemical and Biophysical Research Communications* **446**(1), 231–234, 2014. (Cit. on p. 88).

[158] M. Britto, A. Goulet, S. Rizvi, O. von Loeffelholz, C. A. Moores and R. A. Cross. Schizosaccharomyces pombekinesin-5 switches direction using a steric blocking mechanism. *Proceedings of the National Academy of Sciences* **113**(47), E7483–E7489, 2016. (Cit. on pp. 88, 89, 116, 118, 119).

[159] A. R. Popchock, K.-F. Tseng, P. Wang, P. A. Karplus, X. Xiang and W. Qiu. The mitotic kinesin-14 KlpA contains a context- dependent directionality switch. *Nature Communications* **7**, 1–9, 2016. (Cit. on pp. 88, 89, 118).

[160] O. Shapira, A. Goldstein, J. Al-Bassam and L. Gheber. A potential physiological role for bi-directional motility and motor clustering of mitotic kinesin-5 Cin8 in yeast mitosis. *Journal of Cell Science* **130**(4), 725–734, 2017. (Cit. on pp. 89, 90).

[161] T. Fallesen, J. Roostalu, C. Duellberg, G. Pruessner and T. Surrey. Ensembles of Bidirectional Kinesin Cin8 Produce Additive Forces in Both Directions of Movement. *Biophysical Journal* **113**(9), 2055–2067, 2017. (Cit. on pp. 89, 104, 105, 118, 121).

[162] K. Svoboda, P. P. Mitra and S. M. Block. Fluctuation analysis of motor protein movement and single enzyme kinetics. *Proceedings of the National Academy of Sciences* **91**(25), 11782–11786, 1994. (Cit. on p. 94).

[163] K. Visscher, M. J. Schnitzer and S. M. Block. Single kinesin molecules studied with a molecular force clamp. *Nature* **400**(6740), 184–189, 1999. (Cit. on pp. 94, 103, 104).

[164] S. Verbrugge, S. M. J. L. van den Wildenberg and E. J. G. Peterman. Novel Ways to Determine Kinesin-1's Run Length and Randomness Using Fluorescence Microscopy. *Biophysical Journal* **97**(8), 2287–2294, 2009. (Cit. on pp. 94, 97).

[165] A. A. Hyman, D. Chrétien, I. Arnal and R. H. Wade. Structural changes accompanying GTP hydrolysis in microtubules: information from a slowly hydrolyzable analogue guanylyl-(alpha,beta)-methylene-diphosphonate. *The Journal of Cell Biology* **128**(1-2), 117–125, 1995. (Cit. on pp. 96–98, 101, 118, 124).

[166] J. Yajima, M. C. Alonso, R. A. Cross and Y. Y. Toyoshima. Direct Long-Term Observation of Kinesin Processivity at Low Load. *Current Biology* **12**(4), 301–306, 2002. (Cit. on p. 97).

[167] W. Hua, E. C. Young, M. L. Fleming and J. Gelles. Coupling of kinesin steps to ATP hydrolysis. *Nature* **388**(6640), 390–393, 1997. (Cit. on p. 97).

[168] M. J. Schnitzer and S. M. Block. Kinesin hydrolyses one ATP per 8-nm step. *Nature* **388**(6640), 386–390, 1997. (Cit. on p. 97).

[169] D. T. Gillespie. Stochastic Simulation of Chemical Kinetics. *Annual Review of Physical Chemistry* **58**(1), 35–55, 2007. (Cit. on p. 99).

[170] C. T. Friel and J. Howard. Coupling of kinesin ATP turnover to translocation and microtubule regulation: one engine, many machines. *Journal of Muscle Research and Cell Motility* **33**(6), 377–383, 2012. (Cit. on p. 102).

[171] K. Svoboda and S. M. Block. Force and velocity measured for single kinesin molecules. *Cell* **77**(5), 773–784, 1994. (Cit. on pp. 103, 104).

[172] M. J. Schnitzer, K. Visscher and S. M. Block. Force production by single kinesin motors. *Nature Cell Biology* **2**(10), 718–723, 2000. (Cit. on pp. 103, 104).

[173] S. M. Block, C. L. Asbury, J. W. Shaevitz and M. J. Lang. Probing the kinesin reaction cycle with a 2D optical force clamp. *Proceedings of the National Academy of Sciences* **100**(5), 2351–2356, 2003. (Cit. on pp. 103, 104).

[174] J. O. L. Andreasson, B. Milic, G.-y. Chen, N. R. Guydosh, W. O. Hancock and S. M. Block. Examining kinesin processivity within a general gating framework. *eLife* **4**, 1166, 2015. (Cit. on pp. 103, 104).

[175] M. Nishiyama, H. Higuchi and T. Yanagida. Chemomechanical coupling of the forward and backward steps of single kinesin molecules. *Nature Cell Biology* **4**(10), 790–797, 2002. (Cit. on p. 106).

[176] B. E. Clancy, W. M. Behnke-Parks, J. O. L. Andreasson, S. S. Rosenfeld and S. M. Block. A universal pathway for kinesin stepping. *Nature Structural & Molecular Biology* **18**(9), 1020–1027, 2011. (Cit. on p. 106).

[177] C. Thiede, V. Fridman, A. Gerson-Gurwitz, L. Gheber and C. F. Schmidt. Regulation of bi-directional movement of single kinesin-5 Cin8 molecules. *BioArchitecture* **2**(2), 70–74, 2014. (Cit. on p. 116).

[178] A. Düselder, V. Fridman, C. Thiede, A. Wiesbaum, A. Goldstein, D. R. Klopfenstein, O. Zaitseva, M. E. Janson, L. Gheber and C. F. Schmidt. Deletion of the Tail Domain of the Kinesin-5 Cin8 Affects Its Directionality. *Journal of Biological Chemistry* **290**(27), 16841–16850, 2015. (Cit. on p. 116).

[179] S. Arrhenius. Über die Reaktionsgeschwindigkeit bei der Inversion von Rohrzucker durch Säuren. *Zeitschrift für Physikalische Chemie* **4U**(1), 1889. (Cit. on p. 118).

[180] S. Arrhenius. Über die Dissociationswärme und den Einfluss der Temperatur auf den Dissociationsgrad der Elektrolyte. *Zeitschrift für Physikalische Chemie* **4**(1), 1889. (Cit. on p. 118).

[181] N. Saito and K. Kaneko. Embedding dual function into molecular motors through collective motion. *Scientific reports* **7**(1), 44288, 2017. (Cit. on pp. 119, 121).

[182] D. M. Raskin and P. A. de Boer. Rapid pole-to-pole oscillation of a protein required for directing division to the middle of Escherichia coli. *Proceedings of the National Academy of Sciences* **96**(9), 4971–4976, 1999. (Cit. on p. 131).

[183] L. Rothfield, A. Taghbalout and Y.-L. Shih. Spatial control of bacterial division-site placement. *Nature reviews. Microbiology* **3**(12), 959–968, 2005. (Cit. on p. 131).

[184] M. Thanbichler and L. Shapiro. MipZ, a Spatial Regulator Coordinating Chromosome Segregation with Cell Division in Caulobacter. *Cell* **126**(1), 147–162, 2006. (Cit. on p. 131).

[185] Z. Hu and J. Lutkenhaus. Topological Regulation of Cell Division in E. coli. *Molecular Cell* **7**(6), 1337–1343, 2001. (Cit. on p. 131).

[186] W. B. Schofield, H. C. Lim and C. Jacobs-Wagner. Cell cycle coordination and regulation of bacterial chromosome segregation dynamics by polarly localized proteins. *The EMBO Journal* **29**(18), 3068–3081, 2010. (Cit. on p. 131).

[187] J. Lutkenhaus. The ParA/MinD family puts things in their place. *Trends in Microbiology* **20**(9), 411–418, 2012. (Cit. on p. 131).

[188] E. Bi and J. Lutkenhaus. FtsZ ring structure associated with division in Escherichia coli. *Nature* **354**(6349), 161–164, 1991. (Cit. on p. 131).

[189] D. W. Adams and J. Errington. Bacterial cell division: assembly, maintenance and disassembly of the Z ring. *Nature reviews. Microbiology* **7**(9), 642–653, 2009. (Cit. on p. 131).

[190] J. Lutkenhaus, S. Pichoff and S. Du. Bacterial cytokinesis: From Z ring to divisome. *Cytoskeleton* **69**(10), 778–790, 2012. (Cit. on pp. 131, 132).

[191] M. Ingerson-Mahar and Z. Gitai. A growing family: the expanding universe of the bacterial cytoskeleton. *FEMS Microbiology Reviews* **36**(1), 256–266, 2012. (Cit. on p. 131).

[192] K. M. Schoenemann and W. Margolin. Bacterial Division: FtsZ Treadmills to Build a Beautiful Wall. *Current Biology* **27**(8), R301–R303, 2017. (Cit. on p. 131).

[193] A. Mukherjee and J. Lutkenhaus. Guanine nucleotide-dependent assembly of FtsZ into filaments. *Journal of Bacteriology* **176**(9), 2754–2758, 1994. (Cit. on p. 132).

[194] H. P. Erickson, D. W. Taylor, K. A. Taylor and D. Bramhill. Bacterial cell division protein FtsZ assembles into protofilament sheets and minirings, structural homologs of tubulin polymers. *Proceedings of the National Academy of Sciences* **93**(1), 519–523, 1996. (Cit. on p. 132).

[195] J. Mingorance, M. Tadros, M. Vicente, J. M. González, G. Rivas and M. Vélez. Visualization of single Escherichia coli FtsZ filament dynamics with atomic force microscopy. *Journal of Biological Chemistry* **280**(21), 20909–20914, 2005. (Cit. on p. 132).

[196] M. A. Oliva, S. C. Cordell and J. Löwe. Structural insights into FtsZ protofilament formation. *Nature Structural & Molecular Biology* **11**(12), 1243–1250, 2004. (Cit. on p. 132).

[197] J. Löwe and L. A. Amos. Tubulin-like protofilaments in Ca2+-induced FtsZ sheets. *The EMBO Journal* **18**(9), 2364–2371, 1999. (Cit. on p. 132).

[198] H. P. Erickson, D. E. Anderson and M. Osawa. FtsZ in bacterial cytokinesis: cytoskeleton and force generator all in one. *Microbiology and molecular biology reviews : MMBR* **74**(4), 504–528, 2010. (Cit. on p. 132).

[199] Z. Li, M. J. Trimble, Y. V. Brun and G. J. Jensen. The structure of FtsZ filaments in vivo suggests a force-generating role in cell division. *The EMBO Journal* **26**(22), 4694–4708, 2007. (Cit. on p. 132).

[200] S. L. Milam, M. Osawa and H. P. Erickson. Negative-stain electron microscopy of inside-out FtsZ rings reconstituted on artificial membrane tubules show ribbons of protofilaments. *Biophysical Journal* **103**(1), 59–68, 2012. (Cit. on p. 132).

[201] S. J. Holden, T. Pengo, K. L. Meibom, C. Fernandez Fernandez, J. Collier and S. Manley. High throughput 3D super-resolution microscopy reveals Caulobacter crescentus in vivo Z-ring organization. *Proceedings of the National Academy of Sciences of the United States of America* **111**(12), 4566–4571, 2014. (Cit. on p. 132).

[202] A. W. Bisson-Filho *et al.* Treadmilling by FtsZ filaments drives peptidoglycan synthesis and bacterial cell division. *Science* **355**(6326), 739–743, 2017. (Cit. on p. 132).

[203] X. Yang, Z. Lyu, A. Miguel, R. McQuillen, K. C. Huang and J. Xiao. GTPase activity-coupled treadmilling of the bacterial tubulin FtsZ organizes septal cell wall synthesis. *Science* **355**(6326), 744–747, 2017. (Cit. on p. 132).

[204] S. X. Sun, S. Walcott and C. W. Wolgemuth. Cytoskeletal Cross-linking and Bundling Minireview in Motor-Independent Contraction. *Current Biology* **20**(15), R649–R654, 2010. (Cit. on p. 132).

[205] A. Dajkovic and J. Lutkenhaus. Z ring as executor of bacterial cell division. *Journal of Molecular Microbiology and Biotechnology* **11**(3-5), 140–151, 2006. (Cit. on p. 132).

[206] M. C. Marchetti, J. F. Joanny, S. Ramaswamy, T. B. Liverpool, J. Prost, M. Rao and R. A. Simha. Hydrodynamics of soft active matter. *Reviews of Modern Physics* **85**(3), 1143–1189, 2013. (Cit. on pp. 132–134).

[207] S. Ramaswamy. The Mechanics and Statistics of Active Matter. *Annual Review of Condensed Matter Physics* **1**(1), 323–345, 2010. (Cit. on pp. 132, 133).

[208] N. D. Mermin and H. Wagner. Absence of Ferromagnetism or Antiferromagnetism in One- or Two-Dimensional Isotropic Heisenberg Models. *Physical Review Letters* **17**(26), 1307–1307, 1966. (Cit. on p. 133).

[209] T. Vicsek and A. Zafeiris. Collective motion. *Physics Reports* **517**(3-4), 71–140, 2012. (Cit. on pp. 133, 134).

[210] M. E. Cates and J. Tailleur. Motility-Induced Phase Separation. *Annual Review of Condensed Matter Physics* **6**(1), 219–244, 2015. (Cit. on pp. 133, 134).

[211] T. Vicsek, A. Czirók, E. Ben-Jacob, I. Cohen and O. Shochet. Novel type of phase transition in a system of self-driven particles. *Physical Review Letters* **75**(6), 1226–1229, 1995. (Cit. on p. 133).

[212] G. Grégoire and H. Chaté. Onset of Collective and Cohesive Motion. *Physical Review Letters* **92**(2), 487–4, 2004. (Cit. on p. 134).

[213] H. Chaté, F. Ginelli and G. Grégoire. Comment on "Phase Transitions in Systems of Self-Propelled Agents and Related Network Models". *Physical Review Letters* **99**(22), 229601–1, 2007. (Cit. on p. 134).

[214] J. Toner and Y. Tu. Long-Range Order in a Two-Dimensional Dynamical XY Model: How Birds Fly Together. *Physical Review Letters* **75**(23), 4326–4329, 1995. (Cit. on p. 134).

[215] J. Toner and Y. Tu. Flocks, herds, and schools: A quantitative theory of flocking. *Physical Review E* **58**(4), 4828–4858, 1998. (Cit. on p. 134).

[216] E. Bertin, M. Droz and G. Grégoire. Boltzmann and hydrodynamic description for self-propelled particles. *Physical Review E* **74**(2), 3521–4, 2006. (Cit. on p. 134).

[217] E. Bertin, M. Droz and G. Grégoire. Hydrodynamic equations for self-propelled particles: microscopic derivation and stability analysis. *Journal of Physics A: Mathematical and Theoretical* **42**(44), 445001–32, 2009. (Cit. on p. 134).

[218] I. Theurkauff, C. Cottin-Bizonne, J. Palacci, C. Ybert and L. Bocquet. Dynamic Clustering in Active Colloidal Suspensions with Chemical Signaling. *Physical Review Letters* **108**(26), 268303–5, 2012. (Cit. on p. 134).

[219] J. Palacci, S. Sacanna, A. P. Steinberg, D. J. Pine and P. M. Chaikin. Living crystals of light-activated colloidal surfers. *Science* **339**(6122), 936–940, 2013. (Cit. on p. 134).

[220] I. Buttinoni, J. Bialké, F. Kümmel, H. Löwen, C. Bechinger and T. Speck. Dynamical Clustering and Phase Separation in Suspensions of Self-Propelled Colloidal Particles. *Physical Review Letters* **110**(23), 238301–5, 2013. (Cit. on p. 134).

[221] A. Bricard, J.-B. Caussin, N. Desreumaux, O. Dauchot and D. Bartolo. Emergence of macroscopic directed motion in populations of motile colloids. *Nature* **503**(7474), 95–98, 2013. (Cit. on p. 134).

[222] J. Deseigne, O. Dauchot and H. Chaté. Collective Motion of Vibrated Polar Disks. *Physical Review Letters* **105**(9), 098001–4, 2010. (Cit. on p. 134).

[223] H. Wioland, F. G. Woodhouse, J. Dunkel, J. O. Kessler and R. E. Goldstein. Confinement Stabilizes a Bacterial Suspension into a Spiral Vortex. *Physical Review Letters* **110**(26), 268102–5, 2013. (Cit. on p. 134).

[224] H. P. Zhang, A. Be'er, E.-L. Florin and H. L. Swinney. Collective motion and density fluctuations in bacterial colonies. *Proceedings of the National Academy of Sciences of the United States of America* **107**(31), 13626–13630, 2010. (Cit. on p. 134).

[225] C. Dombrowski, L. Cisneros, S. Chatkaew, R. E. Goldstein and J. O. Kessler. Self-Concentration and Large-Scale Coherence in Bacterial Dynamics. *Physical Review Letters* **93**(9), 193–4, 2004. (Cit. on p. 134).

[226] S. Thutupalli, M. Sun, F. Bunyak, K. Palaniappan and J. W. Shaevitz. Directional reversals enable Myxococcus xanthuscells to produce collective one-dimensional streams during fruiting-body formation. *Journal of The Royal Society Interface* **12**(109), 20150049–9, 2015. (Cit. on p. 134).

[227] J. Buhl, D. J. T. Sumpter, I. D. Couzin, J. J. Hale, E. Despland, E. R. Miller and S. J. Simpson. From disorder to order in marching locusts. *Science* **312**(5778), 1402–1406, 2006. (Cit. on p. 134).

[228] V. T. Natarajan, P. Ganju, A. Ramkumar, R. Grover and R. S. Gokhale. Multifaceted pathways protect human skin from UV radiation. *Nature Chemical Biology* **10**(7), 542–551, 2014. (Cit. on p. 152).

[229] M. M. Rozdzial and L. T. Haimo. Bidirectional pigment granule movements of melanophores are regulated by protein phosphorylation and dephosphorylation. *Cell* **47**(6), 1061–1070, 1986. (Cit. on p. 152).

[230] A. Daniolos, A. B. Lerner and M. R. Lerner. Action of Light on Frog Pigment Cells in Culture. *Pigment Cell Research* **3**(1), 38–43, 1990. (Cit. on p. 152).

[231] A. R. Reilein, I. S. Tint, N. I. Peunova, G. N. Enikolopov and V. I. Gelfand. Regulation of organelle movement in melanophores by protein kinase A (PKA), protein kinase C (PKC), and protein phosphatase 2A (PP2A). *The Journal of Cell Biology* **142**(3), 803–813, 1998. (Cit. on p. 152).

[232] M. Obika and S. Negishi. Effects of hexylene glycol and nocodazole on microtubules and melanosome translocation in melanophores of the medaka Oryzias latipes. *Journal of Experimental Zoology* **235**(1), 55–63, 1985. (Cit. on p. 153).

[233] S. P. Gross, M. C. Tuma, S. W. Deacon, A. S. Serpinskaya, A. R. Reilein and V. I. Gelfand. Interactions and regulation of molecular motors in Xenopus melanophores. *The Journal of Cell Biology* **156**(5), 855–865, 2002. (Cit. on pp. 153, 175).

[234] V. Rodionov, J. Yi, A. Kashina, A. Oladipo and S. P. Gross. Switching between Microtubule- and Actin-Based Transport Systems in Melanophores Is Controlled by cAMP Levels. *Current Biology* **13**(21), 1837–1847, 2003. (Cit. on pp. 153, 157, 161).

[235] B. M. Slepchenko, I. Semenova, I. Zaliapin and V. Rodionov. Switching of membrane organelles between cytoskeletal transport systems is determined by regulation of the microtubule-based transport. *The Journal of Cell Biology* **179**(4), 635–641, 2007. (Cit. on pp. 153, 170).

[236] A. Oberhofer, P. Spieler, Y. Rosenfeld, W. L. Stepp, A. Cleetus, A. N. Hume, F. Mueller-Planitz and Z. Ökten. Myosin Va's adaptor protein melanophilin enforces track selection on the microtubule and actin networks in vitro. *Proceedings of the National Academy of Sciences of the United States of America* **114**(24), E4714–E4723, 2017. (Cit. on p. 153).

[237] J. Snider, F. Lin, N. Zahedi, V. Rodionov, C. C. Yu and S. P. Gross. Intracellular actin-based transport: how far you go depends on how often you switch. *Proceedings of the National Academy of Sciences* **101**(36), 13204–13209, 2004. (Cit. on pp. 158, 174, 176).

[238] I. Zaliapin, I. Semenova, A. Kashina and V. Rodionov. Multiscale Trend Analysis of Microtubule Transport in Melanophores. *Biophysical Journal* **88**(6), 4008–4016, 2005. (Cit. on p. 162).

[239] I. Semenova, A. Burakov, N. Berardone, I. Zaliapin, B. Slepchenko, T. Svitkina, A. Kashina and V. Rodionov. Actin Dynamics Is Essential for Myosin-Based Transport of Membrane Organelles. *Current Biology* **18**(20), 1581–1586, 2008. (Cit. on p. 174).

[240] K. Xu, H. P. Babcock and X. Zhuang. Dual-objective STORM reveals three-dimensional filament organization in the actin cytoskeleton. *Nature Methods* **9**(2), 185–188, 2012. (Cit. on p. 174).

[241] Y. Zhang, A. Yoshida, N. Sakai, Y. Uekusa, M. Kumeta and S. H. Yoshimura. In vivo dynamics of the cortical actin network revealed by fast-scanning atomic force microscopy. *Microscopy* **66**(4), 272–282, 2017. (Cit. on p. 174).

[242] E. Schulze and M. Kirschner. Microtubule dynamics in interphase cells. *The Journal of Cell Biology* **102**(3), 1020–1031, 1986. (Cit. on p. 174).

[243] M. Brunstein, L. Bruno, M. Desposito and V. Levi. Anomalous dynamics of melanosomes driven by myosin-V in Xenopus laevis melanophores. *Biophysical Journal* **97**(6), 1548–1557, 2009. (Cit. on p. 174).

[244] D. Arcizet, B. Meier, E. Sackmann, J. O. Rädler and D. Heinrich. Temporal Analysis of Active and Passive Transport in Living Cells. *Physical Review Letters* **101**(24), 1453–4, 2008. (Cit. on p. 174).

[245] C. Leduc, O. Campàs, K. B. Zeldovich, A. Roux, P. Jolimaitre, L. Bourel-Bonnet, B. Goud, J.-F. Joanny, P. Bassereau and J. Prost. Cooperative extraction of membrane nanotubes by molecular motors. *Proceedings of the National Academy of Sciences* **101**(49), 17096–17101, 2004. (Cit. on p. 175).

[246] A. D. Mehta, R. S. Rock, M. Rief, J. A. Spudich, M. S. Mooseker and R. E. Cheney. Myosin-V is a processive actin-based motor. *Nature* **400**(6744), 590–593, 1999. (Cit. on p. 176).

[247] E. Schrödinger. *What Is Life? The Physical Aspect of the Living Cell*. Cambridge University Press, Cambridge, 1944. (Cit. on p. 177).

Acknowledgements

Scientific advance is rarely the achievement of an individual person but the collaborative effort of many. This holds also true for the work on my PhD thesis over the past years. I therefore want to cordially thank the people listed in the following.

First and foremost, my deepest gratitude goes to Erwin Frey who was a supervisor and mentor over the past years. Without your enduring support, trust in my visions, and without giving me the freedom to explore, this thesis wouldn't have been possible. Your group truly is an inspiring place for scientific research with an omnipresent friendly and helpful atmosphere. Thank you!

I would also like to thank my second referee, Mauro Mobilia. It is an honor that you take the trouble to review my thesis and to travel to Munich for my oral examination. Thanks!

I am very happy about the best collaborators that I could have imagined: The groups of Zeynep Ökten and of Leah Gheber. In particular, I would like to thank Angela Oberhofer, Himanshu Panday, Peter Spieler, Willi Stepp, Leah Gheber, and Zeynep Ökten. It is a real pleasure to work with people who share the same deep passion for science that I feel. By our collaborations, you helped a theorist to understand at least a bit of biology and to be happy to apply his equations to the "real world". Thanks to every one of you for all the fun, support, and inspiration for exciting research!

Over the years, I also had the pleasure to work and discuss with many intelligent and motivated people in the group of Erwin Frey. First of all, I would like to thank Louis Reese for his support over my first years in Erwin's group and during our research projects! Second, I would like to express my gratitude to Patrick Wilke for all the fun we had during our research project, for all the endless discussions about science and anything else, and for becoming a true friend over the years. Along the same lines, I also thank Lorenz Huber and Jonas Denk for the great time during our research project on FtsZ (especially during our "Spezi Energy" powered sessions) and for your help in all kinds of situations. It was always great fun to spend time with you, whether on conferences, holidays, or while working! I would also like to thank all the other people in the group with whom I had plenty of scientific (and non-scientific) discussions and exchange. This includes in particular Silke Bergeler, Philipp Geiger, Isabella Graf, Laeschkir Hassan, Timo Krüger, and Moritz Striebel. Special thanks also go to Silke Bergeler and Isabella Graf with whom I shared the office. You made room A308 a place where I looked forward to go to and I really enjoyed spending my

time with you! In general, I would like to thank the whole group of Erwin Frey for the great and helpful atmosphere!

Further, I want to thank all the people who read parts of this thesis and gave me extremely valuable feedback: David Brückner, Jonas Denk, Isabella Graf, Laeschkir Hassan, Lorenz Huber, Timo Krüger, Ann-Sophie Stephan, Jürgen Stephan, Valentin Stierle, Moritz Striebel, and Patrick Wilke.

I also want to thank those people that were not part of my direct scientific network but who supported me tremendously over the past years by being the best friends ever: Special thanks go to the "Quatro", Jürgen Stephan, Florian Pils, and Regina Wittig, to Markus Dobler and to Valentin Stierle. You have always supported me, ensured tons of great fun, and listened to my problems whenever I was stuck. You guys are the best! I wish to express my deepest gratitude to Ann-Sophie Stephan for her never-ending support and love over the past years! You cheered me up when I was down, made me laugh when I was grumpy, always believed in me, and supplied me with coffee when I was tired. I hope that I'll ever be able to give you back some of the unimaginable help that you have given me! There is no way to thank my mother, Olga Reithmann, enough for her love and help since I'm alive. Without you, none of this work would have been possible in any imaginable way! Thank you so, so much!